



City Research Online

City, University of London Institutional Repository

Citation: Lorenzi, M. (2017). X-ray computed microtomography applications for complex geometries and multiphase flow. (Unpublished Doctoral thesis, City, University of London)

This is the accepted version of the paper.

This version of the publication may differ from the final published version.

Permanent repository link: <https://openaccess.city.ac.uk/id/eprint/19794/>

Link to published version:

Copyright: City Research Online aims to make research outputs of City, University of London available to a wider audience. Copyright and Moral Rights remain with the author(s) and/or copyright holders. URLs from City Research Online may be freely distributed and linked to.

Reuse: Copies of full items can be used for personal research or study, educational, or not-for-profit purposes without prior permission or charge. Provided that the authors, title and full bibliographic details are credited, a hyperlink and/or URL is given for the original metadata page and the content is not changed in any way.

X-ray computed microtomography applications for complex geometries and multiphase flow

B.Eng. Massimo Lorenzi

A thesis submitted for the fulfilment of the requirements of City,
University of London for the degree of Doctor of Philosophy

CITY, UNIVERSITY OF LONDON



School of Mathematics, Computer Science & Engineering

December, 2017

TABLE OF CONTENTS

List of illustrations	5
List of tables	19
Acknowledgments.....	21
Declaration to the University Librarian.....	23
Thesis abstract.....	25
Thesis introduction.....	27
Chapter 1 - Description of microCT technique and equipment.....	31
1.1 Interaction of X-rays with matter.....	31
1.2 How Computed Tomography works.....	39
1.3 Description of the Unibg microCT	46
1.4 Capability of microCT to measure geometries	53
1.5 Assessing volumetric reconstruction accuracy	54
1.6 Scale calibration	64
1.7 Beam hardening correction for metal parts.....	65
1.8 Software used for tomographic reconstruction	69
Chapter 2 - Applications to complex geometries (thermal-fluid dynamics)	71
2.1 Introduction	71
2.2 Literature review on drop shape analysis.....	71
2.3 Drop on Teflon	74
2.4 Drop on record.....	80
2.5 Drop on GDL (Gas Diffusion Layer).....	89
Chapter 3 - Applications to complex geometries (real injectors + test rig model).....	97
3.1 Injector internal geometry reconstruction.....	97
3.2 Cavitation induced erosion detection.....	111
Chapter 4 - Applications to multiphase flow – cavitation.....	115
4.1 Introduction	115
4.2 Experimental test rig design for void fraction measurements.....	116

4.3	Void fraction measurement uncertainty	128
4.4	Experimental results	134
	Conclusions	151
	Recommendations for future work	153
	List of publications	157

LIST OF ILLUSTRATIONS

Figure 1-1 (Top) localization of X-ray wavelengths and energies, distinguished as soft and hard X-rays, in the electromagnetic spectrum; (Bottom - from left to right) application of X-rays to determine the arrangement of atoms in the crystalline solids, breast cancer screening radiography, head and neck computed tomography scan, airport security baggage scanning for safety reasons. [38].....	32
Figure 1-2 Schematic section view of a transmission target X-ray source. From left to right we can find the filament cathode (in red), the produced beam of electrons (in green), the alignment unit and focusing electronic lenses (in orange), the electron target (in grey), the output window (in purple) and the mitted X-ray beam (in yellow).	32
Figure 1-3 Visualization of the production of X-rays through the interaction of electrons with target atoms. Electrons numbered 1 to 4 hit the target from left producing X-rays of energy proportional to the intensity of their interaction with the nucleus and its electrons. Image inspired by an illustration present in [37]...	32
Figure 1-4 Image of the electrons travelling inside the target material produced with software “CASINO” [39].....	33
Figure 1-5 Tungsten (W) target spectrum simulated with Spektr software [40].	33
Figure 1-6 Contribution of each X-ray attenuation mechanism calculated for Beryllium and X-rays energies between 5 keV and 160 keV with software XMuDat [41] based on tabulated values of [42].....	36
Figure 1-7 Representation of the interaction between an incoming monochromatic X-ray radiation and a homogenous object material.....	36
Figure 1-8 X-ray CMOS detector simplified layout. From left to right: incoming X-ray radiation, protection plate (grey), scintillator layer (yellow), fibre optic plate (blue), photodiode (green), CMOS sensor (purple) and electronic readout circuitry (orange).	39
Figure 1-9 Conversion probability of Caesium iodide phosphor doped with Thallium based on incoming X-ray energies form 0 to 120 keV. Source: redrawn from [43].	39
Figure 1-10 Image from (Gdh-commonswiki) First prototype of computed tomography scanner produced by Sir Godfrey Newbold Hounsfield and Allan MacLeod Cormack. In the left image Sir. Hounsfield is pictured with his first commercially available CAT, in the right picture the CAT prototype is visible with a sample brain as object to be scanned.....	41
Figure 1-11 Layout of sample tomographic acquisition. From left to right we have the X-ray source, represented with a pointwise emission, the rotary stage with the cubic object to be scanned positioned on a sustaining cylindrical sample holder, the detector where the transmitted radiation is acquired and sampled to be saved in a 2D image file, the stack of acquired radiographies, one for each positional step, ready to be processed for reconstruction.....	41
Figure 1-12 Illustration of the object shape and position guess through projections observation: the volume to be reconstructed shown in 3D on the left contains a cylinder and a rectangular cuboid: from the three	

projections shown on the right it is clearly impossible to guess the correct shape and position of the two objects even though each projection furnish partial data about the desired information.41

Figure 1-13 Schematic view of the circular cone beam tomography with mid-plane highlighted. Image from [45]42

Figure 1-14 Graphical visualization of the rotation axis of the selected volume to be reconstructed.....42

Figure 1-15 (from top left to bottom right) original projection image without corrections; dark, gain and defect image to be used for projection correction; image corrected with the previous three correction images; legitimized and normalized image; cosine weighted image; ramp filtered image; smoothed image; horizontal and vertical slices resulting from the reconstructed injection channel.....44

Figure 1-16 Sinogram of the proposed sample reconstruction of a cylinder and a parallelepiped. (Right) three sample projections are displayed corresponding to angle 0°, 90° and 135°. (Middle) line profiles of the same detector line extracted for all the three projections. (Right) complete sinogram from 0° to 360° of the analysed line before image logarithmisation and filtration.44

Figure 1-17 Left: unfiltered sinogram (top) and simplified back projection of a point (bottom) showing the image blurring that would results by the back-projection process if the images weren't high-pass filtered. Right: same sinogram image ramp filtered to enhance high frequencies (top) and same back projection of a point with filtered sinogram. It is clear the necessity of the filter enhancing high frequencies.45

Figure 1-18 Back projection process: each projection line is back projected on the projection plane, which represents an horizontal cross section plane of the reconstructed volume, to reconstruct by summation the shape and material property value of the scanned object.....45

Figure 1-19 Outside view of the X-ray machine with door open; control electrical cabinet on the right side of the picture.47

Figure 1-20 Close-up view of the inside of the cabinet with (from right to left) X-ray source, rotary stage and X-ray detector displayed.47

Figure 1-21 Coordinate system of the microCT machine.47

Figure 1-22 Emission axis alignment process: one radiography at each specific distance from the X-ray source is acquired and processed to obtain the emission centre as perceived by the detector. Based on this information the overall emission axis can be calculated and corrected moving the detector if not linear. .48

Figure 1-23 Left – colour coded radiography of the non -aligned X-ray source: the X-ray intensity is not symmetric with respect to the detectors' centre point. Right – same colour coded radiography of the same X-ray source after alignment: X-rays intensity symmetry is evident.....48

Figure 1-24 (left) schematic view of microCT setup evidencing distances of interest for magnification calculation; (right) penumbra phenomenon illustrated: (right-top) a perfect nominally pointwise X-ray source projects a single X-ray emission cone creating a sharp single image of the object on the detector panel, while (right - bottom) an X-ray source with non-negligible dimension produces a penumbra effect causing blurring since in this case X-rays are emitted throughout its full area. N.B. penumbra effect shown

only for the first face of the cube object and for just one side (worst case) of the emitting area, side 1, the same happens symmetrically for emission point 2.	50
Figure 1-25 Air bearing rotary stage produced by Aerotech utilized to rotate the sample during radiographies acquisitions.	50
Figure 1-26 X-ray detector utilized to acquire X-ray images during tomographies. The front surface shows the carbon fibre window that seals and protects the active scintillator area. On the side the BNC trigger in and trigger out connectors are visible. On the same size the power supply connector and the Ethernet cable plug are present.	51
Figure 1-27 Modulation transfer function as communicated by the detector producer.	52
Figure 1-28 Linearity of the detector over its full range scale.	52
Figure 1-29 Illustration of the control equipment layout of the tomography machine.	53
Figure 1-30 (Left) nano-bar phantom positioned near to a match for scale comparison. (right) enlarged view of the middle section of the phantom cylinder revealing the inside with the two chips positioned axially (chip1) and perpendicularly (chip2). Source: image courtesy of QRM GmbH (with own overlays).....	56
Figure 1-31 : (left) layout of the full engraved area of the two silicon chips contained in the phantom. (right) zoom of the central part of the engraved area showing line and point patterns with width from 10 to 1 μm . Source: image courtesy of QRM GmbH	56
Figure 1-32 (left) Slanted edge present on the QRD phantom. (right) indication of the portion of the slanted edge utilized for the calculation of reconstruction resolution.	56
Figure 1-33 (top-left) 3D rendering of the reconstructed volume of the vertical chip of the QRM phantom. (bottom-left) Zoom of the central area of the phantom where it is clearly visible the possibility to distinguish lines of 4 μm with the nominal tomography resolution set at 2.19 μm .(right) from top to bottom cross cut of the 10-8-6-4-2 μm lines to show engraved lines distinguishability down to 4 μm , while the 2 μm apart lines are not clearly identifiable.	57
Figure 1-34 Plot of the Modulation Transfer Function (MTF) for the area selected on the reconstructed phantom slice.	57
Figure 1-35 Zoom of the plot of the Modulation Transfer Function (MTF) for the right hand side of the modulation transfer function of the edge with indication of the function values for 10% transmission. ...	58
Figure 1-36 Plot of the Edge Spread Function (ESF) for the area selected on the reconstructed phantom slice.	58
Figure 1-37 Plot of the Line Spread Function (LSF) for the area selected on the reconstructed phantom slice.	58
Figure 1-38 (top) 2 mm Renishaw stylus utilized as geometrical phantom for the mm size objects. (bottom) measure of stylus diameter with calibrated digital micrometre.	59

Figure 1-39 (left) picture of 2 mm Renishaw stylus with (right) its rendered reconstruction form CT data.	59
Figure 1-40 (left) in red reconstructed stl surface points selected for the fitting operation. (right) in green nominal fitted sphere overlaid to the original reconstructed stl surface shown in grey.	60
Figure 1-41 Table of deviation from nominal sphere of mesh reconstructed from microCT data considering a 3 sigma Gaussian fitting of original sphere surface points.	60
Figure 1-42 Table of deviation from nominal sphere of mesh reconstructed from microCT data considering all available points of original sphere surface.	61
Figure 1-43 Deviation of sphere surface created with all available points to show pole artefact. As it can be seen the mesh deviation points that increase by three times the surface deviation from nominal spherical geometry are concentrated near the tomography rotation axis (dark brown in the figure).	61
Figure 1-44 (left) in red stl surface cylinder points selected for the calculation of the fitting nominal cylinder. (right) in green nominal cylinder created form the selected pints overlaid to the original stl surface shown in grey.	61
Figure 1-45 Table of deviation from nominal cylinder of mesh reconstructed from microCT data considering 3-sigma points of original surface.	62
Figure 1-46 (left) overall and zoomed picture of 0.3 mm Renishaw stylus and (right) its rendered reconstruction from CT data.	62
Figure 1-47 (left) in red selected surface point to fit nominal geometry (right) nominal sphere (in green) created with the fitting operation overlaid to the original mesh (grey).	63
Figure 1-48 Table of deviation from nominal sphere of mesh reconstructed from microCT data considering 3-sigma points of original surface.	63
Figure 1-49 (From top to bottom) picture of the diesel injector tip that will be the object of geometrical reconstruction within this thesis, and the 2 mm and 0.3 mm Renishaw styli to visualize the scale between the three objects.	63
Figure 1-50 (right) schematic section view of the reference scaling phantom created with the two Renishaw styli: the outer plexiglass container has been cut to reveal the layout of the two styli. (left) picture of the real sample produced and utilized.	64
Figure 1-51 (left) stl surface of the two styli reconstructed from the single CT dataset. (right) in green 3-sigma fitting spheres utilized to calculate the distance between the centres, the line connecting the two centres is highlighted as “reference distance”	65
Figure 1-52 (left) axially perpendicular slice of a sample metal cylinder showing beam artefact in the form of degrading greyscale values in the direction going from the outer border to the cylinder centre. (right) plot of greyscale values vs. diameter position of the yellow line over imposed to the cylinder section present in the left image.	65

Figure 1-53 (left) axially perpendicular slice of a Diesel injector tip reconstructed with microCT showing streaks artefacts produced by injection holes, yellow arrows highlight modification of calculated attenuation value which is visible for areas inside the injector material and outside (air). (centre) plot of greyscale values indicated by the line in the left image, blue arrows show lower attenuation due to beam hardening streaks. (right) same slice after beam hardening correction application,.....	66
Figure 1-54 Unfiltered (grey line) versus filtered (blue) spectrum.	66
Figure 1-55 (left) radiography of the step wedge created with a tack of metal foil of 0.4 mm thickness and (right) grayscale values plot of the yellow line through its length.	67
Figure 1-56 (left) radiography of Diesel injector tip without needle with yellow line over imposed to the area utilized for the calculation of the self-wedge map. (right) Illustration of the thicknesses calculation for the object of interest.	68
Figure 1-57 (left) plot of the greyscale value of the radiography indicated by the yellow line showing detected material attenuation through material thickness. (right) table of radiography greyscale values vs position to be used to correlated greyscale valued with calculated thicknesses.	68
Figure 1-58 (left) same axially perpendicular slice of the sample metal cylinder showing beam artefact correction result. (right) plot of greyscale values vs diameter position of the yellow line over imposed to the cylinder section present in the left image revealing grey values homogeneity improvement due to applied correction.	69
Figure 2-1 a) A diagram that shows the contact angle and interphase-energy between 3 phases (gas, liquid, solid). b) drop triple line highlighted in red. Images from a) [68] b) own.	72
Figure 2-2 Section view of the ideally axisymmetric drop visualizing the two radii utilized by the Laplace-Young equation.	73
Figure 2-3 A droplet resting on a solid surface and surrounded by a gas forms a characteristic contact angle θ . If the solid surface is rough, and the liquid is in intimate contact with the solid asperities, the droplet is in the Wenzel state. If the liquid rests on the tops of the asperities, it is in the Cassie-Baxter state. Image from [78]	73
Figure 2-4 Drop of distilled water of almost 5 mm diameter gently deposited on a Teflon surface.	76
Figure 2-5 Level with a resolution of 50 micrometre per meter utilized for the drop on Teflon.	76
Figure 2-6 a) Drop of distilled water on Teflon cylinder (picture taken with a discarded cylinder. b) Sample radiography of the surface with deposited drop.	76
Figure 2-7 Visualization of the drop on Teflon positioned in front of the X-ray source for scanning purposes. The partially anti-evaporation cap and beneath water pool is visible.....	76
Figure 2-8 a) superposition of reference drop radiographies (before and after tomographic acquisition in the same position). b) zoomed view of the drop contours showing the still present evaporation effect. ...	77
Figure 2-9 Overlay of drop radiography before and after tomographic scan without anti-evaporation cap.	77

Figure 2-10 Top-left – reconstructed volume section showing attenuation coefficient difference between drop and Teflon. Bottom-left – coloured render with transparency of the reconstructed drop-surface volume. Right – solid 3D render of the reconstructed volume.	78
Figure 2-11 top left – stl drop surface visualized in green with radial sections shown in black. top right – visualization of only the radial sections contours (36 of the 120 used). Bottom left and right – top and bottom view of the drop-surface stl clearly showing the non-circular footprint of the drop.	79
Figure 2-12 Reprinted with permissions from [79]. 3D rendering of the fitted profiles coloured to represent experimental-fitted profiles deviation. Colour from blue (0%) to red (3.85%) is proportional to the dimensionless error $\Delta R/R_{max}$	79
Figure 2-13 a) – b) Reprinted with permissions from [79]. Graphical visualizations of the triple line trajectory and contact angle measurement comparison between experimental and fitted datasets. a) xy plane localized comparison of drop-surface points: green circles represent experimental points while black circles represent fitted data, the maximum distance between analogous points is 72 μm b) contact angle measurements: green dots represent positions where experimental and fitted contact angle measurements are in good agreement, 192 points of the original 240, while red triangles represent point with bad agreement.....	79
Figure 2-14 top-left – sample drop deposited on the record surface. Top-right schematic section of the record profile to highlight characteristic geometrical measures ($p = 320 \mu m$; $h = 92 \mu m$; $w = 136 \mu m$). bottom-left, bottom-right: side view of a sample surface-drop couple.....	81
Figure 2-15 Picture of a small drop of Glycerol on top of the needle utilized to place it on the patterned surface.....	82
Figure 2-16 Left – section of drop reconstructed volume before application of radiation filtering: the two yellow arrows highlight the position of the artefact caused by the beam hardening showing in the section as a wide horizontal line of pixels with non-correct grey level values. The image has been smoothed to try to minimize via software the detected defect in the first instance. Right – section of a comparable drop reconstructed volume produced after the introduction of the aluminium filter, it can be noted that the beam hardening is diminished.....	82
Figure 2-17 left – angled side view of the reconstructed vinyl record surface showing the groves sides irregularities that produce music when hit by a turntable needle. The yellow arrow highlights the tomography rotation axis artefact. Right – top view of the same record surface.....	83
Figure 2-18 Two side views (top-middle) and a three-quarter view (bottom) of the biggest drop no.5 artificially positioned near to the smallest one no.2 to highlight the difference of drops volume.	83
Figure 2-19 Top left – rendering of drop 1 tomographic reconstruction. Top right – conversion of reconstructed drop-surface volume in STL format after separate identification of drop and surface volume. Bottom left – in yellow recognized footprint of the drop. Bottom right – visualization of the only drop footprint with detected triple line highlighted in red	84

Figure 2-20 1st row-left – drop and surface stl surfaces ¾ view. 1st row, right - only drop stl surface displayed in red with numbered sections (black lines) produced by planes perpendicular to the grooves. 2nd row-left: semi-transparent drop visualization to reveal contours of drop surface sections 1 to 4. 2nd row right – orthogonal view of section 1 (blue) and 4 (red) to reveal the pinning behaviour change: section 1 is characterized by strong left-right side symmetry, while section 4, corresponding to the central section of the drop, is highly non-symmetric since the left side of the drop overflows the edge of the groove while the right side doesn't. 3rd and 4th row: orthogonal display of section 1 to 4 with indication of left-right drop contact angle with difference highlighting the non-symmetric behaviour of the drop-surface pinning 85

Figure 2-21 1st row left: drop and surface stl surfaces ¾ view. 1st row right: only drop stl surface displayed in red with numbered sections (black lines) produced by planes parallel to the grooves. 2nd row-left: semi-transparent drop visualization to reveal contours of drop surface sections 1 to 4. 2nd row right – orthogonal view of section 1 (blue) and 4 (red) to reveal the symmetry in the pinning behaviour. 3rd and 4th row: orthogonal display of section 1 to 4 with indication of left-right drop contact angle with difference highlighting the symmetric behaviour of the drop-surface pinning. 86

Figure 2-22 Visualization of 3D drop base area extraction (yellow) and its projection on surface parallel plane to calculate the 2D footprint of the drop. 88

Figure 2-23 top row: 3D drops footprints on the record surface. Bottom row: 2D projection of the only drops footprints. 88

Figure 2-24 black line presents nominal surface Wenzel roughness ratio calculated utilizing the nominal geometry of the record surface, while the single points present the experimental results for the 4 drops of interest. It can be noted that the latter are in good agreement with the theoretical corresponding value. However, the experimental points referring to drop n.2 and n.3, which have very similar volume, are quite distant one from the other, this can be explained with the different way of covering the surface edges of the two drops, which is not represented by the single nominal value. Image from [85] 88

Figure 2-25 left – 6 x 7 mm size GDL carbon cloth utilized for the tomographic reconstruction presented; single carbon fibres can have a diameter range between 5 and 10 µm. right – same piece of carbon cloth with a drop of distilled water deposited..... 91

Figure 2-26 Top – ¾ view of the GDL reconstructed volume, yellow section at sides represents recognized fibre volume: as it can be seen, inside strands, single carbon fibres are merged in one bigger volume. Bottom – higher zoom top view of a small portion of the GDL to further highlight the visibility of some of the carbon fibres protruding from the strands. 91

Figure 2-27 Grayscale rendering of thresholding window utilized to determine the only drop volume. It is clearly visible that under the drop, the GDL volume is partially visualized meaning that it will be recognized as drop volume after thresholding operation. 91

Figure 2-28 Left - rendering of the tomographic results of GDL with DROP (top) and only GDL (bottom) Right – result of the subtraction showing drop volume remaining. 92

Figure 2-29 Left (top) – side view of the drop volume after thresholding and GDL subtraction. Left (bottom) tilted view of the same drop volume. Right – bottom view of the drop volume showing regularly spaced grooves, determined by the warp and weft surface of the GDL cloth93

Figure 2-30 Top row left: rendering of the reconstructed drop volume. Top row right: visualization of the portion of the drop surface which is inside the GDL. Bottom row, from right to left: visualization of the drop sections as the section plane considered enters the GDL cloth. The remaining drop volume calculated after each section drop volume cut is: 0.951 mm³, 0.294 mm³ and 0.026 mm³93

Figure 2-31 Top-left: in blue 3D rendering of the drop surface with radial sections overlapped in black and red, 18 items in total, one section each 10°. Top-right – visualization of the only drop profiles to reveal the complexity of drop surface footprint. Bottom-left: orthogonal view of red single drop profile present in the previous images. Bottom-right: B-spline drop contour profiling and contact angle measurement of red drop profile presented in the previous images.93

Figure 2-32 From top left to bottom right – tilted view of drop surface sectioned by 6 planes parallel to the GDL surface to show how the drop adapts to the detected surface defect. The sectioning planes are the same utilized in the previous figure.94

Figure 2-33 From top left to bottom right – top view of drop surface sectioned by 6 planes parallel to the GDL surface to show how the drop adapts to the detected surface defect.95

Figure 2-34 Visualization of tomographic reconstruction slices highlighting drop pinning in more than one position. The full slice is visible in the left while in the right the zoomed view of the area where the pinning occurs is zoomed to ease details detectability.....95

Figure 3-1 Top left: closeup view of injector nozzle placed inside the microCT machine ready to be scanned. The nozzle has been disassembled from the body and the needle has been removed to place the nozzle on top of the sample holder. Top right: complete view of injector nozzle inside the microCT machine. The nozzle distance from the X-ray source allows a magnification which produces a tomography with a 4 μm resolution.98

Figure 3-2 Left – CAD drawing of the top mounting sample holder. The only tolerance indicated is the h7 for the base diameter since this must tightly match the diameter of the hollow rotary stage central hole. The tolerance for the top hole where the nozzle sits is not indicated since the nozzle outside shape is conical.98

Figure 3-3 Top left – radiography of the nozzle produced with the reported settings. Top right – false coloured radiographic image showing in false colours the intensity of the radiation received by the X-ray detector. Bottom row – schematic view of the tomography set-up to identify the position of the metal filter utilized to filter the incoming radiation.100

Figure 3-4 Left column, top and middle – nozzle reconstructed slices (horizontal and vertical) without beam hardening correction applied - Right columns, top and middle - same nozzle slices presented in the left part of the figure but with beam hardening correction applied. Bottom, left – histogram of the reconstructed volume without beam hardening correction with numbered peaks indicating the virtually 5 materials present

in the reconstructed volume. Bottom, right – histogram of the reconstructed volume with beam hardening correction applied, showing two main peaks corresponding to air (peak no.2) and nozzle metal material (peak no.4). Peak no. 2 is still present highlighting that not all the beam hardening artefact has been cancelled out by the correction.....	100
Figure 3-5 Top – thresholding of non-beam hardening corrected nozzle slice: yellow line represents the nozzle area recognized contour. The injection holes’ exit is not reconstructed correctly since the pixel value in this position have a higher grayscale value which assigns them to the nozzle material instead that to air as supposed. Bottom – same slice with beam hardening correction; the brighter pixel values of the outer border have been corrected permitting detection of the hole geometry.	101
Figure 3-6 Top, left – histogram of the nozzle tomography showing selected threshold value corresponding to the min histogram value between material peaks. Top, right – same histogram presented in the left image but with air and nozzle histogram values assigned colour coded. Bottom – nozzle slice colour coded using threshold value.	101
Figure 3-7 3D rendering, drawing and picture of DIN bushing utilised for the dimensional checks.....	103
Figure 3-8 Measurement of the DIN guide bushing with the Mitutoyo micrometre.	103
Figure 3-9 Left – 3D rendering of the DIN guide bushing sub-volume reconstructed by microCT. Middle – picture of the real part with reconstructed sub-volume identified by the black square. Right – stl reconstructed surface of inner and outer cylinders utilized for the diameter size calculations: “D” indicates the inner diameter while “d” indicates the outer diameter size.	103
Figure 3-10 Top left – nominal CAD design geometry for the internal volume of the studied nozzle. Top right – reconstructed geometry produced by microCT data. Bottom – over position of CAD and CT geometries with the CT surface colour coded to reflect surface to surface distance.	104
Figure 3-11 Top left – tilted bottom view of the reconstructed nozzle geometry with highlight of the position of the defect detected. Top right – zoomed view of the same geometry presented in the left to better reveal the defect. Bottom left – defect presented with deviation colouring exceeding used scale. Bottom right – picture of the defect produced after cutting the injector in half to reveal the inside.	105
Figure 3-12 Left column – zoomed pictures of the nozzle to locate the nozzle part that will be in the reconstructed volume at the three level of resolution. Right column – radiographies from the tomographic datasets at the three chosen resolution levels.	105
Figure 3-13 Left – 60-degree sector cutting operation inside microEDM machine, the nozzle is being cut by the metal wire which constitutes the eroding electrode; the actual erosion point is visible on the tip of the nozzle as a blue point representing the electrode spark position. Right – 60-degree nozzle tip sector after erosion placed on a fingertip.	107
Figure 3-14 Left column – from top to bottom 3D renderings of the reconstructed volumes with three different reconstruction resolutions (4.665 μm , 1.950 μm , 0.927 μm). Right column – from top to bottom cross cut view of the 3D rendering of reconstructed volumes visualizing one injection channel.	107

Figure 3-15 Top left – 3D rendering of nozzle tip with geometry section visualized. Top right – orthogonal view of channel cross section with numbers indicating the measured dimensions. Bottom left – cross cut view of the nominal CAD geometry. Bottom right – close up of inlet rounding of the nominal CAD channel geometry.....	108
Figure 3-16 Plot of inlet/exit up/down rounding radii (mean values). Tomographic resolution of points is colour coded as per the legend presented in the right part of the image.....	109
Figure 3-17 Left - Inlet and exit diameters (mean values) for the different tomographic resolution utilised. Bottom, right – mean channel length value for the three tomographic resolution.....	110
Figure 3-18 Top left - SEM image of the full nozzle tip. Top right – SEM measurement of the EXIT diameter of one injection hole. Bottom left – Tilted view of the same injection hole exit to reveal channel roughness caused by microEDM machining. The darker region with a ring shape around the channel exit has not been studied further. Bottom right – zoomed view of exit edge of channel.....	111
Figure 3-19 Left – external view of 3D CAD model. Centre – section view of CAD model showing internal injection channel position and geometry. Right – zoomed orthogonal view of only injection channel with needle added visualizing flow path and asymmetric needle utilised.....	112
Figure 3-20 Left column from top to bottom – surface geometry of injection channel after running-in reconstructed with microCT; nominal injection channel cylinder; microCT geometry coloured to represent geometrical deviation of reconstructed surface from nominal cylindrical feature.....	112
Figure 3-21 Shadowgraphy of injection channel showing cavitation as dark area; the flow direction is from left to right and the injection channel is displayed horizontally. Images from top to bottom display three testing conditions with increasing cavitation presence.....	114
Figure 3-22 From top to bottom orthogonal views of the 4 sides of the injection channel presenting geometrical deviation of channel geometry reconstructed after usage versus same channel geometry acquired before usage.....	114
Figure 4-1 Left – 3D CAD image of the test rig as available for the high-speed visualizations. Right, top – Picture of the same rig assembled and utilized: the area surrounded by the red dashed line highlights the rig horizontally mounted on the optical table. Right, bottom – close up CAD and picture of the test chamber, the CAD image presents the hypothetical rotation axis mentioned.....	117
Figure 4-2 Left - 3D CAD image of the test rig as designed and produced for the X-ray tomographic reconstructions. Centre – Picture of the test rig placed inside the microCT machine. Right, top – middle cross section of the test chamber CAD to reveal the inside, the rotation axis of the rig is coincident with the injection channel one. Right, bottom, picture of the new test chamber.....	117
Figure 4-3 Left – Fem analysis of the PEEK test chamber model produced to assess geometrical deformation induced by maximum pressures (100 bar upstream the injection channel and 20 bar downstream). Centre – X-ray radiography of composite materials analysed for X-ray penetrability. Right – Grayscale values corresponding to the yellow line in the central image.....	120

Figure 4-4 Top-left – Section of 3D CAD model showing inner injection channel geometry, sealing O-rings and fixing clamps position. Top-right: 2D CAD drawing of the sample model presenting a section of it showing its design dimensions. Bottom – 2D CAD drawing of the non-symmetric needle.	120
Figure 4-5 Left – microCT customized test rig parts description and localization. Right – Layout of the hydraulic circuit utilised to provide pressurized fluid for the experiment and to monitor interesting experimental conditions.	121
Figure 4-6 Left, top – Peek disk with the 3 mm non-through hole in the middle. Left, bottom – same Peek disk in front of the X-ray source, the back disk of the same dimensions on top of the Peek disk, the brighter one, is carbon fibre reinforced Peek material which was not selected due to its lower X-ray transparency. Right – radiography, mean of one hundred radiographies, of only the hole area with a drop of diesel inside, numbers present the projected attenuation through the sample as perceived by the detector.	123
Figure 4-7 Left – 3D tomographic reconstruction of the central part of the sample, sectioned with a middle plane to reveal the inside. Here a drop of diesel is present. Right – orthogonal view of section presenting reconstructed values for air and diesel to assess the possibility to differentiate liquid diesel and diesel vapour, which was considered for simplicity of equal attenuation as air.	123
Figure 4-8 Plot of simulated Tungsten (W) target emission spectrum determined by an X-ray source voltage of 130 kV. Plot produced with software Spektr 3.0 [40]. Characteristic peaks are indicated by text and added blue lines.	126
Figure 4-9 Simulated plot generated with Spektr presenting the X-ray spectrum produced by an X-ray source voltage of 60 kV. The absence of the higher Tungsten characteristic peaks is evident, while the lower energies peaks are filtered out by the detector lower energy detection threshold.	126
Figure 4-10 Left – Simulated X-ray spectra for an X-ray source voltage set of 60 kV, red line presents generated spectrum as exiting from the X-ray source while blue line presents same spectrum after filtration. Right – zoomed view of the filtered spectrum to better show its quasi Gaussian shape and resulting mean energy.....	126
Figure 4-11 Left – Cross section of visualization test chamber with square recollecting volume. Right – Cross section of microCT test chamber with conical and afterwards cylindrical recollecting volume.	127
Figure 4-12 Shadowgraphy set-up presenting the components mentioned in the text: light source, focussing lenses, test chamber model and high-speed camera.	128
Figure 4-13 Left- schematic view of test injection channel. Right – from top to bottom three shadowgraphy images are obtained with same needle lift equal to 1 mm in different conditions.....	128
Figure 4-14 (top-left) projection of empty channel and (top-right) projection of channel full of Diesel. (Bottom-left) reconstructed slice of empty channel showing attenuation difference, by means of different grayscale values, between surrounding PEEK material and void channel. (Bottom-right) reconstructed slice of channel full of Diesel liquid.....	130
Figure 4-15 (left) axially cut 3D representation of the injection channel of interest with cavitation development (darker area) before application of values calibration and one non-cut slice perpendicular to	

the axis revealed. (right) Same slice of the reconstructed volume shown flat to reveal ring artefacts and shape of cavitation which is also circular in shape.	130
Figure 4-16 (top left) sample slice of liquid reference dataset. (top right) sample slice of air reference dataset. (middle -left) sample slice of 10 percent void dataset before calibration: the probability density function plot of the values inside the channel border, indicated in the image by a yellow circle, is visible on the right of the image. (bottom left) Same sample slice of 10 percent void dataset after calibration and only visual contrast enhancement.	131
Figure 4-17 Illustration of the mixing procedure followed to create 10 to 90 percent void fraction reference datasets for scale linearity check. The projections have been mixed interlacing them in order to obtain an even effect of the modification proposed, better simulating cavitation presence and absence behaviour.	131
Figure 4-18 Void fraction calibration scale with 1-sigma bars	133
Figure 4-19 Void fraction calibration scale with 3-sigma bars.....	133
Figure 4-20 Visual representation of the created calibration scale: it can be noted that vapour fractions which are farther from the reference calibration dataset with 0 and 1 void fraction present more uncertainty.	134
Figure 4-21 Top: high speed shadowgraphy picture of experimental conditions of experiment no.2. Middle: and bottom: Calculated mean and standard deviation images.	136
Figure 4-22 Top – Vertical plane integration of the calculated void fractions multiplied by pixel dimension to retrieve a void fraction thickness in the direction perpendicular to the integration plane. Middle -overlay of the shadowgraphy mean image displayed in Figure 4-21 with the contour of the area presenting more than 25 μm of vapour thickness in the previous image. Bottom – same overlay presented before but with the standard deviation image instead of the mean image. All images refer to experiment no. 2.	136
Figure 4-23 Top-left: 3D rendering of the injection channel volume reconstructed by microCT with liquid fraction rendered transparent. Top-right: Front view of the channel entrance. Bottom cross cut view of the injection channel with shadows to reveal three dimensionalities of the cavitation structures. All images refer to experiment no.2.	137
Figure 4-24 Top: shadowgraphy picture revealing the string like vortex between the needle tip and the channel entrance. Middle: standard deviation image revealing the localization of the string like vortexes. Bottom: cross cut view of microCT reconstructed volume presenting cavitation structures which may be connected to the presence of string like vortexes detected by the shadowgraphy images. All images refer to experiment no. 2.	138
Figure 4-25 (1 of 2) Top: cross cut view of the MicroCT injection channel reconstructed volume presenting a red line every 600 μm . Following numbered images: sections perpendicular to the channel axis produced in the positions located by the previously mentioned red lines. All images refer to experiment no.2.....	140
Figure 4-26 Plane integrated images calculated for all experiments	144

Figure 4-27 Single shot sample shadowgraphy pictures for all experiments	145
Figure 4-28 Calculated mean image for each experimental shadowgraphy dataset.....	146
Figure 4-29 Calculated standard deviation from the mean image for each experimental shadowgraphy dataset.....	147
Figure 4-30 3D rendering, front channel view and axial sections for experiment no. 3.....	148
Figure 4-31 3D rendering, front channel view and axial sections for experiment no. 4.....	149
Figure 4-32 3D rendering, front channel view and axial sections for experiment no. 5.....	150
Figure 33 Top-left: 3D rendering of the drop of Hg based amalgam deposited on the patterned record surface. Top right: cut view of the amalgam surface to reveal its inside. Bottom-left: cut view parallel to the surface of the amalgam drop to reveal only its bottom part which interacts with the surface. Bottom-right: close up of the only bottom of the amalgam.	153

LIST OF TABLES

Table 6-1 Specification of the utilized glycerol.	80
Table 6-2 Table summarizing the characteristics of the drops.....	82
Table 7-1 Extended description of the names utilized in Figure 7-14.....	108
Table 7-2 Average value and correlated standard deviation for measurements of injection channels features introduced in Figure 7-15.....	109
Table 8-1 Range of experimental conditions.....	121
Table 8-2 Diesel physical and chemical properties (as specified by the producer).....	122
Table 8-3 Table of mean and variance values calculated for the non-calibrated and calibrated 10 percent void case (100 slices).	130
Table 8-4 Statistical values calculated for the experimental data after fitting with normal distribution. .	132
Table 8-5 Experimental conditions tested.	134

ACKNOWLEDGMENTS

Firstly, I would like to thank Prof. Manolis Gavaises for starting and making all this research adventure possible through trust and financial support. Secondly, Prof. Maurizio Santini for failing at the beginning to convince me not to embark in such an adventure, having therefore to host me in his laboratory and granting me access to his equipment for all the coming research period, and more. Thirdly, to a true experimental researcher, Dr. Nicholas Mitroglou, for showing me true passion for research.

In addition, I want to thank my wife, born under the stars of hope, love and strength, she uses all her qualities with me every day, and my two sons, Leonardo and Nicola, true shining stars came to planet earth during this period to illuminate my life.

DECLARATION TO THE UNIVERSITY LIBRARIAN

I hereby declare that the work presented in this thesis is my own and was developed in a joint effort with other members of the research group of fluid dynamics of City, University of London, led by Prof. Manolis Gavaises, and the research group of thermodynamics, laboratory of microtomography, of the University of Bergamo, led by Prof. Maurizio Santini.

I grant powers of discretion to the University Librarian to allow this thesis to be copied in whole or in part without further reference to me.

This permission covers only single copies made for study purposes, subject to normal conditions of acknowledgement.

London, 24/12/2017

Faithfully,

(Massimo Lorenzi.)

THESIS ABSTRACT

In all fields, fundamental and applied research seek to produce experimental measurements without causing interferences to the process being observed. This capability is of paramount importance, since small perturbations of the phenomenon can alter it to the point of producing biased or even incorrect results. X-ray techniques, based on synchrotron or laboratory X-ray sources, have attracted the attention of the research and industrial R&D community thanks to their characteristic of having little to no detectable influence on the subject under study. Moreover, if declined as tomography, this technique can provide localized full volume information at the micrometre scale, from which arbitrary shaped geometries and material densities can be deduced.

During this thesis an X-ray microtomography instrument, based on a laboratory X-ray source, has been exploited to gain three main objectives.

The first one is the analysis of how a liquid drop, of water or glycol, adapts its shape to reach an equilibrium state when gently deposited on a flat or patterned surface. So far this has been done using 2D techniques but introducing the knowledge of the third dimension and being able to see the drop shape even in not optically accessible locations, opens new possibilities to better understand the physics that regulate it.

The second one is the reconstruction of the internal geometries of automotive diesel injectors with high resolution to detect and highlight differences between nominal and real geometries, key information to produce more realistic CFD simulations of the flow inside production grade injectors geometries. A scaled-up model made of PEEK was also studied, producing successive tomographies, to detect small geometrical changes induced by part usage, giving an in-depth view of the locations more prone to be damaged by cavitation flow.

The third one is the study of a multiphase flow inside the same scaled-up model injection channel with flowing conditions exhibiting cavitation. The geometry of the non-axisymmetric model mimics the flow pattern of a real diesel injection channel and automotive grade diesel was consequently selected as fluid. Understanding the dependence of cavitation development on flow characteristics in a three-dimensional way, through the determination of the localized void fraction of the multiphase flow, can lead to improvements in the knowledge of such a phenomenon that can guide the design of future fuel injection equipment.

THESIS INTRODUCTION

The present research has been conceived to advance the knowledge of possible usage of micro computed tomography (microCT) to study complex geometries and multiphase flows. The custom build equipment utilised for this scope was already designed and in use before the start of the present research, however applicability of X-ray tomography and of the mentioned instrument to the study of the following research subjects was desired to be assessed.

1. Analysis of liquid-surface interaction.

Knowledge of how a liquid drop wets its resting surface is used to predict performances of processes driven by this characteristic in many engineering fields such as:

- heat exchangers [1]
- lubrication of moving parts [2]
- gas and crude oil extraction from soil [3]

or study how chemical and mechanical artificial modification of surfaces can produce desired surface characteristics:

- functional surface coatings [4]
- functional surface patterning [5]-[7]

Traditionally the understanding of such an interaction was obtained studying the solid-liquid characteristic contact angle, which implies the measurement of the angle between the drop profile and the surface, to deduce the hydrophobic or hydrophilic behaviour of the surface with regards to the used liquid. Techniques such as the telescope-goniometer, the captive bubble method, the tilting plate, the Wilhelmy balance, the pendant drop [8], the immersed plate [9] and the sessile drop method [10] are used.

However, techniques as the reported ones, which are based on the optical acquisition and analysis of drop side views, suffer from drawbacks due to optical lenses aberration, which causes image blurriness and distortion, need of high illumination, which can induce liquid evaporation, and light diffraction at drop surface contact line which produces non-usable pictures. Another drawback of traditional techniques is their impossibility to measure the proposed contact angle for patterned or irregular surfaces where the point of contact between the liquid and the drop is not directly visible.

For regularly patterned surfaces, more modern techniques such as reflection interference contrast microscopy [11], [12] or laser scanning confocal microscopy [13] can produce contact angle measurements but they need transparent surfaces patterned with specific parallel grooves through which they are able to directly visualize the drop-surface contact line.

This research work aims at assessing the possibility to use microCT for the determination of the liquid-drop contact angle in every point of contact line between the liquid and the surface.

To obtain the stated scope, new dedicated experimental set-ups will be created to test microCT technique to analyze liquid-surface interaction in the case of surfaces that are:

- flat
- regularly patterned
- random shaped.

Obtained results with the new proposed method, that was conceived by the research group after the advice of Prof. G.E. Cossali and B. Weigand, will be compared to similar analysis produced with more traditional techniques where possible.

This research subject will be developed in:

Chapter 2: Applications to complex geometries – (thermal-fluid dynamics).

2. Micrometric scale reconstructions of diesel injectors internal geometries for accurate CFD simulations.

The fuel injection process is very actively studied in the will of controlling engine performances, reduce pollutant emission and improve engine's durability [14].

Traditionally CFD simulations have been paired with direct experimental tests to gather the necessary data to improve the design of fuel injectors. However, producing experimental data consumes time and materials which could be partially spared if CFD simulation trustworthy could be improved [15], [16].

Traditionally simulation is performed using as boundary domains CAD reconstructions of nominal injectors internal geometries, however this is known to be inaccurate, especially for simulation of flows with cavitation presence, due to differences that are always present between nominal geometries and real geometries which can be accounted to production tolerances. Moreover, modern injection geometries characterised by injection holes with diameters in the order of 150-200 μm pose severe technological difficulties in their production which can threaten even more production stability of key geometrical characteristics [17], [18] In the will of knowing the true internal geometry of injection nozzles without the will to use destructive testing, techniques such as silicon moulding [19], [20] and direct tactile measurements [21] have been utilised. However, silicon moulding poses significant difficulties in extracting the mould for complex geometries and its intrinsic elasticity raises doubts on its possibility to accurately copy the objects' true dimensions, while direct tactile measurement has the necessity to directly access to the point of measurement. The most promising non-destructive high resolution technique to retrieve the nozzle internal geometry is X-ray tomography which is able to reconstruct its full 3D volume with micrometric resolution, in the range of 3-10 μm , implying the usage of synchrotron X-ray sources [22], [23] or laboratory X-ray sources [24]. This research work aims at testing the possibility to use the available new custom laboratory micro-focus X-ray source to reconstruct with a resolution as high as 1 μm the internal geometry of production grade diesel injectors with injection holes of 150-200 μm diameter and non-cylindrical holes so to be able to create in the future a dataset of real injector geometries that can be used for CFD simulations.

To obtain the stated scope, tests will be first performed to define a specific acquisition set up for automotive diesel injectors and a dedicated reconstruction procedure to reduce the influence of known X-ray microtomography artefacts [25]. Then reconstructions of internal nozzle geometries with resolutions increasing to as much as 1 μm will be performed and compared to similar information obtained with traditional measuring methods (SEM images and direct tactile instruments) to test the capabilities of the available microtomographic machine.

This research subject will be developed in:

Chapter 3: Applications to complex geometries (real injectors + test rig model)

3. Quantitative measurement of void fraction distribution inside fuel injection channel.

Diesel flowing inside injectors nozzles is prone to cavitate due to localized de-pressurization of liquid imposed by nominal operating conditions, small orifice dimensions and sharp flow path deviations [26]. Cavitation can be beneficial, it can improve spray atomization [27], [28], or detrimental, reduces discharge coefficient, modifies spray angle and liquid length penetration, promotes localized nozzle erosion [14].

Traditionally visualization techniques such as shadowgraphy, Schlieren and interferometry have been employed to study cavitation in transparent nozzle replicas, made of plastic or even quartz material, presenting transparent injection channels with direct optical access.

Used nozzle dimensions can vary from real ones to enlarged ones, scaled up 10x to 15x, to improve sample production feasibility and ease experimental conditions through the reduction of injection pressures. Results produced employing enlarged models replicate with a good degree of confidence results observable for real size nozzles thanks to the dimensionless similarity that can be imposed to the flow selecting equal cavitation (C.N.) and Reynolds numbers [29]-[31].

However, the opacity of cavitation structures to visible light doesn't allow gathering shape and density information about their core, particularly in case of strong cavitation, imposing the selection of an alternative technique to obtain the desired knowledge. X-ray can be used to penetrate opaque materials thanks to their characteristic wavelengths, permitting to retrieve sample density information leveraging the well-established relation between sample X-ray absorption and its density.

X-ray radiography and tomography are the two main techniques that can be used to see through even dense cavitation structures, collecting information about the density of their structures. In case of radiography, density information will represent the summed up projected sample density along the X-ray path: this technique has been recently used employing a laboratory X-ray source to study two dimensional cavitating flows obtaining a two-dimensional map void fraction values [32]. In case X-ray tomography is employed, the sample density information will be three dimensionally localized.

Synchrotron X-ray sources have been utilised to study cavitation inside injection nozzles [33], [34], however, due to the limited access to this kind of equipment and the small time slot that can be allocated for a single research, first attempts to use purposely designed laboratory X-ray sources instead of synchrotron light sources are being made such as [35]. This latter work has inspired the work presented in this thesis.

This research work aims at using X-ray tomography to produce three-dimensional quantitative void fraction values distribution maps through experimental data acquisition and analysis which can be used to advance knowledge of cavitation structures dependence on flow properties and injection geometry.

To obtain the stated scope the following steps will be performed:

- Design of a test rig chamber specifically tailored to produce experimental data applying X-ray tomographic technique with interchangeable sample injection geometries. The first sample geometry will be designed taking inspiration by the geometry presented in [36].
- Acquire experimental data to characterize different flow conditions.
- Analyse the obtained experimental data to quantitatively measure the mean flow density in the full 3D volume of the injection channel determining localized void fractions values.

This research subject will be developed in:

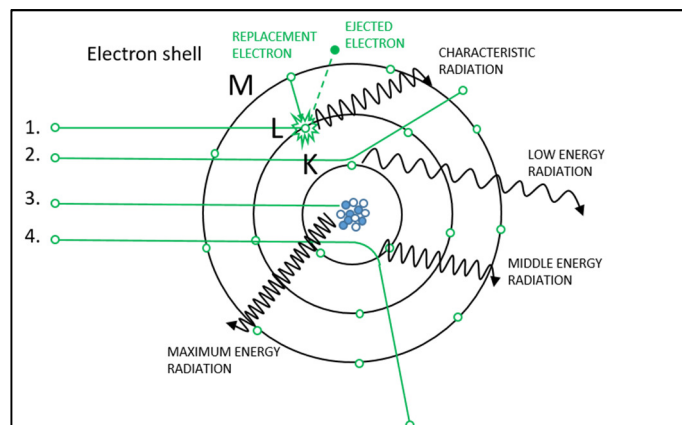
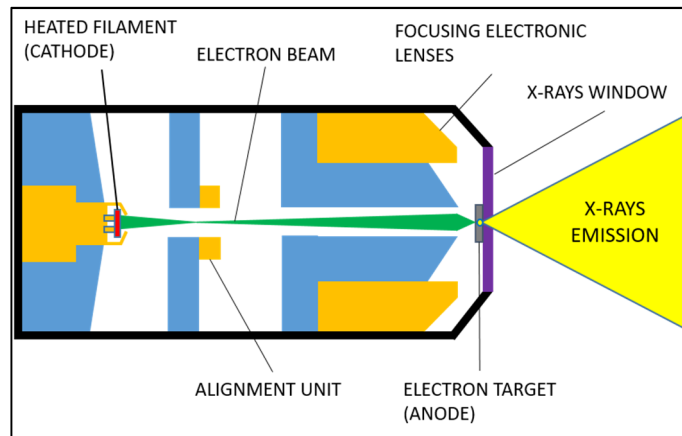
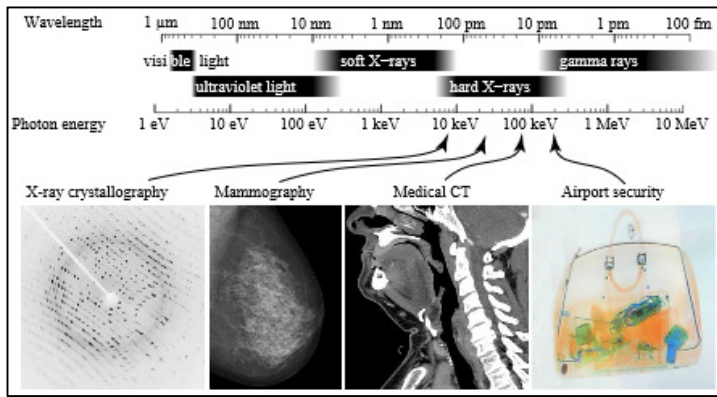
Chapter 4: Applications to multiphase flow – cavitation.

The first chapter of this thesis (*Chapter 1- Description of microCT technique and equipment*) will introduce X-ray tomographic technique and the utilised instrument to present the techniques and method along with the instrument that will be used later on to develop the topics of the presented research.

1 DESCRIPTION OF MICROCT TECHNIQUE AND EQUIPMENT

1.1 INTERACTION OF X-RAYS WITH MATTER.

Electromagnetic radiation with a wavelength between 0.01 and 10 nanometres is termed X-rays. The name to this kind of photons was implicitly given by Wilhelm Conrad Röntgen who accidentally discovered them in 1896: not knowing the nature of the radiation he was detecting, he decided to call it simply “X”, which stands for unknown. Figure 1-1 shows the position of the X-ray radiation in the electromagnetic spectrum and the vast number of applications permitted by its usage. Different X-rays wavelengths correspond to different photon energies, that can go from around 1 keV (kilo electron Volt) to 10 MeV [37]. For laboratory X-ray sources like the one used for this thesis, the production process of X-rays starts in the X-ray source where in a vacuum chamber a heated metallic filament produces free electrons by thermionic effect. The produced electrons are then captured and accelerated in the direction of a metallic target from the presence of a voltage differential, in the order of tenths to hundreds of kilovolts, between the heated filament, which represents the electronically negatively charged cathode of the electronic circuit, and a thin metallic plate which represents the anode. During the travel between the cathode and the anode, the electron beam is focused by a single, or sometimes double, stage of electronic lenses: this equipment reduces the dimension of the cross section of the beam by focusing it on a very small area of a metallic target, of the order of micrometres in diameter as shown in Figure 1-2. The interaction of the electron beam with the target atoms produces X-rays through energy conversion. When the negative charge of an electron interacts with the positive charge of the atom’s nucleus due to their vicinity, its speed is reduced, resulting mainly in the bending effect on its trajectory. This speed reduction, which is called Bremsstrahlung effect, meaning “breaking” in German language, is proportional to the distance between the electron trajectory and the atom’s nucleus position. As it is represented in Figure 1-3 by the case of electrons 2-3-4, different interaction distances make the electron lose different quantities of energy which are converted in X-rays of corresponding wavelengths. The Bremsstrahlung effect can produce X-rays of any energy up to the maximum energy of the electrons of the electron beam, value which is controlled by the X-ray source voltage set. Besides the mentioned breaking effect, X-rays are also produced by incoming electrons impinging directly on the atom’s electrons: their collision can cause the atom’s electron to be ejected and substituted by an electron coming from an outer shell. The jump of the atom’s electron from a higher energy orbital to a lower energy one, forces the electron to lose energy which is converted in an X-ray of a specific wavelength. Since the energy released by this kind of interaction is peculiar to the energies of the orbitals of the target material, it is called characteristic radiation, case of electron 1 in the image above. It must be however underlined that only around 1% of the electrons’ energy is transformed in X-rays, the remaining 99% is destined to heat up the target, creating important target heat dissipation problems due to the high energy density. To have an idea of how much strongly electrons’ trajectories are diverted due to the interaction with the target material, we can quantitatively simulate this phenomenon.



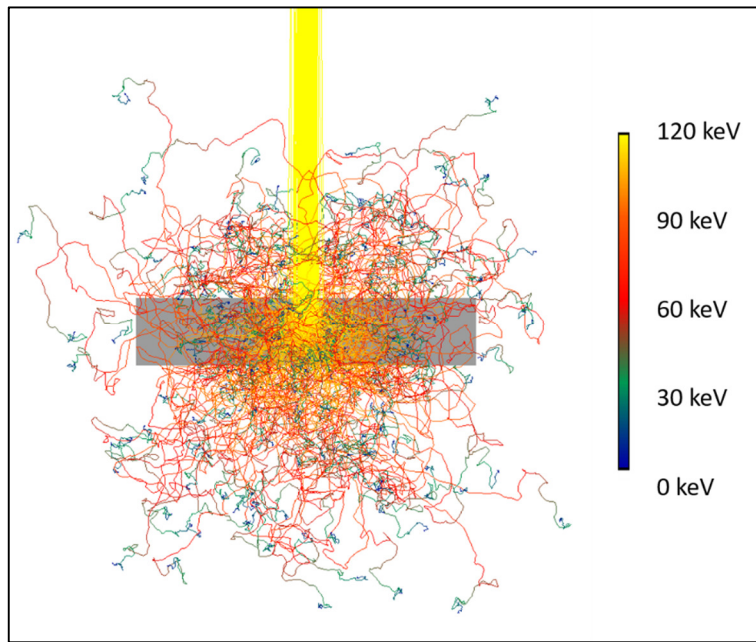


Figure 1-4 Image of the electrons travelling inside the target material produced with software “CASINO” [39].

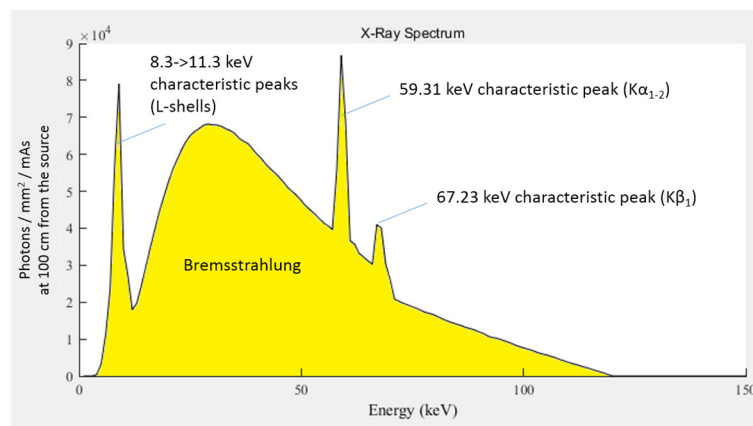


Figure 1-5 Tungsten (W) target spectrum simulated with Spektr software [40].

Figure 1-4 depicts a side view of the trajectories of 1,000 electrons, simulating an electron beam of 1 micrometre diameter, produced by a nominal X-ray source set at 120 keV, hitting a metal target plate of 5 x 5 micrometre and 2 micrometre thickness made of tungsten (W). The plate is represented in grey with 50% transparency to let the inner trajectories of the electrons to be seen; the false colour of the trajectories represents the decreasing of the electrons energies as it is lost while interacting with the target and being diverted. The Bremsstrahlung effect produces X-rays of many different wavelengths that constitute the continuous part of the emitted X-ray spectrum, the other part is given by the characteristic radiation mentioned before. Figure 1-5 represents a simulated spectrum of X-rays produced by a tungsten (W) metallic target when hit by an electron beam produced by an X-ray source set at a voltage between cathode and anode of 120 kV: the characteristic radiation is visible as peaks at 59.31 keV and 67.23 keV over imposed to the continuous radiation produced by the Bremsstrahlung effect. In the same image, it is evident that the maximum energy an X-ray can have is represented by the maximum energy of the incoming

electron, in the case of a complete electron stop. The most of X-rays produced have an energy of about 1/3 of the maximum electron energy and for the proposed sample spectrum the mean photon energy can be calculated to be 55.73 keV.

In the case of a transmission target like the one described, which is only two micrometres thick, a window made of a low X-ray attenuating material such as Beryllium (Be) is necessary to contrast the mechanical forces applied by the presence of the high vacuum inside the ionizing chamber of the X-ray source and to filter the secondary electrons ejected from the target atom shells. The produced X-rays pass through this material before reaching open air and be available for use.

The quantity of X-rays that reaches the object is governed by the inverse square law, since the target material area where the rays are produced can be in the first instance considered as a pointwise source, with divergent X-rays emission and, similarly to light, linear propagation.

The initial intensity (I_0), as well as fluence, of the X-rays diminishes while moving away from the electron target following the inverse square law:

$$I_x = \frac{I_0}{x^2}$$

Equation 1-1

Where I_x represents the intensity of the beam at a distance x from the source.

When the X-rays produced meet an object along their path, target window as previously said and air included, they can interact with it with a probability that depends on:

- X-rays initial energy.
- Material's atomic number.
- Material's density.
- Travelled distance inside the material (material thickness).

The result of the X-rays travel through the object can be either an absorption, a trajectory deviation (scattering), or a non-interaction.

In the energy range produced by laboratory sources, such as the one used for this thesis, from 5 keV to 160 keV, the X-ray interaction mechanisms are the:

- Photoelectric effect

The X-ray photon transfers its total energy to a shell electron of the object material, mainly of the inner shells, ejecting it and forcing another atom's electron of an outer shell to fill the void, releasing energy as electromagnetic radiation of a specific wavelength with unknown direction. The ejected electron is called photoelectron and can contribute to further ionization processes.

The photoelectric effect is more present when the energy of the incoming X-rays is near to the binding energy of the atom's electron to be ejected.

The probability of this kind of effect is proportional to:

$$\frac{Z^3 \rho}{E^3}$$

Equation 1-2

Where Z is the target material atomic number, ρ its density and E the energy of the incoming electrons. As it can be seen, even a small difference in material atomic number Z , causes the effect to increase by a large amount.

- **Compton effect (incoherent/inelastic scattering)**

X-ray photons transfers only partially their energy to a shell electron of the object material, mainly of the outer shells, ejecting it. The photon on the other hand lose part of its energy and deviates its trajectory from the original one. The ejected electron can further ionize electrons of other atoms. The decreased energy of the photon causes also the wavelength of the radiation to become longer, changing its material penetrability. The Compton scattering effect is more presents for atoms with high electron density and therefore for high material density objects, while it reduces with incoming radiation energy.

This kind of attenuation effect does not depend on the target material atomic number.

- **Rayleigh effect (coherent/elastic/Thomson/classic scattering)**

X-ray photons trajectories are deviated by the presence of the target material atoms, considered, but with no loss of energy since the interaction between the photon and the atom is not strong enough to reach the minimum energy necessary to eject an atom's electron. This scattering effect is dependent on the atomic number of the target material as follows:

$$\frac{Z^2}{E}$$

Equation 1-3

Figure 1-6 presents the contribution of each attenuation mechanism described to the total X-rays attenuation for the energies of interest of laboratory X-ray sources. On the x-axis X-ray energies between 5 keV and 160 keV are displayed, while the y-axis presents the mass attenuation coefficient tabulated for the specific material selected, Beryllium.

The presented interaction mechanisms produce an attenuation of the incoming X-rays intensity which is exponential and proportional to the thickness of the passed through material as represented by Figure 1-7. If we consider the simplest case of a monochromatic radiation and an object made of a homogenous material, the following formula describes the attenuation of X-rays:

$$dN = -\mu N dx$$

Equation 1-4

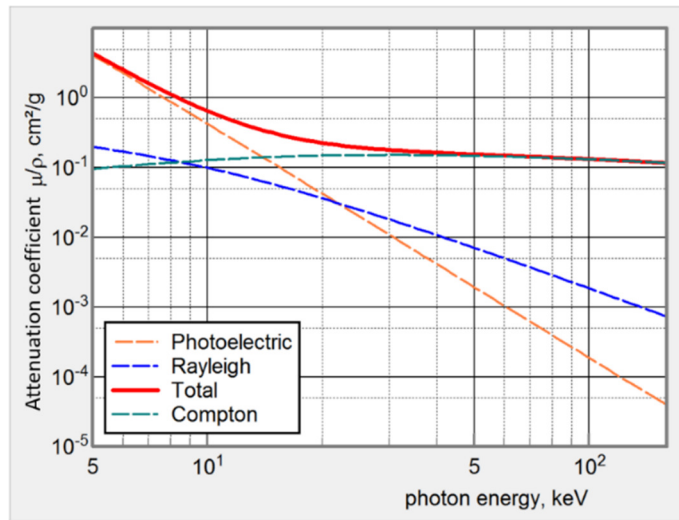


Figure 1-6 Contribution of each X-ray attenuation mechanism calculated for Beryllium and X-rays energies between 5 keV and 160 keV with software XMuDat [41] based on tabulated values of [42]

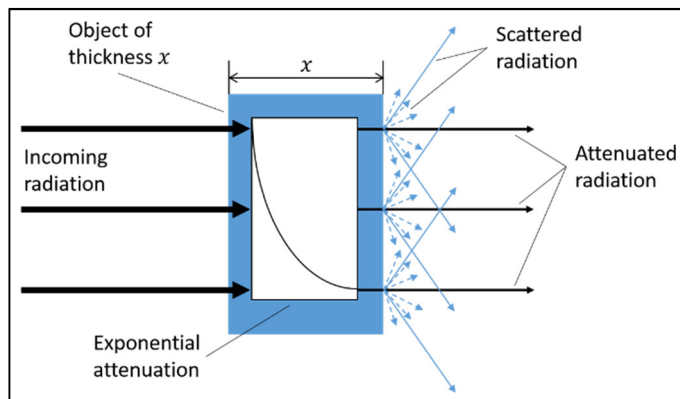


Figure 1-7 Representation of the interaction between an incoming monochromatic X-ray radiation and a homogenous object material.

Where N is the number of incoming photons, μ is the linear attenuation coefficient, and x is the thickness of the passed through material. X-rays that are not attenuated continue to travel on their initial trajectory after passing through the object material. The solution of the proposed differential equation (2) is:

$$N(x) = N(0)e^{-\mu x}$$

Equation 1-5

Which is more commonly used in the following form where the number of photons is referred to as X-ray intensity:

$$I = I_0 e^{-\mu x}$$

Equation 1-6

Where I_0 is the initial intensity of the X-rays reaching the object, I is the intensity of the X-rays that has passed through the object matter, not interacting with it, μ is a tabulated linear attenuation coefficient, and x the distance travelled by the ray inside the material (i.e. material thickness).

The linear attenuation coefficient μ represents the probability p per unit of length x of interaction between the X-ray and the given medium due to the interaction mechanisms detailed before.

$$\mu = \frac{dp}{dx}$$

Equation 1-7

If the linear attenuation coefficient μ is related to the material density ρ it becomes the mass attenuation coefficient, that is more commonly tabulated than μ and expressed as:

$$\frac{\mu}{\rho}$$

Equation 1-8

And calculated as:

$$\frac{\mu}{\rho} = \frac{\sigma_{tot}}{uA}$$

Equation 1-9

Where σ_{tot} is the total cross section, meaning probability when used in physics, of the interaction of the x-rays with the material due to the explained interaction mechanisms, plus other secondary terms, nominally electron and positron pair and triplet production mechanisms, u is the atomic mass unit equal to $1.6605402 \times 10^{-24}$ g and A is the object relative atomic mass. However, laboratory X-ray sources are polychromatic, due to the wide span of wavelengths of the emitted X-ray radiation.

This necessitate a more complex equation to correlate the source emitted X-ray intensity with the X-ray beam intensity I after the object filtration, to consider the dependency of the attenuation coefficient to the span of X-ray energies.

The formula used in these real cases is as follows (2):

$$I = \int_0^{E_{MAX}} I_0(E) \cdot e^{-\mu x} dE$$

Equation 1-10

Where I_0 is the initial X-ray beam intensity, $\mu(E)$ is the material linear attenuation coefficient, depending on the specific emission energy E , over the polychromatic spectrum, and x is the material thickness.

If then we further take into consideration the possibility, which is true for most of the cases, that the object is made of more than one material, then the formula must comprehend also this information which is given by:

$$I = I_0 \cdot e^{-\sum_{n=1}^N x_n \mu_n}$$

Equation 1-11

Where N is the number of materials present inside the object.

Resulting in a final formula comprehending both the wide energy spectrum and non-homogenous material as:

$$I = \int_0^{E_{MAX}} I_0(E) \cdot e^{-\sum_{n=1}^N x_n \mu_n} dE$$

Equation 1-12

X-rays that pass through the object can be then collected and analysed to gain valuable information about the object material leveraging the presented relation.

The conversion of X-ray radiation to a digital signal can be obtained using an X-ray detector which is an equipment usually based on a scintillator and an electronic circuit as depicted in Figure 1-8.

A scintillator is a material able of converting incoming X-rays into visible light thanks to its nature. Such materials, often crystals or doped crystals, when subject to ionizing radiation, have the property of luminescence that means being able to absorb the radiation energy and afterwards release the acquired energy through emission of light photons.

The conversion of X-rays into light is governed by the probability of the incoming radiation with energy E of interacting with the scintillator material, which is a function of the scintillator's linear attenuation coefficient and its active thickness.

Figure 1-9 shows the dependency of the conversion probability to the energy of the incoming radiation for a 500 μm thick CsI:Tl (Caesium iodide doped with Thallium), as it can be seen higher energies X-rays have less probability than low energy X-rays of interacting with the scintillator.

After the conversion to light photon, the produced light is detected by a photodiode which converts it to an electrical signal that can be sampled and converted to usable digital information representing the intensity of the absorbed radiation. It must be noted that common X-ray detectors are therefore not able to distinguish incoming X-ray energies but act usually as energy integrators.

An X-ray tomography machine comprises at least one X-ray source, a rotary stage, an X-ray detector, and a computer with the necessary software able to process the acquired radiographic images to produce the 3D reconstruction of the scanned object. The tomography machine that will be considered as example to illustrate tomographic principles in the following, has the same setup of the tomography machine that was used to fulfill the purposes of this thesis: it is a microCT machine with polychromatic X-ray source with transmission target, cone beam emission, circular object trajectory and flat panel detector

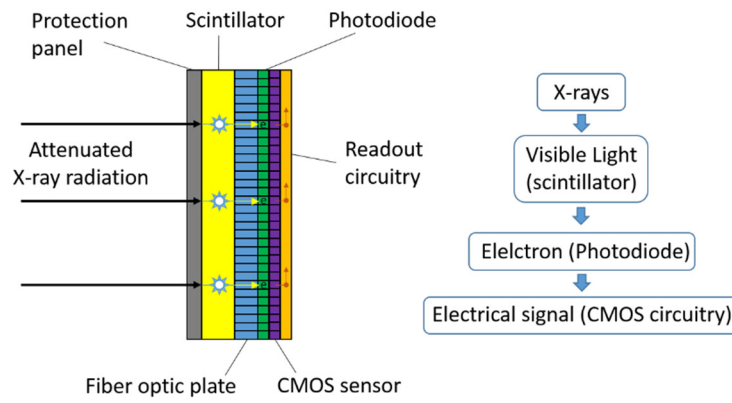


Figure 1-8 X-ray CMOS detector simplified layout. From left to right: incoming X-ray radiation, protection plate (grey), scintillator layer (yellow), fibre optic plate (blue), photodiode (green), CMOS sensor (purple) and electronic readout circuitry (orange).

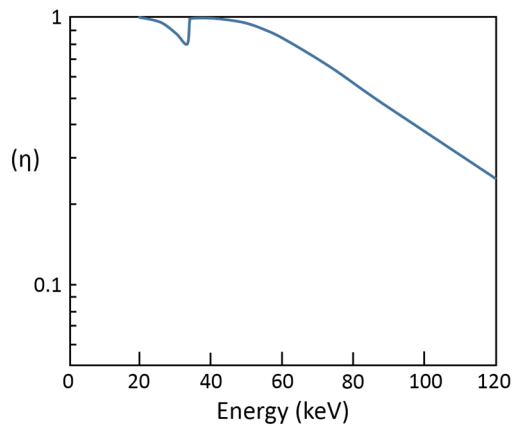


Figure 1-9 Conversion probability of Caesium iodide phosphor doped with Thallium based on incoming X-ray energies form 0 to 120 keV. Source: redrawn from [43].

1.2 HOW COMPUTED TOMOGRAPHY WORKS

When passing through matter X-rays are only partially absorbed by the object giving the possibility to collect the remaining part to gain valuable information of the passed through material.

The application of such a valuable property has been exploited since its discovery to produce images of the interior part of objects without the need to disassemble them, making the so called 2D X-ray radiography the perfect tool for disease detection in the medical field.

The deep medical interest in such a technique led to the design and implementation of X-ray tomography machines that are more commonly known to the public for their clinical application as CAT (Computerized Axial Tomography).

Pictured in Figure 1-10 and firstly designed and built in 1972 by Hounsfield and Cormack, who were awarded a shared Nobel prize in medicine in 1979 for this invention, the first tomography machine was an X-ray head tomographic scanner, meant to add a third dimension to the 2D X-ray radiographic information available until then.

X-ray radiation, with the shape of a cone, is generated by the X-ray source and directed towards the object to be scanned. The object needs to be rotated by a complete revolution of 360° by discrete steps to collect radiographies for each position on a 2D flat panel detector which is in a fixed position after the object aligned with the emission of the X-ray source.

All the acquired radiographies, termed projections in the tomography context, are then acquired and processed: for every projection, the grey scale pixel value represents the measure of the acquired radiation attenuated by the object along the line between the X-ray source and the point of the detector where the considered pixel lays. As we have seen, this measure can be related with an equation to the line integral of the linear attenuation coefficient of the material between the X-ray source and the object.

The idea behind X-ray tomography is to reconstruct a 3D map of the attenuation coefficient inside the sample scanned, to be able to localize and distinguish every different material the object is made of, throughout its volume, starting from 2D views which contain also a depth information. Figure 1-11 represents the set-up of the illustrated tomography machine.

The mathematical background of this possibility was given in 1917 by J.H. Radon who proved that the 2D distribution of a material characteristic in an object can be calculated if its integral value along any number of lines passing through the same layer for which the characteristic should be calculated, is known [44].

Therefore, the information contained in the full set of radiographies can be used to produce the so-called Radon transform first, which is usually termed sinogram, and the anti-transform which represents the result of the reconstruction. As we can understand, if we had only one radiography made in one of the n positions, represented as an example in the Figure 1-12 by projections at angles 0° , 90° and 135° , we couldn't guess what is the relative position of the two shapes in the 3D volume and what kind of shape they are. To make an estimation of the exact position in the 3D space and a guess of the true shape of the objects, we need to have as much projections as possible to refine our guess; nominally as stated by Radon's formulation, the true position and shape can be exactly calculated only if the number of projections is infinite.

Even though the projections produced by cone beam tomography machines are made with the use of non-parallel beams, Radon solution based algorithms have nevertheless been commonly employed to solve reconstruction problems applying the so called filtered back projection algorithm extended to be applicable to the 3D case for small opening angles, as presented by Figure 1-13. One such very successful fully three-dimensional algorithm widely used is the filtered back-projection algorithm in the implementation proposed by Feldkamp, Kress and Devis [46].

The filtered back projection algorithm in its 3D form is a non-exact algorithm that can be applied to cone beam computed tomography with circular trajectory, meaning that the object has only to rotate in front of the X-ray source during the acquisition to produce the necessary views, radiographies, of it to be reconstructed.

To understand better the application of the Radon transform and anti-transform to tomography through the filtered back-projection reconstruction algorithm, we can try to visualize each step of the reconstruction mechanism. As it can be seen in Figure 1-14, the example volume to be reconstructed contains one cylinder and one rectangular cuboid, the two objects have different height, size and are made of different materials, this last characteristic is represented figuratively by the different colours of the shapes, the darker colour representing higher material linear attenuation coefficient than the brighter one.

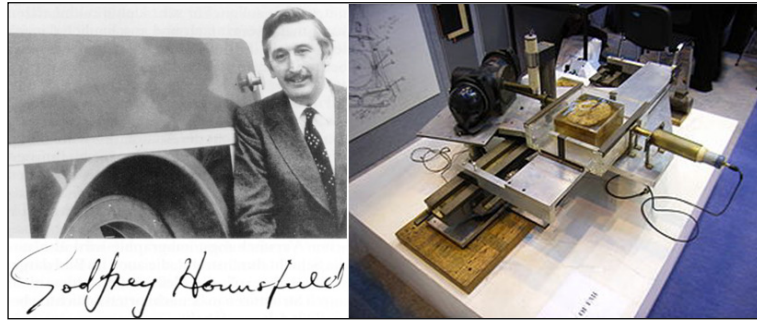


Figure 1-10 Image from (Gdh-commonswiki) First prototype of computed tomography scanner produced by Sir Godfrey Newbold Hounsfield and Allan MacLeod Cormack. In the left image Sir. Hounsfield is pictured with his first commercially available CAT, in the right picture the CAT prototype is visible with a sample brain as object to be scanned.

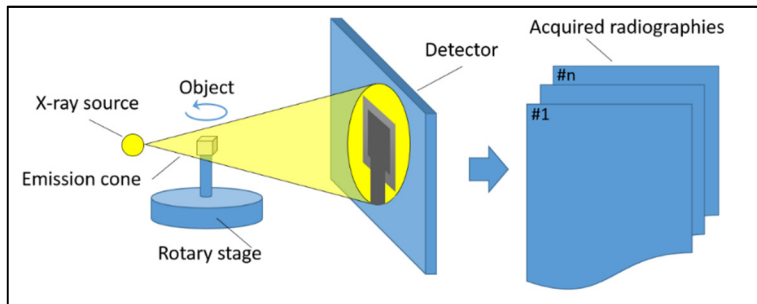


Figure 1-11 Layout of sample tomographic acquisition. From left to right we have the X-ray source, represented with a pointwise emission, the rotary stage with the cubic object to be scanned positioned on a sustaining cylindrical sample holder, the detector where the transmitted radiation is acquired and sampled to be saved in a 2D image file, the stack of acquired radiographies, one for each positional step, ready to be processed for reconstruction

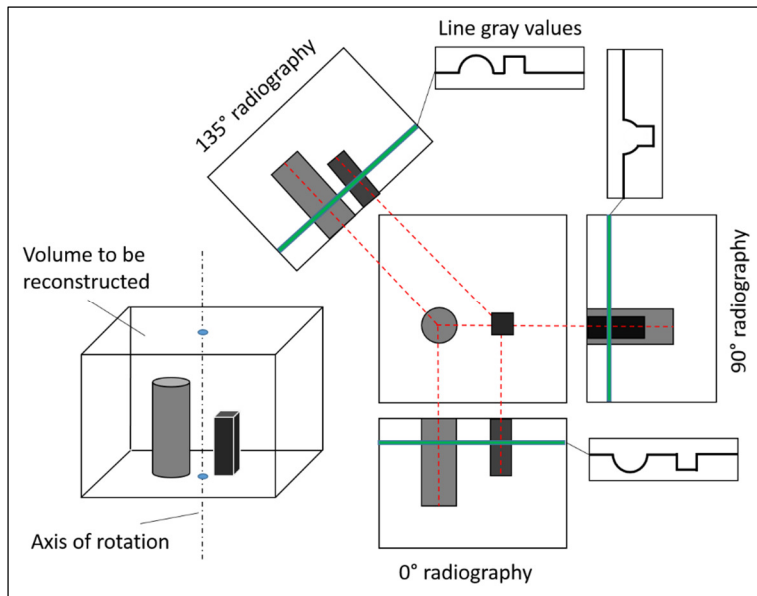


Figure 1-12 Illustration of the object shape and position guess through projections observation: the volume to be reconstructed shown in 3D on the left contains a cylinder and a rectangular cuboid: from the three projections shown on the right it is clearly impossible to guess the correct shape and position of the two objects even though each projection furnish partial data about the desired information.

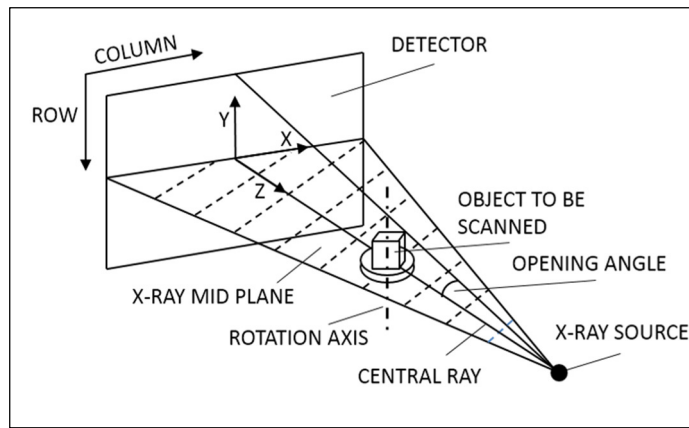


Figure 1-13 Schematic view of the circular cone beam tomography with mid-plane highlighted. Image from [45]

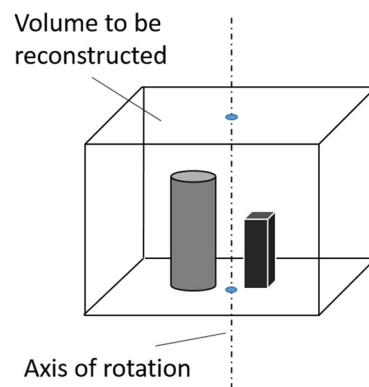


Figure 1-14 Graphical visualization of the rotation axis of the selected volume to be reconstructed.

During the tomography n projections throughout the full 360° rotation are acquired and need to be pre-processed following these steps before tomographic reconstruction:

1. Offset, gain and defect correction.

Offset correction: base detector noise, read by the detector as non-zero-pixel values also when the X-ray source is off, is cancelled out subtracting it from the image.

Gain correction: the unevenness of the detected X-ray intensity on the flat detector given by the point X-ray emission, that causes a physical drop of intensity going from the centre of the image to the sides, and presence of any material between the X-ray source and detector is cancelled out. The images used for this correction are acquired with no object in place but with any filter in position.

Defect correction: detector image area can have one or more defect which can go from single pixels to complete lines.

2. Logarithmisation and normalization.

The logarithmisation of the normalized intensity of x-rays gives the line integral of the attenuation coefficient as:

$$I = I_0 e^{-\mu x} \quad \Rightarrow \quad \int_{-\infty}^{+\infty} \mu(x) dx = -\ln \frac{I}{I_0}$$

Equation 1-13

3. Cosine weighting. (Feldkamp weights)

Every projection is weighted to reduce the weight of the elements of the flat detector that received less intensity due to the pointwise X-ray source.

4. Ramp filtering.

Image high frequencies enhancement necessary for back projection.

5. Smoothing filter.

Filter applied on the results of the back projection to partially smooth the high frequency enhancement caused by the ramp filter. Figure 1-15 shows the evolution of the acquired image using the real case of an injection channel. The next step involves the stacking of each horizontal line of the detector 2D radiographies, considered throughout all the projections acquired, as depicted in Figure 1-16 to form the Radon's transform, or sinogram as it is usually called, name that comes after the sinusoidal shape usually pictured in the final image.

After producing a sinogram for each detector plane, see Figure 1-17, the reconstruction algorithm back projects each row on the plane to do the reconstruction.

The filtered projection plane contained in each sinogram is then back projected along the direction of the original radiography to reconstruct the variation of the interesting material property in the object's volume.

Figure 1-18 shows how the back projection takes place: each projection line value is back projected in the reconstructing plane along the direction of the initial radiography, the sum of all these line values produces a reconstruction of the object pictured in the specific radiography line.

The reconstruction plane represents therefore a horizontal cross section plane of the object's volume corresponding to the selected projection line height. This process must be repeated for every line of the acquired radiographies that represent a plane in 3D, to reconstruct the object in its full height.

The more projections are used for the back-projection process, the more precise the object reconstruction will be.

The final result of the back projection is a stack of slices representing horizontal sections of the object where each pixel has a grayscale value, called CT number, that is proportional to the attenuation coefficient of the material in that specific spatial position.

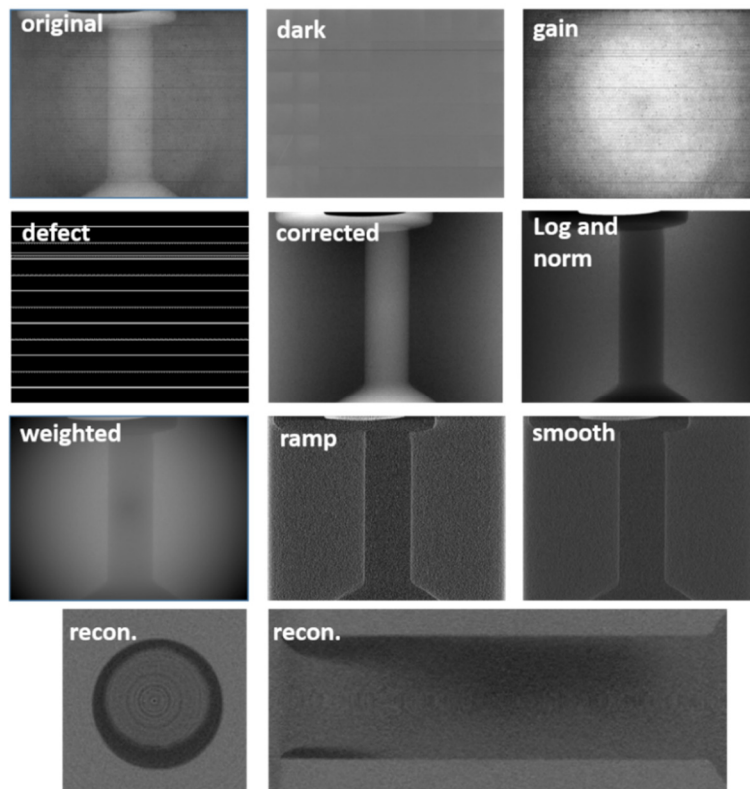


Figure 1-15 (from top left to bottom right) original projection image without corrections; dark, gain and defect image to be used for projection correction; image corrected with the previous three correction images; legitimized and normalized image; cosine weighted image; ramp filtered image; smoothed image; horizontal and vertical slices resulting from the reconstructed injection channel

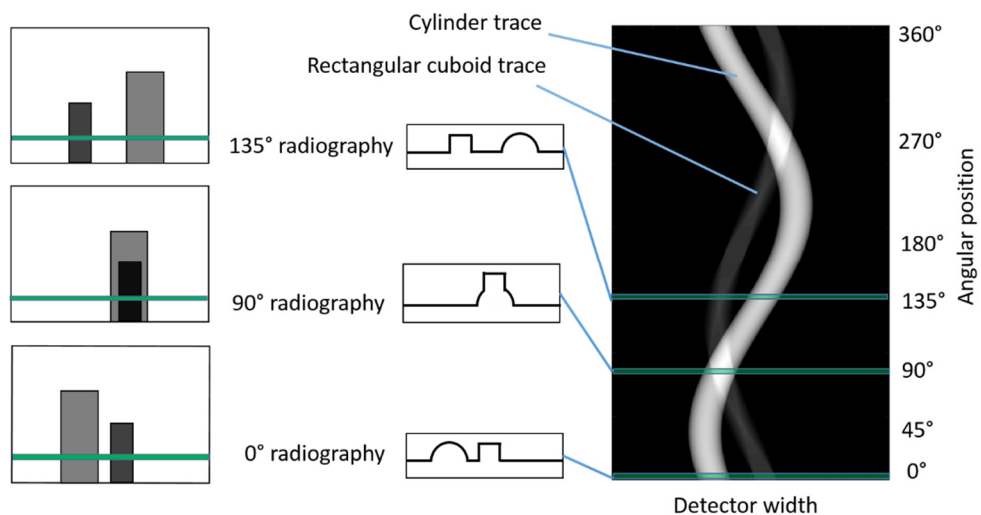


Figure 1-16 Sinogram of the proposed sample reconstruction of a cylinder and a parallelepiped. (Right) three sample projections are displayed corresponding to angle 0°, 90° and 135°. (Middle) line profiles of the same detector line extracted for all the three projections. (Right) complete sinogram from 0° to 360° of the analysed line before image logarithmisation and filtration.

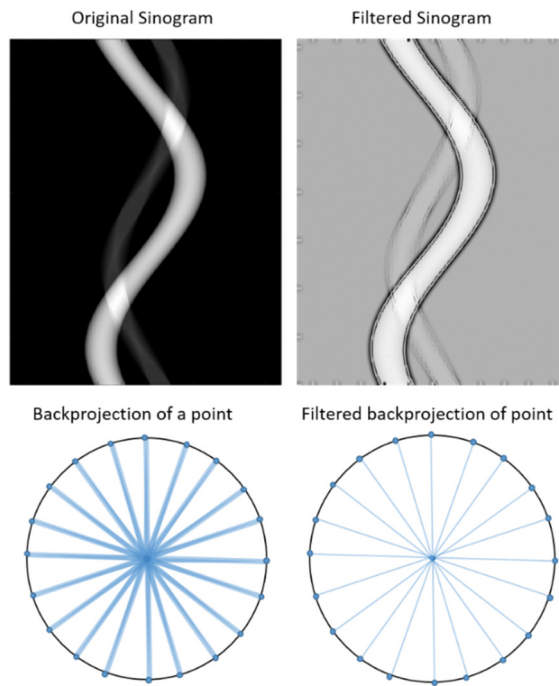


Figure 1-17 Left: unfiltered sinogram (top) and simplified back projection of a point (bottom) showing the image blurring that would result by the back-projection process if the images weren't high-pass filtered. Right: same sinogram image ramp filtered to enhance high frequencies (top) and same back projection of a point with filtered sinogram. It is clear the necessity of the filter enhancing high frequencies.

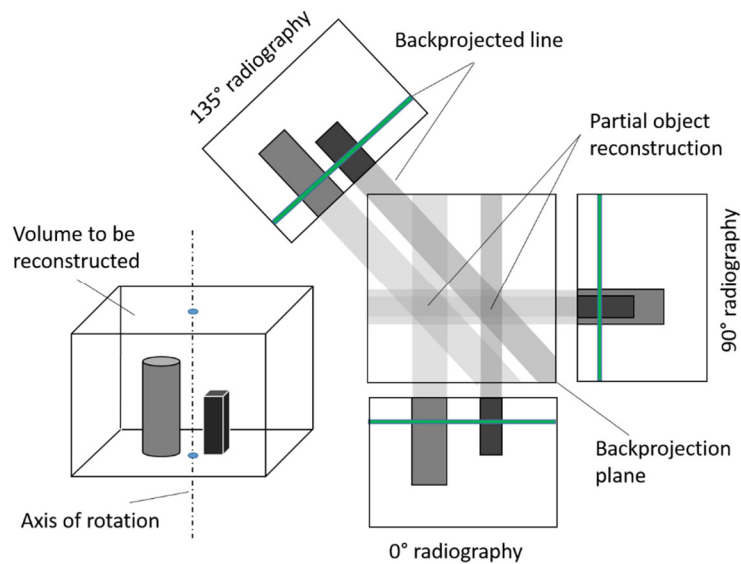


Figure 1-18 Back projection process: each projection line is back projected on the projection plane, which represents an horizontal cross section plane of the reconstructed volume, to reconstruct by summation the shape and material property value of the scanned object.

1.3 DESCRIPTION OF THE UNIBG MICROCT

The microCT machine used for the present thesis, pictured in Figure 1-19 is installed in the “Laboratory of Thermal Physics and Microtomography” of the University of Bergamo. The machine was designed and built by Prof. Maurizio Santini in 2012 to create a machine able of producing high resolution reconstructions preferentially of low attenuating materials. The choice to custom design and build a tomography machine rather than buying an available model from the market, was dictated by the will of selecting each component independently, so to tailor its characteristics to the intended use, and to have the full possibility to modify its layout and configuration if necessary, as it was done for the application to the analysis of multiphase flows presented in this same thesis. The X-ray machine working components are assembled inside an X-ray cabinet with walls made of Pb to shield the produced ionizing radiation so that it does not leave the inside of the cabinet during machine usage. X-ray radiation is harmful for living tissues and therefore for human beings and proper training and protection must be provided to any intended user. The components of the X-ray microCT machine are basically five:

- Supporting frame.
- X-ray source.
- Rotary stage.
- X-ray detector.
- Control equipment.

Figure 1-20 presents the inside of microCT machine showing four components, all the mentioned ones but the control equipment, that will be described in the following.

- **Supporting frame:**

The supporting frame has the function of keeping the alignment between the microCT components while allowing the linear movement of the rotary stage and X-ray detector. These two components need to be movable to adjust acquisition parameters, mainly object magnification. The alignment of the microCT machine is of paramount importance and must be checked every time one of the fixed components is moved due to maintenance or changes in the machine layout. The alignment between the X-ray source, the rotary stage and the detector must be produced Figure 1-21.

The X-ray source emission axis must intersect perpendicularly the rotation axis, and reach the detector, again perpendicularly, in its centre. The plane created by the X-ray emission point and the middle horizontal line of the detector must be perpendicular to the rotation axis to respect the geometry alignment that is requested for the tomography reconstruction: smaller deviation from the nominal condition can be generally tolerated, thus reducing the reconstruction fidelity, or can be better compensated by a specific correction parameter in reconstruction algorithms. Overall machine temperature stability is very important for geometrical stability. Figure 1-21 represents the coordinate system of the microCT machine. The alignment is done between the three components by moving one of the two moveable components, the rotary stage and X-ray detector, one at a time.



Figure 1-19 Outside view of the X-ray machine with door open; control electrical cabinet on the right side of the picture.

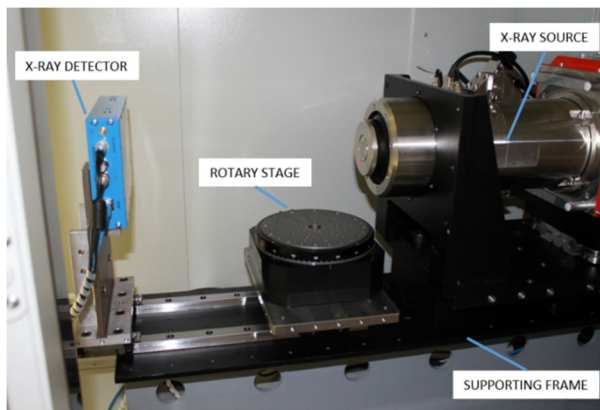


Figure 1-20 Close-up view of the inside of the cabinet with (from right to left) X-ray source, rotary stage and X-ray detector displayed.

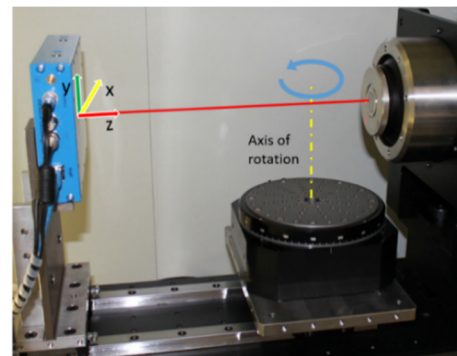
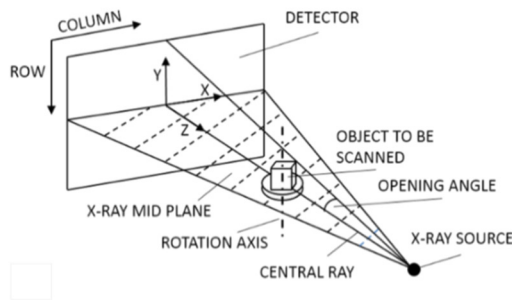


Figure 1-21 Coordinate system of the microCT machine.

First the detector alignment must be produced: the detector is moved in steps of 5-10 centimetres from the nearest position to the X-ray source to the farthest one, collecting images without any object in place. From each image, the central ray of the radiation is calculated and the position of the detector, or the alignment of the supporting linear guides, must be changed so that the radiation centre corresponds to the detector centre. Besides the radiation centre, during the detector alignment also the symmetry of the radiation

intensity must be evaluated to correct the horizontal and vertical tilt of the detector. Figure 1-22 represents four alignment images taken at position 40, 140, 240 and 340 mm from the X-ray source: as it can be seen, the centre of emission is calculated from each radiography, visualized by the red cross, and the position of the overall emission axis is aligned to best approximate the emission centre for each position. Once the detector alignment is complete, see Figure 1-23, the rotary stage position must be aligned so that its rotation axis direction is perpendicular to the X-ray emission axis and coincident with it at the point of intersection. This can be done utilizing a cylindric sample object. The frame dimension permits a maximum distance between the X-ray source and detector of 370 mm granting a magnification of 74x for a sample positioned at 5 mm from the X-ray source so to obtain a nominal resolution in the reconstructed volume of 1 μm .

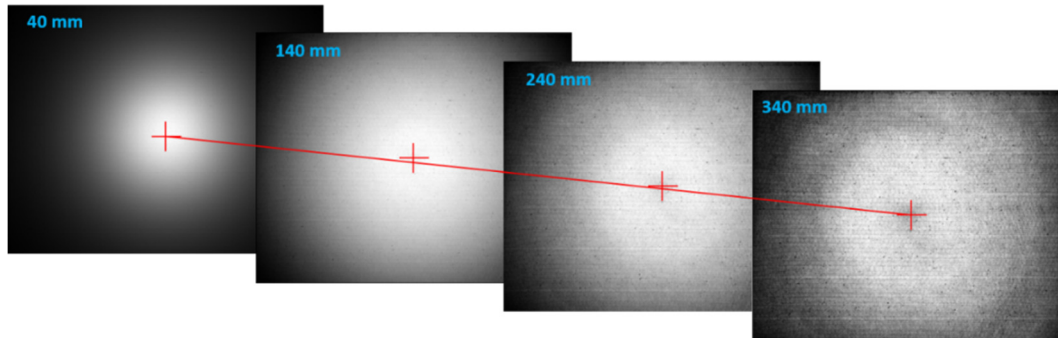


Figure 1-22 Emission axis alignment process: one radiography at each specific distance from the X-ray source is acquired and processed to obtain the emission centre as perceived by the detector. Based on this information the overall emission axis can be calculated and corrected moving the detector if not linear.

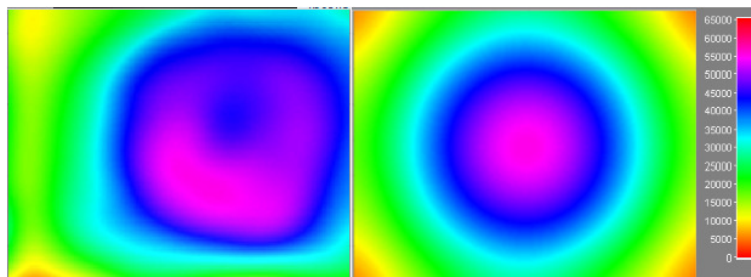


Figure 1-23 Left – colour coded radiography of the non -aligned X-ray source: the X-ray intensity is not symmetric with respect to the detectors’ centre point. Right – same colour coded radiography of the same X-ray source after alignment: X-rays intensity symmetry is evident.

- X-ray source:

The X-ray source utilized is a Hamamatsu open type micro-focus model with interchangeable transmission target characterized by cone beam emission. The production of X-rays for this type of source has been described in the chapter “Interaction of X-rays with matter”. The following are the X-ray tube specifications:

- tube type: open tube
- target: transmission type

- x-ray source type: micro-focus (with interchangeable targets).
- tube voltage: 20-160 KV
- tube current: 0-200 uA
- maximum output power: 8 W
- minimum resolution: 1 μm
- X-ray beam angle: 120°

The most peculiar characteristic of this X-ray source is its possibility to focus the electrons produced by the filament, by means of the electronic lenses, down to an area of only 1 μm which is an important feature.

The maximum resolution obtainable in the reconstructed volume is determined by the magnification factor, which accounts for the geometrical magnification of the sample on the detector area, determined by the X-ray source to object and X-ray source to detector distances, but must be sustained by the dimension of the focal spot area which, is the area of production of X-ray on the target material that has to be equal or smaller than the desired resolution to avoid the blurring phenomenon defined “penumbra”.

Magnification can be modified moving the relative position between the X-ray source, the object to be scanned and the detector since the object and the detector are assembled on moving bases, as it can be seen in the previous picture of the inside of the cabinet.

The magnification can be calculated as:

$$M = \frac{\text{Source to detector distance (SDD)}}{\text{Source to object distance (SOD)}}$$

Equation 1-14

However, the resulting reconstruction resolution must be smaller than the calculated penumbra which is:

$$P = (M - 1) * f$$

Where f is the focal spot size, M the magnification factor and P the calculated penumbra which must be smaller than the single detector pixel dimension. Figure 1-24 presents the schematic view of image magnification and effect of penumbra on detector image.

- Rotary stage

The rotary stage is used to rotate the sample to acquire projections throughout the full 360-degree rotation. The object to be analysed is usually aligned to rotate along the rotary stage axis so to be able to increase its magnification at best and reduce the number of projections that is necessary for the reconstruction. The rotational movement must be highly accurate since any deviation of the movement from perfect rotation is translated in a movement of the sample, magnified in the case of tilt error due to the distance between the stage centre and the sample centre position. This kind of error is usually not adjustable by the reconstruction algorithm resulting in reconstruction errors. Therefore, rotary stage axial, radial and tilt error must be smaller than the maximum expected reconstruction resolution. Moreover, for this thesis, important

characteristic of the used rotary stage is the hollow centre, giving the possibility to pass the stage from top to bottom with a 20-mm diameter pipe, the maximum load, that must be high enough to withstand the load of the full test rig, and the air bearing system which grants smoothness to the movement, necessary for experiments with drops.

The following are the rotary stage specifications, presented in Figure 1-25:

- resolution: 0.383 μ rad
- accuracy: ± 2 arc sec
- repeatability: <1 arc sec
- axial error motion: <100 nm
- radial error motion: <250 nm
- tilt error motion: <0.3 μ rad
- axial load: 30 Kg
- radial load: 15 Kg
- producer: Aerotech

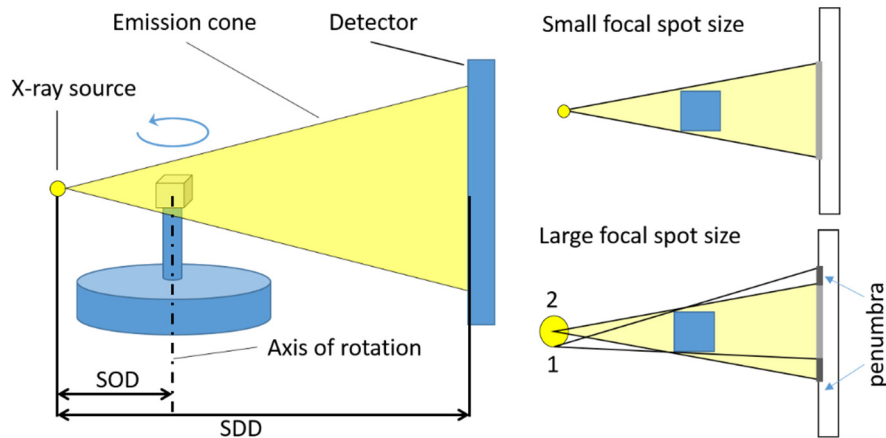


Figure 1-24 (left) schematic view of microCT setup evidencing distances of interest for magnification calculation; (right) penumbra phenomenon illustrated: (right-top) a perfect nominally pointwise X-ray source projects a single X-ray emission cone creating a sharp single image of the object on the detector panel, while (right - bottom) an X-ray source with non-negligible dimension produces a penumbra effect causing blurring since in this case X-rays are emitted throughout its full area. N.B. penumbra effect shown only for the first face of the cube object and for just one side (worst case) of the emitting area, side 1, the same happens symmetrically for emission point 2.



Figure 1-25 Air bearing rotary stage produced by Aerotech utilized to rotate the sample during radiographies acquisitions.

As it can be seen, the microCT utilized had no possibility to adjust the x, y, z coordinates of the rotary stage by means of electro actuated axis, therefore the positioning of the sample has been done manually producing sample holders with the right geometry or modifying the position of the rotary stage sliding it on the supporting flat surface before clamping it or using shims to modify its height when necessary.

- **X-ray detector**

The radiation detector utilized is a high-resolution CMOS flat panel detector produced by Dexela-Perkin Elmer. Such detector utilizes a scintillator plate made of Caesium iodide (CsI) with a carbon fibre shielding and fibre optical coupling to produce images over an area of 145.4 x 114.9 mm. For this detector, Caesium Iodide has a columnar structure and is directly deposited on the electronic photodiodes to have high sensitivity and high spatial resolution. The following is a summary of its specifications:

- 74.8 μ m pixel pitch.
- 1,944 x 1,536 pixels.
- high-sensitivity and high-saturation modes.
- binning to 4x4.
- 26 - 86 frames per second (binning dependent).
- high DQE (DQE >0.7 at 1 lp/mm, 28kV, 260 μ Gy).
- 14-bit digital output.
- Scintillator: CsI 600 μ m.
- BNC input/output for X-ray generator triggering.
- Camera Link, USB or Ethernet data connection.

Figure 1-26 presents a picture of the mentioned detector. A complete characterization of an X-ray detector featuring the same components, but arranged in a different manner to produce a larger imaging area is present in this reference paper [47].

The modulation transfer function provided by the part supplier is visible in Figure 1-27. The linearity over the 14-bit acquisition range is depicted in Figure 1-28.

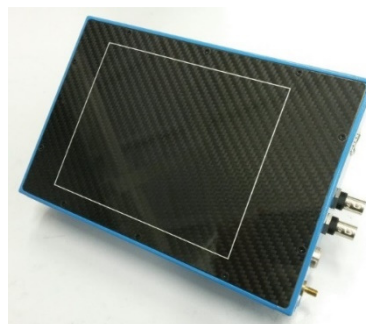


Figure 1-26 X-ray detector utilized to acquire X-ray images during tomographies. The front surface shows the carbon fibre window that seals and protects the active scintillator area. On the side the BNC trigger in and trigger out connectors are visible. On the same size the power supply connector and the Ethernet cable plug are present.

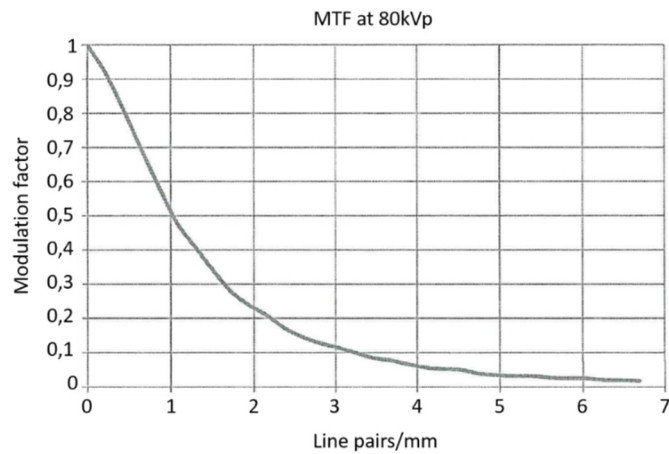


Figure 1-27 Modulation transfer function as communicated by the detector producer.

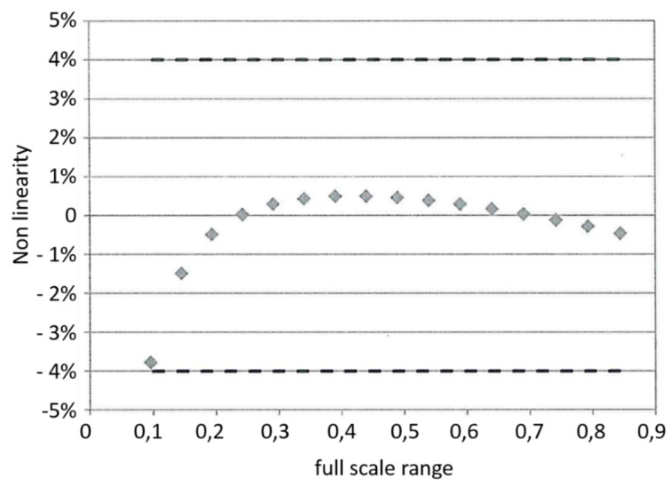


Figure 1-28 Linearity of the detector over its full range scale as communicated by the detector producer.

- **Control Equipment**

The microCT machine is controlled by a remote PC hosting custom software able of monitoring and running the machine. The X-ray source is however operated through the legacy software provided by the X-ray source producer since X-rays production must always be started by a machine operator action due to safety reasons. The control PC has the task of monitoring the machine throughout the acquisition process, however the real-time synchronism between the single frame acquisition and the rotary stage movement and the determination of the single frame acquisition duration is done using the electronic drive of the rotary stage, that can act also as a controller, since these operations require deterministic timings not obtainable with general purpose operating systems.

The rotary stage, through a program compiled and run from its internal memory, moves by the rotational step specified by the operator, find its positional stability within the specified accuracy, and then sends a trigger pulse as TTL signal to the detector to command the start of radiation integration for the current frame. Once the set exposure time is elapsed, the same trigger signal is used to command to the detector to

stop the radiation integration and start the sampling of the collected signal to produce a digital value. The exposure timing has a maximum jitter of 50 μ s, which can be considered negligible as error for normal exposure times of seconds. Once the integrated signal is transformed in a digital value for all the detector area, the image is transferred, by means of the giga-Ethernet link, to the control PC where it is received by the dedicated Ethernet card and stored to the SSD hard drive for later usage.

Figure 1-29 presents the control equipment layout.

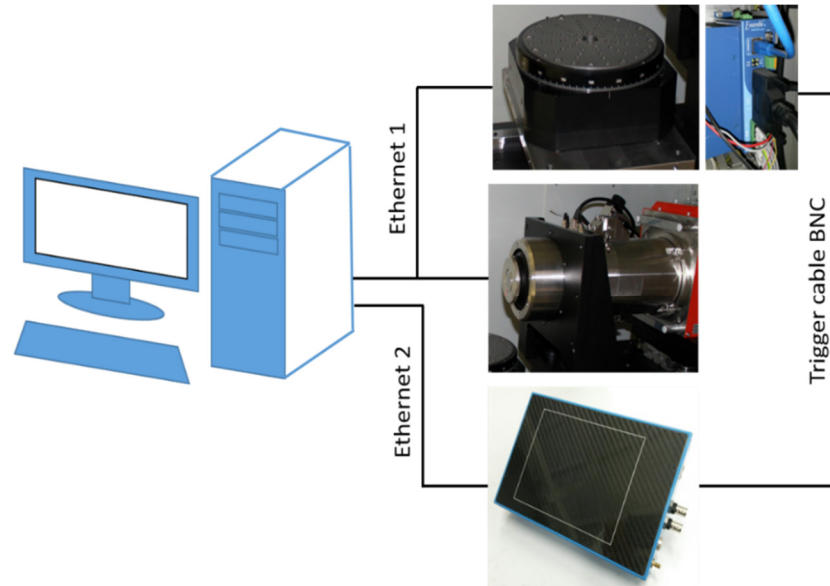


Figure 1-29 Illustration of the control equipment layout of the tomography machine.

1.4 CAPABILITY OF MICROCT TO MEASURE GEOMETRIES

X-ray computed tomography is widely used as a non-destructive technique to characterize the geometry of complex objects in the industrial [48], [49] and research fields [50], [51]. It represents an alternative to direct tactile coordinate metrology machines (CMMs) and structured light optical scanners. However, none of the mentioned alternatives has the capability of reconstructing the full 3D volume of the part under inspection, both on its inside and outside, being limited by the necessity to have direct access or direct view of the surface that must be measured. Especially in the case of completely free shapes, the complete spatial knowledge of the objects granted by microCT is key to the complete knowledge of the object since it produces a measurement nominally for every point in the scanned space with the nominal measurement resolution that applies to all three dimensions.

MicroCT can also be considered as the only usable measuring technique in case of very small objects, where the resolution obtainable from optical scanners is not enough or the necessity to touch the inspected part may not be possible, i.e. for flexible or fragile objects. First usage of computed tomography for the inspection of objects can be dated back to 1991, emerging more consistently from 2005 [48]. However, as any measurement technique that wants to be considered able of furnishing trustable measurements, microCT is undergoing an international validation process aimed at creating an international standard that can constitute the basis of any future utilization of this technology as standardized measuring instrument.

At present working group no. 10 of the ISO TC213 committee is trying to produce such an internationally recognized standard that should be applied to measurements done with microCT equipment.

However, the committee is facing difficulties in the standardization process due to the fact that the X-ray, considered as the measuring tool, is heavily influenced by the object under examination, since it interacts with it, especially for laboratory polychromatic X-ray sources[52], and the measurement chain that comprises X-ray source, X-ray detector and reconstruction process, is very complex, resulting in a difficult adaptation and consequently application of the current standards produced for CMM machines. However, national incomplete standards do already exist, presenting best practices to follow when using microCT machines so to produce trustable measurements. The most trusted one at present is the German VDI/VDE 2617/2630, which is also usually the most references one by microCT machine manufacturers. A review still valid in 2016 of the current status of standardization of CT measurements is presented in [53]. Other very interesting standards related to computed tomography, but not directly related to dimensional measurements are:

- Standard guide for computed tomography (CT) imaging (ASTM E 1441-97).
- Standard practice for computed tomographic (CT) examination (ASTM E1570-00).
- Standard test method for measurement of computed tomography (CT) system performance (ASTM E 1695-95).

Besides standardization committees, many research studies have been and are still being held to assess the characteristics of this technique in terms of measurement traceability[54], [55], uncertainty [54], [56], accuracy[57].

1.5 ASSESSING VOLUMETRIC RECONSTRUCTION ACCURACY

In case geometrical measurements need to be extracted, volumetric X-ray micro-computed tomographic reconstructions must be properly scaled and checked for possible shape errors produced by machine misalignments.

These checks are necessary before usage for any quantitative measurements purpose and must be repeated anytime the X-ray CT machine is realigned or better at constant time intervals, since even without any movement of the machine's components some parts components of the machine wear out due to usage, mainly the X-ray source target, causing possible alignment problems. In the absence of a recognized standard, a common method of scaling and checking geometrical correctness of the reconstructed volume is to measure calibrated reference geometries of known dimension and shape.

Capabilities of the Unibg microCT have been assessed producing reconstructions of the following calibrated objects of known dimension and geometry:

- Micro-CT Bar Pattern nano-chip phantom (produced by QRM GmbH-quality assurance in radiology and medicine).
- 2 mm diameter stylus (producer Renishaw plc).
- 0,3 mm diameter stylus (producer Renishaw plc).

Micro-CT bar pattern nano.

The Micro-CT Bar Pattern nano-chip phantom, presented in Figure 1-30 is a small cylinder made of plastic containing two silicon chips of dimension 3 x 3 x 0.66 mm positioned one parallel and one perpendicular to the axis of the external cylindrical container, that can be used to assess in plane and axial spatial resolution [58]. A phantom in the microCT field is a term utilized for a reference object of known material and geometrical properties that can be scanned repetitively to check if the reconstructed volume mirrors the known object properties. The two chips are engraved with lithographic technique to present on their surface geometric patterns of parallel and converging lines, of series of points and other specific shapes such as an actinomorphic star (Siemens star) and a slanted-edge. Each engraved shape has an engraving depth of 5 to 15 μm and lines and points have a width of 1 to 10 μm (50 to 500 lines per mm). Figure 1-31 presents the layout of the engravings on the chips. The engravings on the chips are positioned in the centre of the chips but also on the corners so to assess the resolution for the full phantom dimension.

The acquisition parameters utilized to scan the QRM Phantom are:

- Projections: 2,400
- Step angle: 0.1125
- SOD:8
- SDD:365
- Tube voltage: 60 kV
- Tube current: 35 μA (17,3 μAt)
- Mode: SFC0 (focal spot 2 μm)
- Time exposure: 1,000 ms
- Bin: 1x1
- Well: High
- Filter: none
- Target thickness: 2 μm

As depicted in Figure 1-33 qualitatively the results obtained from the reconstruction of this phantom with the Unibg microCT indicate that the machine is able of producing a reconstructed volume with a resolution that is slightly less than 4 μm which is consistent with the nominal one, 2.19 μm , calculated by simple magnification, plus the blurring due to the penumbra effect that can be calculated to be equal to 1.19 μm , with the formula mentioned in the previous chapter, resulting in a total reconstruction resolution of $(2.19+1.19)= 3.38 \mu\text{m}$. Apart from a first qualitative visual inspection, a standard method to quantitatively calculate the reconstruction resolution is described by international standard ISO 12233:2014 [59], which describes a technique, known as “slanted edge MTF”, which is widely used for performance evaluation of optical systems. MTF stands for Modulation Transfer Function and defines how different spatial frequencies are handled by an optical system. For the purposes of this thesis the Matlab® code implementation furnished by P. Granton was used [60] for the MTF calculation. The QRM phantom furnishes for the MTF slanted edge calculation a slanted edge in the form of an engraving with an L shape, positioned for this purpose at 5 degrees tilt angle, the mentioned engraving is visible in Figure 1-32. The

result of the calculation on the reconstructed area gives an MTF value of 10% at a spatial frequency of 3.7 μm , meaning that this is the maximum system resolution.

The Matlab® script first calculates the edge spread function of the selected edge oversampling it by 10x, see Figure 1-34 and Figure 1-35, and then the corresponding line spread function, as its derivative, see Figure 1-36 and Figure 1-37; the line spread function is at the end used to calculate the value of the MTF for different spatial frequencies.

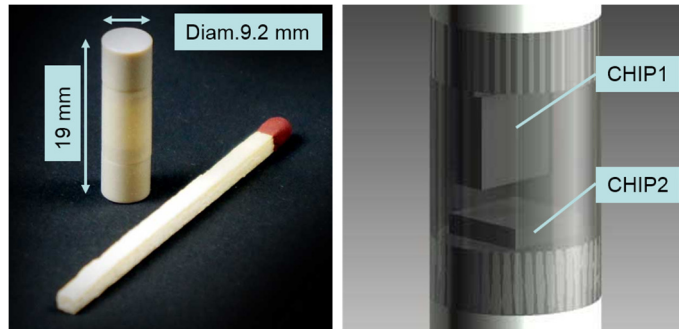


Figure 1-30 (Left) nano-bar phantom positioned near to a match for scale comparison. (right) enlarged view of the middle section of the phantom cylinder revealing the inside with the two chips positioned axially (chip1) and perpendicularly (chip2). Source: image courtesy of QRM GmbH (with own overlays)

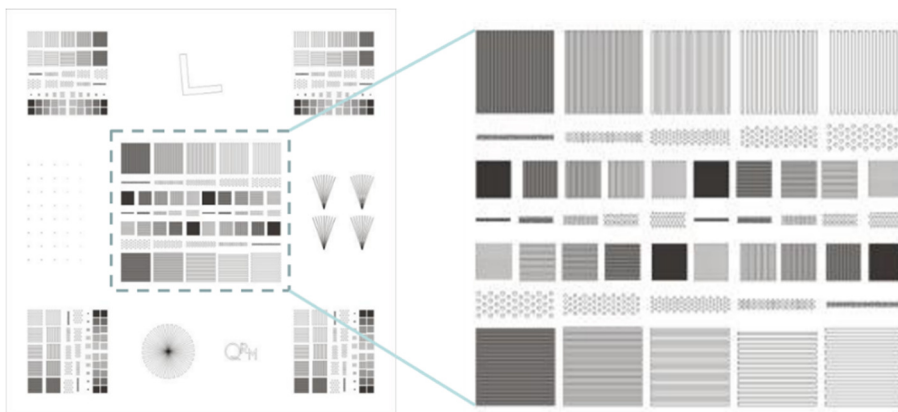


Figure 1-31 : (left) layout of the full engraved area of the two silicon chips contained in the phantom. (right) zoom of the central part of the engraved area showing line and point patterns with width from 10 to 1 μm . Source: image courtesy of QRM GmbH

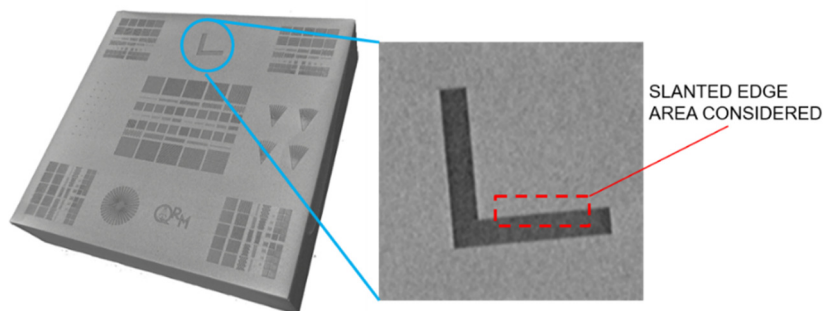


Figure 1-32 (left) Slanted edge present on the QRD phantom. (right) indication of the portion of the slanted edge utilized for the calculation of reconstruction resolution.

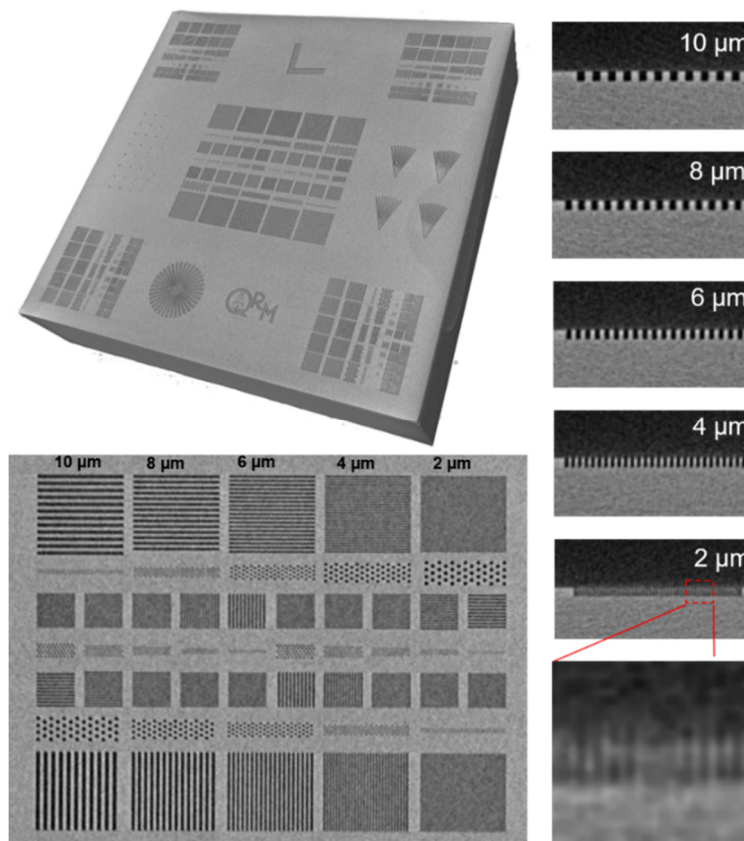


Figure 1-33 (top-left) 3D rendering of the reconstructed volume of the vertical chip of the QRM phantom. (bottom-left) Zoom of the central area of the phantom where it is clearly visible the possibility to distinguish lines of 4 μm with the nominal tomography resolution set at 2.19 μm .(right) from top to bottom cross cut of the 10-8-6-4-2 μm lines to show engraved lines distinguishability down to 4 μm , while the 2 μm apart lines are not clearly identifiable.

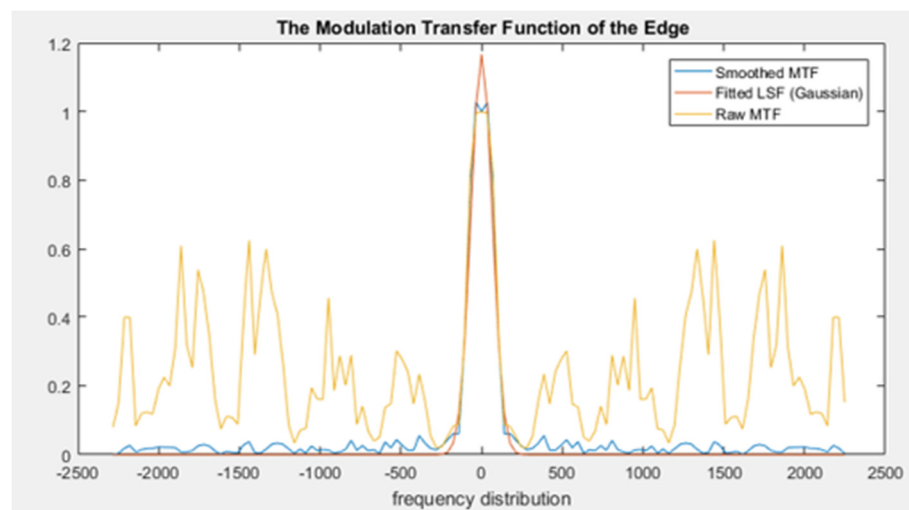


Figure 1-34 Plot of the Modulation Transfer Function (MTF) for the area selected on the reconstructed phantom slice.

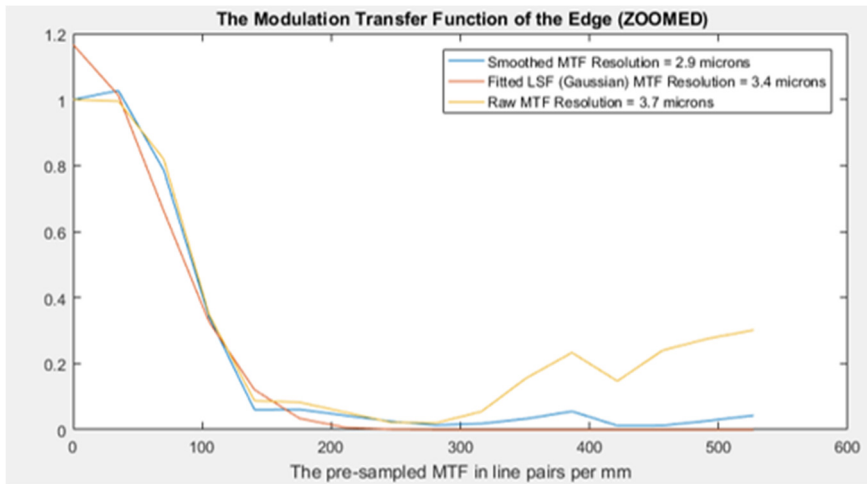


Figure 1-35 Zoom of the plot of the Modulation Transfer Function (MTF) for the right hand side of the modulation transfer function of the edge with indication of the function values for 10% transmission.

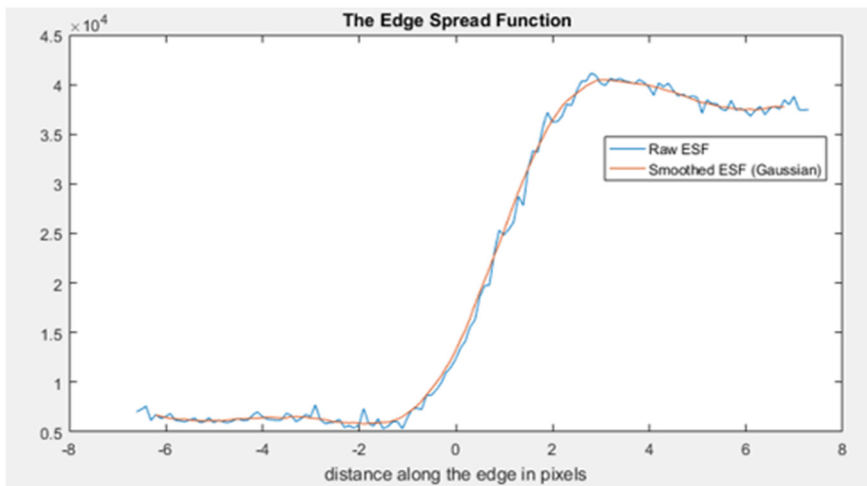


Figure 1-36 Plot of the Edge Spread Function (ESF) for the area selected on the reconstructed phantom slice.

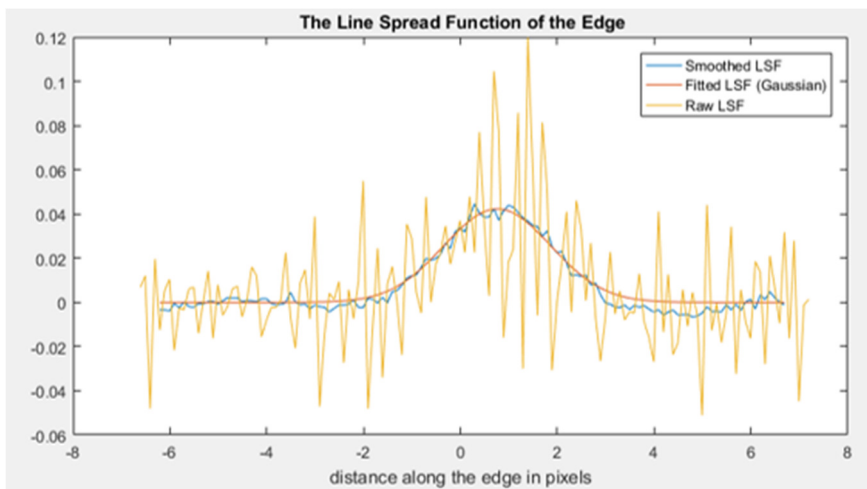


Figure 1-37 Plot of the Line Spread Function (LSF) for the area selected on the reconstructed phantom slice.

Renishaw cylinder and styli

Two calibrated styli produced by Renishaw plc. were utilized to assess the capability of the microCT machine to reconstruct known geometrical shapes, round and cylindrical in this case. The two cylinders selected are common styli utilized with coordinate measuring machines and their dimensions have been chosen to mirror the order of magnitude of the expected average dimension of the samples of interest for the tomographies that were going to be produced. The interesting dimensions were from 6 to 1 mm but for the case of injection holes the interesting dimensions were from 100 to 300 μm . A stylus of 2 mm diameter and one of 0,3 mm diameter were therefore used. The first stylus visible in Figure 1-38, Renishaw product code “A-5000-7812”, is a synthetic ruby (Al_2O_3) cylinder mounted on a stainless-steel support with a half ruby sphere on top. The half sphere is a Grade 5 sphere with 2 mm diameter and maximum deviation from spherical form of 0.13 μm . Since the DIN-5401 ball grade standard imposes the mentioned 0.13 μm constraint only on the sphericity giving a tolerance on the diameter of +/- 5.63 μm , this latter diameter measurement has been measured with a calibrated Mitutoyo digital micrometer 293-666 (with +/- 2 μm accuracy) giving a mean diameter size of 2,000.3 μm and a standard deviation of 1.53 μm . The stylus has been scanned and reconstructed with a machine setup able of granting a nominal resolution of 2 μm . Figure 1-39 presents the result of the reconstruction.



Figure 1-38 (top) 2 mm Renishaw stylus utilized as geometrical phantom for the mm size objects. (bottom) measure of stylus diameter with calibrated digital micrometre.

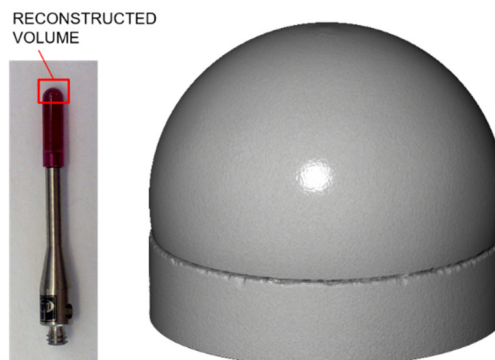


Figure 1-39 (left) picture of 2 mm Renishaw stylus with (right) its rendered reconstruction form CT data.

The reconstructed volume has been converted to a mesh in stl format after thresholding as presented in Figure 1-40. Then the mesh surface points have been interpolated using a 3-sigma Gaussian best fit algorithm to produce nominal sphere and cylinder geometries to highlight reconstructed mesh deviations from nominal shapes. The maximum deviation measured for the spherical surface was 2.04 μm as illustrated in Figure 1-41.

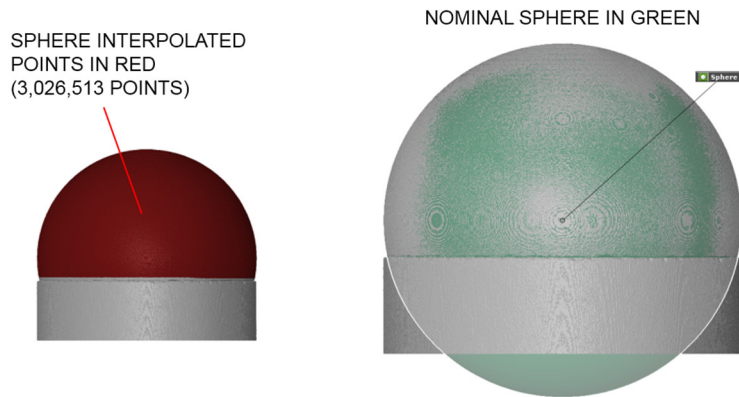


Figure 1-40 (left) in red reconstructed stl surface points selected for the fitting operation. (right) in green nominal fitted sphere overlaid to the original reconstructed stl surface shown in grey.

SPHERE MESH SURFACE DEVIATION

Information	
Selected elements: 1	
Sphere 1	Construct Fitting Sphere
Adjustment result	
Minimum:	-0.00204 mm
Maximum:	0.00204 mm
Minimum absolute deviation:	0.00000 mm
Maximum absolute deviation:	0.00204 mm
Sigma:	0.00065 mm
Residual:	0.00052 mm
Creation base	
Number of points used for creation: 3026513	

Figure 1-41 Table of deviation from nominal sphere of mesh reconstructed from microCT data considering a 3 sigma Gaussian fitting of original sphere surface points.

A test has been done also considering all the produced surface points to create the fitting sphere, this test presented in Figure 1-42 resulted in a sphere with a maximum deviation of 6.61 μm . Increased deviation between the two fitting surfaces produced starting from the same tomography results can be attributed in minor entity to sparse noise or wrong surface mesh elements but mainly to the tomography artefact created in the position of the rotation axis, also known as pole-artefact [61]. The mentioned artefact can be clearly rendered visible colouring the mesh elements with a colour coded on the deviation of the reconstructed sphere from the nominal perfect one. Figure 1-43 presents the result of the deviation calculation with false colours, deviation scale from +/- 2 μm . A similar geometrical deviation analysis has been done utilizing the surface points of the supporting cylinder, resulting in a maximum surface mesh deviation from nominal cylindrical shape of 2.46 deviation μm . In this case no pole axis artefact has been detected since the interesting surface does not intersect the tomography axis, see Figure 1-44 and Figure 1-45. Attention must

be therefore given t tomographic surfaces areas reconstructed in the tomography axis vicinity.

Information	
▼ Selected elements: 1	
Sphere 2	Construct Fitting Sphere
▼ Adjustment result	
Minimum:	-0.00334 mm
Maximum:	0.00661 mm
Minimum absolute deviation:	0.00000 mm
Maximum absolute deviation:	0.00661 mm
Sigma:	0.00067 mm
Residual:	0.00053 mm
▼ Creation base	
Number of points used for creation: 3040466	

Figure 1-42 Table of deviation from nominal sphere of mesh reconstructed from microCT data considering all available points of original sphere surface.

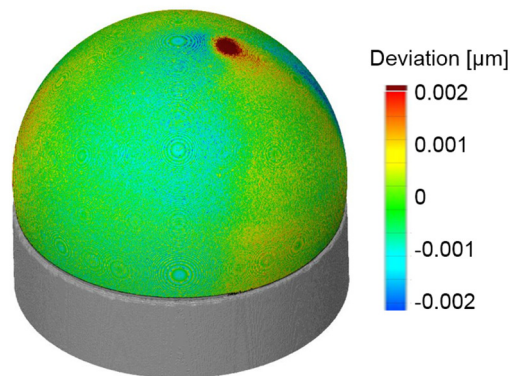


Figure 1-43 Deviation of sphere surface created with all available points to show pole artefact. As it can be seen the mesh deviation points that increase by three times the surface deviation from nominal spherical geometry are concentrated near the tomography rotation axis (dark brown in the figure).

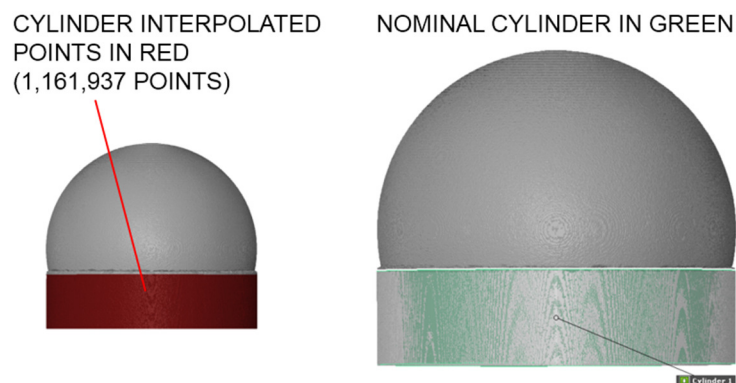


Figure 1-44 (left) in red stl surface cylinder points selected for the calculation of the fitting nominal cylinder. (right) in green nominal cylinder created form the selected pints overlaid to the original stl surface shown in grey.

CYLINDER MESH SURFACE DEVIATION

Information	
▼ Selected elements: 1 Cylinder 1 Construct Fitting Cylinder	
▼ Adjustment result	
Minimum:	-0.00246 mm
Maximum:	0.00245 mm
Minimum absolute deviation:	0.00000 mm
Maximum absolute deviation:	0.00246 mm
Sigma:	0.00080 mm
Residual:	0.00065 mm
▼ Creation base	
Number of points used for creation: 1161937	

Figure 1-45 Table of deviation from nominal cylinder of mesh reconstructed from microCT data considering 3-sigma points of original surface.

The second stylus, Renishaw product code “A-5000-7818”, is a synthetic ruby (Al_2O_3) sphere mounted on a stainless-steel support. The semi complete sphere is again a Grade 5 sphere but this time with 0.3 mm diameter and again maximum deviation from spherical form of 0.13 μm . Due to the smaller dimension of this phantom, the tomography has been set-up to obtain a nominal resolution of 1 μm by translating the object nearer to the X-ray source to increase magnification. Also for this sphere the mentioned 0.13 μm constraint is valid only for the sphericity, and again the dimensional diameter tolerance is instead +/- 5.63 μm , this latter diameter has been measured with the same calibrated Mitutoyo digital micrometre giving a mean diameter size of 299.33 μm and a standard deviation of 0.57 μm . Figure 1-46 presents the result of the tomography reconstruction. The reconstructed volume has been thresholded and again a mesh surface has been created, then the mesh elements have been interpolated using a 3-sigma Gaussian best fit algorithm to produce a nominal sphere geometry, Figure 1-47. The maximum deviation between the reconstructed sphere and the nominal geometry has been calculated to be 2.04 μm , Figure 1-48. No significant differences have been calculated this time considering all the selectable point rather than the 3-sigma ones since no pole artefact was present in the reconstructed surface because the small dimension of the sphere granted the possibility to scan the full sphere volume in an off-rotation axis position. Figure 1-49 visually scales the dimension of the selected Renishaw styli with reference to a common diesel injector tip.

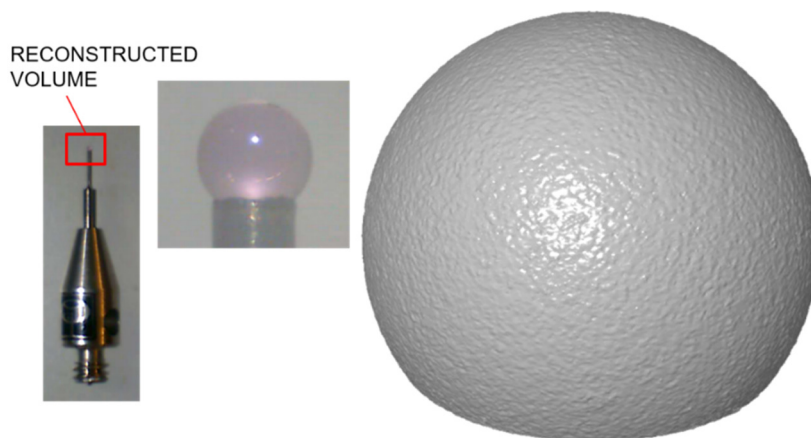


Figure 1-46 (left) overall and zoomed picture of 0.3 mm Renishaw stylus and (right) its rendered reconstruction from CT data.

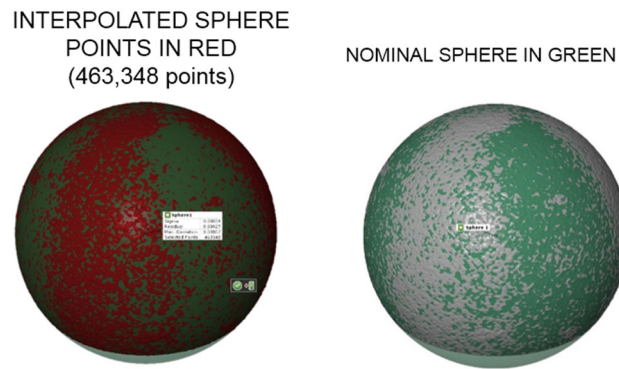


Figure 1-47 (left) in red selected surface point to fit nominal geometry (right) nominal sphere (in green) created with the fitting operation overlaid to the original mesh (grey).

SPHERE MESH SURFACE DEVIATION

Information	
Selected elements: 1	
Sphere	
Adjustment result	
Minimum:	-0.00107 mm
Maximum:	0.00106 mm
Minimum absolute deviation:	0.00000 mm
Maximum absolute deviation:	0.00107 mm
Sigma:	0.00034 mm
Residual:	0.00027 mm
Creation base	
Number of points used for creation: 463348	

Figure 1-48 Table of deviation from nominal sphere of mesh reconstructed from microCT data considering 3-sigma points of original surface.



Figure 1-49 (From top to bottom) picture of the diesel injector tip that will be the object of geometrical reconstruction within this thesis, and the 2 mm and 0.3 mm Renishaw styli to visualize the scale between the three objects.

1.6 SCALE CALIBRATION

Scale calibration is necessary to correctly scale the voxel size of the reconstructed volume so to produce reconstructed geometries with the correct dimensions. Commercial microCT machines are usually equipped with high resolution linear encoders connected to the moving parts of the machine, the rotary stage and the X-ray detector, so to measure their absolute position to calculate the tomography magnification from the measurement of the X-ray source to object distance and X-ray source to detector distance. The Unibg microCT was initially equipped with such an encoder but due to the necessity to modify the machine to adapt it to the different scanning configurations and objects to be scanned, an alternative procedure of calculating the tomography resolution has been conceived to be used when quantitative reconstructions needed to be done. When high precision scaling of the reconstructed volumes is necessary, a further tomography to a reference object is produced right afterwards the object tomography, so to have the possibility to scale the reconstructed volume based on the dimension of the reference object scanned in the same conditions, mainly machine thermal conditions that can influence the scaling. As reference object a composition of the two Renishaw styli, 2 mm half sphere and 0.3 mm semi-complete sphere, already introduced have been used. Figure 1-50 presents the schematic view of the reference object alongside its realization.

The reference object comprises a cylindrical container with inner diameter equivalent to the maximum diameter of the Renishaw styli stainless steel support, this has been designed to act as axial aligning surface between the two styli. The two styli are then positioned in the cylinder with the two spheres touching each other, a rubber damping element has been added to grant the contact between the two spheres regardless of any small movement of the container, see Figure 1-51 for reference set-up. With this configuration, the distance calculated in the reconstructed volume between the two spheres centres is equal to the sum of their radiuses, which is a known dimension that can be therefore utilized to scale the voxel dimension. The measure of the distance between the two spheres centres is independent from the value chosen for the thresholding of the material value, that is a common problem of dimensioning volumes reconstructed starting from CT data when only dimension non-independent form this parameter can be measured.

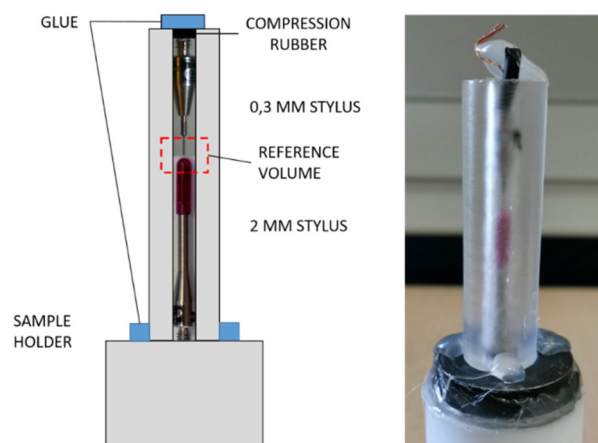


Figure 1-50 (right) schematic section view of the reference scaling phantom created with the two Renishaw styli: the outer plexiglass container has been cut to reveal the layout of the two styli. (left) picture of the real sample produced and utilized.

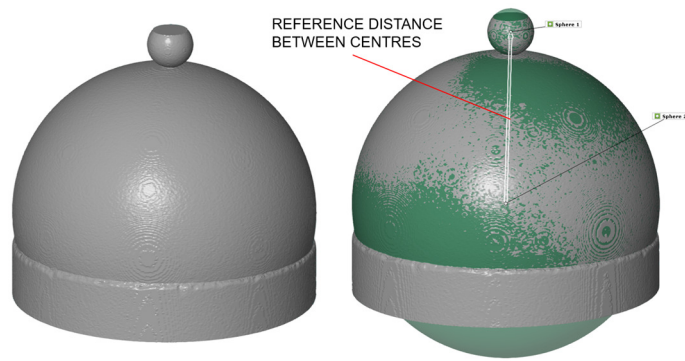


Figure 1-51 (left) stl surface of the two styli reconstructed from the single CT dataset. (right) in green 3-sigma fitting spheres utilized to calculate the distance between the centres, the line connecting the two centres is highlighted as “reference distance”.

1.7 BEAM HARDENING CORRECTION FOR METAL PARTS.

Laboratory polychromatic X-ray sources suffer from beam hardening effect which makes nonlinear the logarithmic attenuation of the X-ray radiation through the object material.

During reconstruction, this results in the calculation of a non-uniform attenuation value for samples made of only one material.

Visually the effect shows up in the reconstructed slices as a so-called cupping artefact or dark streaks or areas.

Cupping artefact can be easily visualized if we take as an example a cylindrical sample reconstruction, see Figure 1-52: the reconstructed slice perpendicular to the axis will show degrading grayscale values going from the outer border to its centre, therefore if we plot in 2D the grayscale values of any diameter, a cup like shape will be present instead of a straight line.

Dark streaks, see Figure 1-53 are visible in the case of geometrically more complex samples or samples made of differently attenuating materials since they originate from the different filtration of X-rays dependent on the sample rotational position. In this case the sample material itself acts as a non-uniform filter creating localized false variations of the calculated attenuation coefficient. The beam hardening effect has been corrected applying two techniques presented in the following when necessary:

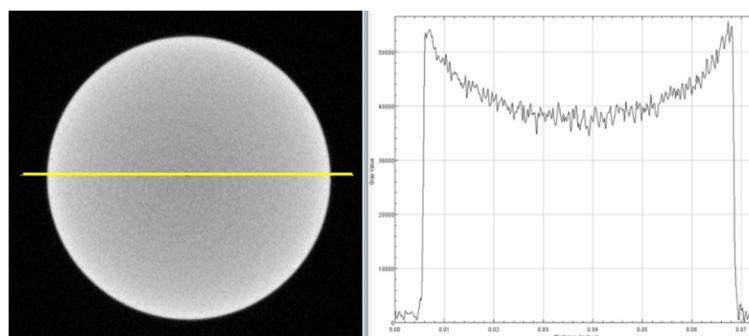


Figure 1-52 (left) axially perpendicular slice of a sample metal cylinder showing beam artefact in the form of degrading greyscale values in the direction going from the outer border to the cylinder centre. (right) plot of greyscale values vs. diameter position of the yellow line over imposed to the cylinder section present in the left image.

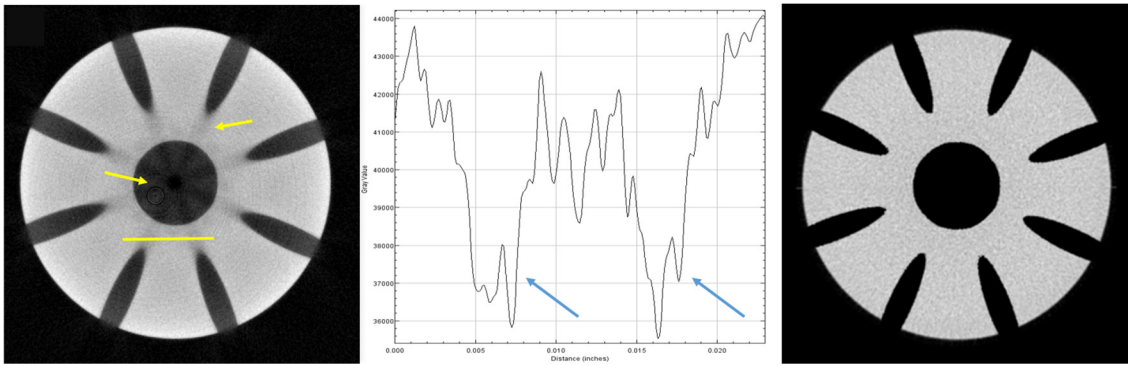


Figure 1-53 (left) axially perpendicular slice of a Diesel injector tip reconstructed with microCT showing streaks artefacts produced by injection holes, yellow arrows highlight modification of calculated attenuation value which is visible for areas inside the injector material and outside (air). (centre) plot of greyscale values indicated by the line in the left image, blue arrows show lower attenuation due to beam hardening streaks. (right) same slice after beam hardening correction application,

- **Beam pre-hardening by means of metallic filters**

Low energy components of the X-ray radiation produced by the X-ray source are filtered out by means of metal filters, purposely positioned between the emission point and the object to be scanned, to narrow the radiation spectrum. This way the object interacts only with the higher energy components of the radiation, that has made it through the filter, limiting the radiation hardening caused by the sample material itself. The selection of the metallic filter must be done wisely since its introduction decreases the beam hardening effect, which is the desired effect, but it also reduces the image contrast and increases the image noise [62], which is an undesired effect.

Figure 1-54 presents a simulation of the radiation hardening caused by filtration.

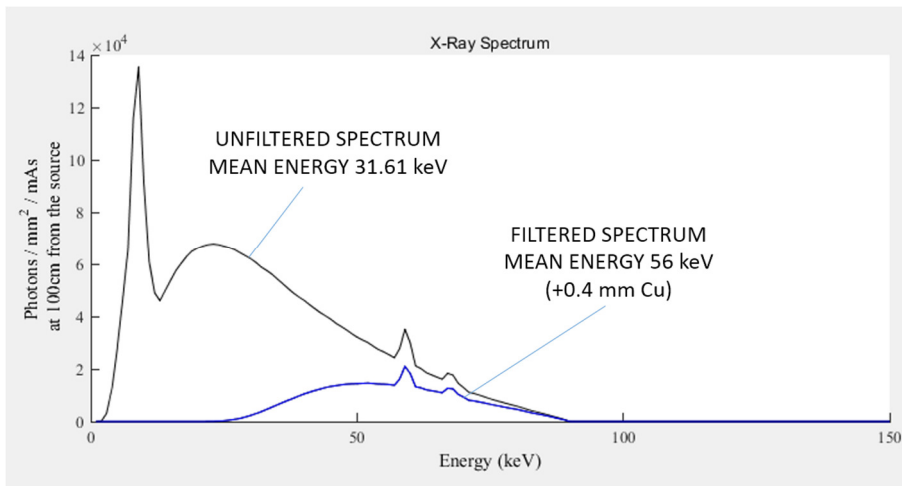


Figure 1-54 Unfiltered (grey line) versus filtered (blue) spectrum.

- **Linearization and post reconstruction beam hardening correction**

Beam hardening can be corrected modifying the calculated attenuation values to regain the attenuation

linearity utilizing either:

- a calibration of the radiography greyscale values vs material thickness produced with a reference sample of a specific material with known thicknesses Figure 1-55
- methods of image processing (reprojection, analytic)

In case a step wedge correction is used, the correction map is usually created utilizing a staircase like step wedge of the same material of the object, exhibiting different thicknesses so to map the known dimensions to the grayscale value of the corresponding area on the detector obtaining a calibration line by interpolation of the experimental points. The following figure presents the standard shape and utilization of a step wedge for beam hardening correction; the reference sample has been obtained stacking 12 iron metal foils of 0.4 mm thickness to be able to calibrate iron samples thicknesses up to 4.8 mm.

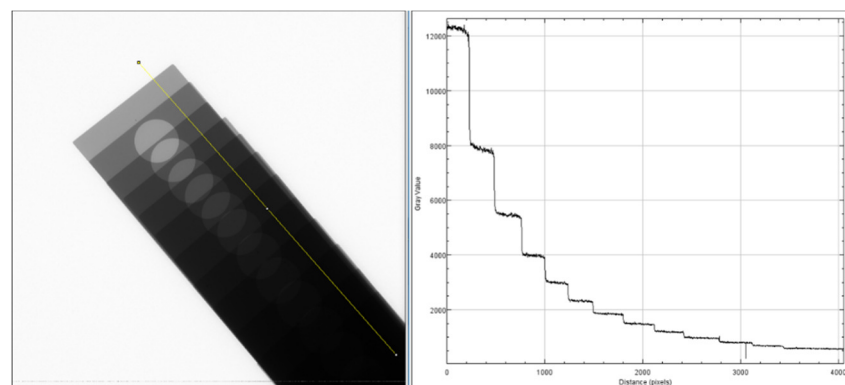


Figure 1-55 (left) radiography of the step wedge created with a tack of metal foil of 0.4 mm thickness and (right) grayscale values plot of the yellow line through its length.

However, for the work contained in this thesis concerning microCT of metallic parts, mainly diesel injectors, the beam hardening correction map has been created using a method called “self-wedge” due to the fact that a step wedge made of the material of the object to be scanned was not available. The self-wedge method was initially believed to be new but afterwards it was found referenced and in use also by the computed tomography laboratory of the University of Texas [63]. Differently from the standard step-wedge technique, the proposed self-wedge technique, see Figure 1-56 and Figure 1-57, doesn't require a separate calibration tomography to a step wedge phantom of the same material of the scanning sample, but it instead combines known sample information, mainly kind of material and geometry, with a sample radiography, to derive the correction map. For the case of Diesel injectors for example, the following procedure has been utilized:

- Collection of the radiographies necessary for the tomographic reconstruction.
- Reconstruction of the tomography and production of the injector geometry as. stl file utilizing a best guess threshold value.
- Scaling of the reconstructed injector surface to retrieve known injector dimensions.
- Creation of the beam hardening correction map utilizing the thickness information retrieved from

the geometry reconstruction and grey value present in the radiography.

- Iteratively:
- Re-reconstruction of the tomography applying the beam hardening correction.
- Re-production and scaling of the injector surface.

While the step- or self-wedge beam hardening correction method tries to simulate beam monochromaticity by changing the projections values based on a reference or self-reference measurement, correction methods based on image processing use the information contained in the acquired sample radiographies and reconstruction to produce a beam hardening correction. This kind of methods, can be based on rigorous knowledge of all the sample materials characteristics (mass density, mass attenuation coefficient, atomic number) and the used X-ray spectrum energies, or on an estimation of these information from the available projection and reconstruction.

In the first case the correction method is properly defined post-reconstruction method, while in the second case the method could be called pseudo-post reconstruction or analytic and this is the usual beam hardening correction method available in commercial reconstruction software as the one utilized for tomographic reconstruction produced during this thesis. Usually, to obtain effective beam hardening suppression in the reconstructed volume, the beam hardening effect is first reduced by hardware filtration by means of appropriate metal filters, then the remaining part is further reduced by software correction. The result of beam hardening correction on the first of the two proposed images is presented in Figure 1-58

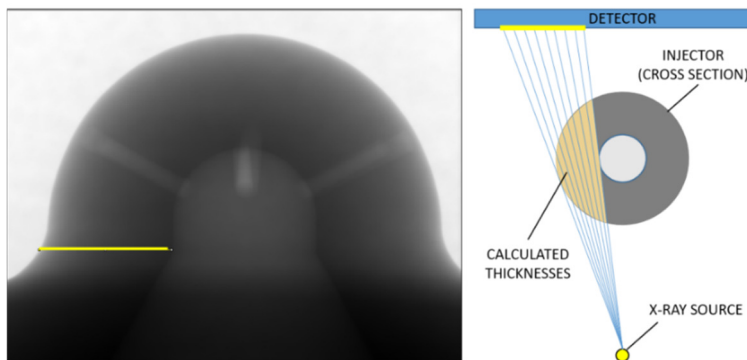


Figure 1-56 (left) radiography of Diesel injector tip without needle with yellow line over imposed to the area utilized for the calculation of the self-wedge map. (right) Illustration of the thicknesses calculation for the object of interest.

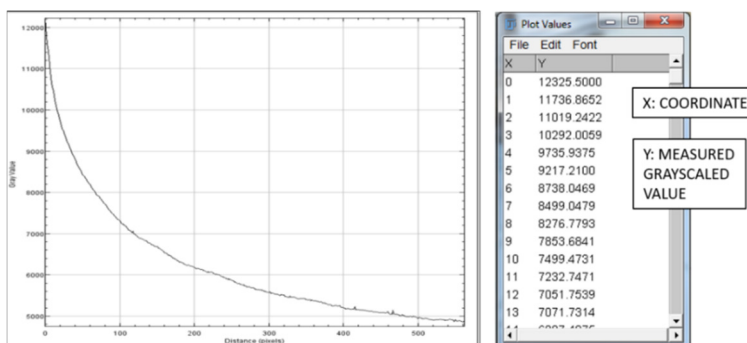


Figure 1-57 (left) plot of the greyscale value of the radiography indicated by the yellow line showing detected material

attenuation through material thickness. (right) table of radiography greyscale values vs position to be used to correlated greyscale valued with calculated thicknesses.

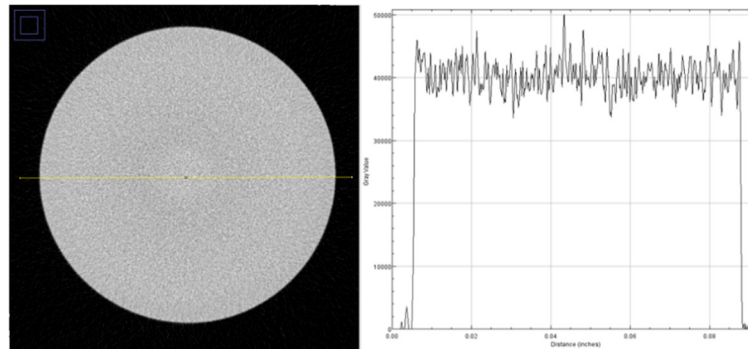


Figure 1-58 (left) same axially perpendicular slice of the sample metal cylinder showing beam artefact correction result. (right) plot of greyscale values vs diameter position of the yellow line over imposed to the cylinder section present in the left image revealing grey values homogeneity improvement due to applied correction.

1.8 SOFTWARE USED FOR TOMOGRAPHIC RECONSTRUCTION

Tomographic reconstruction within the scope of this thesis were produced using commercial reconstruction software VGStudio MAX [64] (Volume Graphics GmbH, Germany), at the beginning in its 2.2 version and afterwards in its 3.0 version.

The choice to use a commercial software rather than an open source one was led by the fact that VGStudio MAX was the official reconstruction software of the microtomography laboratory of the university of Bergamo. It was selected by Prof. Maurizio Santini after test trials done with almost all the available open source free software available at the beginning of my PhD (March 2013) and none of them was found to have the same good compromise between available features, support, ease of usage and performances.

In particular, the reconstruction speed of VGStudio MAX was much higher than similar open source reconstruction software based on the same FDK reconstruction algorithm, the performance improvement was mainly due to the implementation of extensive reconstruction calculations through the usage of GPU CUDA cores rather than CPU.

Moreover, open source reconstruction software was usually not able to handle big datasets like the ones produced with the available detector that were in the order of 1,944x1,944x1,536 pixels with 16-bit image depth each, meaning datasets of around 12 GB. Another very useful feature of VGStudio MAX, if compared to open source software, was the possibility to produce fast previews of reconstruction slices which is essential for reconstruction parameter tuning. VGStudio MAX is also a very well tested software instrument that is leading the market of industrial tomography.

However, the drawback of selecting a commercial software rather than an open source solution means no possibility to modify the reconstruction algorithm and limited possibility to set up its parameters.

Since the focus of this thesis is on applications, a review of currently available reconstruction software and algorithms has been considered out of scope, so already tested and selected reconstruction software has been used.

2 APPLICATIONS TO COMPLEX GEOMETRIES (THERMAL-FLUID DYNAMICS)

2.1 INTRODUCTION

X-ray micro computed tomography has been used for the analysis of the equilibrium state of liquid drops gently deposited on rough surfaces. The usage of microCT has granted the possibility to reconstruct the complete volumes of both surface and drop without altering it, so to understand in the 3D space their equilibrium state, granting the possibility to know how the drop pins to the surface also in positions inaccessible to conventional techniques based on 2D images.

Contact angle measurement were possible in every point of the triple line giving the possibility to compare them to the same measurements performed with conventional techniques, showing that the proposed technique is very promising for this kind of measurements.

A patterned surface made of parallel slightly curved micro grooves of trapezoidal section has been then used to understand how drops of different sizes adapt to the same surface anisotropically, spreading on it in the preferential direction of the grooves, resulting in contact angle values which are dependent on the measuring position. On top of this the volumetric reconstruction of the surface has granted the possibility to calculate the real Wenzel ratio of the surface. The total volume reconstruction capability has been afterwards applied to investigate the wettability of gas diffusion layers hydrophobized by fluoropolymers (PTFE and PFA) in the technological application of fuel cells. Gas diffusion layers (GDLs) are membranes made of cloth which have a very complex structure which can be realistically modelled for CFD simulation starting from tomographic reconstruction. The presented technique has been also used to study how the drop lays on the GDL, confirming that it is in a Cassie-Baxter state.

2.2 LITERATURE REVIEW ON DROP SHAPE ANALYSIS

Knowledge of wetting behavior of liquids on solid surfaces is known to be of paramount importance for many engineering applications where the degree of interaction between liquid and surface deeply influences the process performances. Such engineering applications include among others heat exchangers [1], lubrication of moving parts [2], gas and crude oil extraction from soil [3] and surface coatings [4].

More recently the interest in the knowledge of wettability has been boosted by the possibility, granted by technological advance in microfabrication [65], [66], to produce geometrically complex patterned surfaces that can mimic desired properties in particular of natural materials and biological surfaces [5]-[7] exhibiting very interesting properties among which one of the most famous is the auto-cleaning effect of the lotus leaf [67]. The wettability of a surface by a specific liquid and at specific ambient conditions is determined by the thermodynamic equilibrium of the triple line which is the line of contact that forms between the solid, the liquid and the vapor phase.

When a liquid drop gently deposited, or sprayed, on a surface reaches an equilibrium state, its interaction with the surface can be described by the contact angle measurement which is the tangential angle formed

at the point of contact of the liquid with the surface, see Figure 2-1 The contact angle measurement determines if the surface wettability is high, corresponding to a contact angle greater than 90° , or low, corresponding to an angle smaller than 90° , this measure gives an information of how much the liquid tends to spread on the surface and therefore how much it is able to wet it, lower angle corresponding to more tendency to spread.

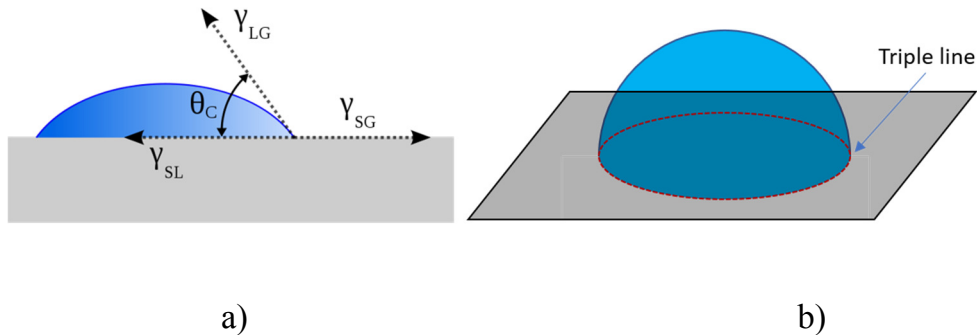


Figure 2-1 a) A diagram that shows the contact angle and interphase-energy between 3 phases (gas, liquid, solid). b) drop triple line highlighted in red. Images from a)[68] b) own.

The equation that regulates the contact angle value in equilibrium state is the well-known Young equation [69] that correlates the contact angle θ_Y to the interfacial energies γ_{IJ} of the phases with the following formula:

$$\cos \theta_C = (\gamma_{SG} - \gamma_{SL})/\gamma_{LG}$$

Equation 2-1

Where θ_C is the measured contact angle, γ_{SG} is the solid-gas interfacial energy, γ_{SL} is the solid-liquid interfacial energy and γ_{LG} is the liquid-gas interfacial energy, usually known as surface tension.

Young's equation however is able to describe the equilibrium state only in ideal circumstances since to be applicable it requires the surface to be perfectly flat, rigid, smooth and chemically homogeneous, and that any external force, potentially interfering with the equilibrium, is absent, including the gravitational force. In this ideal condition the shape of the contact line would be perfectly spherical and the drop would have a spherical based shape. To address the case of more real conditions, by including the presence of hydrostatic pressure which changes the shape of the drop flattening it on the surface, the Laplace-Young equation [70] has been introduced to describe the pressure difference at the interface between liquid and gas, due to the liquid surface tension, giving the possibility to relate it to the shape of the liquid drop. The equation related to the illustration in Figure 2-2 is the following:

$$\Delta p = \gamma_{LG} \left(\frac{1}{R_1} + \frac{1}{R_2} \right)$$

Equation 2-2

Where Δp is the difference of pressure at the liquid-gas interface, γ_{LG} is the liquid-gas interfacial energy

and R_1 and R_2 are the two principal radii of curvature of the drop.

In real conditions, however the interaction between drop and surface is subject to the presence of gravitational force, resulting in a deformation of the drop shape [71], and the drop interacts with the surface. The surface interaction can be mechanical, the drop adapts to the surface geometry and pins to the surface edges [72], [73], or due to the surface material chemical or physical properties [74], [75].

Because of all these non-idealities, the contact angle is not constant along the drop contour, being different from point to point along the triple line, and the triple line itself adapts to the surface diverging from its nominal circular trajectory. When a surface is not flat, i.e. it is naturally or artificially patterned, an apparent contact angle is measured instead of the real one which is hidden by the surface roughness, see Figure 2-3. A correlation between the apparent contact angle and the real contact angle can be done utilizing models which consider the two extremes of how the drop can lay on a rough surface: it can rest in equilibrium on the patterned surface without filling its grooves or it can rest on it completely copying its geometry. The relation between the real contact angle and the apparent contact angle that can be measured in the two states have been defined respectively by Wenzel [76] and Cassie-Baxter [77]. Figure 2-3 shows the same drop resting on a patterned surface in the Wenzel state and in the Cassie-Baxter state.

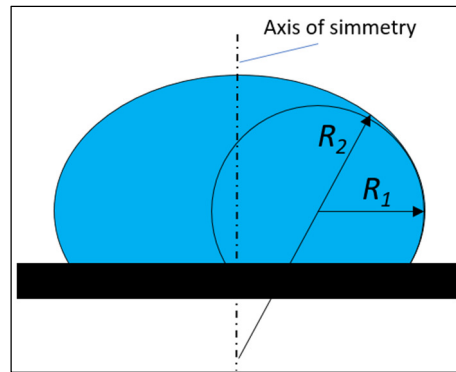


Figure 2-2 Section view of the ideally axisymmetric drop visualizing the two radii utilized by the Laplace-Young equation.

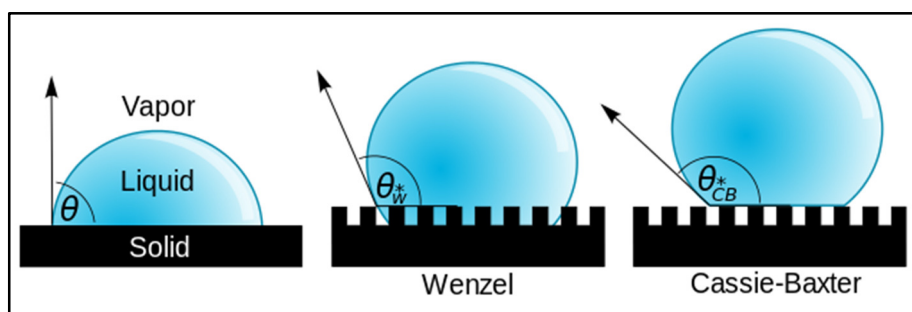


Figure 2-3 A droplet resting on a solid surface and surrounded by a gas forms a characteristic contact angle θ . If the solid surface is rough, and the liquid is in intimate contact with the solid asperities, the droplet is in the Wenzel state. If the liquid rests on the tops of the asperities, it is in the Cassie-Baxter state. Image from [78]

Many techniques have been conceived through the ages to produce the liquid-solid contact angle measurement, namely historically the telescope-goniometer, the captive bubble method, the tilting plate,

the Wilhelmy balance, the pendant drop and the immersed plate [8], [9]

Despite contact angle measurement could be perceived as a simple task, measurements techniques, which are mainly based on direct optical measurements, such as the most used method of the sessile drop [10] based on the acquisition and analysis of a side picture of the deposited drop, suffer from problems such as: necessity to have high illumination, which can cause fast liquid evaporation, lenses image aberration, light diffraction near fluid-surface contact points and non-parallel illumination direction. Moreover, as reported before, in real cases and for non-flat surfaces, the side view image can only provide data to calculate the apparent contact angle instead of the real one, introducing an approximation to the knowledge of the real contact angle. 3D measurements of the apparent contact angle can be obtained by rotating the sample by 360° and reconstructing the contour using the calculated drop profile.

More modern and advanced techniques are used to picture the real contact angle using reflection interference contrast microscopy [11], [12] or laser scanning confocal microscopy [13] but they need transparent surfaces patterned with specific grooves through which they are able to directly visualize the drop boundary.

Part of the work done within the scope of this thesis proposes, for the first time up to the author's knowledge, the usage of X-ray microtomography to gain full 3D knowledge of the equilibrium state of a drop over a surface [79], so that local real contact angle measurements can be obtained and moreover, due to the complete digitalization of the drop and underneath surface volumes, the drop 3D shape and volume measurement are possible. Afterwards X-ray computed tomography has been used to measure the contact angle of liquids contained in porous media, X-ray microcomputed tomography has been used with success to measure contact angles of oil and water inside reservoir and carbonates rocks [80], [81].

2.3 DROP ON TEFLON

The study of the applicability of microCT to drop-surface equilibrium studies started utilizing a surface made of Teflon (PTFE) and distilled water as liquid. The test case was designed to be as simple as possible from the point of view of utilized materials, PTFE and distilled water are very common, and from the geometrical point of view, the surface was designed to be flat and smooth, approximating as much as possible an idealized non-chemically reagent flat surface, and the liquid utilized had very well-known properties.

The aim of this first study was to understand if microCT could reconstruct correctly the drop-surface couple with spatial resolution high enough to give the possibility to identify the triple line along the full perimeter of the drop, so to produce localized contact angle measurements starting from the reconstructed sample volume.

Figure 2-4 presents a picture of the first sample produced showing a base cylinder made of Teflon with a small drop of distilled water placed on top of it. The drop has been manually placed on the surface with the aid of a small syringe. To obtain a flat and smooth surface, the Teflon material was cut with a sharp surgical knife. Previous attempts to produce the same flat surface with mechanical machining didn't produce the desired result since in every trial machining grooves were visible on sample surface with the naked eye. The surface roughness obtained with the knife cut was instead considered adequate since it was not visible and expected to be less than the tomographic resolution of 9 μm. Moreover, reference contact angle

measurements, planned to be done with standard 2D techniques, would have used the same Teflon surface so to have best comparability, therefore an accurate surface roughness measurement was not strictly necessary. In the real case studied gravitational force played an important role in the determination of the drop shape, so maximum effort has been done to assure that the Teflon surface utilized was placed horizontally and moreover, since the sample must be placed and rotated on a rotational stage to produce the tomography, also the rotary stage surface must be accurately levelled and its rotational axis has to be parallel to the gravitational force direction.

To produce the levelling proposed, a level with a precision of 0.05/1,000 mm visualized in Figure 2-5 was utilized. To obtain the highest tomographic resolution, sample and drop dimensions had to be reduced to 5 mm for the diameter of the Teflon supporting cylinder and to around 3 mm for the drop diameter, resulting in the set-up illustrated in Figure 2-6. The set-up of the microCT was selected to have a reconstruction voxel size of 9 μm was the following:

- Number of projections: 1,200
- Source voltage: 30 kV
- Source current: 85 μA
- Exposure time: 800 ms
- Source to object distance: 44.1 mm
- Source to detector distance: 365 mm
- Magnification factor: 16
- Rotational acceleration: 0.1 $^\circ/\text{s}$

For any tomography, the stillness of the sample is of paramount importance during the scanning since all the projections' information are summed up at the end to reconstruct one single sample volume, so if anything moves during the acquisition this reflects in an incorrect reconstruction. In the case of the drop deposited on the surface this stillness must be granted reducing at best the possibility of the drop to evaporate during the acquisition, thus reducing its volume and changing its shape, and moreover, since the drop-surface is a non-rigid system, caution in the form of very slow rotational acceleration during rotation, must be taken to avoid any movement of the drop.

Therefore, to address the last two problems mentioned, during scanning the drop has been contained in a closed volume so to reduce water evaporation and the acceleration of the rotational stage has been lowered to 0.01 $^\circ/\text{s}^2$. The positioning of the plastic cap seals the volume that contains the drop since it sits in a pool filled with the same water utilized for the drop, which also contributes to reduce evaporation in the close volume.

At constant X-ray cabinet temperature, to check if the drop has reached the equilibrium state desired for the tomography, successive radiographies can be taken at fixed time intervals: comparing the present one with the previous one will show if the drop contour has moved or if nothing has changed, so that equilibrium state can be considered present.

Figure 2-7 is a picture of the sample and sample holder inside the cabinet.

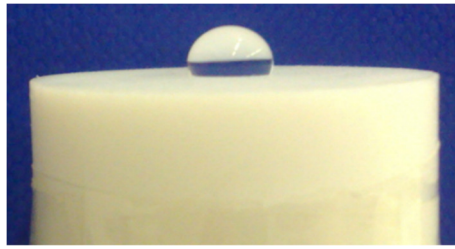


Figure 2-4 Drop of distilled water of almost 5 mm diameter gently deposited on a Teflon surface.



Figure 2-5 Level with a resolution of 50 micrometre per meter utilized for the drop on Teflon.

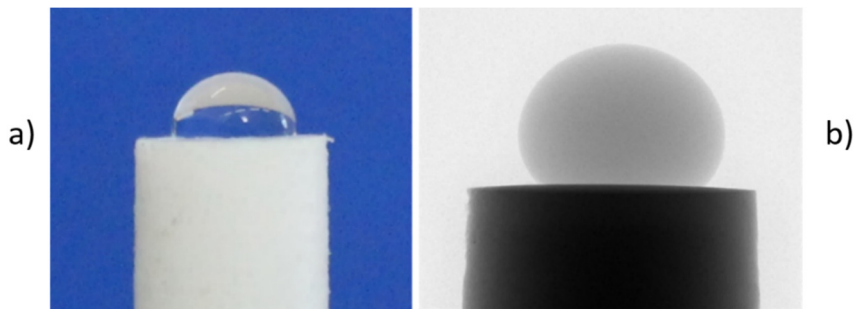


Figure 2-6 a) Drop of distilled water on Teflon cylinder (picture taken with a discarded cylinder. b) Sample radiography of the surface with deposited drop.

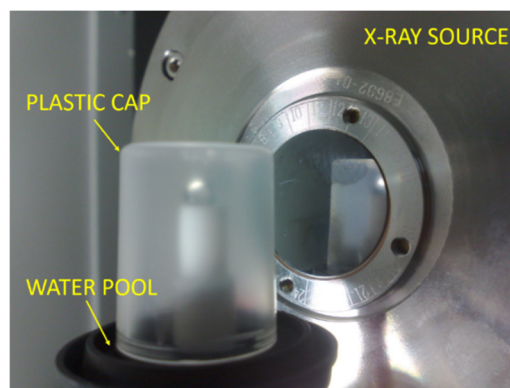


Figure 2-7 Visualization of the drop on Teflon positioned in front of the X-ray source for scanning purposes. The partially anti-evaporation cap and beneath water pool is visible.

It must be noted that the necessity to add a plastic cap to create a sealed volume is something negative from the point of view of the tomography result quality since it acts as an X-rays filter, reducing the low energy X-ray radiation that is the most attenuated by water, thus reducing the resulting image contrast.

Even starting the tomography with the drop in a steady state is not enough due to X-rays heating the drop. In the final proposed scanning configuration, the drop evaporation is still present and has been measured comparing a reference radiography of the drop in the same rotational position before and after the scan, giving thus a movement of the apex drop contour of 3 pixels, corresponding to 19.68 μm , see Figure 2-8. However, the detected apex difference has not been detected at the drop base, where the triple line is, meaning that this area is less sensitive to drop evaporation.

As a reference the following Figure 2-9 is an overlay of the same start-stop radiographies of the drop produced after a tomography with anti-evaporation cap removed.

The result of the tomographic reconstruction is the surface-drop volume digitalized in 2D dimension files saved as tiff image; the stack of all the reconstructed 2D slices, considering a distance between them as the reconstruction resolution, can be then used to produce a 3D representation of the reconstructed volume as done in Figure 2-10.

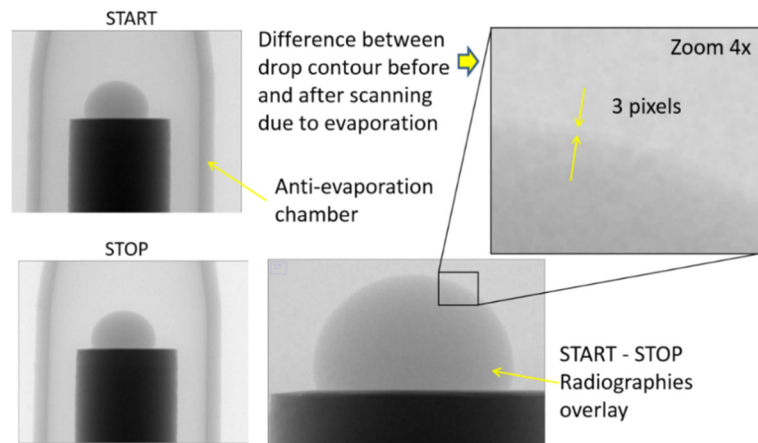


Figure 2-8 a) superposition of reference drop radiographies (before and after tomographic acquisition in the same position).
b) zoomed view of the drop contours showing the still present evaporation effect.

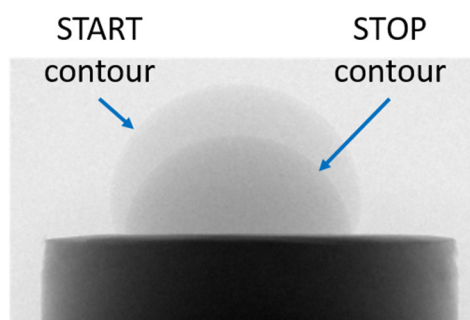


Figure 2-9 Overlay of drop radiography before and after tomographic scan without anti-evaporation cap.

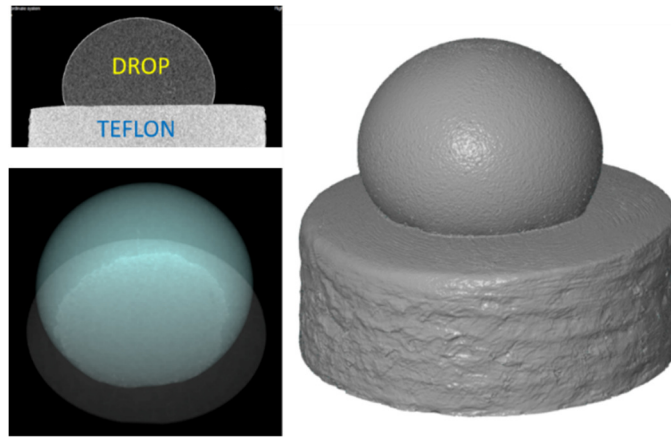


Figure 2-10 Top-left – reconstructed volume section showing attenuation coefficient difference between drop and Teflon. Bottom-left – coloured render with transparency of the reconstructed drop-surface volume. Right – solid 3D render of the reconstructed volume.

Due to the difference of the attenuation coefficient of Teflon and water, separation of drop from surface is possible. Once the digitalized volume has been produced it is converted to an exportable STL surface and then the drop-surface triple line and contact angle are analysed as follows, with reference Figure 2-11:

- the drop apex (x, y) coordinates is determined by fitting circumferences to the drop contour of the 10 top most xy STL sections, distant one from the other as the tomographic resolution, and then the mean value of the centre is used. The z coordinate of the apex is the z value of the drop. stl which intersects the line passing through the x, y centre point calculated and parallel to the z axis. (n.b. the surface plane where the drop rests must be previously aligned with the xy plane).
- the stl surface is radially sectioned with planes passing through the drop apex and perpendicular to the xy plane. The following image presents this operation showing only 36 of the 120 planes utilized to ease visualization. The top and bottom view of the drop stl reveal that the drop rests on the surface producing a far from theoretically circular trajectory for the triple line.
- The sections contours are then divided in half at the drop apex and used as described in [79] to obtain a Laplace-Young fitting for each half profile.
- Then the deviation of the fitted profiles from the original ones can be calculated to assess the goodness of the reconstructed profiles versus an accepted model.

The goodness of the reconstructed volume comparing the drop-surface contact points from the original sections with the Laplace-Young fitted ones shown in Figure 2-12. The same comparison can be done calculating the contact angle for every profile of each dataset.

Figure 2-13 shows the result of this calculations which is good for both along most of the triple line trajectory. Contact angle measurements produced over the full set of experimental microCT results gave a final mean value of 127.9° with a standard deviation of 4.9° which has been compared to contact angle measurements produced with an optical acquisition system [82] utilizing the same surface and type of water, resulting in a mean contact angle of 129.3° with a standard deviation of 4.5° . The presented experiment has validated the usage of microCT as a novel tool for contact angle measurement, providing a full 3D

knowledge and representation of the surface-drop couple that can be processed with software tools to provide meaningful data for research purposes.



Figure 2-11 top left – stl drop surface visualized in green with radial sections shown in black. top right – visualization of only the radial sections contours (36 of the 120 used). Bottom left and right – top and bottom view of the drop-surface stl clearly showing the non-circular footprint of the drop.

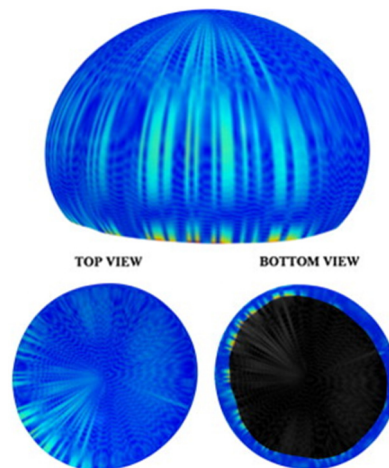


Figure 2-12 Reprinted with permissions from [79]. 3D rendering of the fitted profiles coloured to represent experimental-fitted profiles deviation. Colour from blue (0%) to red (3.85%) is proportional to the dimensionless error $\Delta R/R_{max}$

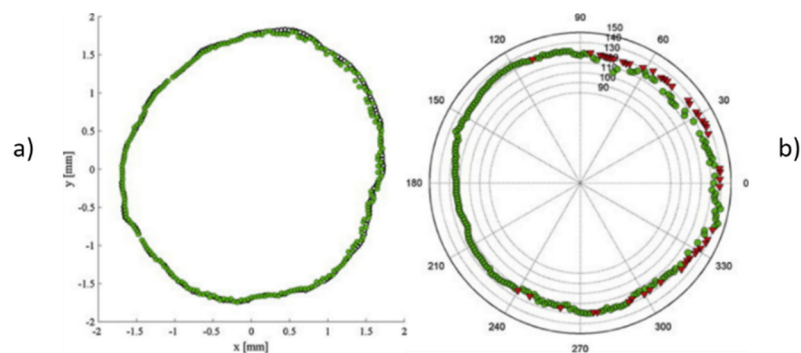


Figure 2-13 a) – b) Reprinted with permissions from [79]. Graphical visualizations of the triple line trajectory and contact angle measurement comparison between experimental and fitted datasets. a) xy plane localized comparison of drop-surface points: green circles represent experimental points while black circles represent fitted data, the maximum distance between analogous points is $72 \mu\text{m}$ b) contact angle measurements: green dots represent positions where experimental and fitted contact angle measurements are in good agreement, 192 points of the original 240, while red triangles represent point with bad agreement.

2.4 DROP ON RECORD

After validating the use of the X-ray microtomographic technique for contact angle measurements and triple line 2D localization for the geometrically simple case of a drop deposited on a flat surface, the next step was to increase the complexity of the geometry to understand what kind of information could be gathered from the tomographic reconstruction in case of a more complex, geometrically defined, surface geometry.

The experimental work presented in this sub-chapter has the aim of validating the use of microCT to extract from the tomographic reconstruction the triple line trajectory and the contact angle information in case of a 3D surface morphology. Moreover, thanks to the volumetric reconstruction, the discrimination between the Wenzel and Cassie-Baxter wetting regimes is made easier and the calculation of the real wetted area ratio is possible utilizing non-idealized surfaces. Instead of purposely producing a micro-patterned surface, a piece of an old broken vinyl record was used after cutting it to the desired shape, taking the inspiration from the optical visualization experiences reported in [83].

The vinyl record surface can be described as characterized by parallel trapezoidal grooves that are anisotropically wetted if a drop is gently deposited on top of them; a picture of the sample utilized clearly shows the high anisotropic equilibrium state of the distilled glycerol drop when resting on the surface: elongation in the direction of the grooves is clearly visible, while pinning to the surface edges limits the drop expansion in the direction perpendicular to them, see Figure 2-14. The liquid selected for the presented experiments is glycerol since the previous experiences with distilled water showed that the tendency to evaporate of this latter liquid create problems during tomographic reconstruction, if not diminished as done with specific hardware, which was not desired for the present experiments to have a simpler configuration than before. The use of glycerol effectively simplifies the evaporation problem since it was calculated that, for the experimental ambient conditions and duration of the designed experiments, for a 1 mm drop dimension, the evaporation accounts for less than 0,1 $\mu\text{m}/\text{h}$, well below the utilized scanning resolution. Table 2-1 reports the characteristics of the glycerol:

Producer	Carlo Erba Reagents S.r.l.
Name	Glycerol ACS-For-Analysis
Code no.	453752
Chemical formula	C ₃ H ₈ O ₃
Minimum assay	99.5%
Density @25 °C	1,250 kg/m ³

Table 2-1 Specification of the utilized glycerol.

To visualize how the drop adapts to the patterned surface depending on its 2D dimensions and volume, four tomographies of drops with different volumes, gently deposited on the mentioned patterned surface, were produced, so to be able to compare results from different cases. To guarantee that the drop was resting in its steady state condition of equilibrium before starting the tomographic acquisition, drops were left resting

on the surface for 12 hours before acquisition start. Figure 2-15 shows how the small drops of glycerol were deposited on the patterned surface: the glycerol was taken from the cap of its bottle, which was filled with the same liquid, by means of a small needle and then transferred to the patterned surface. This method was utilized since any attempt to create small drops utilizing the syringe previously used with distilled water resulted in the production of drops which were too big for the intent of the planned tests. The first test tomographies denoted the necessity to add a filtration, selected to be 0.5 mm of aluminium, to the incoming X-ray radiation since the vinyl record was found to contain unknown impurities characterized by higher X-ray attenuation than simple vinyl. These impurities were later identified as regular record filler materials, comprising slate, various clays, metal oxides and silicate, commonly added to the raw vinyl compound during production to make the records less brittle. The added filter diminished also the beam hardening effect caused by the sample itself due to non-homogeneous thickness that X-rays must pass which changes with rotational position. Figure 2-16 presents two 2D section views (slices): the left one is form one of the first test reconstructions produced without beam filtration, in this case beam hardening is evident and highlighted by yellow arrows, while the right one presents the effect of the applied radiation filtration, the beam hardening is clearly diminished.

The following is the X-ray tomography machine setup utilized for all the drop tomographies.

- Number of projections: 1,200
- Source voltage: 50 kV
- Source current: 100 μ A
- Exposure time: 1,200 ms
- Source to object distance: 19.52 and 45 mm
- Source to detector distance: 365 mm
- Rotational acceleration: 0.1 $^{\circ}$ /s
- Focus mode: SFC1
- Additional filtration: 0.5 mm Al

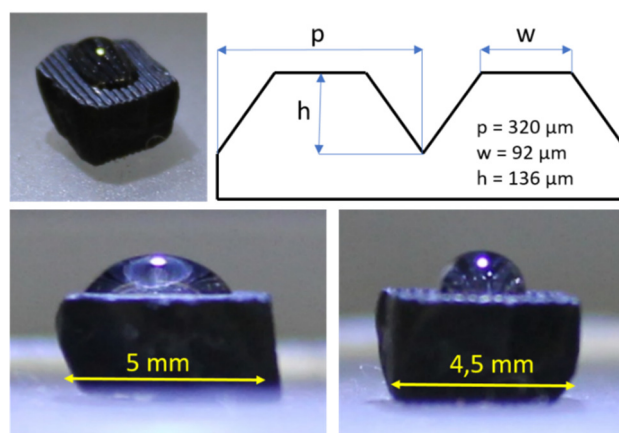


Figure 2-14 top-left – sample drop deposited on the record surface. Top-right schematic section of the record profile to highlight characteristic geometrical measures ($p = 320 \mu\text{m}$; $h = 92 \mu\text{m}$; $w = 136 \mu\text{m}$). bottom-left, bottom-right: side view of a sample surface-drop couple.

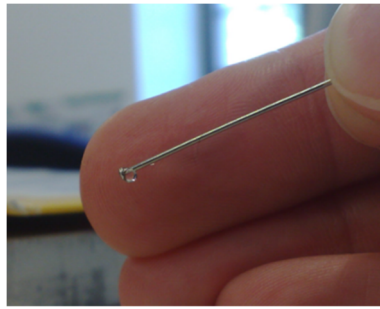


Figure 2-15 Picture of a small drop of Glycerol on top of the needle utilized to place it on the patterned surface.

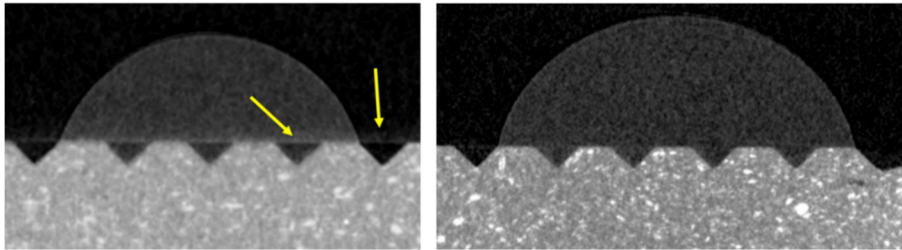


Figure 2-16 Left – section of drop reconstructed volume before application of radiation filtering: the two yellow arrows highlight the position of the artefact caused by the beam hardening showing in the section as a wide horizontal line of pixels with non-correct grey level values. The image has been smoothed to try to minimize via software the detected defect in the first instance. Right – section of a comparable drop reconstructed volume produced after the introduction of the aluminium filter, it can be noted that the beam hardening is diminished.

The two “Source to object distance” indicated, 4 and 9.2 mm, were utilized to obtain two different reconstruction resolutions as indicated, along with the drops characteristics, in the following table.

Drop number [-]	Voxel dimension [μm]	Volume [mm^3]	Drop radius [μm]	Number of grooves [-]
1	4.0	0.757 ($\pm 64 \mu\text{m}^3$)	566 \pm 4.0	4
2	4.0	3.638 ($\pm 64 \mu\text{m}^3$)	954 \pm 4.0	6
3	4.0	3.873 ($\pm 64 \mu\text{m}^3$)	974 \pm 4.0	7
4	9.2	26.675 ($\pm 783.78 \mu\text{m}^3$)	1,854 \pm 9.2	12

Table 2-2 Table summarizing the characteristics of the drops

The smaller distance corresponds to the smaller voxel dimension, while the longer one to the biggest voxel dimension; this was necessary to use the maximum magnification for the scanned drops, therefore drop no. 4 requested to be scanned with lower resolution due to its bigger dimension.

As reference the clear vinyl surface was initially scanned, producing a high-resolution image of it able to

show the groove sides irregularities that produce the desired music when encountered by the turntable needle. Figure 2-17 shows the rendering of the clear vinyl surface. The reconstructed volumes are then analysed to extract information which can be utilized to characterize the wetting behaviour:

- 3D Triple line trajectory.
- Contact angle hysteresis.
- Type of wetting and real to apparent wetting area ratio determination.

Figure 2-18 displays two scaled side views and a three-quarter view of the 3D renderings of the reconstructed drop-surface couple volumes to visually show the difference in dimensions of two extreme drops, case 1-smallest drop and case 4-biggest drop, justifying the necessity to decrease the tomography resolution for the biggest one to maintain it in the field of view of the X-ray detector.

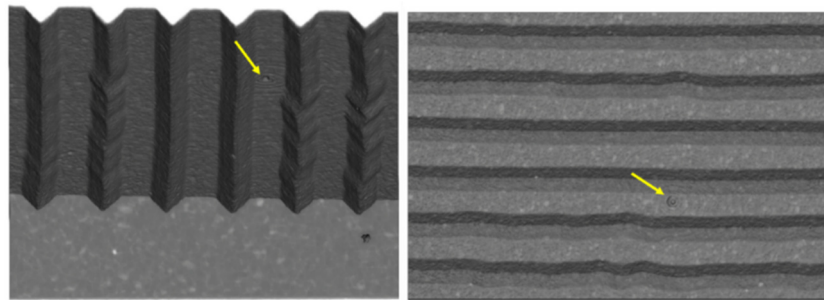


Figure 2-17 left – angled side view of the reconstructed vinyl record surface showing the grooves sides irregularities that produce music when hit by a turntable needle. The yellow arrow highlights the tomography rotation axis artefact. Right – top view of the same record surface.

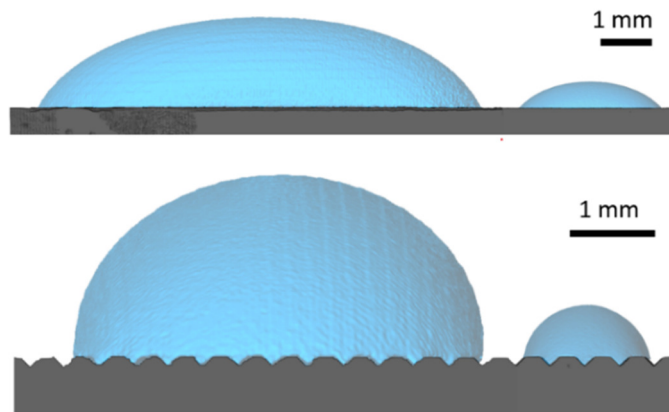


Figure 2-18 Two side views (top-middle) and a three-quarter view (bottom) of the biggest drop no.5 artificially positioned near to the smallest one no.2 to highlight the difference of drops volume.

- **Triple line trajectory extraction**

The directional grooves of the selected patterned surface determine different drop pinning behaviour which is dependent on the considered position, the two main directions being the one parallel to the grooves and

the one perpendicular to them. Optical systems can furnish only 2D views of the drop, usually two side views and a top view, from which the triple line must be inferred.

With the use of 3D tomography instead, the triple line trajectory information can be extracted from the reconstructed volumes, resulting in the knowledge of its path even in the case of patterned surfaces. As it is displayed in Figure 2-19, the reconstructed drop-surface volume can be decomposed to extract the triple line information as the collection of points where the drop surface touches the surface volume.

The complete knowledge of the triple line trajectory gives the possibility to study how the drop behaves inside the surface grooves which is an information not deducible from optical 2D images.

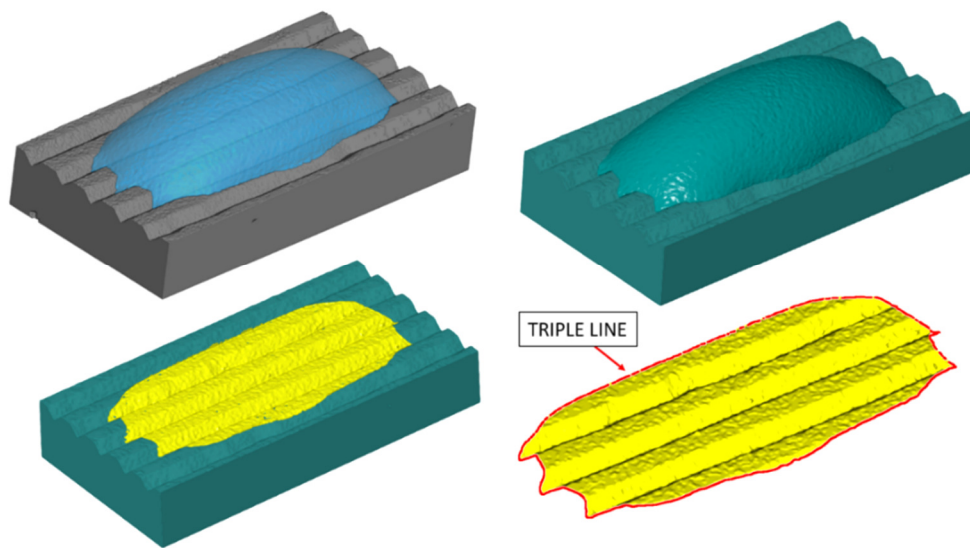


Figure 2-19 Top left – rendering of drop 1 tomographic reconstruction. Top right – conversion of reconstructed drop-surface volume in STL format after separate identification of drop and surface volume. Bottom left – in yellow recognized footprint of the drop. Bottom right – visualization of the only drop footprint with detected triple line highlighted in red

- Contact angle hysteresis

The pinning of the drop to the surface grooves determines strong contact angle hysteresis. It is expected that no pinning occurs in the direction of the grooves where the liquid is free from obstacles that can interfere with its spreading, while on the other hand a strong pinning is expected to be present in the direction perpendicular to the grooves.

As we have already seen in the rendering of the reconstructed volume, in the direction of the grooves the drop tends to spread more, creating fingers inside the grooves, while in the other direction it strongly deforms anisotropically to adapt to the encountered surface edges.

Figure 2-20 and Figure 2-21 illustrate this behaviour presenting sections of the drop in the two most interesting directions.

Figure 2-20 presents in detail four sections of the drop surface produced perpendicularly to the grooves direction: as it can be noted from the over position of the four drop profiles analysed, the behaviour of the drop is highly non-symmetrical since proceeding from the border to the middle of the drop, the drop pins to the right groove edge while oversteps the left edge determining a high contact angle value difference which raises up to 30.39° for the worst case presented.

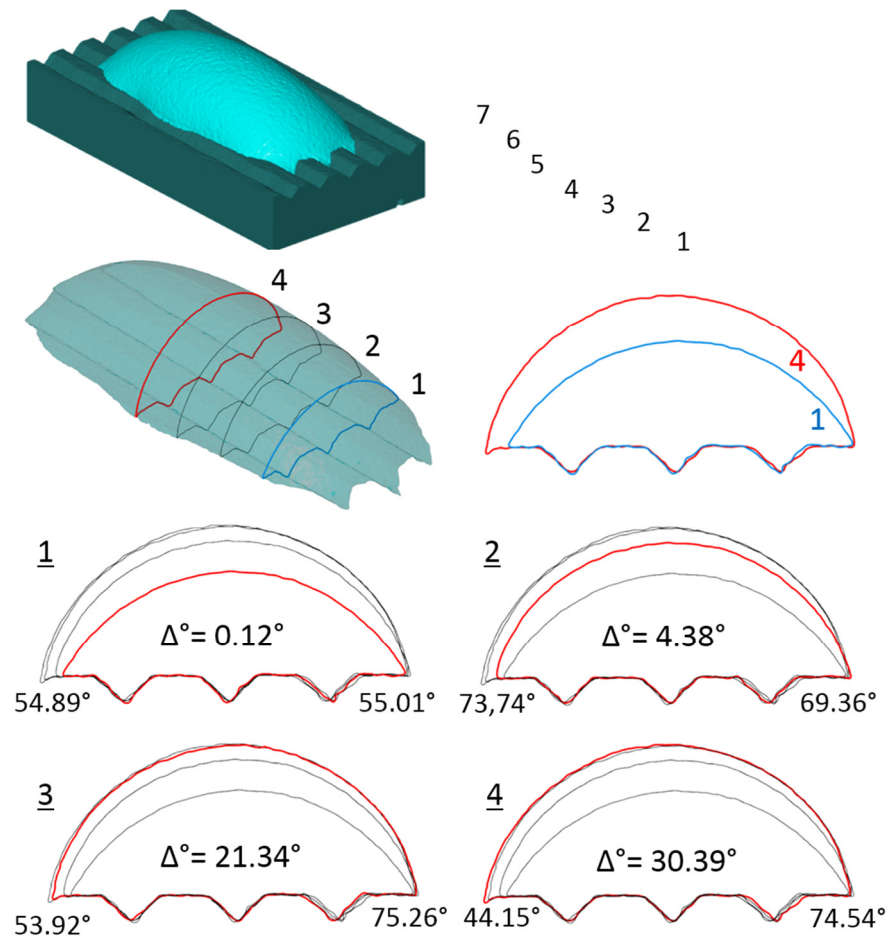


Figure 2-20 1st row-left – drop and surface stl surfaces ¾ view. 1st row, right - only drop stl surface displayed in red with numbered sections (black lines) produced by planes perpendicular to the grooves. 2nd row-left: semi-transparent drop visualization to reveal contours of drop surface sections 1 to 4. 2nd row right – orthogonal view of section 1 (blue) and 4 (red) to reveal the pinning behaviour change: section 1 is characterized by strong left-right side symmetry, while section 4, corresponding to the central section of the drop, is highly non-symmetric since the left side of the drop oversteps the edge of the groove while the right side doesn't. 3rd and 4th row: orthogonal display of section 1 to 4 with indication of left-right drop contact angle with difference highlighting the non-symmetric behaviour of the drop-surface pinning

Figure 2-21 presents sections of the same drop parallel to the grooves direction: in this case, it can be noted that the difference in contact angle value between the right and left side is negligible if compared to the previous case, being the maximum contact angle variation detected equal to 6.14°.

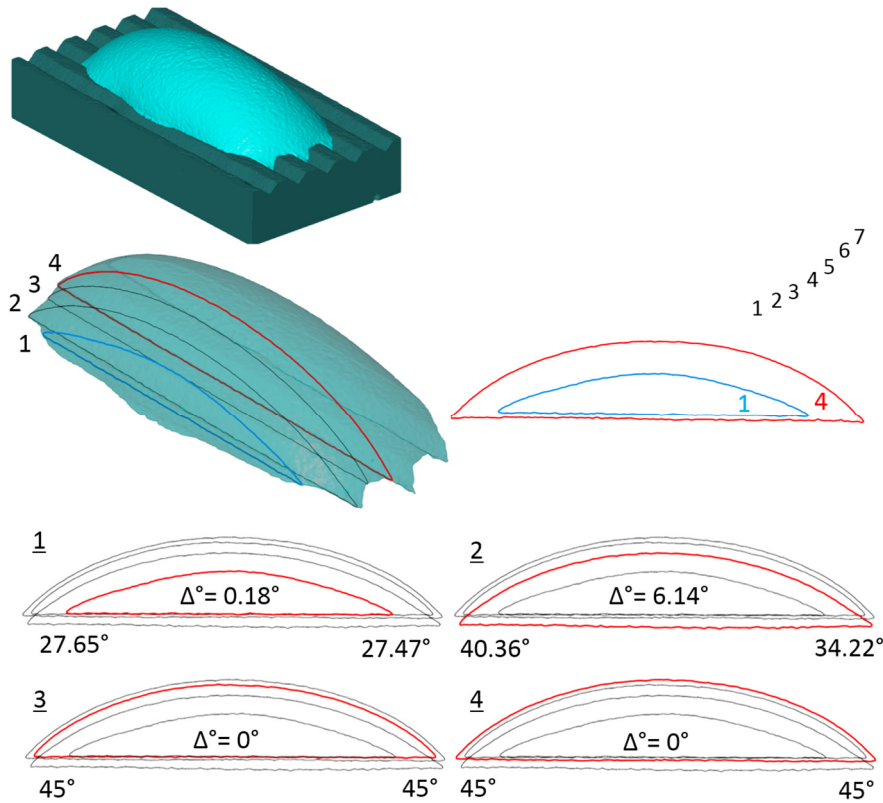


Figure 2-21 1st row left: drop and surface stl surfaces ¾ view. 1st row right: only drop stl surface displayed in red with numbered sections (black lines) produced by planes parallel to the grooves. 2nd row-left: semi-transparent drop visualization to reveal contours of drop surface sections 1 to 4. 2nd row right – orthogonal view of section 1 (blue) and 4 (red) to reveal the symmetry in the pinning behaviour. 3rd and 4th row: orthogonal display of section 1 to 4 with indication of left-right drop contact angle with difference highlighting the symmetric behaviour of the drop-surface pinning.

- **Wetted area ratio determination**

When the surface is rough, macroscopically mono-component and hydrophilic to the drop liquid, as the case presented, the Wenzel equation can be utilized to describe the apparent contact angle modification due to the surface roughness. The ratio between the two-dimensional area of the drop volume projected on a flat surface and the three-dimensional area of the rough surface corresponding to the two-dimensional area projected are utilized in the Wenzel equation to create the following relation:

$$\cos\theta_A = r * \cos\theta_Y$$

Equation 2-3

Where θ_A is the apparent contact angle, θ_Y is the contact angle determined with the Young equation for the drop-surface couple considered and r is the mentioned ratio between the 2D and 3D drop footprint area. Usually the mentioned 2D and 3D areas are calculated utilizing the top view of the drop, so to delineate its contour and calculate its inner area, and considering the nominal geometry of the rough surface, to calculate the nominal drop-surface area of contact.

Lack of accuracy however affects the calculation of these two areas: the top view of the drop is not able to represent correctly the drop base contour, especially for high contact angles, and the nominal surface geometry doesn't consider surface geometry deviations due to production tolerances which are always present. X-ray microCT instead produces reconstructed volumes that can be used to calculate real wetted area dimensions, since the area of contact between the two recognized volumes can be clearly identified and analysed to determine how the drop is resting on the surface Cassie-Baxter Wenzel state.

Figure 2-22 presents the recognized drop base surface in 3D (yellow) along with its projection on a 2D plane, the area of these two surfaces can be easily calculated by integration. However, 3D drop footprint extracted from tomographic reconstruction is nevertheless affected by artificial roughness due to the voxel based representation of the volume.

The first attempt to reduce this artificial roughness, was done by simply applying in sequence a 3D despeckle filter, a kind of filter that replaces aberrant values by the mean value of their neighbours, and a Gaussian smoothing filter, both with a kernel of 3x3x3 pixels. This however, while removing the surface steps created by the voxelization, resulted also in an undesired smoothing of the footprint edges.

Therefore, an alternative method was selected: an algorithm previously developed to solve the measurement problem of free shapes, reported by [84], was used to calculate the real drop footprint area starting from the measurement of the footprint profile on a slice basis. The 3D drop footprint, still in its voxel representation, was sectioned by planes perpendicular to the grooves, distant one from the other as the reconstruction resolution, obtaining a multitude of single profiles represented by lines. Then the length of each profile was calculated with the mentioned algorithm to obtain a real profile length L_{real} as follows:

$$L_{real} = 0.980 * N_{even} + 1.406 * N_{odd} + 0.091 * N_{corner}$$

Equation 2-4

Where, considering starting from one of the profile's ends and following it to reach the other end moving by one pixel each time, N_{even} is the number of vertical or horizontal movements of the profile, N_{odd} is the number of diagonal movements and N_{corner} is the number of corners in the profile, that indicate how many times the profile changes from horizontal, to vertical, to diagonal. The area of the two-dimensional projection instead was calculated without applying any modification.

Figure 2-23 displays in two rows the top view of the 3D representation of the drop footprints and their 2D projections for all the drops considered.

The Wenzel ratio was then calculated by integrating the n L_{real} produced for each profile and then dividing it by the area A_{2D} calculated utilizing the 2D drop footprint projection as follows:

$$R_W = \sum_n L_{real} / A_{2D}$$

Equation 2-5

The Wenzel ratio calculated utilizing the experimental data were then compared to the theoretical values calculated utilizing the nominal surface dimensions obtaining good agreement as presented in Figure 2-24

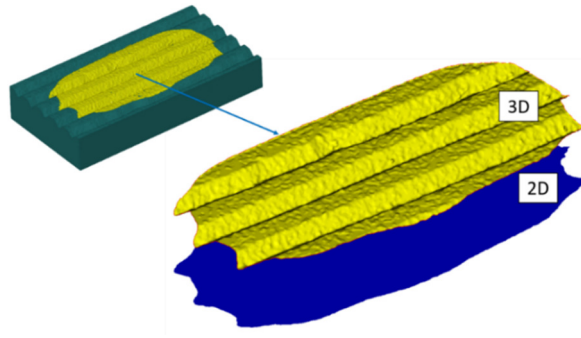


Figure 2-22 Visualization of 3D drop base area extraction (yellow) and its projection on surface parallel plane to calculate the 2D footprint of the drop.

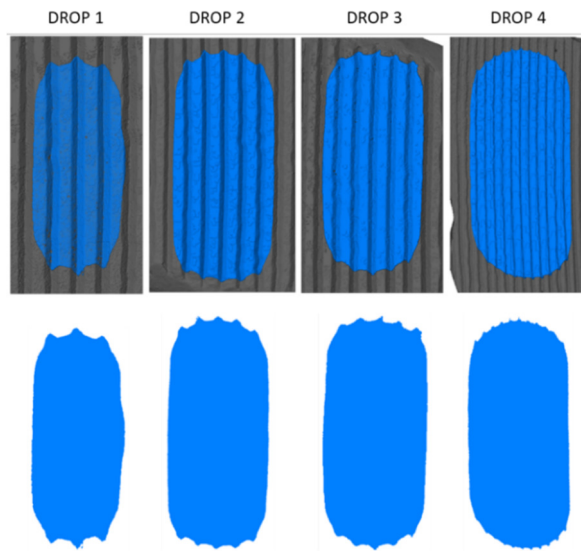


Figure 2-23 top row: 3D drops footprints on the record surface. Bottom row: 2D projection of the only drops footprints.

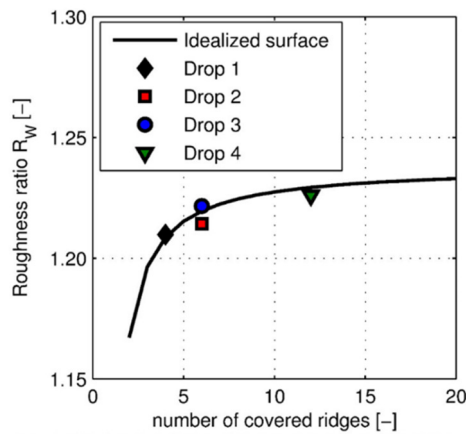


Figure 2-24 black line presents nominal surface Wenzel roughness ratio calculated utilizing the nominal geometry of the record surface, while the single points present the experimental results for the 4 drops of interest. It can be noted that the latter are in good agreement with the theoretical corresponding value. However, the experimental points referring to drop n.2 and n.3, which have very similar volume, are quite distant one from the other, this can be explained with the different way of covering the surface edges of the two drops, which is not represented by the single nominal value. Image from [85]

2.5 DROP ON GDL (GAS DIFFUSION LAYER)

Applicability of the X-ray microtomographic technique to the analysis of wetting phenomena for flat and regularly patterned surfaces has been illustrated in the previous sub-chapters. This third sub-chapter tries to extend the applicability of the proposed technique to the case of drops resting on completely free form surfaces. In this case, the drop interaction with the surface is very complex and conventional optical techniques can't be easily applied to assess the drop-surface interaction as for the two cases previously shown, but furthermore, this kind of surfaces also can't be accurately modelled due to the non-conformity of the surface geometry to a specific known pattern, if not macroscopically. However, this kind of complex surfaces represents the most generic case, of wide interest for many engineering applications such as the case of electrochemical power generation systems, known as proton exchange membrane fuel cells (PEMFCs), that will be used in the following as test case. A key component of PEMFCs is the gas diffusion layer (GDL), a membrane that has the role of managing water inside the cell [86] thanks mainly to the selective hydrophobicity of its surface and its high porosity. Therefore, a key selection parameter for the discrimination of the performance of new GDL membranes is the assessment of their surface hydrophobicity, such as wettability analysis and contact angle measurements. GDLs are characterized by far from regular surface geometries since they are formed by crossed carbon fibres packed in strands and arranged as a cloth. This fibres layout determines a highly irregular surface topology and a multi-scale surface roughness, the big topology being determined by the strands and the small one by the single fibres themselves. Moreover, the hydrophobicity of GDLs is usually increased up to the limit of super hydrophobicity by sputtering them with chemicals, the most common one being Polytetrafluoroethylene (PTFE). The GDL utilized for the present experiments has been treated with Perfluoroalkoxy alkane (PFA). Figure 2-25 presents two pictures of the GDL surface with and without a drop of water deposited on it, to visually show the complexity of the surface geometry.

In the leftmost picture the macroscopic surface topology of the crossed carbon fibre strands is visible, creating a wavy surface with a pitch of about 0.4 mm which can be considered as a first level roughness. Furthermore, knowing that the carbon fibres are arranged in strands inside the tissue, a second level roughness can be considered, determined by the profile of the single strand of fibres packed together. A third level of roughness can be ascribed to single carbon fibres exiting randomly from strands as visible in the rightmost picture. As previously done for the drop on record case, the first tomographies were produced to correctly set up the acquisition parameters of the X-ray tomography machine on the GDL -distilled water couple, the GDL cloth utilized in these experiments is SCCG 5N (99.999% Carbon Fabric) purchased from SAATI S.P.A. Italy.

The following is the X-ray machine set up utilized to produce the experimental tomographies utilized in the following.

- Number of projections: 1,200
- Source voltage: 50 kV
- Source current: 50 μ A
- Exposure time: 1,200 ms
- Source to object distance (SOD): 25

- Source to detector distance (SDD): 365 mm
- Rotational acceleration: 0.1 °/s
- Focus mode: SFC1

The SOD and SDD distances were chosen according to the sample size to obtain the maximum sample magnification which in this case resulted in a final tomographic resolution for the reconstructed volume of 5.12 μm . The resolution obtained is not enough to clearly capture the detailed geometry of each single carbon fibre, due to their small diameter, expected to be between 5 and 10 μm as reported by carbon cloth specifications, even though increased by the PFA addition. However, the macroscopic warp and weft topology of the GDL surface, mainly regulating the interaction with the drop, will be captured with enough detail since each strand forming the GDL tissue is composed by several single carbon fibres having an overall average diameter of 400 μm .

Figure 2-26 presents a rendering of the tomographic reconstruction of the only GDL to show the quality of the reconstruction: small surface features like single carbon fibres emerging from strands are adequately represented, while fibres inside strands are too close one to the other to be singularly distinguished, therefore as expected they are merged in a single element during reconstruction. After the reconstruction of the first tomographies, it became evident that the separation between the carbon fibre and the water volumes, based only on their different X-ray attenuation, was not possible due to the similarity of the grayscale value calculated for many points of both materials that were matching, leading to the creation of merged drop-surface volumes and noise in the contact area. The result of a direct thresholding of the reconstructed tomography is visible in Figure 2-27 where it is evident that an extended part of the GDL volume is recognized as drop volume due to same attenuation values calculated for both the drop and part of the GDL tissue.

Therefore, an alternative method to separate the two volumes was conceived and applied. For each experimental condition analysed, two separate tomographies were produced: the first one to the only GDL surface and the second one to the GDL surface after depositing a drop on it. The two tomographies were made one right after the other with the same machine set-up, apart from the number of radiographies produced that has been doubled for the tomographies of the only GDL.

This last decision was taken to improve the signal to noise ratio of the reconstruction, leveraging the possibility to extend the scanning time of the tomographies of the only surface since they didn't have to respect the time constraint dictated by drop evaporation. After reconstruction and thresholding of both tomographies, the only GDL volume was subtracted from the GDL with drop volume to obtain the only drop volume. Figure 2-28 visually explains this operation showing the renderings of the two starting tomographies and of the final product of the subtraction.

The drop volume produced after the subtraction is much more representative of the only drop volume than the previous one, having only small isolated clusters of voxels recognized as drop while belonging to the GDL; these blocks can be completely cancelled by a 3D 3 x 3 x 3 matrix voxel erosion followed by a dilation of the same extent. Before introducing this subtraction technique, tests were done to validate it against the possibility of the drop weight and interaction to modify the position of the GDL surface, especially of single threads, resulting in the impossibility to produce the volumetric subtraction proposed.

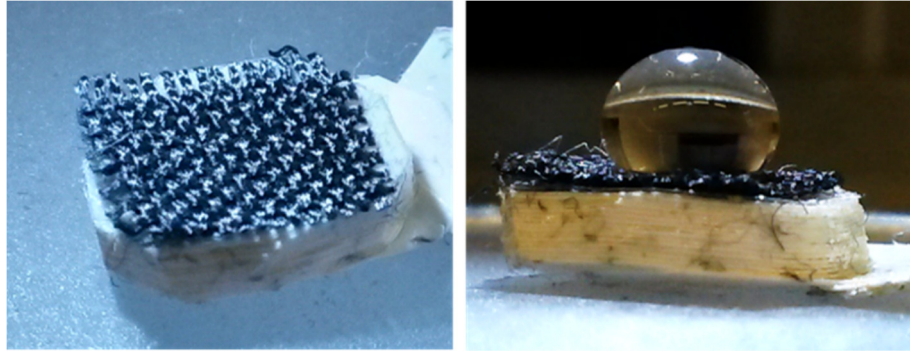


Figure 2-25 left – 6 x 7 mm size GDL carbon cloth utilized for the tomographic reconstruction presented; single carbon fibres can have a diameter range between 5 and 10 μm . right – same piece of carbon cloth with a drop of distilled water deposited.



Figure 2-26 Top – 3/4 view of the GDL reconstructed volume, yellow section at sides represents recognized fibre volume: as it can be seen, inside strands, single carbon fibres are merged in one bigger volume. Bottom – higher zoom top view of a small portion of the GDL to further highlight the visibility of some of the carbon fibres protruding from the strands.

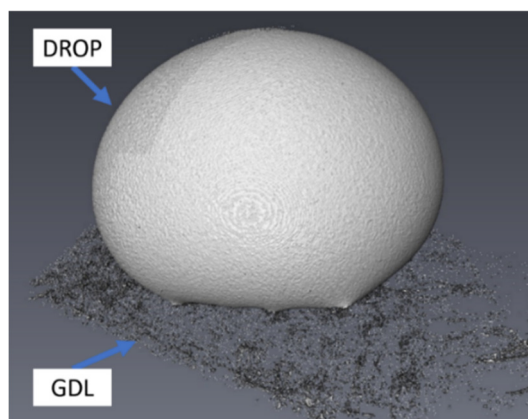


Figure 2-27 Grayscale rendering of thresholding window utilized to determine the only drop volume. It is clearly visible that under the drop, the GDL volume is partially visualized meaning that it will be recognized as drop volume after thresholding operation.

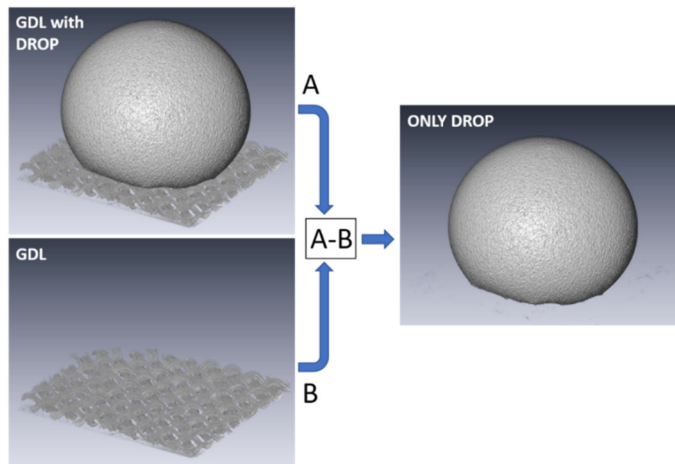


Figure 2-28 Left - rendering of the tomographic results of GDL with DROP (top) and only GDL (bottom) Right – result of the subtraction showing drop volume remaining.

Fortunately, it was found that surface changes due to the drop deposition occurred were not detectable with tomographic resolution utilized: even single carbon fibre threads were holding their position after drop deposition thanks to their high flexural modulus (7.5 MPa) and tensile strength (19.25 N/cm). Once the drop volume has been isolated, see Figure 2-29, it is possible to visualize the drop footprint determined by the interaction with the GDL surface. The measurements produced for the presented drop are the following:

- Drop volume: 40.495 mm³
- Drop surface: 60.057 mm³
- Wetting volume: 0.951 mm³
- Wetting area: 11.870 mm³

Figure 2-30 presents graphically the render of the drop (top row left), its wetting area visualized with an orange middle cross section to enhance the visibility of the drop profile (top row right) and three top view of the drop render (bottom row) showing solid blue cross planes of the drop as it enters the GDL surface. Measurement of the drop volume penetrating the GDL surface can be used to assess the characteristics of the GDL coating used constituting a valid tool for coating selection and discrimination.

Digital three-dimensional representation of the GDL with drop produced using the tomographic technique grants the possibility to study drop wetting since radial sections of the reconstructed surface can be easily produced and analysed to assess the drop contact angle value even complex cases as the one presented.

For the test sample proposed, drop of distilled water deposited on a GDL with PFA coating, contact angle measurement by X-ray microCT radial profiles gives a mean value of 154.88° with standard deviation of 2.22° while the same surface-drop setup measured with optical techniques gives as a result a mean contact angle of 151° with a standard deviation of 0.6°. The difference between the two values and relative standard deviation can be ascribed to the better possibility granted by microCT profiles to represent the true contact angle, which is varying due to surface pattern, rather than the optical technique which is able to detect only the apparent contact angle since direct triple line visibility is missing. Figure 2-31 presents graphically the possibility to slice the reconstructed drop profile radially after having recognized the drop apex and using

the surface perpendicular direction.

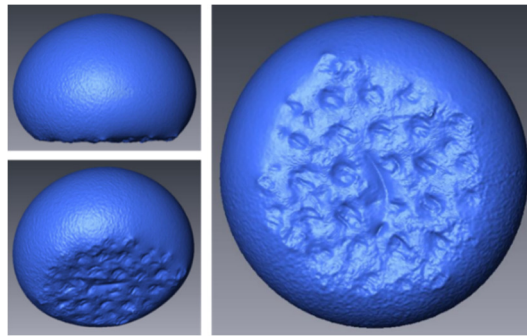


Figure 2-29 Left (top) – side view of the drop volume after thresholding and GDL subtraction. Left (bottom) tilted view of the same drop volume. Right – bottom view of the drop volume showing regularly spaced grooves, determined by the warp and weft surface of the GDL cloth

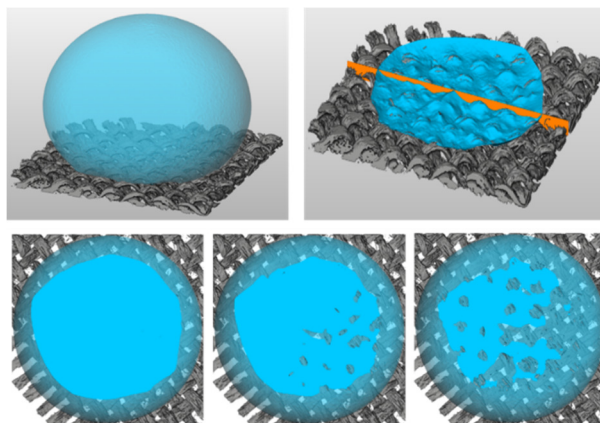


Figure 2-30 Top row left: rendering of the reconstructed drop volume. Top row right: visualization of the portion of the drop surface which is inside the GDL. Bottom row, from right to left: visualization of the drop sections as the section plane considered enters the GDL cloth. The remaining drop volume calculated after each section drop volume cut is: 0.951 mm^3 , 0.294 mm^3 and 0.026 mm^3 .

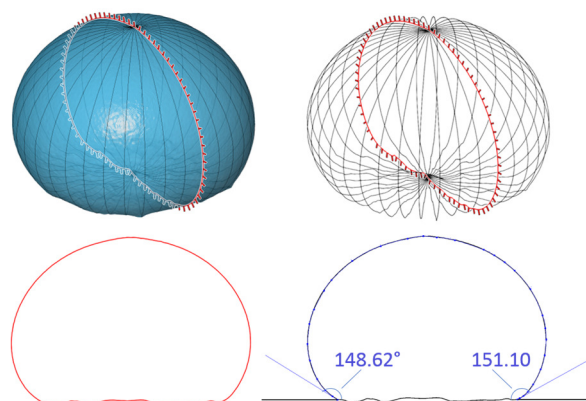


Figure 2-31 Top-left: in blue 3D rendering of the drop surface with radial sections overlapped in black and red, 18 items in total, one section each 10° . Top-right – visualization of the only drop profiles to reveal the complexity of drop surface footprint. Bottom-left: orthogonal view of red single drop profile present in the previous images. Bottom-right: B-spline drop contour profiling and contact angle measurement of red drop profile presented in the previous images.

Then the measurements of the contact angle have been produced using axisymmetric drop shape analysis (ADSA) for the optical technique case and using an active contour method implying a B-spline as described in [87] for the microCT profiles.

The digital representation of the sample gives the possibility to detect and analyse features that are usually not visible to optical approaches. In Figure 2-32 and Figure 2-33, two simultaneous GDL surface defects are visualized: in the centre of the GDL a carbon fibre wire exits the surface with a considerable angle while another one follows the tissue wave but is in an higher position than the other ones.

The effect of the first one on the drop interface is negligible since the wire is angled enough to enter the drop volume without interfering significantly with it. The second one instead produces a significant deformation of the drop surface since, as we have state previously, the wire is able to withstand the drop weight, therefore the drop adapts to it creating a non wetted area that is negative forr the performances of the GDL.

Even if very gently deposited on the surface, the drop will spread by a certain extent on the surface due to gravitational acceleration and then will reach an equilibrium condition reducing surface to volume ratio.

This drop movement can produce drop pinning to the surface, especially in surface points where the hydrophobic coating process was not successful or where the surface has defects as previously presented. Figure 2-34 presents three images with zoomed views where pinning occurs.

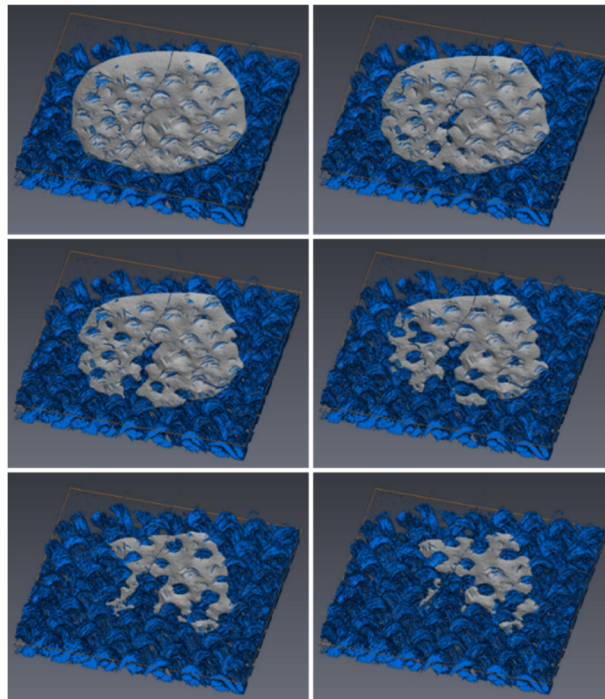


Figure 2-32 From top left to bottom right – tilted view of drop surface sectioned by 6 planes parallel to the GDL surface to show how the drop adapts to the detected surface defect. The sectioning planes are the same utilized in the previous figure.

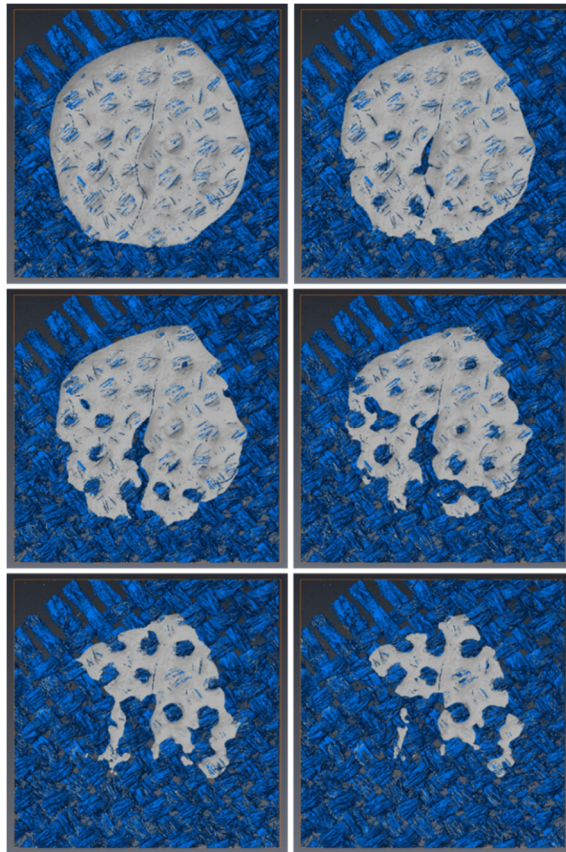


Figure 2-33 From top left to bottom right – top view of drop surface sectioned by 6 planes parallel to the GDL surface to show how the drop adapts to the detected surface defect.

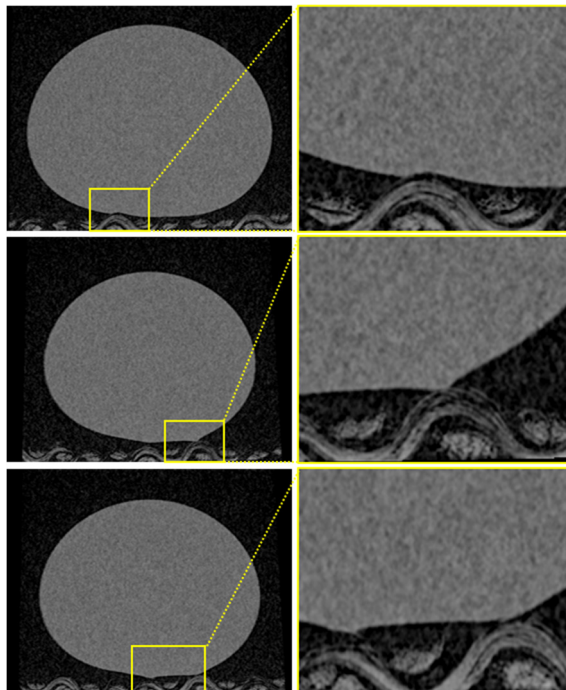


Figure 2-34 Visualization of tomographic reconstruction slices highlighting drop pinning in more than one position. The full slice is visible in the left while in the right the zoomed view of the area where the pinning occurs is zoomed to ease details detectability.

3 APPLICATIONS TO COMPLEX GEOMETRIES

(REAL INJECTORS + TEST RIG MODEL)

3.1 INJECTOR INTERNAL GEOMETRY RECONSTRUCTION

X-ray tomographic scans of car fuel injectors to retrieve their internal geometries is a very active research topic due to the large interest of car manufacturers to study the fuel injection process so to control engine performances, reduce pollutant emissions and avoid injection failures. The reconstructed internal geometries resulting from CT scans can be used for CFD calculations instead of nominal geometries, as traditionally done, reducing the simulation inaccuracy in representing the real injection process caused by discrepancies between the real nozzle geometric features and the nominal three-dimensional model utilized. The geometrical differences between the two models are due to the always present production tolerance and the hydrogrinding process [18], the last one being a post-production process which is commonly actuated on the nozzle to get the desired injection flow: the nozzle is flushed with an abrasive fluid until the desired flow rate is reached, causing mainly a geometrically semi-controlled rounding of the injection orifices entrances and a smaller uncontrolled change in the full internal geometry.

CT scans of injectors are also produced whenever the nominal drawing of the studied injector is not available, most of the times due to a specific will of the producer to maintain secret about this information. In the following results of microCT scans of real diesel injectors will be presented, first to analyze the influence of tomographic resolution on the possibility to describe geometrical features, then to distinguish very similar injectors based on quantitative measurements. The last results presented illustrate the possibility to use microCT to detect geometrical erosion of nozzles due to operational wear; this possibility was applied to study the wear of the PEEK nozzle model produced for density measurements also illustrated in this thesis.

In the first instance, injector nozzles to be scanned were disassembled from the injector body to be placed on the sample holder with the nozzle tip up so to use the same sample holder for every nozzle featuring the same base to top dimension, see Figure 3-1.

However, dismantling the nozzle from the body was not considered adequate since during this operation the injector parts could be damaged, moreover successive tomographies of the same injector after different operating hours wouldn't have been feasible since the relative position of the injector components (body-needle-nozzle) could be changed from this operation.

Therefore, a reverse mounting sample holder was designed and produced out of acrylic glass to avoid the dismantling procedure. Figure 3-2 presents the new sample holder drawing and the produced part during usage: the size of the sample holder inner hole diameter must be coupled with the smallest nozzle outside diameter since the nozzle is conical on its outside. Leveraging the presence of a cylindrical hole the nozzle can be placed inside the sample holder very firmly. Set-up configuration of the microCT scans was selected performing tests varying the X-ray source voltage, current, exposure time and radiation filtration. The aim was to get in the radiographic image of the nozzle grayscale values ranging from 3,000 to 14,500, enhancing the contrast inside the object volume.

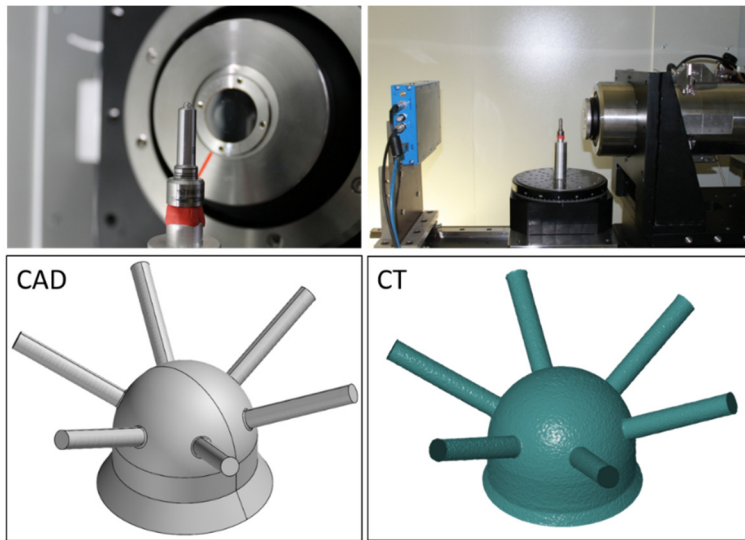


Figure 3-1 Top left: closeup view of injector nozzle placed inside the microCT machine ready to be scanned. The nozzle has been disassembled from the body and the needle has been removed to place the nozzle on top of the sample holder. Top right: complete view of injector nozzle inside the microCT machine. The nozzle distance from the X-ray source allows a magnification which produces a tomography with a 4 μm resolution.

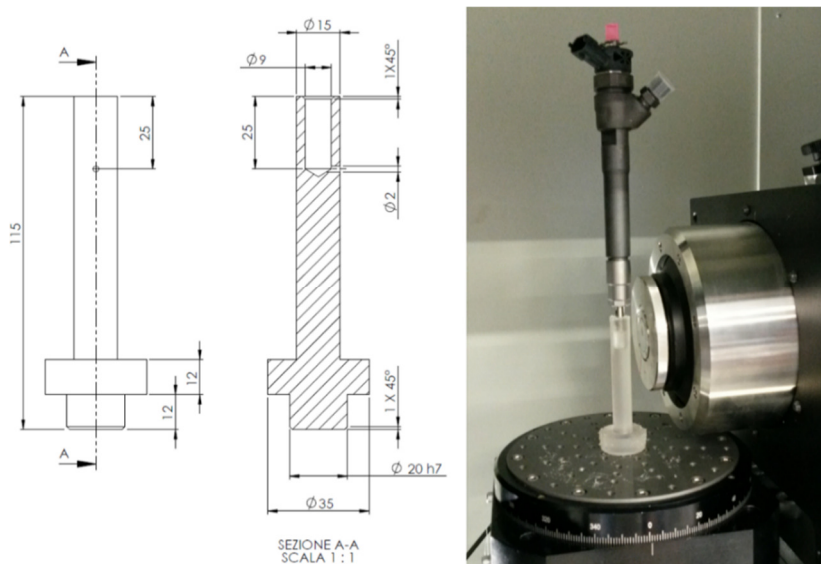


Figure 3-2 Left – CAD drawing of the top mounting sample holder. The only tolerance indicated is the h7 for the base diameter since this must tightly match the diameter of the hollow rotary stage central hole. The tolerance for the top hole where the nozzle sits is not indicated since the nozzle outside shape is conical.

Specifically, the contrast was enhanced preferring a low X-ray source voltage and a minimum radiation filtration, while increasing the image signal to noise ratio using a longer exposure time, up to the limit imposed by the necessity to avoid focal spot drift always present for long exposure times. In fact, tests denoted the tendency of the X-ray focal spot to drift during acquisition due to heating if higher X-ray source tension or current were used paired with scanning times exceeding 1-1,5 hours. In this case, the thermal drift was also worse than other cases due to the presence of the metal filter which had to be positioned very near, using a 2 mm thin spacer, to the X-ray point of emission preventing the X-ray window and target to

cool down in free air as designed by the equipment producer.

The following are the acquisition parameters selected:

- Number of projections: 2,400
- Source voltage: 90 kV
- Source current: 30 μ A
- Exposure time: 2,300 ms
- Source to object distance (SOD): 20 mm
- Source to detector distance (SDD): 365 mm

Figure 3-3 presents in its top row a sample grayscale radiography and its false colored version highlighting the grayscale values obtained for the full nozzle tip. As it can be seen, the most interesting area comprehending the injection holes and sac volume is compressed in a window of about 2,000 grayscale values.

Metallic components like nozzles harden the polychromatic radiation passing through them, requiring a modification of the grayscale values present in the radiographies, based on a calibration.

As explained in the first chapter of this thesis, a mapping of the real nozzle thicknesses versus radiation intensity perceived by the X-ray detector, passing through that thickness, has been utilized.

Figure 3-4 illustrates the effect of the application of the beam artifact reduction technique on the nozzle tomographic results. The correction of this artifact is crucial for the correct detection of the injection holes exits geometry, since it causes wrong reconstructed pixel values localized on the border of the object, as pictured by the two topmost images in the left column of the previous Figure 3-4.

Wrong pixel values result in a false reduction of the holes diameter near to their exit after the thresholding operation, applied to define what has been recognized as the objects volume. In the right column of the Figure 3-4 we can see the same nozzle sections shown in the left column but with beam hardening artifact reduction applied: here the brighter outer border of the nozzle has disappeared, and the injection holes area have a much more uniform grayscale value.

The two bottom images of the Figure 3-4 present the full nozzle volume histogram before and after the application of the beam hardening correction. Analyzing this image is key to grants us the possibility to understand that the correction has worked as supposed cancelling out histogram peaks numbered as 3 and 5 in the non-beam hardening corrected histogram, corresponding respectively to the bright outer ring area of the horizontal section and to the bright injection hole exit area of the vertical section, while it has only diminished the number of pixel contributing to peak no. 2 which represents the air pixels inside the nozzle sac and injection holes.

- Pixel dimension: 4,098 μ m
- Rotational acceleration: 10 °/s
- Focus mode: SFC0
- Filter: 0.4 mm of Brass

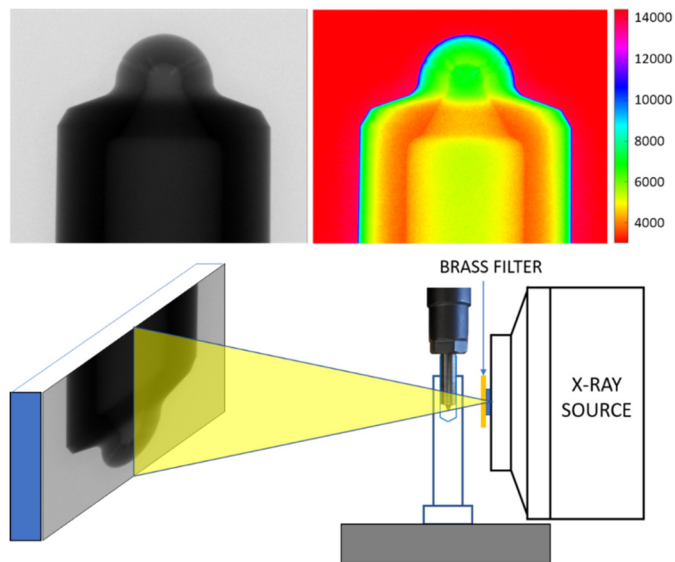


Figure 3-3 Top left – radiography of the nozzle produced with the reported settings. Top right – false coloured radiographic image showing in false colours the intensity of the radiation received by the X-ray detector. Bottom row – schematic view of the tomography set-up to identify the position of the metal filter utilized to filter the incoming radiation.

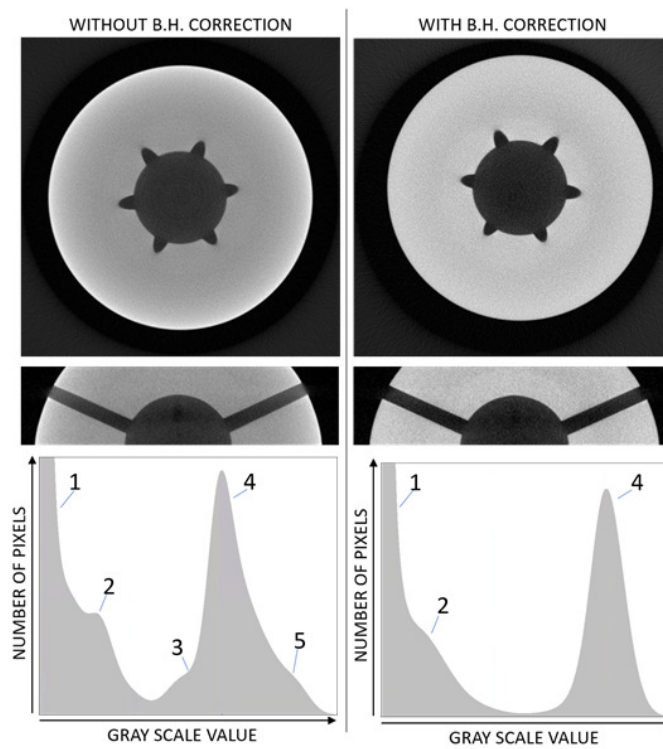


Figure 3-4 Left column, top and middle – nozzle reconstructed slices (horizontal and vertical) without beam hardening correction applied - Right columns, top and middle - same nozzle slices presented in the left part of the figure but with beam hardening correction applied. Bottom, left – histogram of the reconstructed volume without beam hardening correction with numbered peaks indicating the virtually 5 materials present in the reconstructed volume. Bottom, right – histogram of the reconstructed volume with beam hardening correction applied, showing two main peaks corresponding to air (peak no.2) and nozzle metal material (peak no.4). Peak no. 2 is still present highlighting that not all the beam hardening artefact has been cancelled out by the correction.

The presence of peak no 2 reveals that the beam hardening correction is not able to correct all the artifacts: the histogram of the nozzle tomography should nominally present only two peaks corresponding to the only two material present in the X-ray path which are air and metal. Figure 3-5 proves how the beam hardening correction modifies the reconstructed pixel values permitting a correct thresholding of the grayscale image. The yellow line reflects the recognized contour of the nozzle area: this contour is macroscopically wrong for the non-corrected slice while it follows the nozzle contour after the artifact correction. The selection of the thresholding value determines the reconstructed volume borders: for the reconstruction of nozzles within the scope of this thesis the minimum value between the two material peaks recognized as materials in the histogram has been selected, see Figure 3-6.

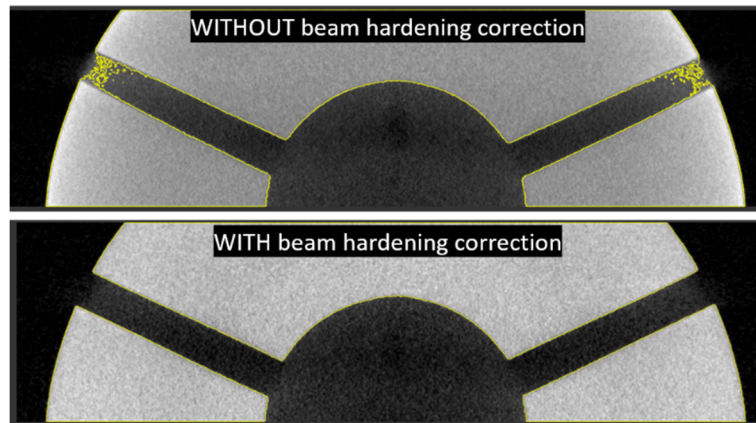


Figure 3-5 Top – thresholding of non-beam hardening corrected nozzle slice: yellow line represents the nozzle area recognized contour. The injection holes’ exit is not reconstructed correctly since the pixel value in this position have a higher grayscale value which assigns them to the nozzle material instead that to air as supposed. Bottom – same slice with beam hardening correction; the brighter pixel values of the outer border have been corrected permitting detection of the hole geometry.

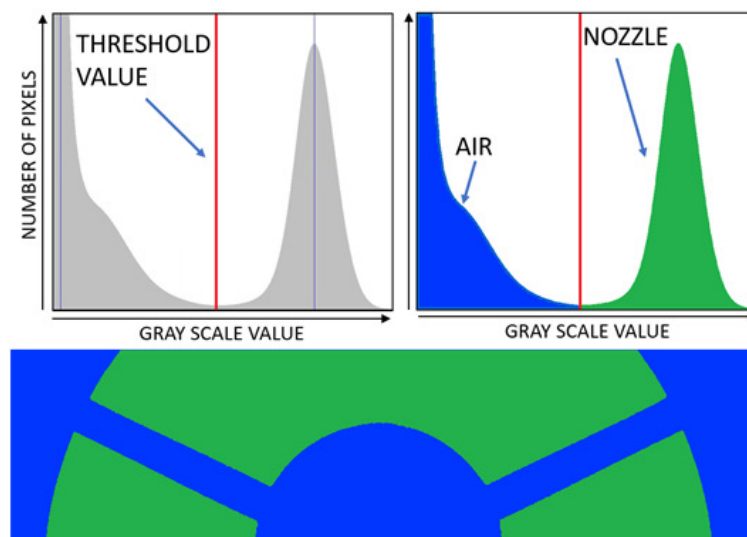


Figure 3-6 Top, left – histogram of the nozzle tomography showing selected threshold value corresponding to the min histogram value between material peaks. Top, right – same histogram presented in the left image but with air and nozzle histogram values assigned colour coded. Bottom – nozzle slice colour coded using threshold value.

This threshold selection grants good separation of materials especially when just two materials are present as in the nozzle case, Figure 3-6 shows with a red line the separation of the histogram values and their assignment to either air or nozzle volume, presented respectively in blue and green.

To check for the correctness of the reconstructed geometry dimensions a reference part made of metal with dimensions comparable to the nozzle tip was scanned and reconstructed. The item selected was a DIN 172 A guide bushing, see Figure 3-7, with the following specifications:

- Material 16CrNi4, hardness HRC 60 +/-2
- Internal diameter 1 mm, tolerance F7 (+6/+20)
- Outer diameter 3 mm, tolerance n6 (+4/+10)
- Producer: Normteilwerk Robert Blohm GmbH

The geometry of the part was reconstructed using the same procedure and parameters standardized for the diesel nozzles; the reconstructed geometry was scaled according to the calculated voxel size of 1.980 μm . A Mitutoyo digital micrometre 293-666 with an accuracy of 2 μm was then used to directly measure the external diameter of the guide bushing so to compare this value with the one obtained from the tomographic reconstruction, see Figure 3-8 The external diameter was measured to have a mean value of 3,007 with a standard deviation of 1 μm : this result agrees with the DIN tolerance n6, requesting a diameter between 3,004 and 3,010 μm , declared for the outer diameter of the part. The measurements on the stl surface reconstructed from the tomography instead gave an outer diameter of 2,996 μm . The CT measured outer diameter is therefore less than expected. The inner diameter was measured using a Leica VMM50 visual microscope previously calibrated with a linear glass scale of 50 mm and an accuracy of 2 μm . The internal diameter gave a mean value of 1,007.4 μm with a standard deviation of 2.94 μm ; the mean diameter is within the DIN tolerance F7 (diam. between 1,006 and 1,020 μm). the measurement of the inner diameter using the CT reconstructed volume gave a value of 1,010 μm , see Figure 3-9.

From the comparison of the part measurements produced with traditional equipment and with microCT, it could be stated that the volumetric reconstruction, produced with the procedure purposely set up for nozzles tomographies and for the typical dimension of nozzles tips, is subject to an error in the determination of the outer contour of the part of -0.366 %, while for the internal diameter the same calculation gives a smaller value equal to +0.257%. As it has been detected, and as it has been stated by [56], [88], [89], beam hardening can introduce a dimensional error and reduce the accuracy of the measurements produced using microCT reconstructed volumes, but it has been found to be essential from the point of view of correct geometry detection since only applying beam hardening correction during the tomographic reconstruction of the injector nozzles, their injection holes exits can be correctly shaped as depicted in the previous Figure 3-5 showing thresholding contour on corrected and non-corrected nozzle slices.

Besides single measurements, the major advantage of tomographic reconstructions is the availability of the full geometry of the reconstructed object permitting 3D comparison against nominal 3D geometry resulting in a pointwise calculation of the difference between the two geometries. This difference is usually calculated as the deviation of the reconstructed geometry versus the nominal geometry resulting in a full volume deviation map.

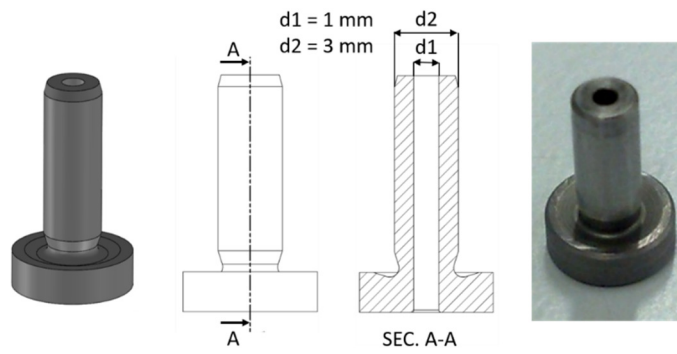


Figure 3-7 3D rendering, drawing and picture of DIN bushing utilised for the dimensional checks.

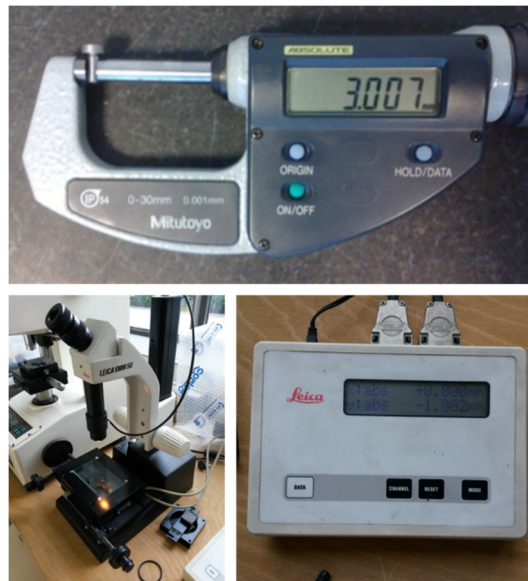


Figure 3-8 Measurement of the DIN guide bushing with the Mitutoyo micrometre.

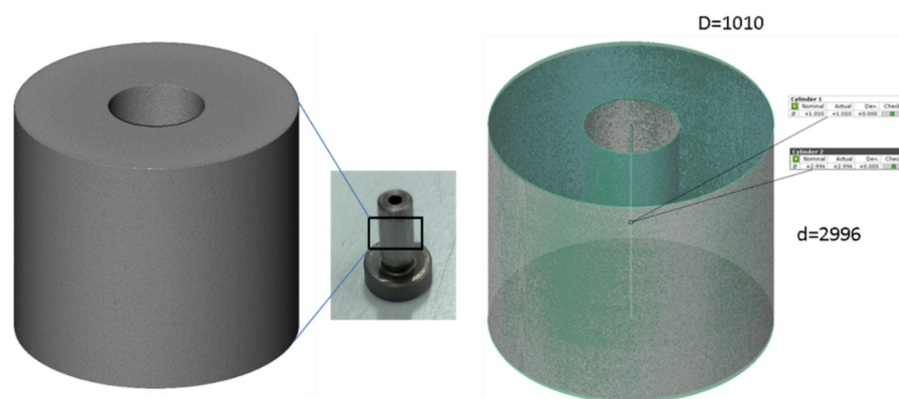


Figure 3-9 Left – 3D rendering of the DIN guide bushing sub-volume reconstructed by microCT. Middle – picture of the real part with reconstructed sub-volume identified by the black square. Right – stl reconstructed surface of inner and outer cylinders utilized for the diameter size calculations: “D” indicates the inner diameter while “d” indicates the outer diameter size.

An example of the mentioned comparison is graphically presented in Figure 3-10 where the deviation of the geometry of the inner part of the injector, the only one for which we succeed in retrieving the nominal design geometry, is color coded and applied to the reconstructed internal sac and injection holes surfaces. The alignment between the two surfaces was produced minimizing the average overall deviation between them. From the analysis of the calculated surface deviation it is evident that the sac volume, which has a spherical top geometry in this case, presents the most deviation from the nominal geometry, while the most deviating area of the injection holes is the injection hole entrance and the first part of the channel exhibiting an average deviation of around 10 μm .

The higher geometrical differences at the channel entrances could be ascribed to the hydrogrinding operation which is specifically meant to increase the nozzle flow increasing the inlet rounding; this operation unfortunately has a very large tolerance on the resulting geometry. However, it must be stressed that the deviation is strictly dependent on the alignment between the two surfaces, which can be easily biased by even only one of the geometrical features being out of production tolerances, considering both feature size or shape. The uncertainties of the production process appear to be evident considering Figure 3-11 of the same injector showing a noticeable defect at the beginning of the sac area, starting right after the end of the needle seat area which was not known before the performed tomographic reconstruction and analysis. From the dimension and position of the defect it can be guessed that it was produced during part manufacturing, either during the manufacturing of the internal sac volume or the production of the injection holes with microEDM. This latter hypothesis is sustained by the fact that the defect is almost perfectly aligned with the axis of one of the injection holes on the opposite side of the nozzle, making feasible the possibility that the defect was produced by the microEDM wire going too deep during opposite injection channel drilling, and by the fact that it has a circular footprint as the microEDM electrode head.

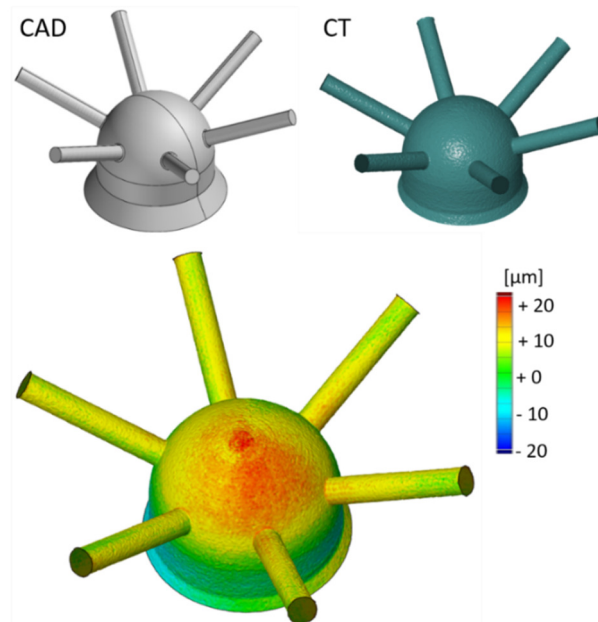


Figure 3-10 Top left – nominal CAD design geometry for the internal volume of the studied nozzle. Top right – reconstructed geometry produced by microCT data. Bottom – over position of CAD and CT geometries with the CT surface colour coded to reflect surface to surface distance.

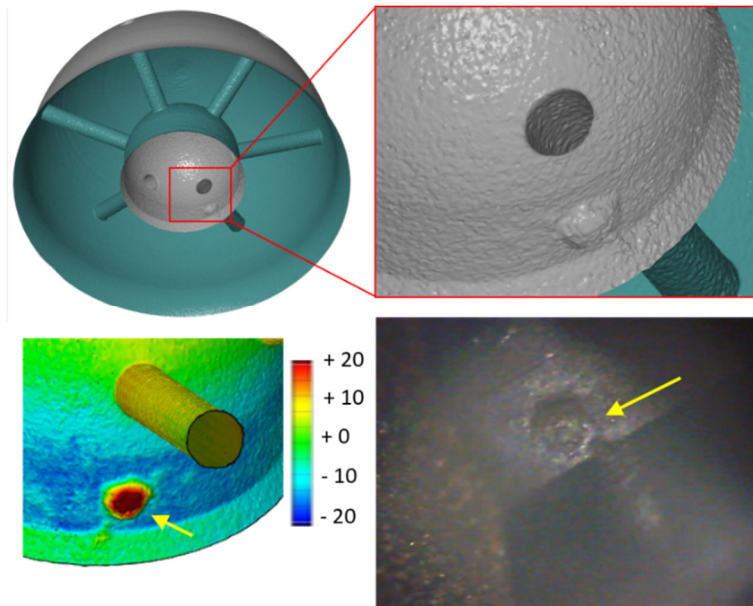


Figure 3-11 Top left – tilted bottom view of the reconstructed nozzle geometry with highlight of the position of the defect detected. Top right – zoomed view of the same geometry presented in the left to better reveal the defect. Bottom left – defect presented with deviation colouring exceeding used scale. Bottom right – picture of the defect produced after cutting the injector in half to reveal the inside.

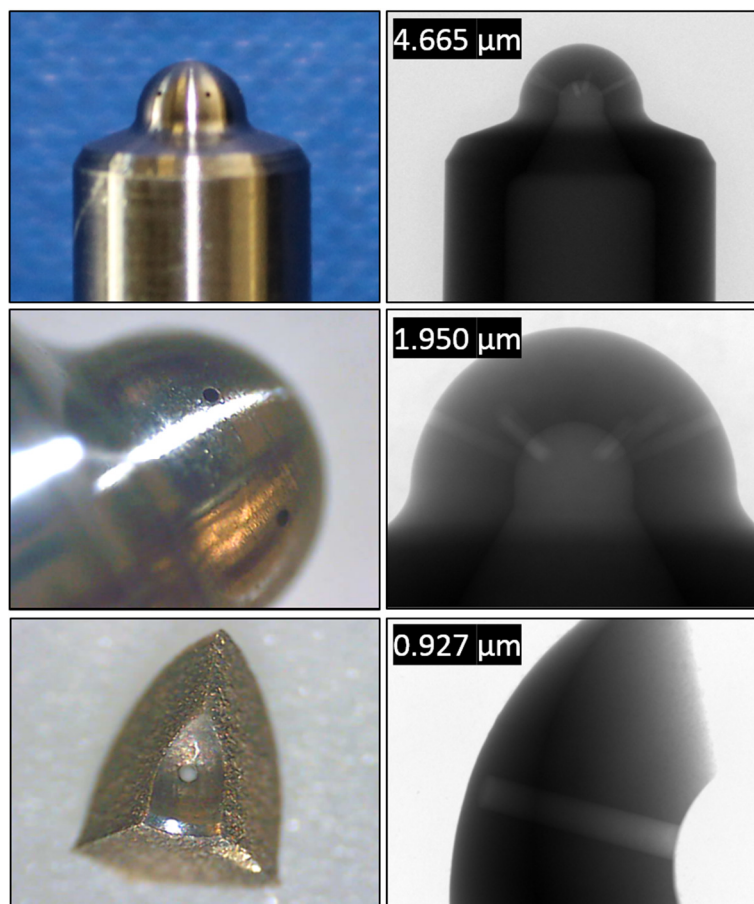


Figure 3-12 Left column – zoomed pictures of the nozzle to locate the nozzle part that will be in the reconstructed volume at the three level of resolution. Right column – radiographies from the tomographic datasets at the three chosen resolution levels.

The influence of tomographic resolution on the reconstructed surface has been further investigated producing three different tomographies with increasing resolution to detect how the interesting features such as injection hole diameter, length and inlet and outer radii change due to tomographic resolution. Figure 3-12 presents a picture of the nozzle tip and three sample radiographies selected from the tomographic dataset acquired in three different positions to give a reconstructed volume voxel size of respectively 4.665 μm , 1.950 μm and 0.927 μm . The highest resolution of 0.927 μm required the cutting of the nozzle tip to extract a 60°-degree sector since the sample must be rotated 5.27 mm from the X-ray source to obtain this resolution.

Considering the dimensions of the nozzle body radii, exceeding in its bottom part 7 mm, and the presence of the metallic filter, cutting the single sector using a microEDM machine (micro Electrical Discharge Machining) was the only possibility to reach the desired sample to X-ray source distance. MicroEDM technology was selected instead of traditional mechanical machining because of its peculiar characteristics of being very precise and mechanically stress free for the machined part. Figure 3-13 presents the nozzle microEDM machining process and the resulting 60-degree sector on a finger to show the scale dimension of the part.

For the first two cases with higher resolution value, all six injection holes were measured to obtain reported mean values and standard deviations; for the single hole case instead, only two 60° sectors, corresponding to two holes, have been measured since the other four holes were destroyed during microEDM cutting.

Figure 3-14 presents a rendering of the reconstructed surfaces at three resolution levels along with a cross cut view of one injection hole to visualize reconstructed surface differences due to different tomographic resolutions.

The same figure shows that the increase of resolution corresponds to a proportional decrease of scanned volume, which is dependent on the microCT hardware and setup. All the three reconstructions were produced following the procedure mentioned before for nozzle reconstructions, except for the beam hardening correction which has been tailored to the much different actual thickness of each part, varying from a maximum of 4.2 mm for full tip case to 1.1 mm for the 60°-sector case.

From Figure 3-14 it is evident how the increased magnification is better able to detail the geometry of the injection channel, however, from the measurement values produced, the difference between the three reconstructed geometries is quantified.

From the nominal CAD geometry provided by the nozzle manufacturer only the top and bottom inlet rounding values, considering creating a channel cross section with a plane parallel to the nozzle axis and containing the channel axis, and the channel diameter could be measured.

The measurement of each channel diameter in the reconstructed volume was produced in two locations, start and end of the same channel, to be able to detect eventual channel conicity which should not be present in this case since the nominal channel geometry by design is purely cylindrical. Figure 3-15 and Table 3-1 introduce the nomenclature for the measurements produced and locate them on the reconstructed geometry. Table 3-2 presents the measured dimensions for the three tomographic resolutions utilized.

Considering values reported in Table 3-2 it is evident that the lower resolution tomography, voxel size 4.665 μm , presents for most of the cases, values that are away from the corresponding values measured on the other two reconstructed volumes and distant from the reference nominal value.

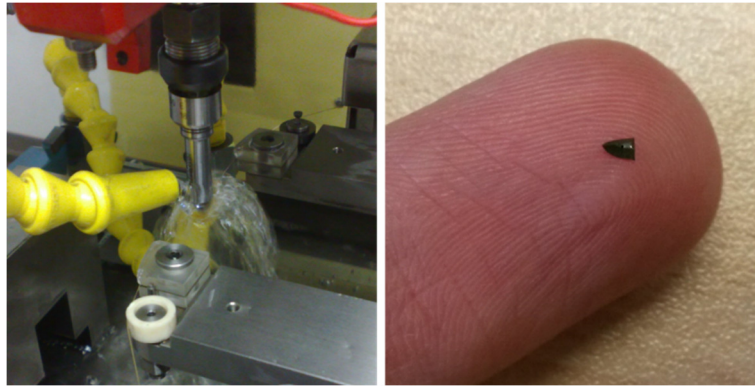


Figure 3-13 Left – 60-degree sector cutting operation inside microEDM machine, the nozzle is being cut by the metal wire which constitutes the eroding electrode; the actual erosion point is visible on the tip of the nozzle as a blue point representing the electrode spark position. Right – 60-degree nozzle tip sector after erosion placed on a fingertip.

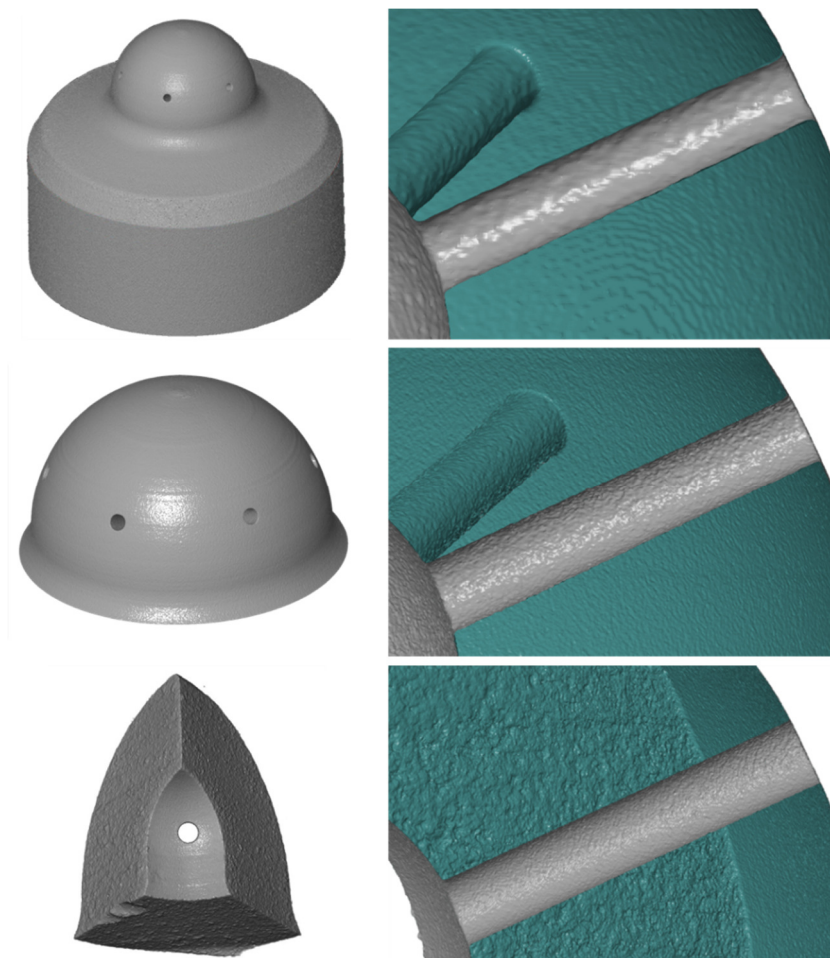


Figure 3-14 Left column – from top to bottom 3D renderings of the reconstructed volumes with three different reconstruction resolutions (4.665 μm , 1.950 μm , 0.927 μm). Right column – from top to bottom cross cut view of the 3D rendering of reconstructed volumes visualizing one injection channel.

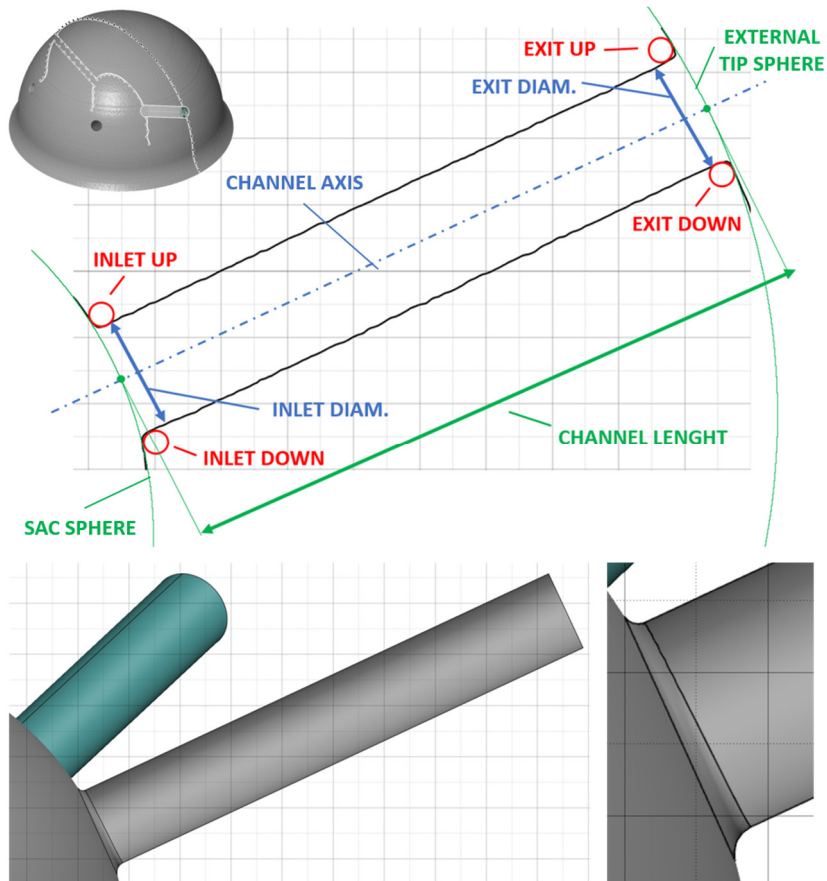


Figure 3-15 Top left – 3D rendering of nozzle tip with geometry section visualized. Top right – orthogonal view of channel cross section with numbers indicating the measured dimensions. Bottom left – cross cut view of the nominal CAD geometry. Bottom right – close up of inlet rounding of the nominal CAD channel geometry.

Feature name	Description
INLET UP	Upper inlet rounding of injection channel.
INLET DOWN	bottom inlet rounding of injection channel.
INLET DIAM.	Diameter of injection channel measured right after inlet rounding.
EXIT UP	Upper exit rounding of injection channel.
EXIT DOWN	Bottom exit rounding of injection channel.
EXIT DIAM.	Diameter of injection channel measured right before exit rounding.
CHANNEL LENGHT	Total channel length measured

Table 3-1 Extended description of the names utilized in Figure 3-15

Unit	[μm]							
Tomographic resolution	4.665		1.950		0.927		REF.	
	Mean	St.dev.	Mean	St.dev.	Mean	St.dev.	Mean	St.dev.
Inlet UP	21.38	2.48	10.65	2.62	10.07	1.21	14	N.A.
Inlet DOWN	19.83	2.42	14.11	5.62	12.9	0.41	20	N.A.
Exit UP	18.44	2.74	11.36	3.20	8.34	0.25	N.A.	N.A.
Exit DOWN	19	2.74	7.93	2.26	9.27	0.07	N.A.	N.A.
Inlet DIAM.	176.08	1.54	174	0.82	175.45	0.64	160	N.A.
Exit DIAM.	171.58	0.49	172.5	0.5	176.45	0.78	160	N.A.
Channel LENGHT	992.16	0.75	977	0.58	979	1.41	N.A.	N.A.

Table 3-2 Average value and correlated standard deviation for measurements of injection channels features of Figure 3-15.

Since scaling of all volumes was performed utilising the same procedure, we could correlate the bigger deviation to the beam hardening correction which is the only correction applied in a dedicated manner to the three objects. In the lower resolution case, the scanned object is thicker than the other two cases since this tomography was performed on the whole injector top volume that was inside the detector field of view, see Figure 3-16 and Figure 3-17.

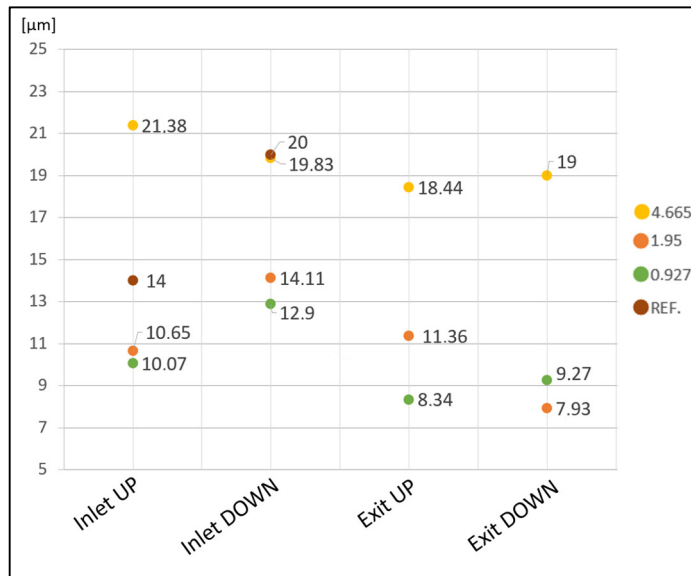


Figure 3-16 Plot of inlet/exit up/down rounding radii (mean values). Tomographic resolution of points is colour coded as per the legend presented in the right part of the image.

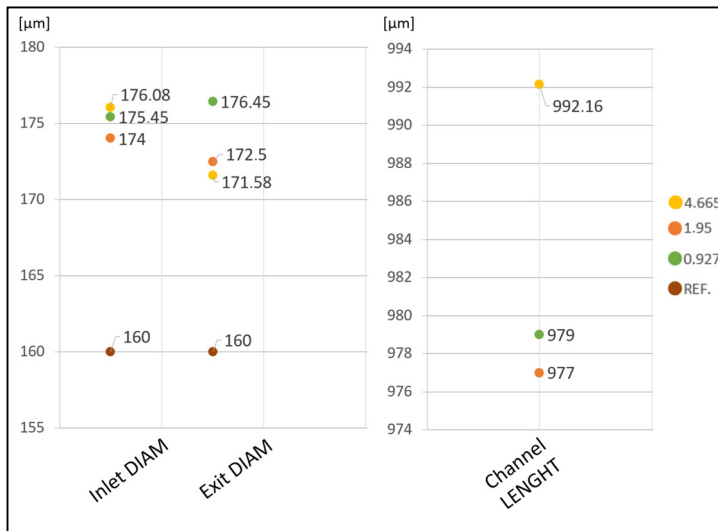


Figure 3-17 Left - Inlet and exit diameters (mean values) for the different tomographic resolution utilised. Bottom, right – mean channel length value for the three tomographic resolution

This results in a much wider window of grayscale values present in the radiographies to be corrected by the beam hardening correction algorithm which results in a lower resolution for the correction.

A less precise border identification causing the wrong value of the measurements, can be due to more sharp grayscale value variation in the reconstructed slices, producing a different recognized border for the object.

Most probably the first dimension of the larger than expected diameter detected was compared against SEM images of the same injector which revealed for the outer diameter of the injection hole a size of 177.5 µm against the mean diameter of 175.18 µm measured on the reconstructed volumes.

Since even the highest resolution tomography showed the presence of roughness inside the injection channel, SEM imaging of the cut 60°-sector was used to assess its presence, which has also been reported in literature [17], [90]. Figure 3-18 presents the SEM images produced for the mentioned purposes.

The channel roughness pictured in the SEM images, Figure 3-18, was caused by microEDM hole drilling which in literature is reported to have a mean value R_a of 0.3 µm [17] for holes of similar size produced with the same production process.

The reconstructed channel instead presents an R_a of 0.59 µm with a standard deviation of 0.46 µm, an R_z of 7.5 µm and an R_{max} of 7.8 µm. It is worth underlining that the roughness calculation applied to tomography data corresponds to a 100% surface control instead of the localized control usually performed with standard contact rugosity equipment.

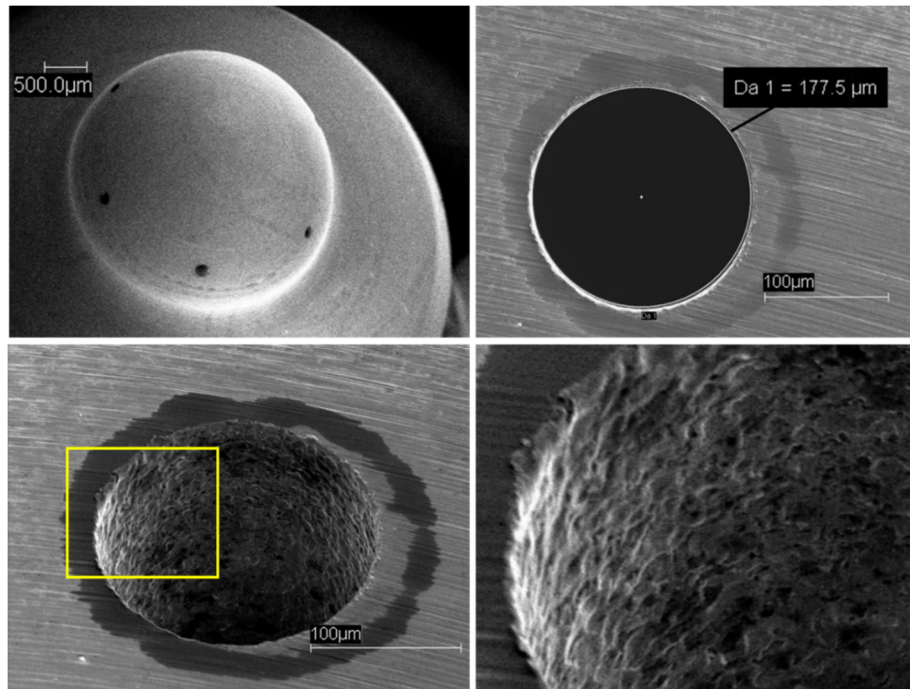


Figure 3-18 Top left - SEM image of the full nozzle tip. Top right – SEM measurement of the EXIT diameter of one injection hole. Bottom left – Tilted view of the same injection hole exit to reveal channel roughness caused by microEDM machining. The darker region with a ring shape around the channel exit has not been studied further. Bottom right – zoomed view of exit edge of channel.

3.2 CAVITATION INDUCED EROSION DETECTION.

It has been mentioned that tomographic scanning can be used for non-destructive testing purposes, however this capability can be further exploited considering producing more than one reconstruction of the same object over time. In fact, being non-destructive, grants the possibility to compare the reconstructed volumes resulting from successive scans in search of geometrical or local density differences. This means being able to detect morphological differences due to expected or unexpected mechanical wear or unexpected events that have caused local or general damage to the part. The detection of chemical changes to the part is also possible provided the part local density or chemical formula changes. The capability of detecting part wear that has caused geometrical changes to the part has been tested during this research utilising as example the injection channel designed for the cavitation experiments also presented in this thesis. The model injection channel pictured in the next Figure 3-19 was designed to act as a common diesel injection channel present in modern diesel injection equipment utilised in the automobile field. The presence of cavitation inside the channel was granted through design geometry and selection of operating pressures. The part is made from PEEK (Polyether ether ketone), a material selected for its low X-ray attenuation. Figure 3-19 presents the designed model. A first injection channel tomographic reconstruction was performed after an initial 8 hours long running in of the part, so to check the full functionality of the part and let the part adapt to the process. The comparison of the reconstructed geometry with the nominal cylindrical geometry designed for the part, see Figure 3-20, revealed that the part was far from being cylindrical and with nominal dimensions. The entrance edge of the channel which should have been sharp was detected to be much smooth than designed, in particular on the main flow side, which permits to guess that besides production tolerances, the main

flow side has been rounded by the flow during the running in operation.

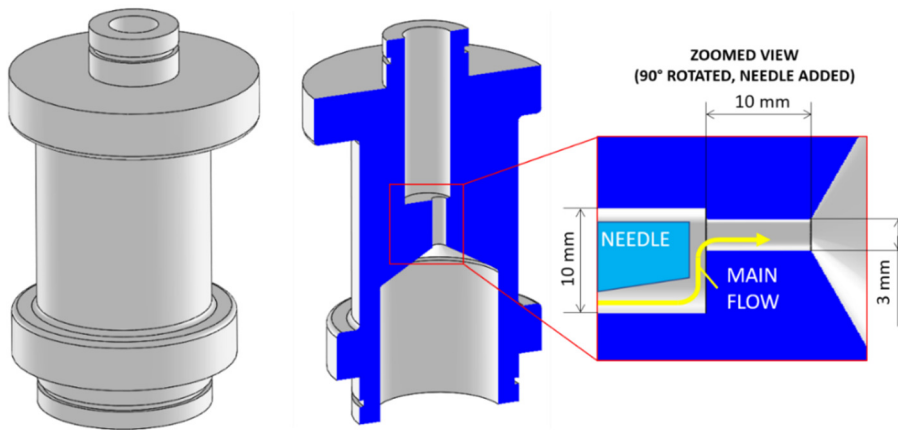


Figure 3-19 Left – external view of 3D CAD model. Centre – section view of CAD model showing internal injection channel position and geometry. Right – zoomed orthogonal view of only injection channel with needle added visualizing flow path and asymmetric needle utilised.

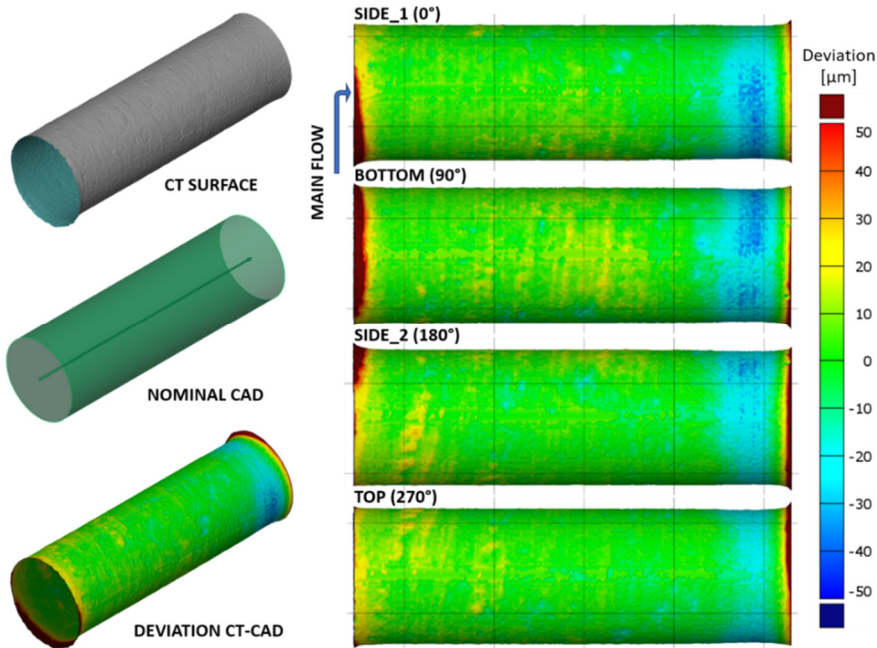


Figure 3-20 Left column from top to bottom – surface geometry of injection channel after running-in reconstructed with microCT; nominal injection channel cylinder; microCT geometry coloured to represent geometrical deviation of reconstructed surface from nominal cylindrical feature.

Along the channel spiral marks, depicted in yellow in the next Figure 3-20, were produced by the tool used to drill then hole. The channel diameter restriction at the end of the channel instead is due to the production process. The presence of cavitation, starting at the sharp edge entrance of the injection channel and developing further inside the orifice, depending on selection of inlet and outlet pressures, can cause material erosion as widely reported in the case of turbines, hydraulic pumps and ship propellers. To produce erosion in the selected PEEK model, the same was operated in a test rig for around 45 hours flowing it with common

Diesel fuel utilising a mean pressure difference of 22.7 bar between injection channel inlet and outlet, while maximum and minimum pressures were respectively 55 bar and 6.8 bar.

The wearing of the part can be attributed mainly to cavitation erosion being the liquid utilised chemically compatible with PEEK, granting no chemical changes are determined by the contact of the material with the liquid, and being the utilised liquid free of abrasive particles.

To visualize the location where cavitation takes place inside the channel, Figure 3-21 presents a side view shadowgraphy of the injection channel in three working condition presenting increasing cavitation presence. The dark area corresponds to the cavitation area: it is evident that cavitation takes place inside the channel starting from the entrance and developing almost up to the end of the channel when pressure differential across the injection channel increases.

Comparison of injection channel tomographic reconstructions produced before and after usage can detect part geometrical changes. Utilising as reference geometry the reconstructed surface of the injection channel produced before usage, a colour coded deviation map can be applied to the same channel geometry reconstructed after cavitation erosion.

Figure 3-22 displays the 4 orthogonal views of the eroded channel geometry where erosion area is made evident by colour coding (colours from yellow to red-dark red).

Erosion due to cavitation was detected mainly in two areas, centred respectively at 2.5 mm and 7 mm after the channel entrance on the main flow side of the channel.

The magnitude of the two erosion areas is different, the first area is smaller but deeper than the second one, reaching a maximum depression of $-70\ \mu\text{m}$, the second depression is instead larger than the first one but with less depth, reaching a maximum of $55\ \mu\text{m}$.

To better interpret the result of the geometry comparison, dedicated CFD simulations [91] were performed at a later time aimed at finding cavitation structures collapse locations inside the channel which were supposed to be the location where cavitation erosion would take place. To produce the simulations, the reconstructed geometry of the channel after running in was employed, constituting the real starting geometry of the channel which have contributed in obtaining results that were dedicated and reasonable.

Performed simulations results confirmed that the discovered locations were in good agreement with places characterized by pressure peaks originating from the collapse of the formed cavitation structures. For low pressure differential conditions, illustrated by the first and middle image of the previous Figure 3-21 presenting shadowgraphies, the main collapse location is centred near the hole entrance, while for high pressure differentials, illustrated by the bottom image of the same Figure 3-21, two erosion sites can be predicted: one near the channel entrance and one more downstream the entrance where the cavitation cloud closes.

The presence of a bigger channel deformation near the channel entrance is therefore in accordance with the simulation results predicting pressure peaks in this location for a vast range of operation, from low to high pressure differential, while the smaller deformation present in the channel away from the entrance is due only to limited operational conditions.

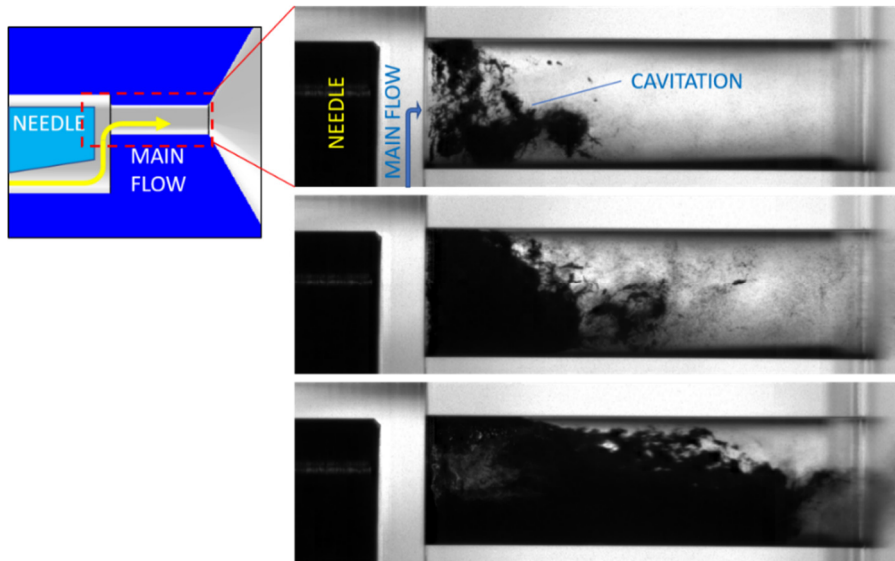


Figure 3-21 Shadowgraphy of injection channel showing cavitation as dark area; the flow direction is from left to right and the injection channel is displayed horizontally. Images from top to bottom display three testing conditions with increasing cavitation presence.

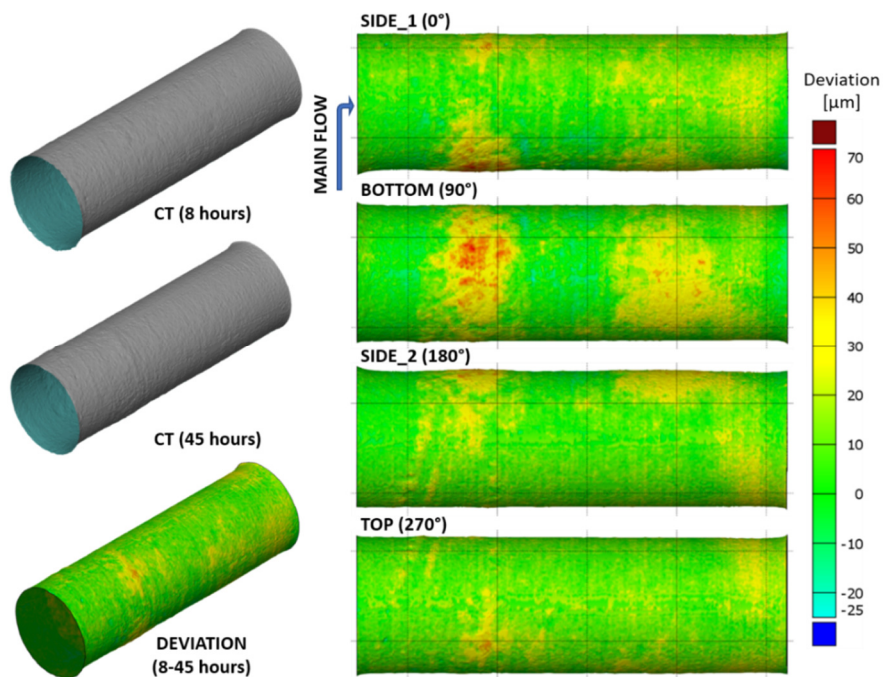


Figure 3-22 From top to bottom orthogonal views of the 4 sides of the injection channel presenting geometrical deviation of channel geometry reconstructed after usage versus same channel geometry acquired before usage.

4 APPLICATIONS TO MULTIPHASE FLOW – CAVITATION

4.1 INTRODUCTION

X-ray tomographic reconstruction of an object's volume results in a spatially distributed map of its density. This characteristic was exploited to study the density distribution of a multiphase fluid flow present inside a model injection channel designed to resemble the flow behaviour occurring inside high-pressure diesel injectors commonly utilised in the automotive field. The main objective was to produce volumetrically localized quantitative measurements of the vapour fraction of the flowing fluid inside the channel which was subject to cavitation due to the selected operating conditions and selected channel geometry. Laboratory X-ray tomography was not expected to be able to freeze the cavitation phenomenon, due to its highly dynamic behaviour, but rather to give time averaged measurements of it. Moreover, thanks to the non-symmetric geometry of the needle and the off-centre position of the injection holes, highly non-symmetric cavitation structures develop inside the tested model. The description of such a complex cavitation geometry can be produced only utilising 3D techniques.

The injection geometry utilised was inspired by the work of [36] and aimed at replicating the flow behaviour of a valve covered orifice (VCO) injector, where the fluid flow path is forced to enter, with a sharp turn, inside the injection channel being therefore subject to cavitation at the sharp channel entrance. The designed model is a large scale one with an injection channel diameter of 3 mm and a nominal length of 10 mm while commonly used injection channels have diameters in the order of less than 200 μm [92] and variable lengths in the order of 1 mm. Investigations produced employing visualization techniques such as shadowgraphy, Schlieren and interferometry [93], [94] were used in the past to study cavitation utilizing transparent replicas of the desired injection geometry.

The model replicas were either of the same size of the injection model to be studied [95]-[97], produced with difficulties out of transparent plastic material or even quartz, or large scale replicas with dimensions from 10 to 15 times the real ones [29]-[31]. True scale models were operated with injection pressures similar to the ones present in real injectors in the order of 500-2,000 bar [16], [92], [98]-[100], while the large-scale replicas were operated at much lower pressures, between 1 and 15 bar. The result of visualization studies was that dimensionless similarity producing the same flow behaviour could be observed utilising true scale injection channels with high pressures and large scale models with low pressures if cavitation (C.N.) and Reynolds (Re) numbers were kept similar in both cases [101]-[103].

The experimental setup designed for this thesis utilises the mentioned similarity behaviour so to use a large-scale model operated at moderate injection pressures to simulate flow behaviour inside real size high-pressure VCO diesel injectors. The reasons for choosing such an experimental set-up were the availability of a suitable mid-pressure hydraulic equipment and the will to avoid complex mechanical micro-machining of the injection channel model utilised which would have been high to produce real size injection channel models with materials compatible with X-rays.

4.2 EXPERIMENTAL TEST RIG DESIGN FOR VOID FRACTION MEASUREMENTS

The experimental test rig utilised was a modified version of a flow test rig designed and assembled for high speed shadowgraphy visualizations by Dr. Mitroglou.

The hydraulic circuit which provided controlled flow of pressurized diesel through a test chamber was used as is, while the test rig chamber section of the circuit was completely redesigned to suit the X-ray tomographic technique.

The original test chamber was designed to produce 2D high speed shadowgraphy images of cavitation inside an enlarged model sample made of Perspex®. The model material was selected to have a refraction index near to that of diesel fluid, while the square geometry was selected to avoid image distortion caused by model walls not perpendicular to the viewing direction.

Figure 4-1 presents the original layout of the high -speed shadowgraphy visualization test chamber. Therefore, X-ray tomography was not considered during the initial test rig design. In the depicted high-speed visualization test rig, we can define the following characteristics as non-optimal for straight use for X-ray tomographic acquisition:

- Presence of 4 metallic screws:
Vertical screws of metallic material with high X-ray attenuation coefficient impede the possibility to see the interesting injection channel section throughout the full 360° rotation which is necessary for complete tomographic acquisition. Attenuation coefficients of metal and diesel are very different determining a substantial impossibility to picture them correctly within the same radiography.
- Big chamber size:
Cone beam X-ray tomography can act as a magnifying lens for the volume of interest provided the X-ray source to object and X-ray detector to source distances can be purposely selected. A big test chamber doesn't allow the object to be placed near to the X-ray source which is a constraint to reach maximum magnification.
- No possibility to rotate:
The shadowgraphy test rig was designed to be static, therefore it had no built-in possibility to rotate which is a requirement to produce a tomographic reconstruction utilising a laboratory X-ray tomographic machine. Medical CT machines instead keep the patient, which is the sample, static and rotate synchronously the X-ray source and detector, however medical machines were not suitable in our case due to insufficient reconstruction resolution.
- Out of axis rotation:
If few consider the main axis of the test rig, which is the one of the square Perspex model and of the round metal plates present in the test rig assembly, we can note that is different from the injection channel one. If we would use this as rotation axis during tomographic acquisition we would lose the possibility to obtain maximum magnification for the volume of interest since the channel would occupy, during rotation over 360°, a cylindrical volume bigger than the minimum one, increasing the necessary field of view of the radiography that results in a lower magnification.

Considering the non-ideal features mentioned, a redesign of most of the test rig was necessary. The new design, dedicated to X-ray tomography, is visually presented in Figure 4-2.

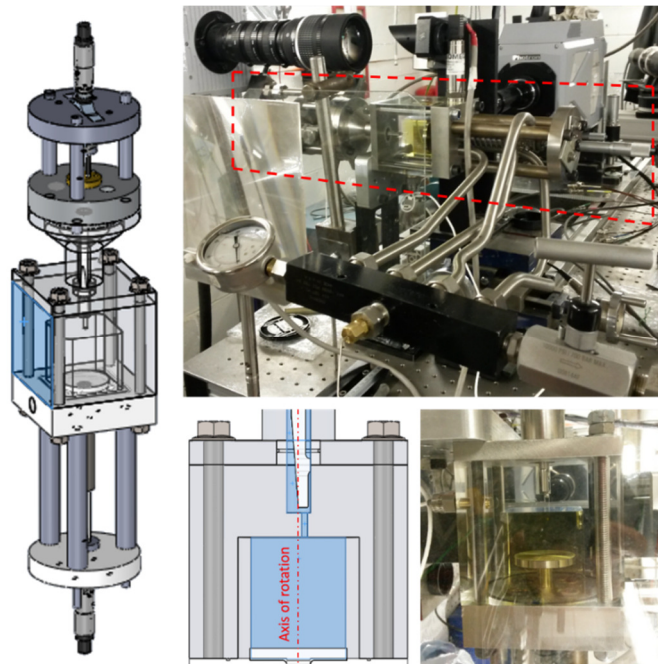


Figure 4-1 Left – 3D CAD image of the test rig as available for the high-speed visualizations. Right, top – Picture of the same rig assembled and utilized: the area surrounded by the red dashed line highlights the rig horizontally mounted on the optical table. Right, bottom – close up CAD and picture of the test chamber, the CAD image presents the hypothetical rotation axis mentioned.

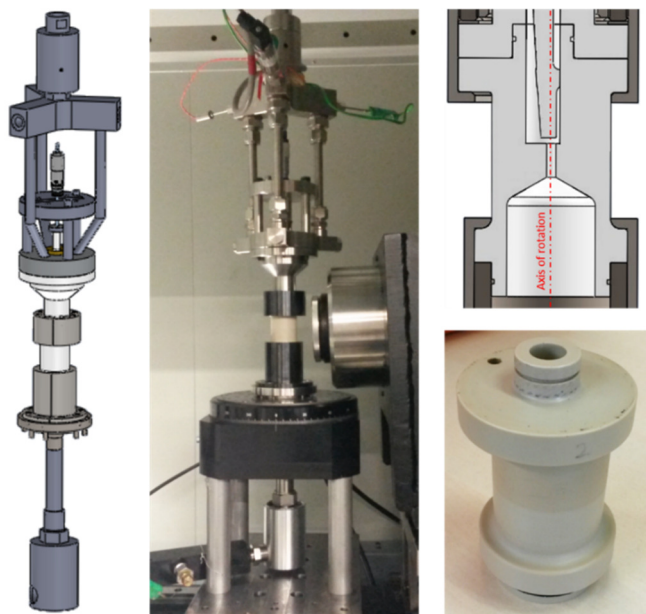


Figure 4-2 Left - 3D CAD image of the test rig as designed and produced for the X-ray tomographic reconstructions. Centre – Picture of the test rig placed inside the microCT machine. Right, top – middle cross section of the test chamber CAD to reveal the inside, the rotation axis or the rig is coincident with the injection channel one. Right, bottom, picture of the new test chamber.

The new design featured the following characteristics:

- Clamps instead of screws:
The use of clamps to hold in place the sample chamber permits the absence in the field of view of the detector of any other material than the sample granting a free 360° direct view.
However, a drawback of this configuration is that the sample itself must be strong and stiff enough to hold some of the weight of the top part of the test rig, even though this weight can be limited by proper sustaining of the test rig with an external frame.
- Small chamber size with cylindrical shape:
The dimension of the chamber was reduced and made cylindrical to be able to get the sample as close as possible to the X-ray source to obtain the highest magnification of the injection channel permitted by the machine.
- Rotation axis:
The rotation axis of the test rig is now coincident with the injection channel axis. This feature, along with the cylindrical shape of the test chamber, having the same rotation axis, permits an even X-ray beam filtration throughout the full 360° rotation granting that the injection channel is radiated in the same way in each rotational position.
- Ability to rotate:
Test chamber rotation is made possible by two rotary joints which are connected to the high-pressure inlet and to the low-pressure outlet.

The test rig was specifically customized for usage with the Unibg tomographic machine, which had, among other characteristics, the necessary hollow rotary stage. However, the same setup can be easily adapted to other tomographic machines or even synchrotrons.

Most of the re-design effort was spent in the selection of the model material, which had to withstand the desired working pressures, 100 bar at the inlet and 20 bar at the outlet, and at the same time to be as transparent as possible to X-rays, to permit good low energy radiation penetration which was required to be used to visualize diesel inside the sample. A further constraint to the mechanical stiffness of the model was set limiting the geometrical deformation caused by maximum pressure application to 15 μm , to grant comparability among datasets acquired with low and high inlet pressures, being confident that the small geometrical deformation, equal to the expected tomographic resolution, would have caused minimal flow change. Various commercially available composite and plastic materials were evaluated utilising: finite element method (FEM) analysis, in search of the desired mechanical strength and stiffness, X-ray attenuation simulations, to do a first screening of the transmittance of the material, and direct transmittance tests through radiographies. Fem analysis were produced utilising using Etilysis software from BETA-CAE Systems [104] and X-ray attenuation calculations with Spektr [40]. Commercially available metal materials considered in the first instance were discarded due to their high attenuation of X-rays. After evaluations, PEEK (polyether ketone) material was selected since simulations predicted for this material good X-ray transparency at X-ray energies compatible with diesel visualization and good mechanical properties granting a maximum deformation of 15 μm for the injection channel volume and 20 μm for the sac walls, which was considered adequate.

Figure 4-3 presents the result of the FEM simulation regarding Peek and a radiography of PEEK various composite and plastic material to assess their penetrability to the X-ray radiation.

The new design components other than the model chamber was produced in stainless steel (AISI 316) to be corrosion resistant and grant the desired stiffness.

To obtain leakage free operation, NBR radial O-rings were used to seal the fluid passage, permitting also ease dismantling and reassembling of the model chamber which was designed to be as much interchangeable as possible to permit the test of different injection geometries.

As mentioned, clamps were used to hold the sample chamber in place, these configuration grants also that they act as first barrier to possible diesel leakage, avoiding possible radial spill of fluid that in the used configuration would damage the X-ray source or detector.

Figure 4-4 presents a middle section of the 3D CAD assembly showing the positions of the mentioned O-rings and clamps, an equal middle section from the drawing of the large-scale Peek model, to show its design dimensions, and the drawing of the non-symmetric needle utilised.

As mentioned in the introduction, an upscale geometry was selected to be able to use the available mid-pressure hydraulic unit, the sizes chosen for the injection channel were 3 mm for the diameter and 10 mm for its length.

The first section presents also the needle position: the needle lift can be adjusted between 0 and 4 mm, even though during the tests it was used only from 0.5 to 3 mm, being the first a condition with high cavitation presence and the second one a condition of very low cavitation presence when coupled with interesting inlet and outlet pressures.

Liquid contained in the hydraulic unit tank is pressurized and sent to the rig through a high pressure flexible hose provided with quick couplings, there, after entering the rig through the top rotary joint, the flow is divided in three feed pipes that converge afterwards in a single volume cavity upstream the injection volume and needle.

This flow path was designed to reduce flow turbulence before entering the injection chamber. After injection, the fluid recollects in a chamber filled with liquid, before exiting the test rig passing through the bottom rotary joint and the exit flow control knob, which was used to regulate exit pressure, before entering the bottom high pressure flexible pipe that takes it back to the tank, closing the circuit.

The hydraulic unit is a customized Hopkins VHP503 power pack capable of delivering a fluid flow, from 20 to 40 litres per minute, pressurized at maximum 150 bar. Test rig's inlet fluid pressure is regulated by means of the flow knob present on the hydraulic unit.

The inlet (P_{in}) and outlet (P_{out}) fluid pressures and corresponding temperatures (T_{in} ; T_{out}) are monitored by specific sensors placed at the entrance of the test rig and at its exit to record the experimental parameters with the aid of the control PC at a rate of 1 Hz. Besides the mentioned pressures and temperatures, also the flow rate (Flow) was measured with a flow meter, with an accuracy of 3%, as well as the fluid tank temperature (T_{tank}). Figure 4-5 graphically locates the mentioned test rig components and presents with simplified graphics the hydraulic circuit utilised.

To keep the fluid temperature constant during the test rig, warm up and experimental phases, a water-fuel heat exchanger unit was added to the hydraulic unit to cool down the fluid coming back from the rig.

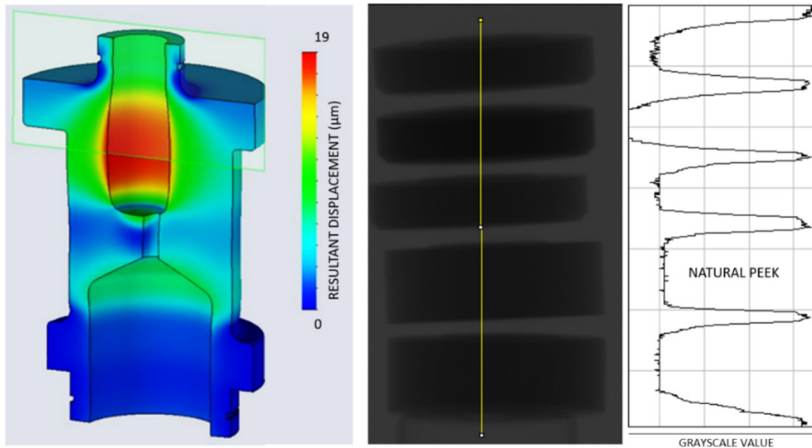


Figure 4-3 Left – Fem analysis of the PEEK test chamber model produced to assess geometrical deformation induced by maximum pressures (100 bar upstream the injection channel and 20 bar downstream). Centre – X-ray radiography of composite materials analysed for X-ray penetrability. Right – Grayscale values corresponding to the yellow line in the central image.

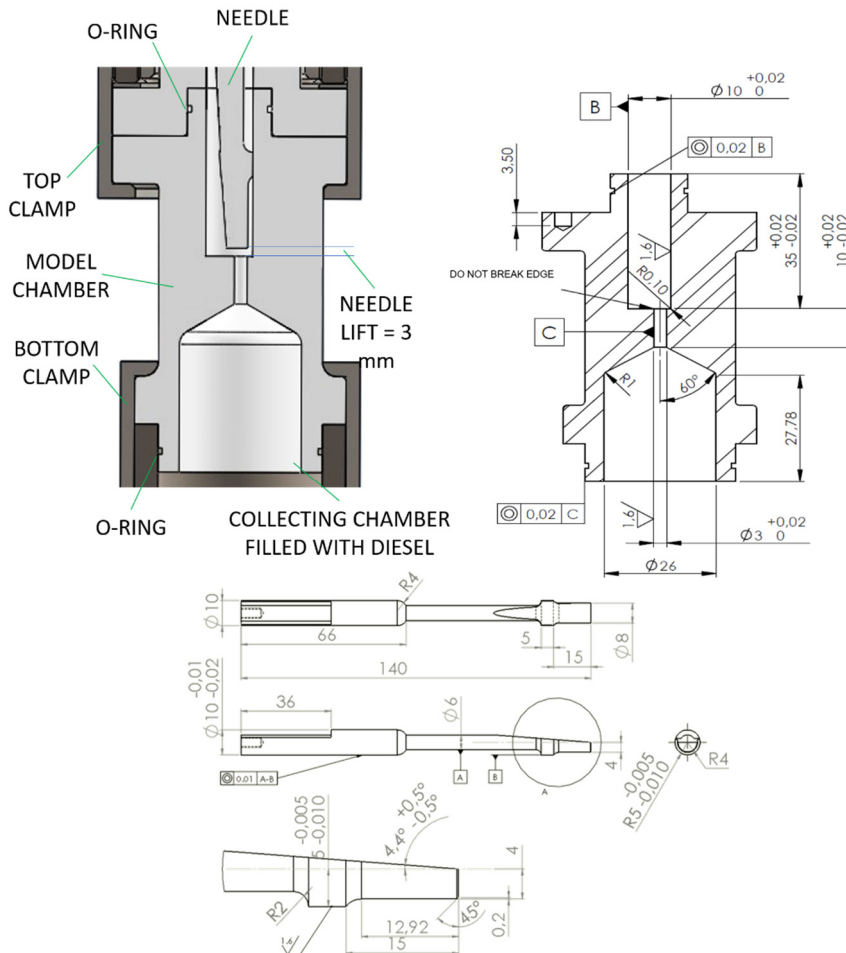


Figure 4-4 Top-left – Section of 3D CAD model showing inner injection channel geometry, sealing O-rings and fixing clamps position. Top-right: 2D CAD drawing of the sample model presenting a section of it showing its design dimensions. Bottom – 2D CAD drawing of the non-symmetric needle.

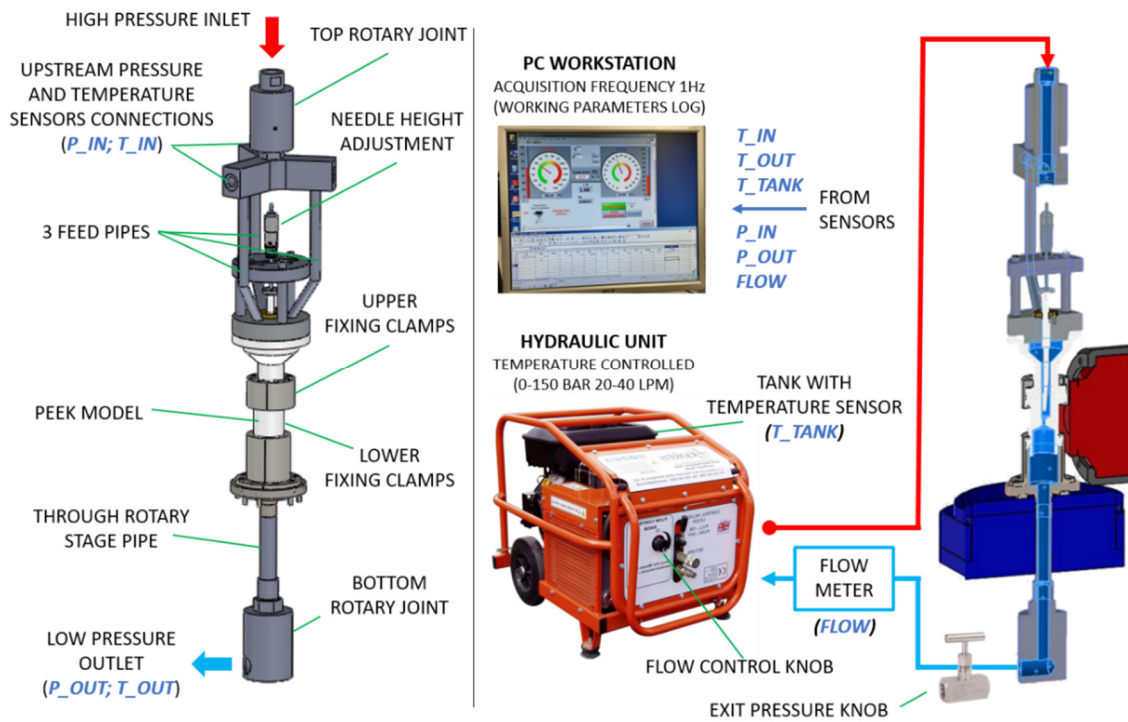


Figure 4-5 Left – microCT customized test rig parts description and localization. Right – Layout of the hydraulic circuit utilised to provide pressurized fluid for the experiment and to monitor interesting experimental conditions.

Table 4-1 presents the experimental conditions investigated: highest pressure reached was not the desired one, corresponding to 100 bar, due to some leakages in the top part of the test rig due to one of the mechanical parts being slightly out of design tolerances.

EXPERIMENTAL CONDITIONS	
P _{in} [bar]	17 – 57
P _{out} [bar]	6 – 20
CN	1.2 – 2.4
Flow rate [l/m]	14.5 – 27.5
Re	35k – 65k
Flow velocity [m/s]	34.5 – 65
C _d *	0.6 – 0.75
T _{in} [°C]	40 ± 0.5

Table 4-1 Range of experimental conditions.

Liquid studied was base diesel fuel commonly available on the market without any additives. Table 4-2

details the diesel specifications as declared by the producer:

DIESEL PHYSICAL AND CHEMICAL PROPERTIES	
Relative Vapour Density	4.7 (Air = 1)
Relative liquid Density	0.86 @ 15.6 °C
Viscosity	3.9 Centistoke @ 40 °C

Table 4-2 Diesel physical and chemical properties (as specified by the producer).

Monitored values of the inlet and outlet pressure were used to calculate the cavitation number proper of the tests set-ups utilising the following formula, being the diesel vapour pressure (P_v) considered equal to 10 kPa.

$$C.N. = \frac{P_{in} - P_{out}}{P_{out} - P_v}$$

Equation 4-1

After performing every tomography, the diesel fuel contained in the hydraulic unit tank and remaining part of the rig was exchanged with fresh new one to always start the next experimental case with fluid with the same chemical and physical characteristics as the previous one. This was decided a-priori since there is experimental evidence that cavitation can cause sonochemical pyrolysis of diesel [105] changing its chemical and physical properties. Experimentally it was observed but not measured a slight colour change in the diesel after performing the experiments, being it darker afterwards. Selection of tomographic parameters was performed starting from the test chamber material selection phase already illustrated. After selecting PEEK material, a first test radiography was performed to a sample piece of PEEK material with the same outer dimensions of the final chamber and with a central non-through hole with a diameter identical to the injection hole. A drop of diesel was placed inside the central hole and a test radiography produced. The result assessed the possibility to separate the diesel drop from the surrounding PEEK chamber based on its different X-ray attenuation thanks to the good attenuation contrast, even though during this test diesel was static while for the final experiments, diesel will be flowing, and diesel vapour cavitation pockets will appear. Figure 4-6 presents the results of the mentioned test. Considering the produced radiography as successful, the next step was to produce a full tomography with the same configuration. As visible in Figure 4-7, diesel and air have attenuation values that are very separated one from the other granting the possibility to distinguish between them with tomographic reconstruction.

Tomographic set-up utilised is as follows:

- Source to object distance (SOD): 36.8 mm
- Source to detector distance (SDD): 370 mm
- Magnification resulting from SOD and SDD: 10x

- Rotation step: 0.6°
- Number of steps: 600 (full 360° rotation)
- Number of projections per step: 5
- Single step exposure time: 1,000 ms
- X-ray source voltage: 60 keV
- X-ray source current: 40.2 μ A
- Detector binning: 2x2
- Tomographic resolution: 14.7 μ m.

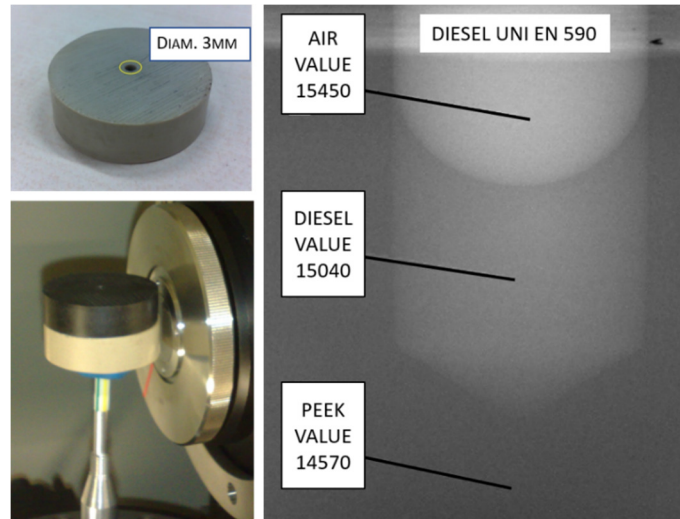


Figure 4-6 Left, top – Peek disk with the 3 mm non-through hole in the middle. Left, bottom – same Peek disk in front of the X-ray source, the back disk of the same dimensions on top of the Peek disk, the brighter one, is carbon fibre reinforced Peek material which was not selected due to its lower X-ray transparency. Right – radiography, mean of one hundred radiographies, of only the hole area with a drop of diesel inside, numbers present the projected attenuation through the sample as perceived by the detector.

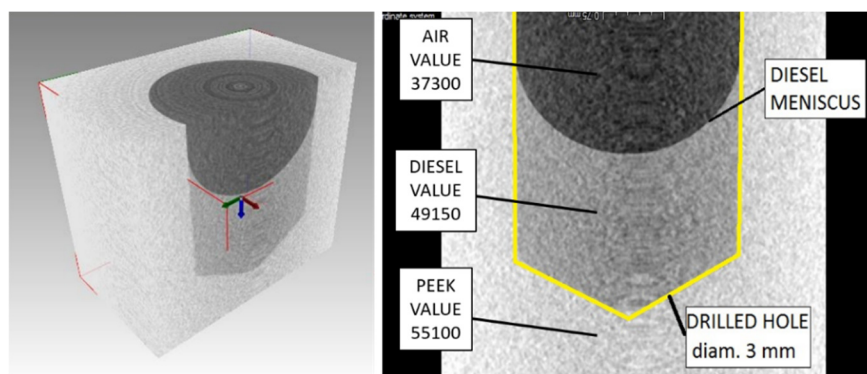


Figure 4-7 Left – 3D tomographic reconstruction of the central part of the sample, sectioned with a middle plane to reveal the inside. Here a drop of diesel is present. Right – orthogonal view of section presenting reconstructed values for air and diesel to assess the possibility to differentiate liquid diesel and diesel vapour, which was considered for simplicity of equal attenuation as air.

The number of projections acquired for each step is 5, these five projections were afterwards averaged to

produce one single image with a better signal to noise ratio; the detector binning was also set to 2x2 to improve image quality even further.

The last binning operation reduces tomographic resolution by a factor of 2, this was considered acceptable as the flow orifice diameter was 200 times the resolution, and adequate to capture the average shape of the cavitation structures. The total exposure time for each angular position was therefore 5 s in total, five consecutive radiography of 1 s each, which was considered a long enough period to picture the average behaviour of the highly dynamic cavitation structures.

The most critical tomographic parameters to be selected were the tube voltage and the radiation filtration. Quantitative measurements of the vapour fraction inside the channel were to be produced leveraging the possibility to distinguish the localized material's density through the knowledge of its attenuation coefficient via the Beer Lambert law of attenuation.

$$I = I_0 e^{-\sum_1^n \mu_n x_n}$$

Equation 4-2

The mentioned formula is valid only if purely monochromatic X-rays are employed. However, for the present experiments, a polychromatic laboratory X-ray source was used, requesting specific precautions to narrow as much as possible the width of its radiation spectrum so to approach the quality of a monochromatic spectrum. The following are the precautions implemented to reach the mentioned aim:

- Filter out the X-ray target characteristic peaks.
- Reduce the beam hardening effect

As illustrated in the first chapter of this thesis, the polychromatic X-ray source utilised produces X-rays by Bremsstrahlung mechanism. The collision of accelerated electrons with the target made of Tungsten (W) forces the electrons to slow down and deviate trajectory losing energy: this energy is converted in heat (99%) and in X-rays (1%) converted to X-rays with a wide spectrum of wavelengths. Within the produced spectrum there is however a higher number of X-rays with specific energies that are characteristic of the target's atom being determined by its electronic configuration. These preferential energies correspond to the difference of energy between electrons of different atomic orbitals, which is characteristic of each different kind of atom. The characteristic radiation wavelengths of Tungsten material are due to electrons releasing energy during the X-ray generation process while moving between L-orbitals, producing so called L-peaks at 8.4 and 11.3 kV, and K-orbitals, producing K-peaks at 59.3kV and 67.3kV. The following Figure 4-8 graphically presents a simulation of the emission spectrum of a Tungsten target where the position of the Tungsten characteristic peaks is localized in the spectrum.

As depicted in Figure 4-8, the presence of X-ray peaks can constitute a notable deviation from the monochromatic radiation desired to be able to apply the Beer Lambert Law of attenuation. If characteristic peaks can't be profitably used centring the mean energy of the generated spectrum on their specific energy, their presence in the generated spectrum must be avoided.

For the present case, due to the necessity to use X-ray source voltages lower than the K-peaks for the

planned tomographies, to increase the contrast for diesel which is a low X-ray attenuating material, and the used X-ray source and detector characteristics, the mentioned peaks couldn't be utilised. Therefore, the generation of K-peaks was avoided selecting an X-ray source generation tension of 60 kV, while L-peaks were filtered by the detector undetectability of X-rays with energies lower than 12 keV. Figure 4-9 presents a simulation of the X-ray spectrum generated by the X-ray source set at 60 kV without filtration applied and limited to the detection range of the used detector (12-130 keV).

The second undesired difference between polychromatic and monochromatic X-rays is the so-called beam hardening effect which can be identified as the preferential attenuation of the low energy radiation of the generated spectrum when passing through a sample object. To reduce its non-beneficial effects, a filter made of a suitable material must be placed between the X-ray source and the object to be scanned so to anticipate the filtration of low voltages X-rays in the filter, rather than in the target object, to let only the higher energetic part of the spectrum hit the sample to be scanned.

Through dedicated filtration, the width and shape of the X-ray radiation can be modified to avoid beam hardening which means at the same time utilising a radiation more near to the monochromatic one, since filtration narrows the incoming radiation spectrum.

Figure 4-10 presents the spectrum modification due to the applied filtration: as it can be seen, the incoming spectrum width has been reduced by 1/4th and the distribution of its wavelength made more symmetric so to be able to determine a mean radiation energy of 34.83 keV that can be used to compare the effects of the obtained radiation to the monochromatic radiation effects with the same energy if needed. As it can be seen in the same Figure 4-10, application of the radiation filtration reduces the magnitude of the generated radiation by a factor of almost 10. Beam filtration is usually applied by inserting a foil of specific thickness, made from a determined material, between the X-ray source and the sample. In the present case instead, beam filtration was obtained utilising the test chamber itself as a filter.

This was implemented by increasing the thickness of the cylindrical test chamber more than what was found to be strictly necessary to withstand the working pressure and respect the deformation constraints imposed during the FEM analysis. Utilising a thicker sample chamber improved the chamber stiffness.

This decision required the injection channel to be centred on the rotation axis so to be always surrounded by the same quantity of filter material for each of the rotational steps. As mentioned in the beginning of this chapter, the aim of this part of the research activity was to demonstrate the possibility to use microCT tomography to quantify the mean vapour volume fraction inside a model injection channel and to assess the cavitation's three-dimensional average shape.

However, before starting to use the tomographic technique, a more traditional visualization technique such as 2D shadowgraphy was employed to produce visualizations results to be used later as reference for the tomographic results.

The result of tomographic reconstruction is a 3D representation of the injection volume, therefore a side view with the same projection angle of the shadowgraphy image should give similar information assessing that the tomographic reconstruction is plausible.

The visualization test rig formerly configured, before applying the modifications necessary to use it with microCT, was employed.

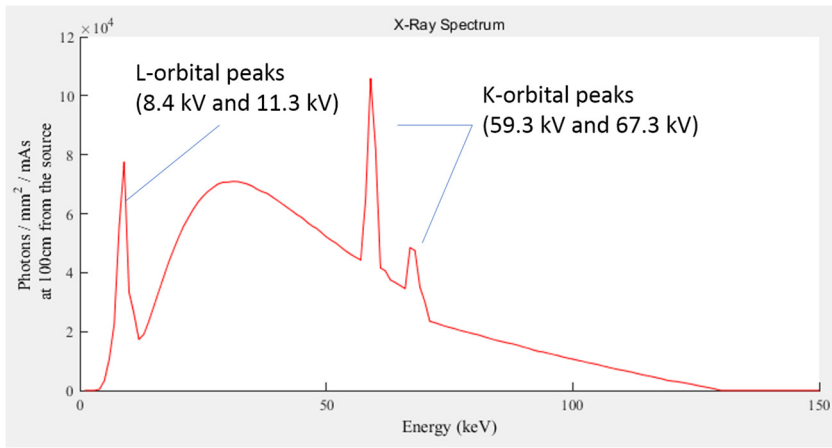


Figure 4-8 Plot of simulated Tungsten (W) target emission spectrum determined by an X-ray source voltage of 130 kV. Plot produced with software Spektr 3.0 [40]. Characteristic peaks are indicated by text and added blue lines.

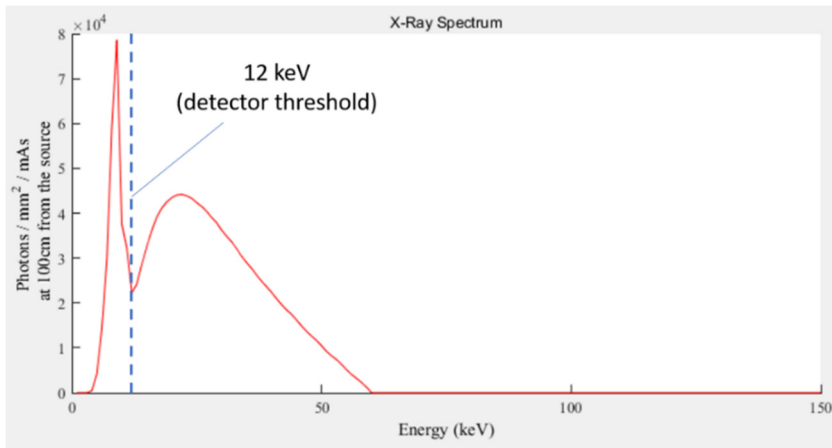


Figure 4-9 Simulated plot generated with Spektr presenting the X-ray spectrum produced by an X-ray source voltage of 60 kV. The absence of the higher Tungsten characteristic peaks is evident, while the lower energies peaks are filtered out by the detector lower energy detection threshold.

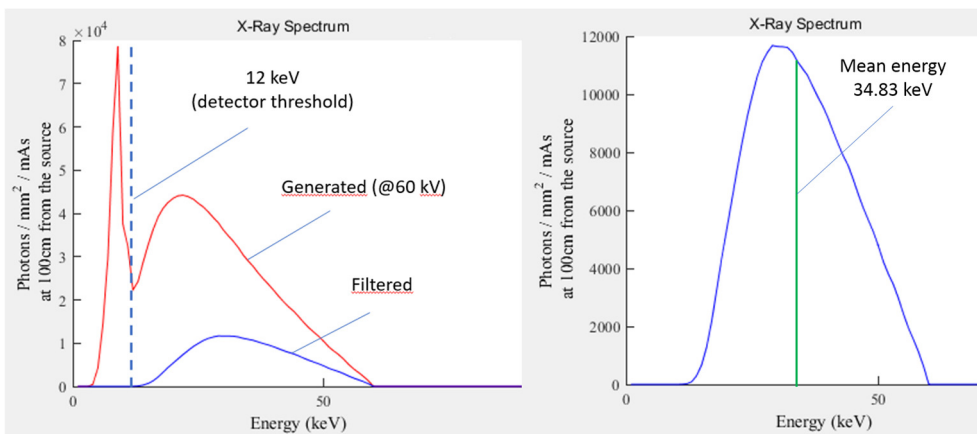


Figure 4-10 Left – Simulated X-ray spectra for an X-ray source voltage set of 60 kV, red line presents generated spectrum as exiting from the X-ray source while blue line presents same spectrum after filtration. Right – zoomed view of the filtered spectrum to better show its quasi Gaussian shape and resulting mean energy.

The only key difference between the two set ups is that for the visualization test chamber, the volume where diesel exit the injection channel is square, while for the microCT test chamber is first conical and afterwards cylindrical. The previously mentioned necessities originated this difference which is depicted in Figure 4-11. The difference was considered acceptable since experimental cases previewed a full collapse of the cavitation structures before exiting the injection channel foreseeing only liquid diesel in the collecting chamber and a precise control of the experimental variables influencing flow, helping to cancel out the mentioned difference. The visualization model was fabricated out of Perspex® material and nominally identical to the PEEK model up to the manufacturing accuracy of 0.02 mm for the injection channel geometry and upper sac volume. The same needle and upper geometry were employed to avoid geometrical differences that could have created differences in the flow.

The shadowgraphy set up employed was:

- A white light source produced with a halogen floodlight lamp set to deliver the desired light intensity by means of a manual control knob.
- A focusing lens to focus light over a smaller area.
- A Fresnel lens to make light rays parallel before reaching the test chamber.
- A glass to divert some of the infrared part of the light from the Perspex model to avoid overheating.

Then after light has passed the test chamber, remaining light is captured by a Photron SA-X high-speed camera with adequate optics to give a final image resolution of 15.47 μm for a total imaged area of 896 x 264 pixels. The image resolution was set up to be able to picture the entire injection channel since in some experimental conditions, cavitation structures occupy almost the full length of the channel. For each test case, 1 second of the phenomenon was recorded at 80 kHz with a shutter speed of 0.37 μs to freeze the highly dynamic cavitation structures. Figure 4-12 presents the shadowgraphy set-up illustrated. The result of shadowgraphy visualizations is a set of 2D 12-bit grayscale images where the reduction or even absence of the incoming light, set up to illuminate the injection channel, experiences partial or total scattering due to the presence of the cavitation bubbles making visible their shape and overall topology. Collected image sets are then post-processed to qualitatively study the phenomenon and extract statistical information on the cavitation localization and its variation by means of standard deviation and mean images. Figure 4-13 presents single shadowgraphy images of three test cases corresponding to three different working conditions.

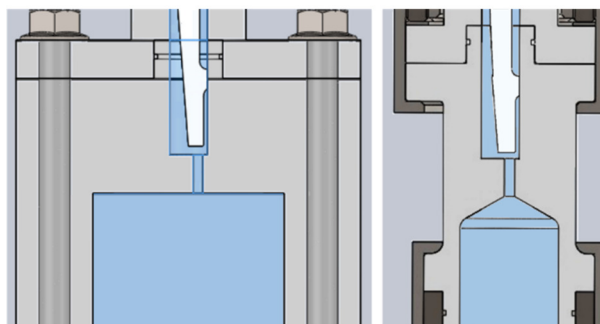


Figure 4-11 Left – Cross section of visualization test chamber with square recollecting volume. Right – Cross section of microCT test chamber with conical and afterwards cylindrical recollecting volume.

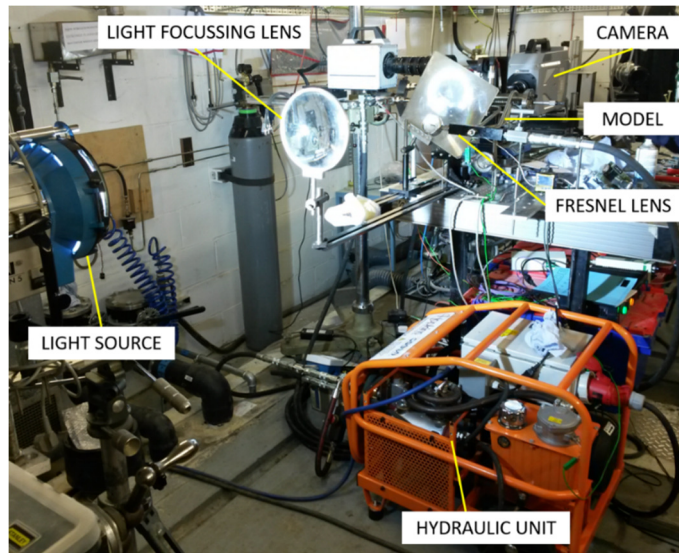


Figure 4-12 Shadowgraphy set-up presenting the components mentioned in the text: light source, focussing lenses, test chamber model and high-speed camera.

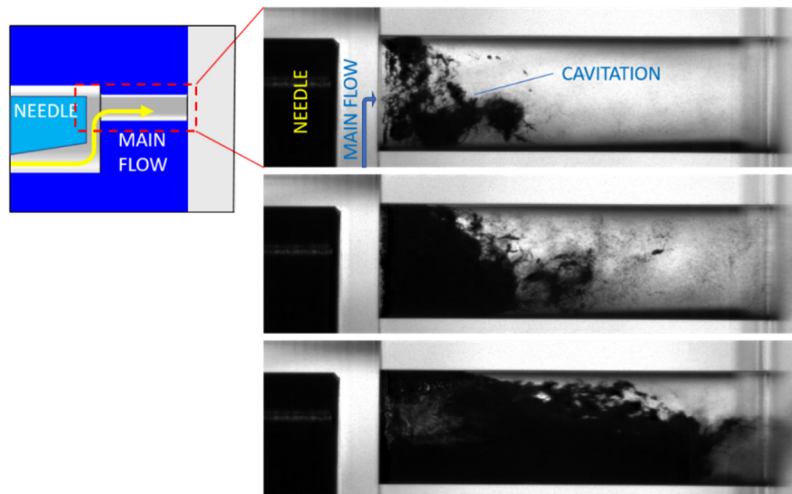


Figure 4-13 Left- schematic view of test injection channel. Right – from top to bottom three shadowgraphy images are obtained with same needle lift equal to 1 mm in different conditions.

4.3 VOID FRACTION MEASUREMENT UNCERTAINTY

Scaling of experimental data

The product of the reconstruction process is a stack of grayscale images (slices) where the grey value of each pixel corresponds to the calculated attenuation coefficient of the material in the specific point of the volume occupied by the pixel taken into consideration.

To produce a value that can be utilized for the volume rather than only for the two-dimensional case of a flat image, the pixel value is simply extended into the third dimension to produce the volumetric reconstruction of the full sample volume. For the reconstructed datasets, the X, Y, Z axis had the same dimension and resolution since the detector utilized have square pixels. The attenuation values

reconstructed in each image must be scaled to obtain a gray value that is proportional to the quantity of interest, in this case the vapor fraction.

To create the extremes of the scale, for each different experimental configuration a reference tomography has been produced with the channel completely empty, full of air, and with the channel completely full of liquid, meaning full of non-flowing Diesel fuel.

The datasets reconstructed from these two cases have been considered as reference sets representing the case of full channel cavitation, assuming the density of air equal to the density of diesel vapour, and the case of no cavitation presence with only liquid in the channel.

As it can be noted from the reconstructed slices shown in Figure 4-14, the contrast between Diesel liquid and PEEK material is less than the contrast between the same material and air in the empty case, meaning that the different attenuation of X-ray of the two materials can be exploited to recognize the presence of cavitation in the experimental cases of interest. The formula utilized to scale the slices gray values is the following:

$$\text{Void fraction} = \frac{\mu_{ij} - \mu_{ij}^{liq}}{\mu_{ij}^{air} - \mu_{ij}^{liq}}$$

Equation 4-3

Where μ_{ij} is the value of the attenuation coefficient calculated for the pixel in the slice to be scaled with i,j position, μ_{ij}^{liq} is the value of the pixel in the same position but for the liquid set, and μ_{ij}^{air} is the value of the pixel again for the same i,j but for the air calibration set.

A pixel by pixel calibration has been utilized to correct for the repetitive unevenness of the pixel values of the reference datasets due to artefacts caused by the tomographic reconstruction which are visible in Figure 4-15 and are known as ring artefacts.

An a priori correction of this kind of artefacts has not been done since their topology shares the ring like shape of cavitation structures seen in the channel entrance in almost all the cases where cavitation exists, so algorithms aimed at its correction, usually specifically based on the recognition of its ring like structure and suppression of pixel value differences, could influence also the cavitation structure reconstruction, which must be avoided.

The effect of a pointwise calibration rather than a calibration done using a mean value for the void and liquid conditions calculated from the full set of slices representing the full vapour and full liquid conditions, is a decrease of the variance of the pixel values of the interesting area inside the channel.

To increase the statistics of the calculated values, the number of pixels considered for the estimation of the variance drop due to scaling has been done utilising 6,760,000 pixels, which represent the area of one hundred slices of the reconstructed volume, each of area 260x260 pixels. The results are presented in Figure 4-16.

Dataset	Mean	Var
Not scaled 10 perc void	0.102114	0.076335
Scaled 10 perc void	0.0996703	0.0277201

Table 4-3 Table of mean and variance values calculated for the non-calibrated and calibrated 10 percent void case (100 slices).

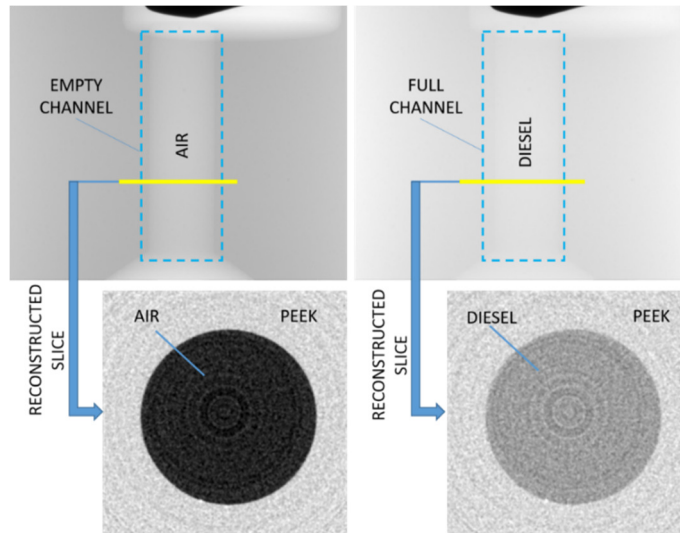


Figure 4-14 (top-left) projection of empty channel and (top-right) projection of channel full of Diesel. (Bottom-left) reconstructed slice of empty channel showing attenuation difference, by means of different grayscale values, between surrounding PEEK material and void channel. (Bottom-right) reconstructed slice of channel full of Diesel liquid.

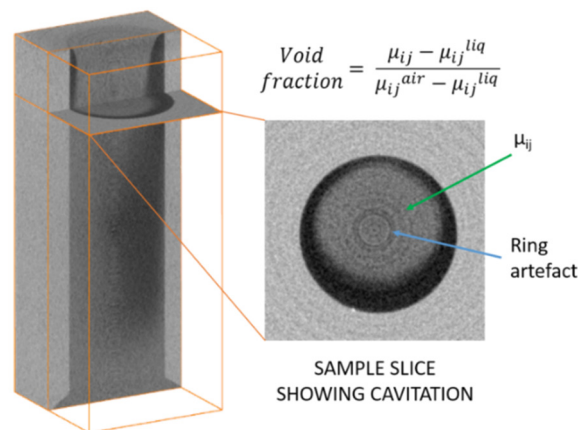


Figure 4-15 (left) axially cut 3D representation of the injection channel of interest with cavitation development (darker area) before application of values calibration and one non-cut slice perpendicular to the axis revealed. (right) Same slice of the reconstructed volume shown flat to reveal ring artefacts and shape of cavitation which is also circular in shape.

To check for the linearity of the considered scale, calibration datasets have been created representing vapour fractions going from 10 to 90 percent in steps of 10 percent. This has been achieved in a virtual way since it was not possible to simulate interesting vapour fractions inside the channel with enough confidence due to its small size, therefore an alternative method has been conceived.

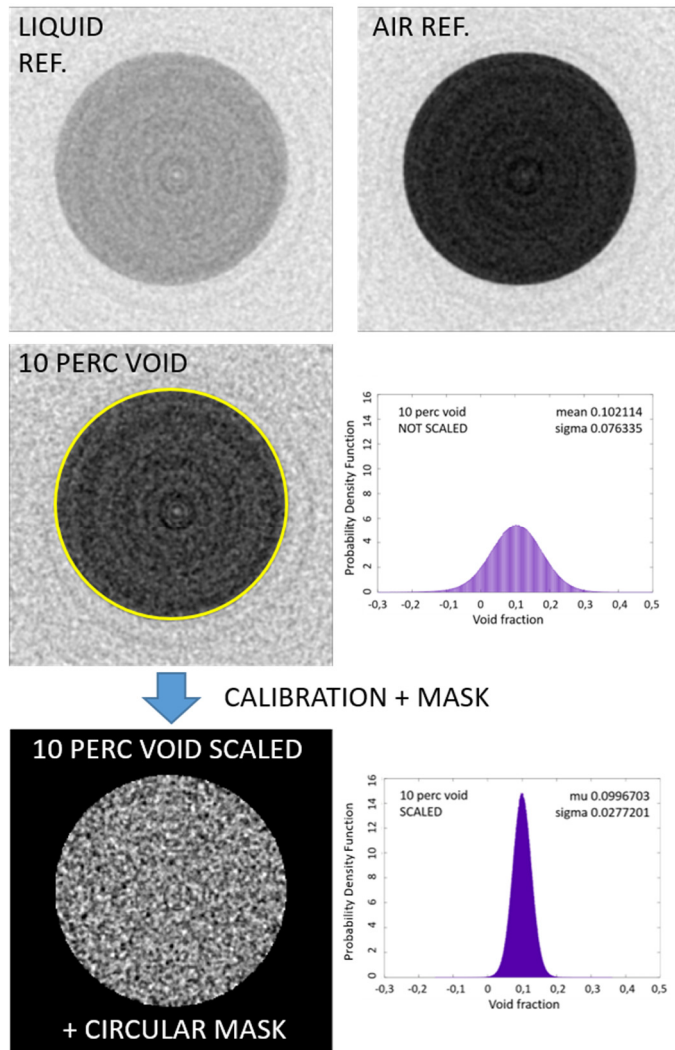


Figure 4-16 (top left) sample slice of liquid reference dataset. (top right) sample slice of air reference dataset. (middle -left) sample slice of 10 percent void dataset before calibration: the probability density function plot of the values inside the channel border, indicated in the image by a yellow circle, is visible on the right of the image. (bottom left) Same sample slice of 10 percent void dataset after calibration and only visual contrast enhancement.

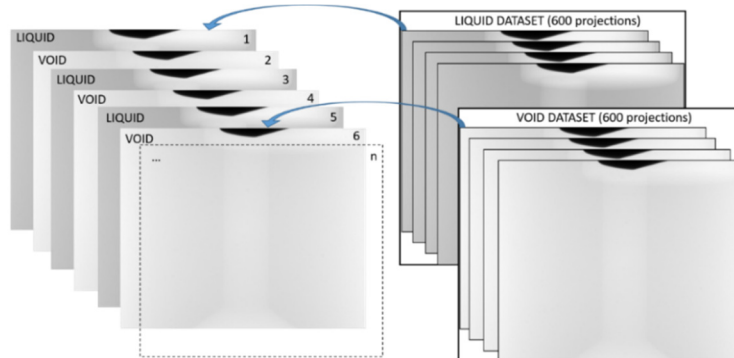


Figure 4-17 Illustration of the mixing procedure followed to create 10 to 90 percent void fraction reference datasets for scale linearity check. The projections have been mixed interlacing them in order to obtain an even effect of the modification proposed, better simulating cavitation presence and absence behaviour.

The method conceived, graphically presented in Figure 4-17, uses the projections of the full void and full liquid condition datasets as representative of an instant when inside the channel full cavitation occurs or no cavitation occurs.

This way it is possible, by mixing proportionally the projections of either datasets, to create datasets able of simulating the desired void fraction. From the reconstruction point of view, mixing the projections of the two datasets, acquired with equal machine setup, means simulating the presence of full channel cavitation when a full void projection is inserted in the dataset, and a full liquid condition when a full liquid projection is inserted in the dataset.

This has been considered adequate to mimic the real condition of the channel since also in the real case cavitation pockets are very dynamic, meaning that they appear and disappear, even though at a much higher rate than the projection acquisition rate.

To produce a better mixing of the two considered datasets for the reconstruction purposes, the projections to insert in the base dataset, substituting the original ones, have been equally spaced in the base dataset, meaning that if a 10 percent void fraction had to be obtained each projection coming from the void dataset has been inserted in position 10, 20, 30..up to 600, the number of projections available for each dataset. To produce the scale 100 slices of the reconstructed volumes have been taken into consideration, moreover, to account for the reconstructed slices noise, the same mean and variance calculation has been done producing the pixelwise mean of all the slices in the Z direction.

Table 4-4 Statistical values calculated for the experimental data after fitting with normal distribution. presents the mean value and variance of the slices pixel values resulted from the mixing only, and mixing and mean process: the proposed values are the fitting of a normal distribution over the population data.

NORMAL FITTING OF DATA				
Void percentage	Mean value	Variance	Mean value (100 slices)	Variance (100 slices)
10	0.0996703	0.0277201	0.0996791	0.00582883
20	0.20005	0.0359206	0.200107	0.00751923
30	0.300369	0.0411848	0.300413	0.00888058
40	0.400103	0.0439558	0.400139	0.00925527
50	0.498217	0.0482403	0.498238	0.0112912
60	0.600192	0.0440173	0.600219	0.00926198
70	0.700316	0.041204	0.700339	0.00871282
80	0.800002	0.0360065	0.800016	0.0076475
90	0.899811	0.0272952	0.899836	0.00594727

Table 4-4 Statistical values calculated for the experimental data after fitting with normal distribution.

Results are presented in Figure 4-18: the linearity of the obtained scale for the experimental data without the mean over the hundred slices is described by Equation 4-4:

$$y = 0.01x - 0.0002 \quad (R^2 = 1)$$

Equation 4-4

Figure 4-19 presents the same scale interpolation provided with 1, 2 and 3 sigma bars to represent 68.27%, 95.45% and 99.73% confidence bands of the experimental and mean experimental data. Visually the scale can be represented as in Figure 4-20 Visual representation of the created calibration scale: it can be noted that vapour fractions which are farther from the reference calibration dataset with 0 and 1 void fraction present more uncertainty.

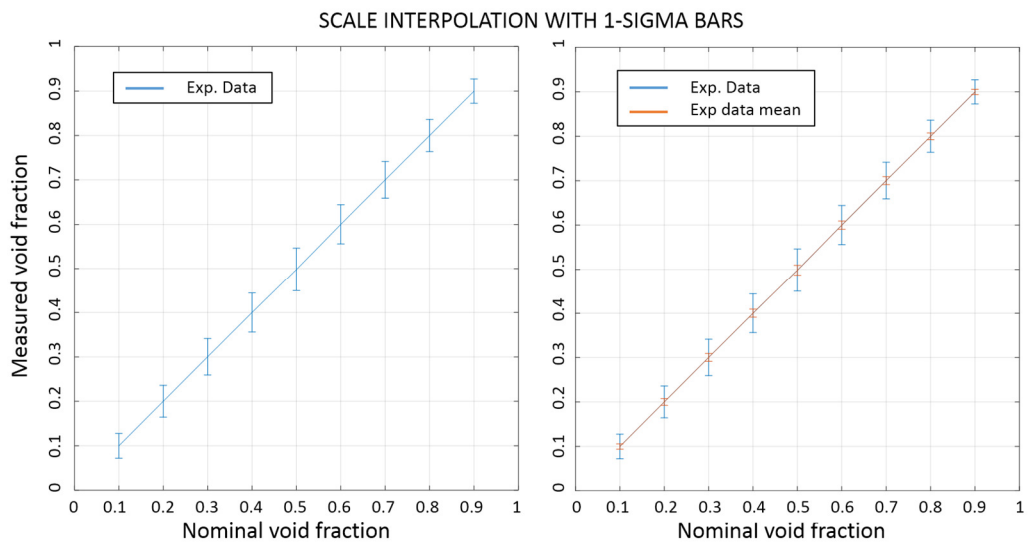


Figure 4-18 Void fraction calibration scale with 1-sigma bars

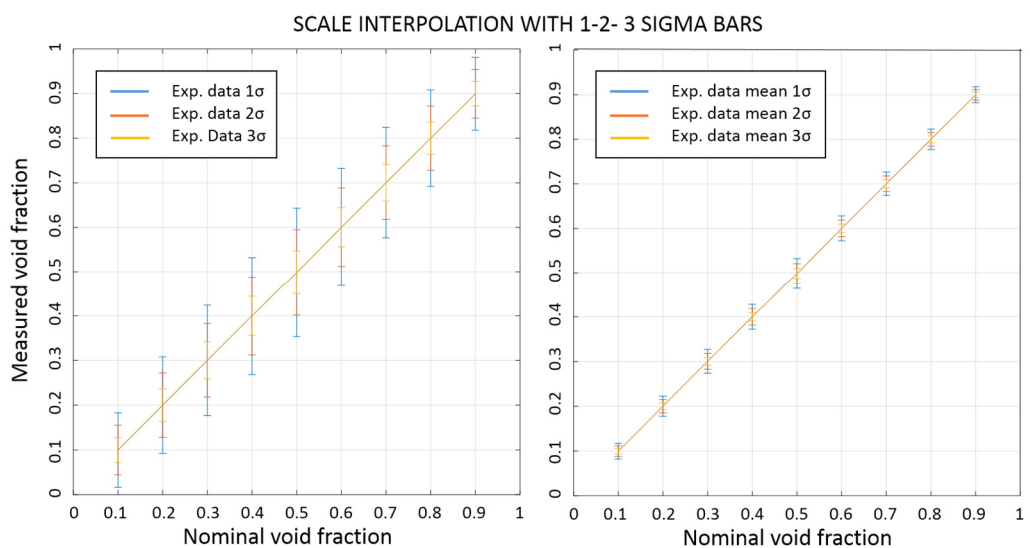


Figure 4-19 Void fraction calibration scale with 3-sigma bars

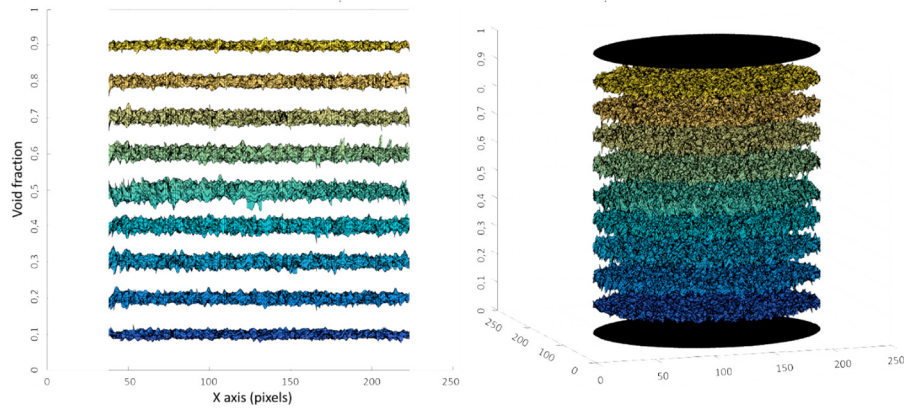


Figure 4-20 Visual representation of the created calibration scale: it can be noted that vapour fractions which are farther from the reference calibration dataset with 0 and 1 void fraction present more uncertainty.

4.4 EXPERIMENTAL RESULTS

Numerous X-ray tomographies were produced of the injection channel while cavitating diesel fuel flow was present inside to analyse the locations where cavitation was present. Table 4-5 presents the experimental conditions evaluated.

	Range	Experimental parameters				
Experiment no.		1	2	3	4	5
Needle lift [mm]	0.5 ; 1 ; 2	0.5	1	1	1	2
Pin [bar]	10-60	30	42	17	45	25
Pout [bar]	5-20	9.7	13.5	7	18	10
Flow rate [l/min]	14-30	15.5	23.5	14.7	23.5	20
CN	0.8 – 3.8	2.1	2.1	1.5	1.5	1.5
Re	30k – 67k	36,500	55,500	34,600	55,500	47,000
Cd	0.5 – 0.78	0.52	0.66	0.7	0.7	0.78
T [°C]	40 +/- 0.5					

Table 4-5 Experimental conditions tested.

Before collecting microCT experimental data, shadowgraphy visualizations were performed in the same experimental conditions utilizing the transparent nozzle to picture cavitation locations with a traditional imaging technique. The high speed shadowgraphy acquisitions were then post-processed to produce statistical information about the topology of cavitation structures to produce for each set, consisting of 80k images acquired over 1 second, a mean shadowgraphy image, giving information about the channel

locations where cavitation is present for most of the time, and a standard deviation image, which reflects channel locations where cavitation structures are only transiently present.

These images were then compared to images produced utilizing microCT results to assess the plausibility of the latter ones and, most interesting, to extend the assessed plausibility to the three dimensionalities of the microCT results, which is a peculiarity of the tomographic technique. In the following figures, shadowgraphy pictures originated by the light extinction mechanism, will be visually compared to images produced processing microCT results to obtain quantitative vapour fraction measurements: this can be considered plausible if we consider that locations which exhibit vapour fractions higher than 0,1 correspond to locations where cavitation is present steadily and therefore extinct light in the shadowgraphy pictures. Figure 4-21 presents the results, for experimental condition no.2 reported in the table, of the analysis on the shadowgraphy images. Specifically, from top to bottom, it presents a sample shadowgraphy image, the mean image of the full image set and the relative standard deviation image, calculated as the mean standard deviation of each image with respect to the mean of the full set.

The top shadowgraphy image presents a dark area inside the injection channel which denotes cavitation structures presence, while the brighter area locates the only liquid presence across the injection channel. As it can be seen high-speed shadowgraphy is able to almost freeze cavitation structures permitting their precise localization.

The incoming flow enters the channel from left to right: this is understandable from the main part of the dark area to be in the left part of the channel, moreover the bottom side of the channel is darker than the upper one due to the flow being forced to enter the orifice from this side from the asymmetrical injection sac volume and needle, promoting cavitation at the bottom entrance edge. Due to the selected experimental conditions (Flow rate 23.5 l/min, Re 55k, C.N. 2.1) cavitation structures are present in most part of the channel, identifying this as a high cavitation case.

The mean shadowgraphy image confirms that for the total duration of the experiment, cavitation is present in most part of the injection channel: the mean image wide red area is the area where cavitation is detected to be present for more than 90% of the acquisition time.

The standard deviation image instead reveals the locations of the more transient cavitation: for the analyzed case, these can be found before the channel entrance, caused by very intermittent and randomly present string cavitation going from the needle surface to the channel entrance, in the middle-up part of the channel, being caused by top channel cavitation collapse, and upstream the exit from the channel central axis up, being caused by central and bottom main cavitation structures collapse (bubble cloud shedding mechanism already reported by [106]-[108]).

A direct visual comparison, visible in Figure 4-22, of the shadowgraphy results with the microCT results can be done producing a vertical plane integration of the microCT calculated vapour fractions multiplied for the pixel size to retrieve the corresponding length of the vapour passed through by an imaginary ray going through the injection channel from side to side. Areas where vapour fraction are more present, meaning that they have higher depth of vapour considering the selected projection direction, will correspond to an area in the shadowgraphy where there is more probability to have steady light extinction, resulting is a dark area. presents the same mean and standard deviation images presented before but with overlay of the contour of the microCT vapour fraction surface having a value higher than 200 μm .

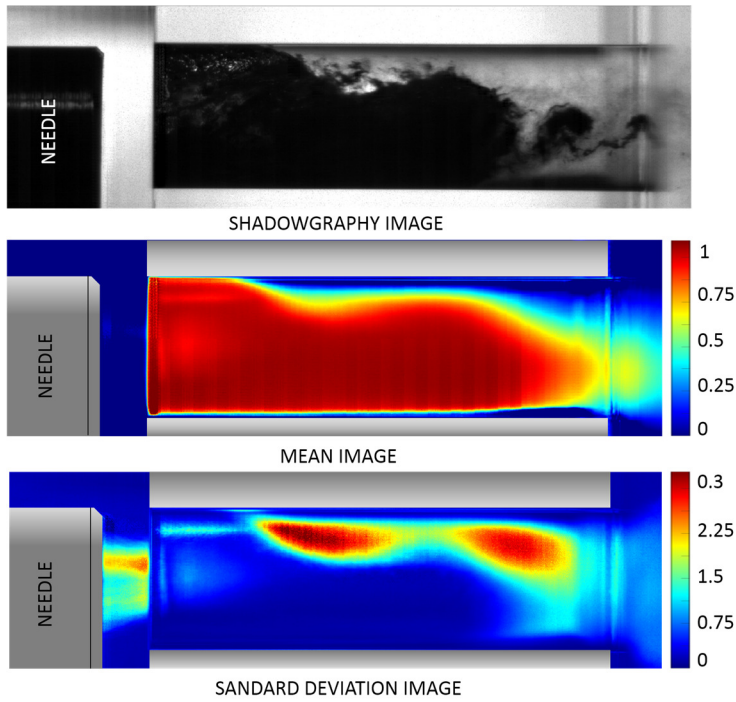


Figure 4-21 Top: high speed shadowgraphy picture of experimental conditions of experiment no.2. Middle: and bottom: Calculated mean and standard deviation images.

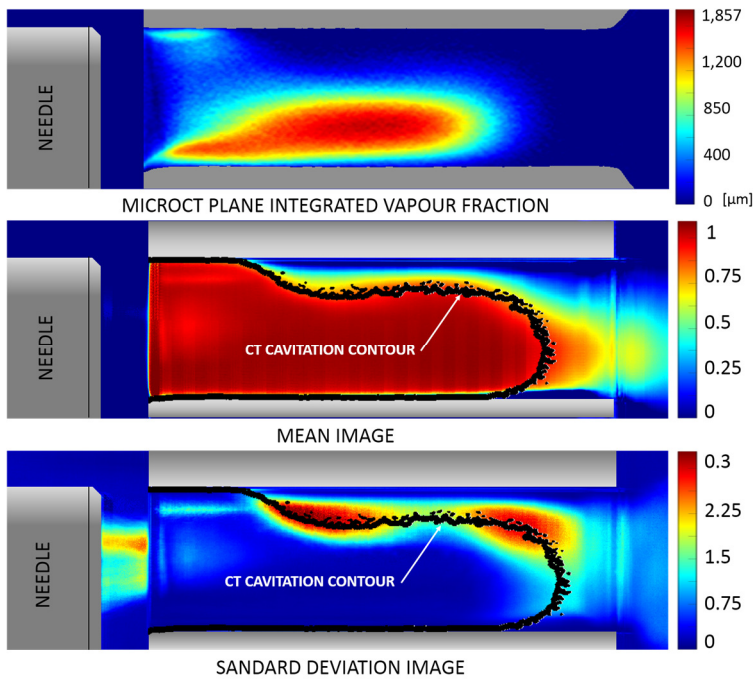


Figure 4-22 Top – Vertical plane integration of the calculated void fractions multiplied by pixel dimension to retrieve a void fraction thickness in the direction perpendicular to the integration plane. Middle -overlay of the shadowgraphy mean image displayed in Figure 4-21 with the contour of the area presenting more than 25 μm of vapour thickness in the previous image. Bottom – same overlay presented before but with the standard deviation image instead of the mean image. All images refer to experiment no. 2.

Especially in the case of the mean shadowgraphy image, the microCT calculated contour is very well overlapped with the contour of the shadowgraphy image presenting a value higher than 0.9. This means that microCT reconstructions can detect locations where cavitation is present for most of the time, while it is not able to detect the areas of transient cavitation. Moreover, from a first consideration of the shadowgraphy results it could be inferred that cavitation occupies all the injection volume while this is not since in this case the coefficient of discharge calculated for the experimental conditions utilized would be much lower than the 0.66 obtained value. The main drawback of shadowgraphy, while being a very sensitive method to study cavitation transient behavior, is that it is not able to see through cavitation but only to picture it in 2D from an outside point of view. Here microCT plays an important role in supporting cavitation studies adding the possibility to detect the 3D geometry of cavitation structures and producing quantitative vapor fraction measurements for each reconstructed volume location. Figure 4-23 presents the 3D reconstruction of the injection channel produced by microCT. From the top left image, a $\frac{3}{4}$ view of the inside channel volume only false colored to represent vapor fractions between 0.05 and 0.95, it is clear the impression given by shadowgraphy of a channel filled with cavitation is false and caused by cavitation starting the inlet of the injection channel as a full ring. The second image of the Figure 4-23, top row-right position, is a front view of the same rendering which confirms the presence of a cavitation ring at the entrance of the channel, green area and a 2D channel area interested by cavitation of almost 90%. The bottom row presents a cross cut view of the reconstructed volume to highlight with added shadows the shape of the initial cavitation ring which creates a neck at the channel entrance and that develops in a single cavitation structure afterwards while entering the channel.

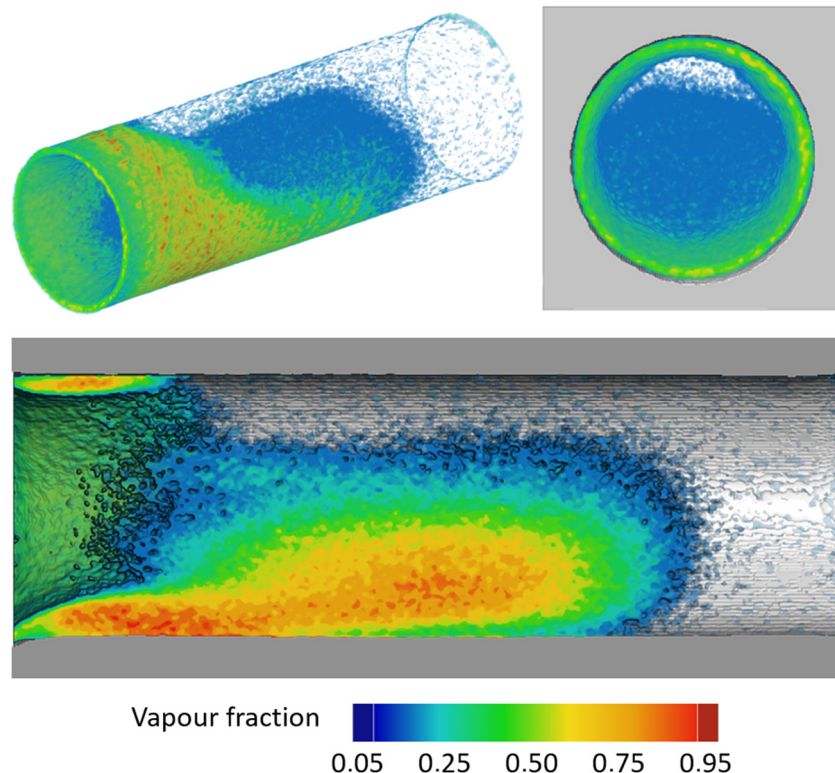


Figure 4-23 Top-left: 3D rendering of the injection channel volume reconstructed by microCT with liquid fraction rendered transparent. Top-right: Front view of the channel entrance. Bottom cross cut view of the injection channel with shadows to reveal three dimensionalities of the cavitation structures. All images refer to experiment no.2.

A further comparison of the already presented standard deviation image from shadowgraphy and the cross-cut view of the channel volume reconstructed by microCT has revealed a possible correlation that has still to be proved yet between the string, or vortex, like structures detected by high speed shadowgraphy and the sting like structure recorded in the microCT image. Figure 4-24 graphically supports this thesis showing in the top row a high speed shadowgraphy image where the very transient and unstable phenomenon of sting like, or vortex, cavitation is visible.

A string like cavitation is a structure formed by a core of vapour appearing as a dark tube in the shadowgraphy image; this phenomenon has an average lifetime of only 25 to 50 μs and is therefore only observable with high speed imaging techniques. The second image is the standard deviation calculation of the full shadowgraphy dataset, 1 s. duration, where the sting like cavitation is clearly pictured before the injection channel entrance thanks to its very unsteady nature. The third image presents again the microCT volume cross cut where the large string like structure is highlighted and found to have the same position of the string like structures observed in the previous two images.

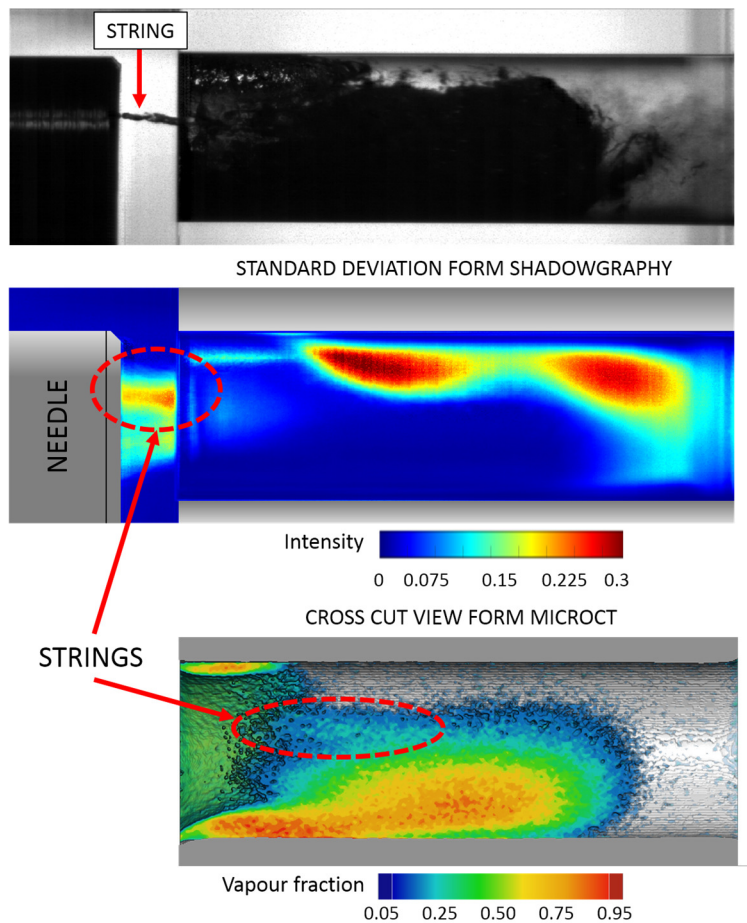


Figure 4-24 Top: shadowgraphy picture revealing the string like vortex between the needle tip and the channel entrance. **Middle:** standard deviation image revealing the localization of the string like vortices. **Bottom:** cross cut view of microCT reconstructed volume presenting cavitation structures which may be connected to the presence of string like vortices detected by the shadowgraphy images. All images refer to experiment no. 2.

A more in-depth analysis of cavitation geometry along the injection channel paired with the information of its localized vapour fraction is presented in Figure 4-25 illustrating a series of volume cross sections perpendicular to the injection axis separated one from the other by a fixed distance of 600 μm .

In section no 1 cavitation appears to be present as a green ring on the edge of the injection channel since its vapour fraction is already as high as 0.5. Section no.2 and 3 reveals that the cavitation ring rapidly increases as an attached sheet of vapour which increases its thickness reaching also vapour fractions as high as 0.95 which means that cavitation is present for the complete duration of the experiment. From section no.4 to section no.6 the vapour fraction value at the top of the injection channel diminishes rapidly to become negligible because of the different flow velocities and turbulence caused by the asymmetric needle and non-axial injection channel. The same sections denote a slight asymmetry in the cavitation structures even for the middle vertical axis of the section image. From section no.7 to section no.12, cavitation can be described as a detached structure filling the bottom half of the injection channel up to almost 80% of the channel length as depicted further after by section from no.8 to 15 which sees complete cavitation collapse and closure. A peculiar experimental case which has demonstrated the usefulness of microCT tomographic reconstruction over the more traditional shadowgraphy technique is case no. 1 of experimental condition which was not possible at all to investigate with the aid of shadowgraphy because the channel was completely full of cavitation in its middle part, which prevented any light to pass the test model. On the other hand, microCT provided reconstruction visible in Figure 4-26 which can describe the high cavitation situation proper of the mentioned experimental condition.

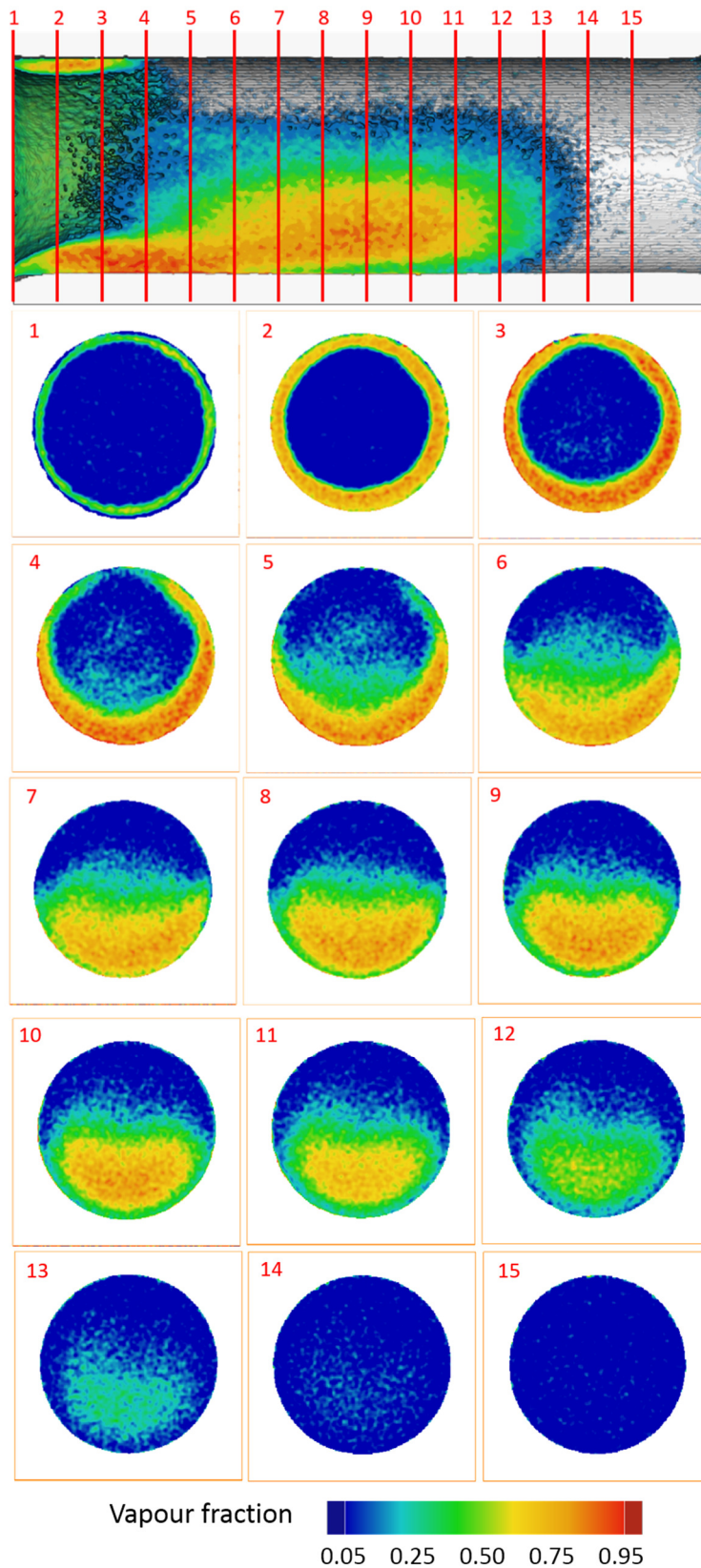


Figure 4-25 (1 of 2) Top: cross cut view of the MicroCT injection channel reconstructed volume presenting a red line every 600 μm . Following numbered images: sections perpendicular to the channel axis produced in the positions located by the previously mentioned red lines. All images refer to experiment no.2.

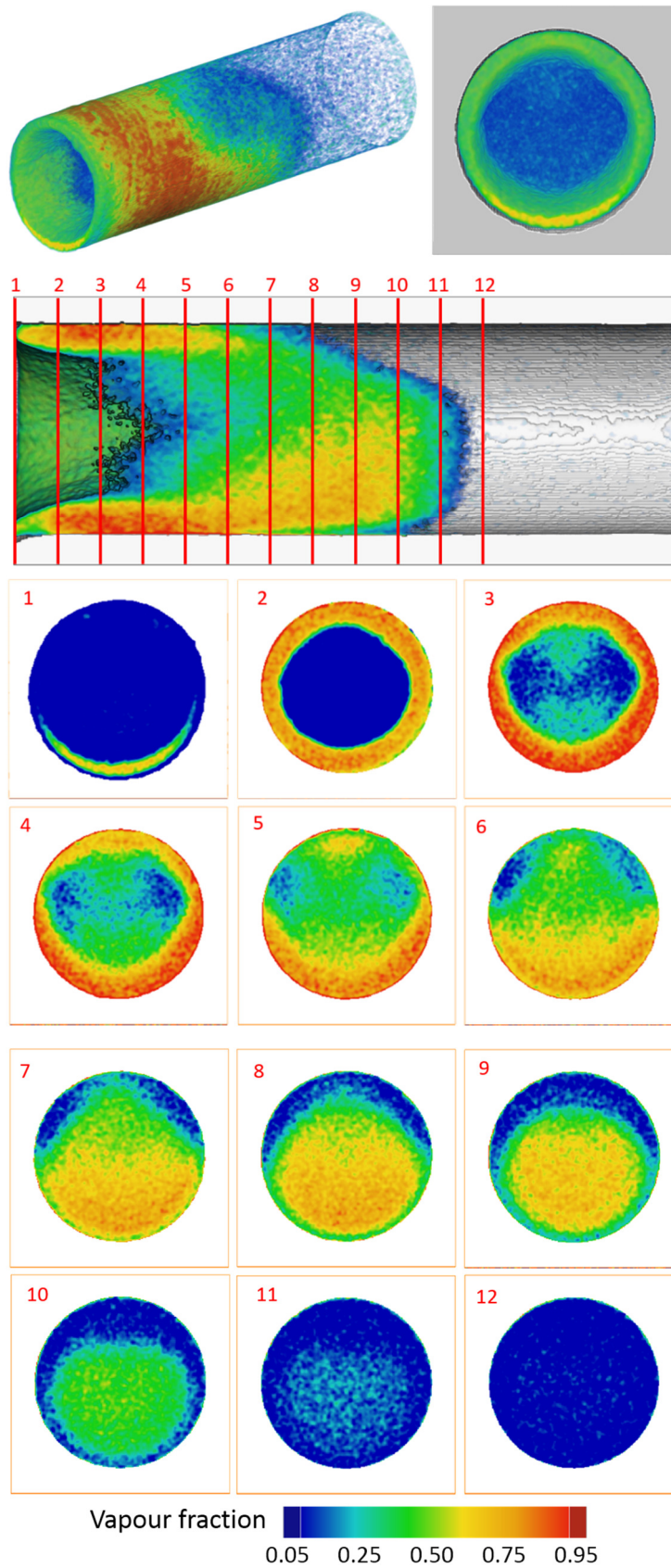


Figure 4-26 (1 of 2) Top: cross cut view of the MicroCT injection channel reconstructed volume presenting a red line every 600 μm . Following numbered images: sections perpendicular to the channel axis produced in the positions located by the previously mentioned red lines. All images refer to experiment no.2.

**NEXT PAGES CONTAIN FIGURES PRESENTING THE SAME RESULTS ILLUSTRATED
FOR EXPERIMENT NO.2 PRODUCED ALSO FOR THE OTHER SETS AS REFERENCE
ALONG WITH SOME USEFUL SUMMARY IMAGES.**

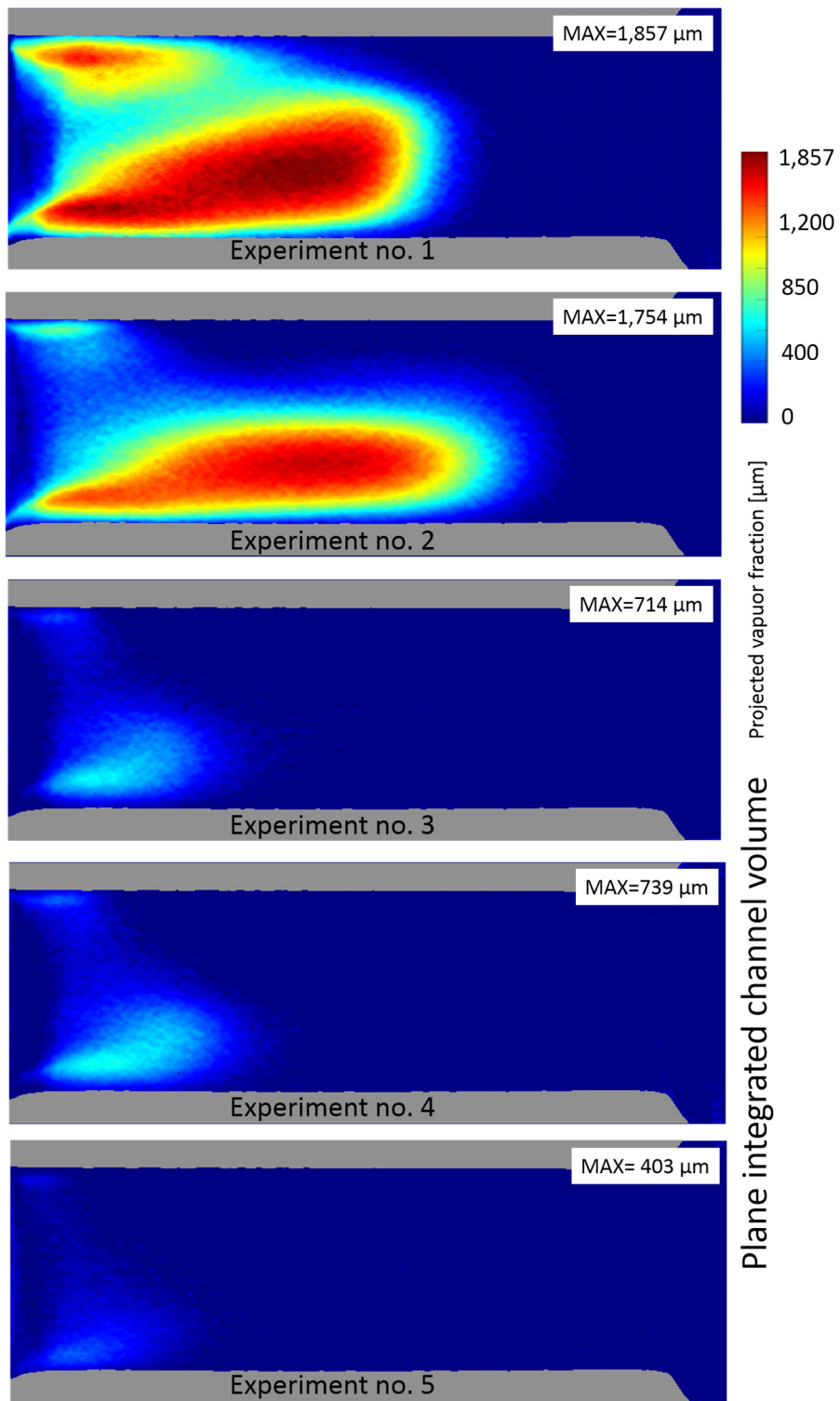


Figure 4-26 Plane integrated images calculated for all experiments

Experiment no. 1
Shadowgraphy picture not available due to no light transmitted through the test chamber for this experimental conditions.

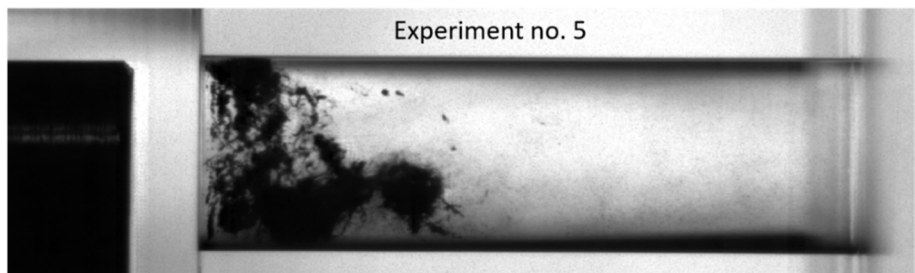
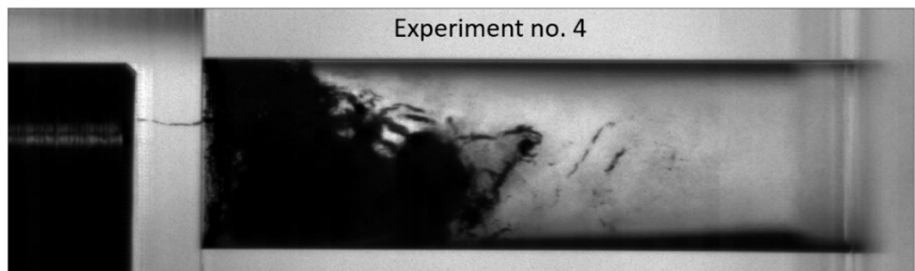
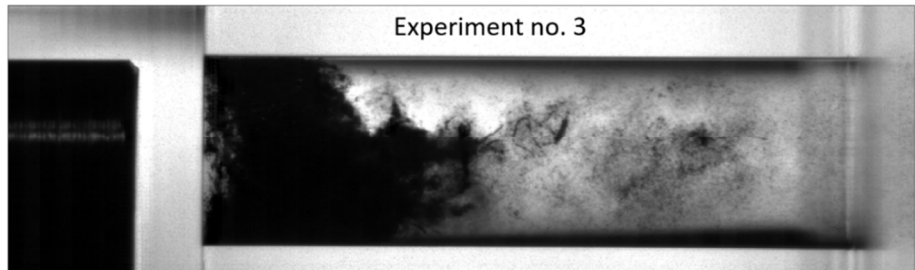
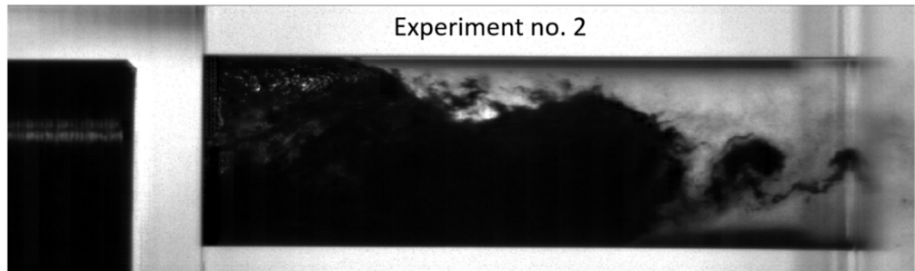


Figure 4-27 Single shot sample shadowgraphy pictures for all experiments

Experiment no. 1
Shadowgraphy picture not available due to no light transmitted through the test chamber for this experimental conditions.

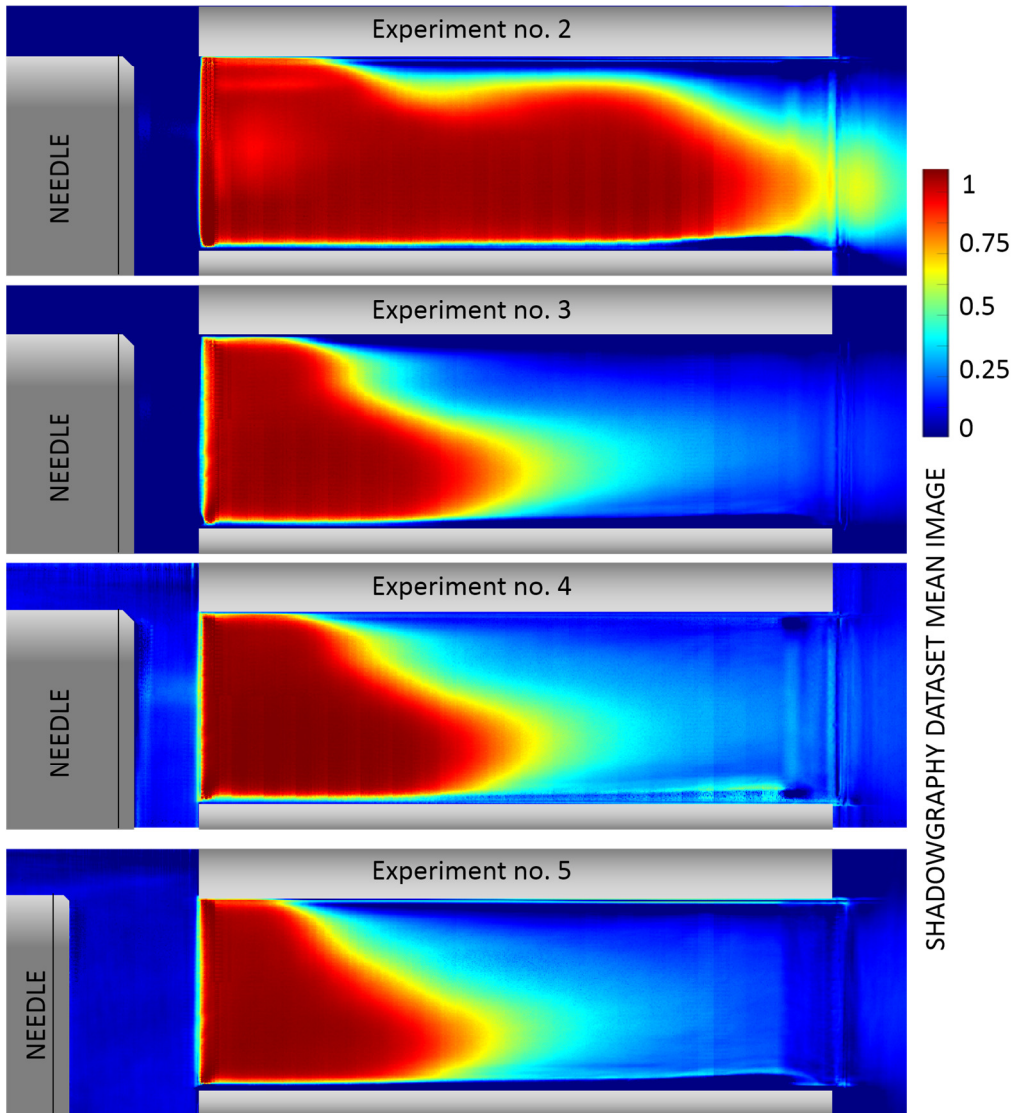


Figure 4-28 Calculated mean image for each experimental shadowgraphy dataset.

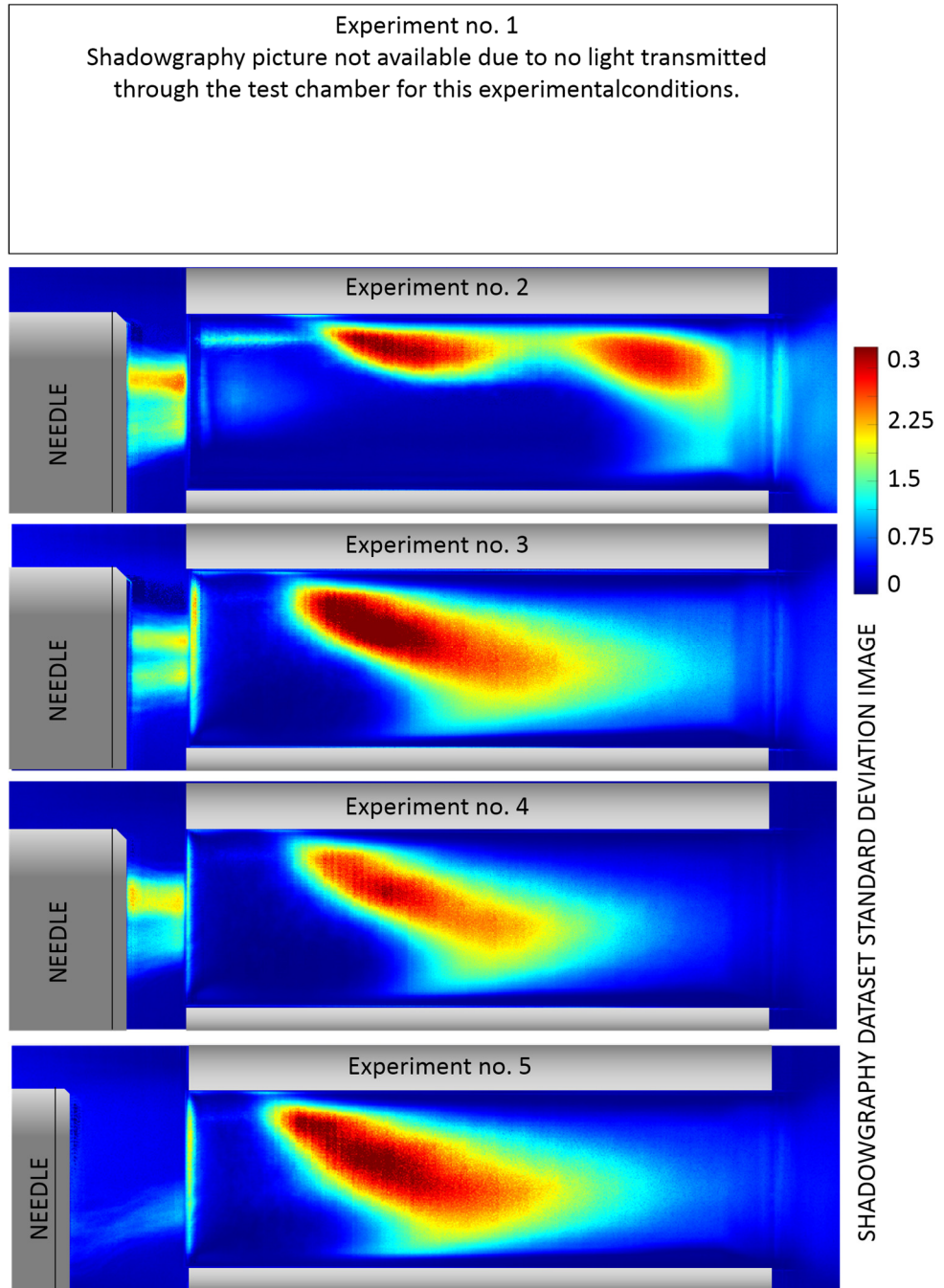


Figure 4-29 Calculated standard deviation from the mean image for each experimental shadowgraphy dataset.

Experiment no. 3

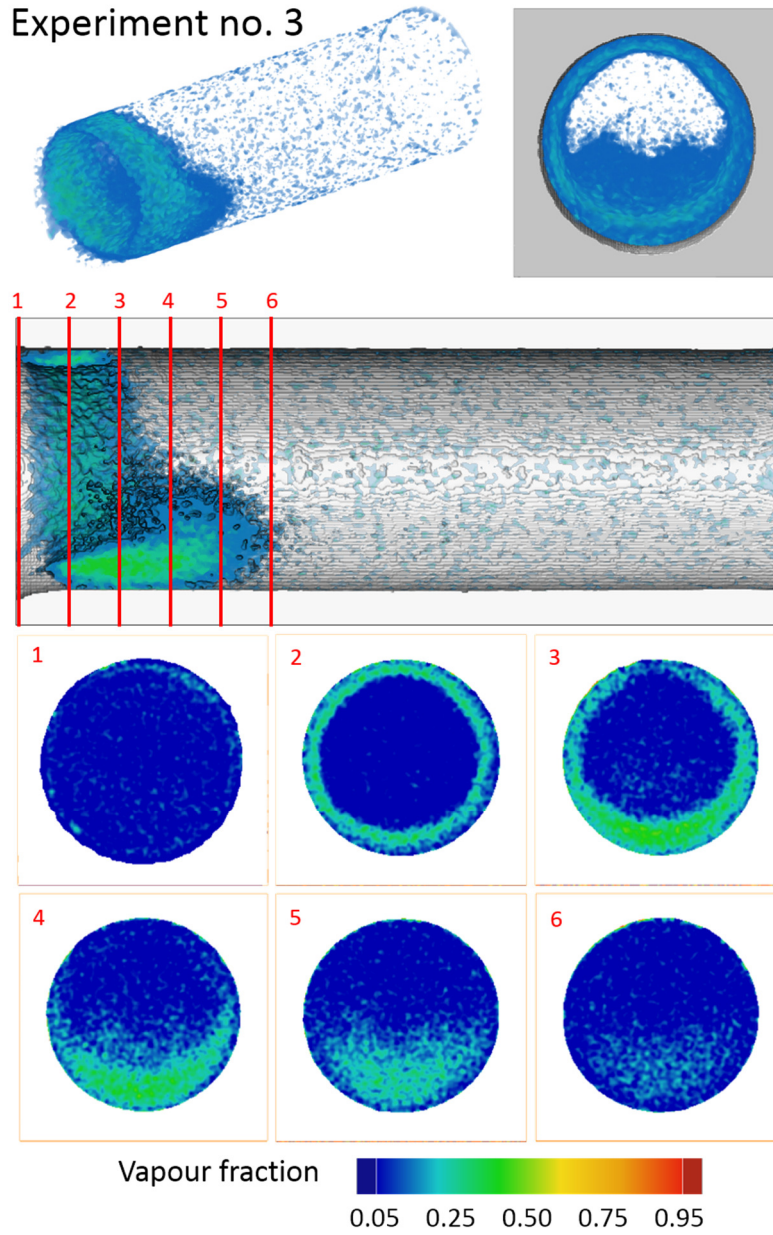


Figure 4-30 3D rendering, front channel view and axial sections for experiment no. 3

Experiment no. 4

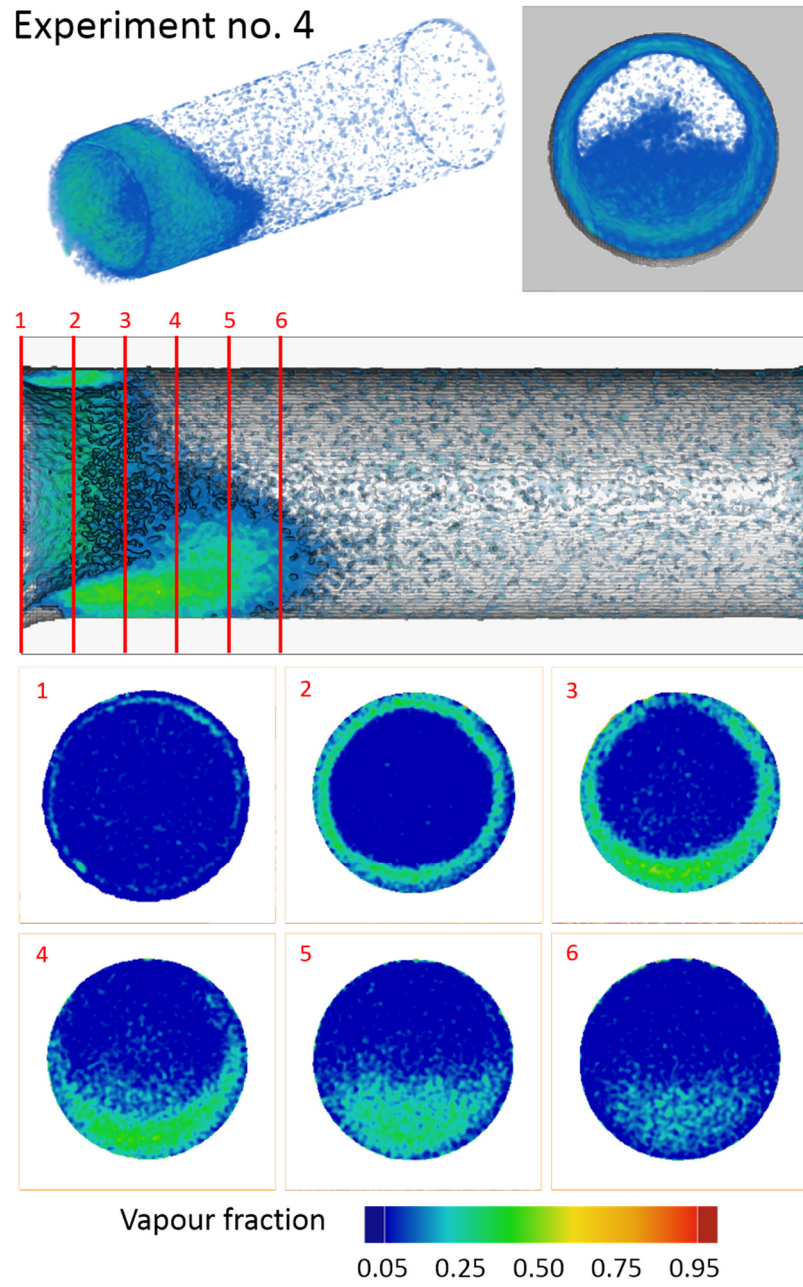


Figure 4-31 3D rendering, front channel view and axial sections for experiment no. 4

Experiment no. 5

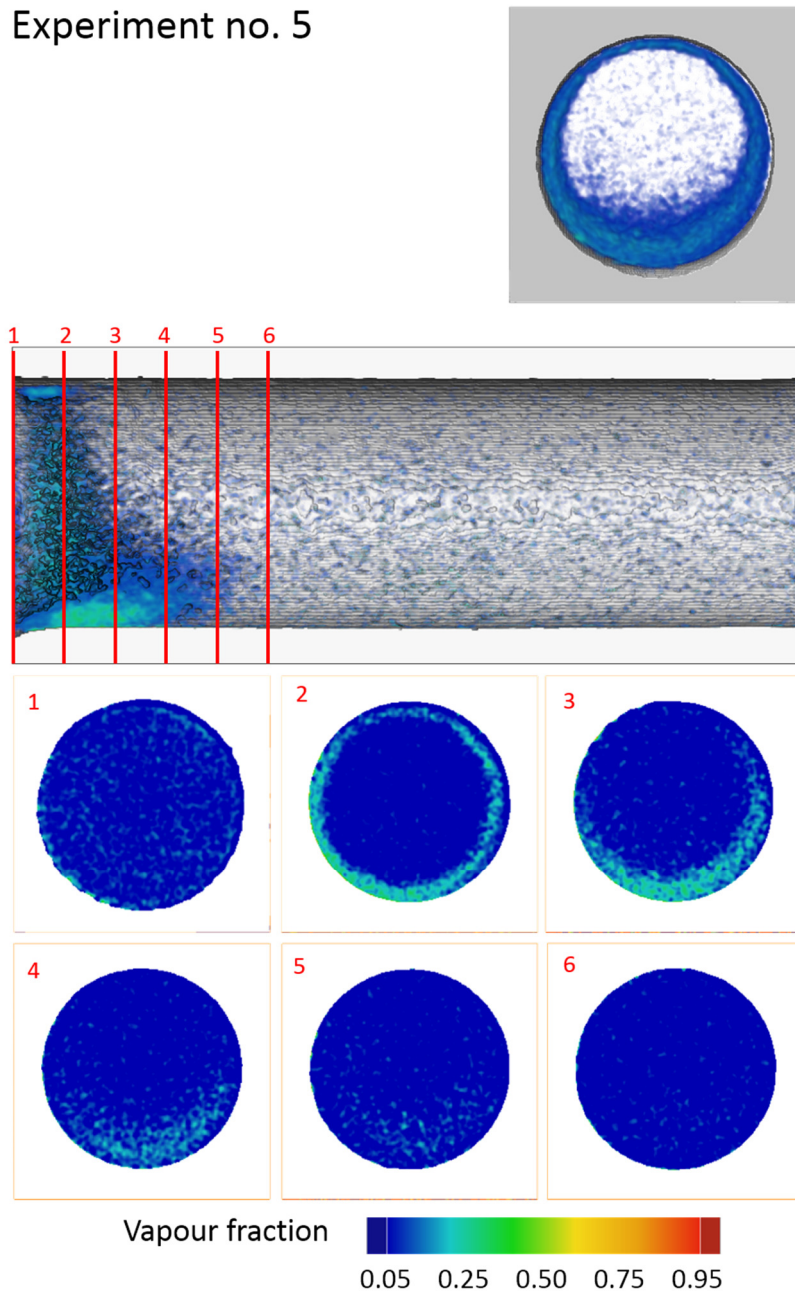


Figure 4-32 3D rendering, front channel view and axial sections for experiment no. 5

CONCLUSIONS

The aim of this thesis was to design and test novel experimental set-ups for a laboratory X-ray microtomographic machine to evaluate its applicability to investigating at the microscale complex geometries and multiphase interfaces.

To make this real the microCT machine was used to:

1. Reconstruct the internal geometry of commonly utilized automotive diesel injectors with injection channels diameters in the order of 150 μm : specific machine and acquisition set-ups were designed and tested and dedicated calibration and result analysis procedures were put in place.
2. Study in 3D the liquid-gas-solid equilibrium state of liquid drop resting on a surface: three differently patterned surfaces have used to determine the drop equilibrium shape to quantitatively study its multiphase interface with the substrate.
3. Investigate multiphase flows characterized by cavitation: a scaled-up injection model which simulates diesel flow in real diesel injectors was designed to purposely fit the X-ray microtomography technique. A novel technique comprehending machine set-up, image analysis and calibration of the results to obtain quantitative vapor fraction measurements was conceived and successfully tested. Moreover, microtomography was used to correlate cavitation presence and injection channel erosion.

RECOMMENDATIONS FOR FUTURE WORK

After the completion of my research period, all the applications of X-ray microtomography pioneered are still being used and improved by the research group. The following are my recommendations for future work that have been conceived during that period, of course most of them have been realized in collaboration with the other staff of the mentioned research groups.

Chapter 2 - Applications to complex geometries (thermal-fluid dynamics)”

The anti-evaporation chamber designed and utilised is only able of slowing down the drop evaporation but does not eliminate it since it is a passive equipment. The slower liquid evaporation obtained by its usage, grants the possibility to use longer times for the tomographic acquisition, resulting in higher single radiography quality and higher number of views that can be acquired to improve reconstruction resolution. However, a considerable step forward would comprehend the design and usage of a sample climatic chamber able of fine controlling the inner volume temperature and humidity, to almost cancel out drop evaporation. The use of such a chamber would permit the drop to be almost still during tomographic acquisition permitting acquisition times and number of views to be selected to obtain best reconstruction results. The need for such an equipment would permit to study even highly evaporating liquids that are now impossible to scan utilising just the passive anti-evaporation chamber. The expected result of the proposed improvement has been tested scanning an almost non- evaporating non-Newtonian liquid, an amalgam mainly constituted of mercury, with best acquisition set-up (single slice acquisition time and number views) obtaining results equal to the case of a static sample. A further very interesting application of the technique can be to employ it to study free or induced evaporation calculating local and global mass transfer rates around arbitrary shaped particles by analysis of sample volume before and after evaporation. The following images present the amalgam reconstruction results.

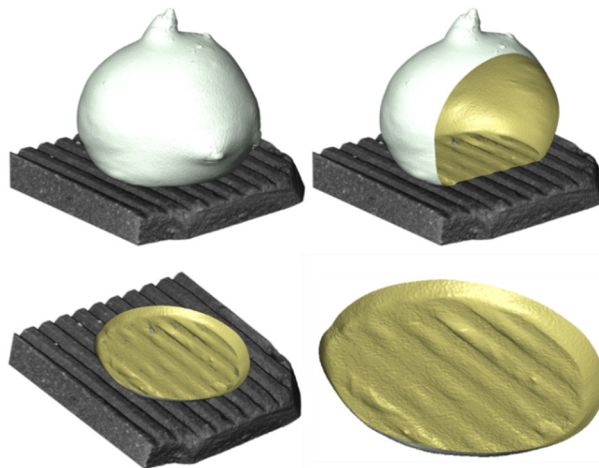


Figure 33 Top-left: 3D rendering of the drop of Hg based amalgam deposited on the patterned record surface. Top right: cut view of the amalgam surface to reveal its inside. Bottom-left: cut view parallel to the surface of the amalgam drop to reveal only its bottom part which interacts with the surface. Bottom-right: close up of the only bottom of the amalgam.

This can be done using the suggested climatic chamber to stop, during the tomographic acquisition, sample evaporation, and removing it between one acquisition and the other to let the sample evaporate before acquiring the second tomography. The proposed application has already been tested scanning a sublimating solid, a sphere made of camphor, obtaining the possibility to measure volume differences due to free evaporation as pictured in the following figure.

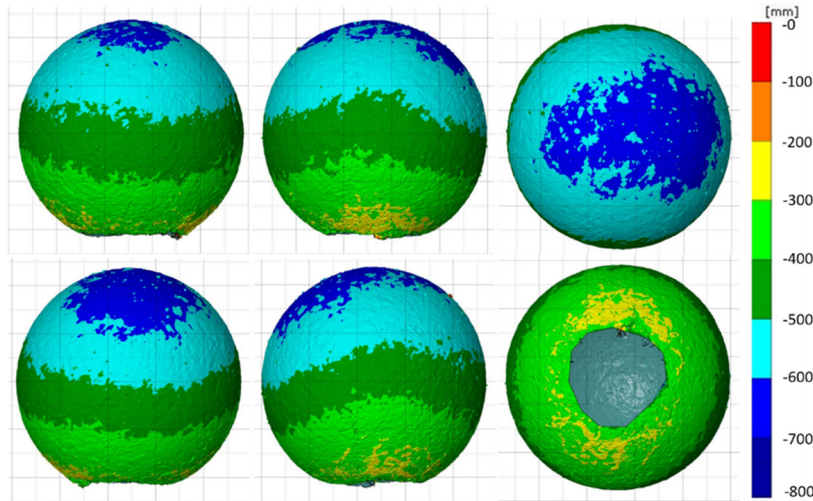


Figure 2 From left to right and from top to bottom: six views of the camphor sphere volume after evaporation presenting areas of different evaporation, the four side views are view at angles 0°, 90°, 180° and 270°, while the other two are the top and bottom view where the later one is the one where the surface presents the hole due to the presence of a supporting pin during tomographic acquisition that has been eliminated for clarity of representation.

This application has already produced the following paper from the respective authors:

Maurizio Santini, Fest-Santini Stephanie, and Foltyn Patrick.

“On the local mass transfer rates around arbitrary shaped particles calculated by X-ray computed microtomography: Prospective for a novel experimental technique.”

International Communications in Heat and Mass Transfer, 79:135–139, 2016.

Chapter 3 - Applications to complex geometries (real injectors + test rig model)

The number of injectors scanned after the completion of my research work has been considerable, producing many different injector nozzle internal geometries that can be used for research purposes. To assess further the precision of the reconstructed volumes, I would recommend testing some of them against silicone moulds of their inner volumes, that can be produced and afterwards measured with both coordinate measuring machines (CMMs), to have a standard measuring method for comparison and microCT. In case of microCT reconstruction, the reconstruction of the silicon mould won't suffer from the beam hardening which is peculiar of metal objects, therefore will produce a volume reconstruction possibly less influenced by post acquisition corrections.

The possibility to use at the same time microCT for both quantification of cavitation induced erosion and analysis of cavitation structures through the knowledge its mean void fraction values, grants the possibility to correlate precisely these two-information since they are acquired at the same time. The proposed sample

erosion analysis has been produced utilising data produced in different days, making it difficult to geometrically correlate data, since the rig has been disassembled and reassembled between tests, necessitating to realign for calculation purposes the reconstructed volumes. The recommendation to overtake this unnecessary operation would be to provide the rig with at least three reference points placed outside the interesting area that can be used as alignment references.

Chapter 4 - Applications to multiphase flow – cavitation

The use of a laboratory X-ray source for quantitative measurements of cavitating flows void fractions has produced interesting results. However, the obtained accuracy of calculated void fractions must be improved by increasing the quality of the reconstructed volume. This requires improving both the quality of the single radiographic images, reducing signal to noise ratio, and acquire more angular views within at least the same time period.

To improve the accuracy of void fraction measurements I would suggest to:

- Reduce material thickness in the X-ray path if used pressures are lower than expected ones:
Maximum inlet pressure used during experiments was lower than maximum pressure planned to be used at design stage (100 bar) since even values around 50 bar produced high cavitation presence. This means that the thickness of the model could be reduced for future experiments to reduce the absorption of X-rays by the sample, improving image contrast.
- Select an X-ray target material with characteristic peaks at energies lower than tungsten (W):
A target made of Molybdenum would have characteristic peaks (K-alpha) at 17.9 keV and (K-beta) at 19.5 keV. This would improve X-ray flux at low energies, which are the ones that are more prone to interact with “soft” matter as diesel is, if compared to the used tungsten target since in this case the characteristic peaks could be used to improve flux rather than having to be filtered out as done for the tungsten target due to their too high energy. The use at the same time of a suitable Molybdenum filter would cut out the part of the spectrum higher than 20 keV, making the X-ray spectrum more monochromatic.
- Match the thickness of the target with desired tomographic resolution:
The used target was 2 μm thick, this has granted a high resolution for the geometrical reconstruction of the sample model, permitting to evidence and localize injection channel erosion due to cavitation, however it has also diminished the available flux for density measurements due to its lower value of maximum current, proportional to the flux, that was possible to use if compared to a thicker target.
A thicker target would permit increasing the X-ray flux since it will be able to sustain more current at the cost of reducing image resolution; this would therefore be beneficial for density measurements, whose resolution was about 15 μm , very far from the used 2 μm , but detrimental for geometrical reconstruction. The use of two different targets should be carefully evaluated.
- Increase X-ray detector image resolution:
The use of a higher resolution X-ray detector with 16-bit image depth should be evaluated to improve image contrast and reduce signal to noise ratio.
- Be able to measure the true X-ray spectrum:

Rather than using simulations to make assumptions of the emitted X-ray spectrum and the same spectrum after filtration, I would suggest equipping the research group with a suitable spectrum analyser. If this can't be done, more in-depth knowledge of the simulation software should be acquired.

- Provide temperature control for X-ray source/detector and cabinet:

The improvement of temperature stability of X-ray source, X-ray detector and X-ray machine cabinet, would permit to plan longer acquisitions without the need to stabilize the single components temperatures with long warm-ups before their usage. Moreover, it will improve the repeatability of conditions especially in case of dimensional measurements.

The research group is considering all the aforementioned improvements; however, tests have been planned to use a synchrotron light source to leverage all the benefits that come from the use of a quasi-monochromatic X-ray source for density measurements. The use of a synchrotron however can't be considered for repetitive or long tests, however it can provide trustable data for selected cases that can be afterwards used as references, and even calibration, for the experimental tests produced with the laboratory X-ray source.

LIST OF PUBLICATIONS

The results presented in this thesis have been also used to produce the following papers in cooperation with the other researcher mentioned as stated by each paper authors list:

Journal papers

Lorenzi Massimo, Mitroglou Nicholas, Santini Maurizio, and Gavaises Manolis.

“Novel experimental technique for 3D investigation of high-speed cavitating diesel fuel flows by X-ray micro computed tomography”. *Review of Scientific Instruments*, 88:033706–1–033706–11, 2017.

Koukouvinis Phoevos, Mitroglou Nicholas, Gavaises Manolis, **Lorenzi Massimo**, and Santini Maurizio.

“Quantitative predictions of cavitation presence and erosion-prone locations in a high-pressure cavitation test rig”. *Journal of Fluid Mechanics*, 819:21–57, 2017

Mitroglou Nicholas, **Lorenzi Massimo**, Santini Maurizio and Gavaises Manolis.

“Application of X-ray microcomputed tomography on highspeed cavitating diesel fuel flows”. *Experiments in Fluids*, 57:1–14, 2016.

Santini Maurizio, Guilizzoni Manfredo, **Lorenzi Massimo**, Plamen Atanassov, Marsili Enrico, Fest-Santini Stephanie, Cristiani Pierangela, and Santoro Carlo.

“Three-dimensional X-ray microcomputed tomography of carbonates and biofilm on operated cathode in single chamber microbial fuel cell” *Biointerphases*, 10:1–9, 2015.

Santini Maurizio., Guilizzoni Manfredo, Fest-Santini Stephanie, and **Lorenzi Massimo**.

“A novel technique for investigation of complete and partial anisotropic wetting on structured surface by X-ray microtomography” *Review of Scientific Instruments*, 86:1–9, 2015.

Conference papers

Mitroglou Nicholas, **Lorenzi Massimo**, Santini Maurizio, Gavaises Manolis, and Assanis Dennis.

“Application of cone-beam micro-CT on high-speed diesel flows and quantitative cavitation measurements” *Journal of Physics. Conference series*, 656:1–4, 2015.

Guilizzoni Manfredo, Santini Maurizio, **Lorenzi Massimo**, Knisel Viola, and Fest-Santini Stephanie.

“Micro computed tomography and CFD simulation of drop deposition on gas diffusion layers” *Journal of Physics. Conference series*, 547:1–12, 2014.

REFERENCES

- [1] K. Hong and R. Webb, "Performance of dehumidifying heat exchangers with and without wetting coatings," *Transactions-American Society of Mechanical Engineers Journal of Heat Transfer*, vol. 121, pp. 1018-1026, 1999.
- [2] A. Ulman, "Wetting studies of molecularly engineered surfaces," *Thin Solid Films*, vol. 273, (1-2), pp. 48-53, 1996.
- [3] N. R. Morrow and G. Mason, "Recovery of oil by spontaneous imbibition," *Current Opinion in Colloid & Interface Science*, vol. 6, (4), pp. 321-337, 2001. DOI: [http://dx.doi.org/10.1016/S1359-0294\(01\)00100-5](http://dx.doi.org/10.1016/S1359-0294(01)00100-5).
- [4] C. Zhang and M. Fujii, "Influence of Wettability and Mechanical Properties on Tribological Performance of DLC Coatings under Water Lubrication," *Journal of Surface Engineered Materials and Advanced Technology*, vol. 5, (03), pp. 110, 2015.
- [5] X. Yao, Y. Song and L. Jiang, "Applications of Bio-Inspired Special Wettable Surfaces," *Adv Mater*, vol. 23, (6), pp. 719-734, 2011.
- [6] E. A. Favret, *Functional Properties of Bio-Inspired Surfaces: Characterization and Technological Applications*. 2009.
- [7] E. Bormashenko *et al*, "Why do pigeon feathers repel water? Hydrophobicity of pennaes, Cassie–Baxter wetting hypothesis and Cassie–Wenzel capillarity-induced wetting transition," *J. Colloid Interface Sci.*, vol. 311, (1), pp. 212-216, 2007.
- [8] A. Krishnan *et al*, "An evaluation of methods for contact angle measurement," *Colloids and Surfaces B: Biointerfaces*, vol. 43, (2), pp. 95-98, 2005. . DOI: <http://dx.doi.org/10.1016/j.colsurfb.2005.04.003>.
- [9] Y. Yuan and T. R. Lee, "Contact angle and wetting properties," in *Surface Science Techniques* Anonymous 2013, .
- [10] Y. Hung *et al*, "A simple method for measuring the superhydrophobic contact angle with high accuracy," *Rev. Sci. Instrum.*, vol. 81, (6), pp. 065105, 2010.
- [11] S. Moulinet and D. Bartolo, "Life and death of a fakir droplet: Impalement transitions on superhydrophobic surfaces," *The European Physical Journal E*, vol. 24, (3), pp. 251-260, 2007.
- [12] J. W. Chesna *et al*, "Aerial wetting contact angle measurement using confocal microscopy," *Measurement Science and Technology*, vol. 27, (12), pp. 125202, 2016.
- [13] P. Papadopoulos *et al*, "How superhydrophobicity breaks down," *Proc. Natl. Acad. Sci. U. S. A.*, vol. 110, (9), pp. 3254-3258, 2013. . DOI: [10.1073/pnas.1218673110](https://doi.org/10.1073/pnas.1218673110) [doi].
- [14] R. Payri *et al*, "Effects of nozzle geometry on direct injection diesel engine combustion process," *Applied Thermal Engineering*, vol. 29, (10), pp. 2051-2060, 2009. . DOI: <https://doi.org/10.1016/j.applthermaleng.2008.10.009>.
- [15] S. Som *et al*, "Effect of nozzle orifice geometry on spray, combustion, and emission characteristics under diesel engine conditions," *Fuel*, vol. 90, (3), pp. 1267-1276, 2011.

- [16] S. Jollet *et al*, "Comparison of experiments and numerical simulations of high pressure transparent injection nozzles," in *ILASS-Europe*, 2013, .
- [17] C. Diver *et al*, "Micro-EDM drilling of tapered holes for industrial applications," *J. Mater. Process. Technol.*, vol. 149, (1–3), pp. 296-303, 2004. . DOI: <http://doi.org/10.1016/j.jmatprotec.2003.10.064>.
- [18] C. Diver *et al*, "Improving the geometry and quality of a micro-hole fuel injection nozzle by means of hydroerosive grinding," *Proc. Inst. Mech. Eng. Pt. B: J. Eng. Manuf.*, vol. 221, (1), pp. 1-9, 2007.
- [19] V. Macián *et al*, "New technique for determination of internal geometry of a diesel nozzle with the use of silicone methodology," *Exp Tech*, vol. 27, (2), pp. 39-43, 2003.
- [20] A. J. Butcher, P. G. Aleiferis and D. Richardson, "Development of a real-size optical injector nozzle for studies of cavitation, spray formation and flash-boiling at conditions relevant to direct-injection spark-ignition engines," *International Journal of Engine Research*, vol. 14, (6), pp. 557-577, 2013.
- [21] E. Peiner, M. Balke and L. Doering, "Form measurement inside fuel injector nozzle spray holes," *Microelectronic Engineering*, vol. 86, (4), pp. 984-986, 2009.
- [22] A. L. Kastengren *et al*, "Engine combustion network (ECN): measurements of nozzle geometry and hydraulic behavior," *Atom.Sprays*, vol. 22, (12), pp. 1011-1052, 2012.
- [23] Z. Wu *et al*, "Comparisons of nozzle orifice processing methods using synchrotron X-ray micro-tomography," *Journal of Zhejiang University SCIENCE A*, vol. 13, (3), pp. 182-188, 2012.
- [24] D. Lazaro *et al*, "Metrology of steel micro-nozzles using X-ray microtomography," in *International Symposium on Digital Industrial Radiology and Computed Tomography (DIR)*, Lyon, France, 2007, .
- [25] F. E. Boas and D. Fleischmann, "CT artifacts: causes and reduction techniques," *Imaging in Medicine*, vol. 4, (2), pp. 229-240, 2012.
- [26] A. Andriotis, M. Gavaises and C. Arcoumanis, "Vortex flow and cavitation in diesel injector nozzles," *J. Fluid Mech.*, vol. 610, pp. 195-215, 2008. . DOI: 10.1017/S0022112008002668.
- [27] A. Sou, S. Hosokawa and A. Tomiyama, "Effects of cavitation in a nozzle on liquid jet atomization," *Int. J. Heat Mass Transfer*, vol. 50, (17), pp. 3575-3582, 2007.
- [28] F. Payri *et al*, "The influence of cavitation on the internal flow and the spray characteristics in diesel injection nozzles," *Fuel*, vol. 83, (4), pp. 419-431, 2004.
- [29] M. Gavaises *et al*, "Characterization of string cavitation in large-scale Diesel nozzles with tapered holes," *Physics of Fluids (1994-Present)*, vol. 21, (5), pp. 052107, 2009.
- [30] N. Mitroglou and M. Gavaises, "Mapping of cavitating flow regimes in injectors for medium/heavy duty Diesel engines," *International Journal of Engine Research*, vol. 14(6), pp. 590-605, 2013.
- [31] C. Soteriou *et al*, "The flow characteristics of high efficiency diesel nozzles with enhanced geometry holes," in *Proc. THIESEL International Conference on Thermo-and Fluid Dynamic Processes in Diesel Engines. Valencia, Spain*, 2006, .
- [32] S. A. Mäkiharju *et al*, "Time-resolved two-dimensional X-ray densitometry of a two-phase flow downstream of a ventilated cavity," *Exp. Fluids*, vol. 54, (7), pp. 1-21, 2013.
- [33] D. J. Duke *et al*, "Time-resolved X-ray tomography of gasoline direct injection sprays," *SAE*

International Journal of Engines, vol. 9, (2015-01-1873), 2015.

[34] A. Kastengren *et al*, "The 7BM beamline at the APS: a facility for time-resolved fluid dynamics measurements," *Journal of Synchrotron Radiation*, vol. 19, (4), pp. 654-657, 2012.

[35] D. Bauer, H. Chaves and C. Arcoumanis, "Measurements of void fraction distribution in cavitating pipe flow using x-ray CT," *Meas. Sci. Technol.*, vol. 23, (5), pp. 055302, 2012.

[36] B. A. Reid *et al*, "An investigation of string cavitation in a true-scale fuel injector flow geometry at high pressure," *Physics of Fluids (1994-Present)*, vol. 22, (3), pp. 031703, 2010.

[37] J. A. Seibert, "X-ray imaging physics for nuclear medicine technologists. Part 1: Basic principles of x-ray production," *J. Nucl. Med. Technol.*, vol. 32, (3), pp. 139-147, 2004. . DOI: 32/3/139 [pii].

[38] (). [CC BY-SA 3.0 (<http://creativecommons.org/licenses/by-sa/3.0/>)], via *Wikimedia Commons*.

[39] H. Demers *et al*, "Three-dimensional electron microscopy simulation with the CASINO Monte Carlo software," *Scanning*, vol. 33, (3), pp. 135-146, 2011.

[40] J. Punnoose *et al*, "Technical Note: spektr 3.0—A computational tool for x-ray spectrum modeling and analysis," *Med. Phys.*, vol. 43, (8), pp. 4711-4717, 2016.

[41] R. Nowotny, "XMuDat: Photon attenuation data on PC," *IAEA Report IAEA-NDS*, vol. 195, 1998.

[42] D. C. Creagh and J. H. Hubbell, "X-Ray Absorption (or Attenuation) Coefficients, ed. by AJC Wilson," *International Tables for Crystallography*, 1992.

[43] M. Yaffe and J. Rowlands, "X-ray detectors for digital radiography," *Phys. Med. Biol.*, vol. 42, (1), pp. 1, 1997.

[44] J. Radon, "On the determination of functions from their integral values along certain manifolds," *IEEE Trans. Med. Imaging*, vol. 5, (4), pp. 170-176, 1986.

[45] M. Lorenzi *et al*, "Novel experimental technique for 3D investigation of high-speed cavitating diesel fuel flows by X-ray micro computed tomography," *Rev. Sci. Instrum.*, vol. 88, (3), pp. 033706, 2017.

[46] L. Feldkamp, L. Davis and J. Kress, "Practical cone-beam algorithm," *Josa A*, vol. 1, (6), pp. 612-619, 1984.

[47] A. C. Konstantinidis *et al*, "The Dexela 2923 CMOS X-ray detector: A flat panel detector based on CMOS active pixel sensors for medical imaging applications," *Nuclear Instruments and Methods in Physics Research Section A: Accelerators, Spectrometers, Detectors and Associated Equipment*, vol. 689, pp. 12-21, 2012.

[48] J. P. Kruth *et al*, "Computed tomography for dimensional metrology," *CIRP Annals-Manufacturing Technology*, vol. 60, (2), pp. 821-842, 2011.

[49] S. Kasperl, J. Hiller and M. Krumm, "Computed tomography metrology in industrial research and development," *Materials Testing*, vol. 51, (6), pp. 405-411, 2009.

[50] A. P. Merkle and J. Gelb, "The Ascent of 3D X-ray Microscopy in the Laboratory," *Microscopy Today*, vol. 21, (02), pp. 10-15, 2013.

[51] V. Cnudde and M. N. Boone, "High-resolution X-ray computed tomography in geosciences: A review of the current technology and applications," *Earth-Sci. Rev.*, vol. 123, pp. 1-17, 2013.

- [52] J. Gui *et al*, "Investigation of the effect of tube voltage and imaging geometry on phase contrast imaging for a micro-CT system," *Nuclear Instruments and Methods in Physics Research Section A: Accelerators, Spectrometers, Detectors and Associated Equipment*, vol. 669, pp. 97-102, 2012.
- [53] M. Bartscher *et al*, "Current state of standardization in the field of dimensional computed tomography," *Measurement Science and Technology*, vol. 25, (6), pp. 064013, 2014.
- [54] P. Müller *et al*, "A study on evaluation strategies in dimensional X-ray computed tomography by estimation of measurement uncertainties," *International Journal of Metrology and Quality Engineering*, vol. 3, (02), pp. 107-115, 2012.
- [55] M. Bartscher *et al*, "Achieving traceability of industrial computed tomography," in *Key Engineering Materials*, 2010, .
- [56] W. Dewulf *et al*, "Uncertainty determination and quantification for dimensional measurements with industrial computed tomography," *CIRP Annals-Manufacturing Technology*, vol. 62, (1), pp. 535-538, 2013.
- [57] L. De Chiffre *et al*, "Industrial applications of computed tomography," *CIRP Annals-Manufacturing Technology*, vol. 63, (2), pp. 655-677, 2014.
- [58] D. Weiß, Q. Shi and C. Kuhn, "Measuring the 3D resolution of a micro-focus x-ray CT setup," in *ICT'12: Conf. on Industrial Computed Tomography*, 2012, .
- [59] ISO standardization comitee, "Photography - Electronic still picture imaging - Resolution and spatial frequency responses," *Iso 12233:2014*, 2014.
- [60] G. P, "Slant edge script - retrieved December 7th, 2016," 2012.
- [61] F. B. DE OLIVEIRA, M. BARTSCHER and U. NEUSCHAEFER-RUBE, "Analysis of Combined Probing Measurement Error and Length Measurement Error Test for Acceptance Testing in Dimensional Computed Tomography," .
- [62] B. Li, Q. Zhang and J. Li, "A novel beam hardening correction method for computed tomography," in *Complex Medical Engineering, 2007. CME 2007. IEEE/ICME International Conference On*, 2007, .
- [63] (21/12/21016). *Artifacts and partial volume effects High-Resolution X-ray Computed Tomography Facility at The University of Texas at Austin (UTCT) Department of Geological Sciences, University of Texas at Austin, Austin, TX 78712-9000*. Available: <http://www.ctlab.geo.utexas.edu/about-ct/artifacts-and-partial-volume-effects/>.
- [64] Anonymous "VGStudio MAX," *Copiright © 1997-2013 Volume Graphics GmbH*, vol. 2.2.6.80630 64bit, 2014-08-04.
- [65] T. Matsumura *et al*, "Micro fabrication on cylinder surface for control of wettability," *Journal of Manufacturing Processes*, vol. 15, (1), pp. 8-13, 2013. DOI: <http://dx.doi.org/10.1016/j.jmapro.2012.09.010>.
- [66] S. Falah Toosi *et al*, "Microfabrication of polymeric surfaces with extreme wettability using hot embossing," *Appl. Surf. Sci.*, vol. 378, pp. 426-434, 2016. DOI: <http://dx.doi.org/10.1016/j.apsusc.2016.03.116>.
- [67] M. Yamamoto *et al*, "Theoretical explanation of the lotus effect: superhydrophobic property changes

- by removal of nanostructures from the surface of a lotus leaf," *Langmuir*, vol. 31, (26), pp. 7355-7363, 2015.
- [68] Anonymous "Joris Gillis~commonswiki assumed (based on copyright claims). [Public domain], via Wikimedia Commons." .
- [69] T. Young, "An essay on the cohesion of fluids," *Philosophical Transactions of the Royal Society of London*, vol. 95, pp. 65-87, 1805.
- [70] O. Del Rio and A. Neumann, "Axisymmetric drop shape analysis: computational methods for the measurement of interfacial properties from the shape and dimensions of pendant and sessile drops," *J. Colloid Interface Sci.*, vol. 196, (2), pp. 136-147, 1997.
- [71] C. Extrand and S. I. Moon, "Contact angles of liquid drops on super hydrophobic surfaces: understanding the role of flattening of drops by gravity," *Langmuir*, vol. 26, (22), pp. 17090-17099, 2010.
- [72] R. Tadmor, "Approaches in wetting phenomena," *Soft Matter*, vol. 7, (5), pp. 1577-1580, 2011.
- [73] R. Tadmor *et al*, "Drop retention force as a function of resting time," *Langmuir*, vol. 24, (17), pp. 9370-9374, 2008.
- [74] H. Tavana *et al*, "Contact angle hysteresis on fluoropolymer surfaces," *Adv. Colloid Interface Sci.*, vol. 134-135, pp. 236-248, 2007. . DOI: <http://dx.doi.org/10.1016/j.cis.2007.04.008>.
- [75] M. E. Diaz *et al*, "Hysteresis during contact angles measurement," *J. Colloid Interface Sci.*, vol. 343, (2), pp. 574-583, 2010. . DOI: <http://dx.doi.org/10.1016/j.jcis.2009.11.055>.
- [76] R. N. Wenzel, "Resistance of solid surfaces to wetting by water," *Industrial & Engineering Chemistry*, vol. 28, (8), pp. 988-994, 1936.
- [77] A. Cassie and S. Baxter, "Wettability of porous surfaces," *Transactions of the Faraday Society*, vol. 40, pp. 546-551, 1944.
- [78] Vladsinger, "[CC BY-SA 3.0 (<http://creativecommons.org/licenses/by-sa/3.0>)], via Wikimedia Commons," .
- [79] M. Santini, M. Guilizzoni and S. Fest-Santini, "X-ray computed microtomography for drop shape analysis and contact angle measurement," *J. Colloid Interface Sci.*, vol. 409, pp. 204-210, 2013.
- [80] M. Andrew, B. Bijeljic and M. J. Blunt, "Pore-scale contact angle measurements at reservoir conditions using X-ray microtomography," *Adv. Water Resour.*, vol. 68, pp. 24-31, 2014. . DOI: <http://dx.doi.org/10.1016/j.advwatres.2014.02.014>.
- [81] K. Singh, B. Bijeljic and M. J. Blunt, "Imaging of oil layers, curvature, and contact angle in a mixed-wet and a water-wet carbonate rock," *Water Resour. Res.*, 2016.
- [82] M. Guilizzoni, "Drop shape visualization and contact angle measurement on curved surfaces," *J. Colloid Interface Sci.*, vol. 364, (1), pp. 230-236, 2011. . DOI: <http://dx.doi.org/10.1016/j.jcis.2011.08.019>.
- [83] M. Guilizzoni and G. Sotgia, "EXPERIMENTAL ANALYSIS ON THE CHARACTERISTICS OF WATER DROPS DURING EVAPORATION ON HIGH-EFFUSIVITY, MICROFINNED SURFACES,"
- [84] A. M. Vossepoel and A. W. Smeulders, "Vector code probability and metrication error in the representation of straight lines of finite length," *Computer Graphics and Image Processing*, vol. 20, (4),

pp. 347-364, 1982.

[85] M. Santini *et al*, "A novel technique for investigation of complete and partial anisotropic wetting on structured surface by X-ray microtomography," *Rev. Sci. Instrum.*, vol. 86, (2), pp. 023708, 2015.

[86] W. Dai *et al*, "A review on water balance in the membrane electrode assembly of proton exchange membrane fuel cells," *Int J Hydrogen Energy*, vol. 34, (23), pp. 9461-9478, 2009.

[87] A. Stalder *et al*, "A snake-based approach to accurate determination of both contact points and contact angles," *Colloids Surf. Physicochem. Eng. Aspects*, vol. 286, (1), pp. 92-103, 2006.

[88] W. Dewulf, Y. Tan and K. Kiekens, "Sense and non-sense of beam hardening correction in CT metrology," *CIRP Ann. Manuf. Technol.*, vol. 61, (1), pp. 495-498, 2012. DOI: <http://doi.org/10.1016/j.cirp.2012.03.013>.

[89] Y. Tan *et al*, "Beam hardening correction and its influence on the measurement accuracy and repeatability for CT dimensional metrology applications," 2012.

[90] V. Csala *et al*, "Application Benchmark of Three Micro Hole Machining Processes for Manufacturing the Nozzle of a Medical Water Jet Machine," *Acta Polytechnica Hungarica*, vol. 12, (2), pp. 53-69, 2015.

[91] P. Koukouvinis *et al*, "Quantitative predictions of cavitation presence and erosion-prone locations in a high-pressure cavitation test rig," *J. Fluid Mech.*, vol. 819, pp. 21-57, 2017.

[92] N. Mitroglou *et al*, "Instantaneous and ensemble average cavitation structures in Diesel micro-channel flow orifices," *Fuel*, vol. 116, pp. 736-742, 2014.

[93] R. Miranda *et al*, "Cavitation in a transparent real size VCO injection nozzle," *Proceedings of ICLASS, Sorrento Italy*, 2003.

[94] C. Mauger *et al*, "Shadowgraph, Schlieren and interferometry in a 2D cavitating channel flow," *Exp. Fluids*, vol. 53, (6), pp. 1895-1913, 2012.

[95] H. Roth, M. Gavaises and C. Arcoumanis, *Cavitation Initiation, its Development and Link with Flow Turbulence in Diesel Injector Nozzles*, 2002.

[96] E. Winklhofer *et al*, "Comprehensive hydraulic and flow field documentation in model throttle experiments under cavitation conditions," in *Proceedings of the ICLASS-Europe Conference, Zurich*, 2001.

[97] H. Chaves *et al*, "Experimental study of cavitation in the nozzle hole of diesel injectors using transparent nozzles," *SAE Technical Paper*, 1995.

[98] M. Blessing *et al*, "Analysis of flow and cavitation phenomena in diesel injection nozzles and its effects on spray and mixture formation," in *Fuel Injection Systems 2003: IMechE Conference Transactions 2003*, 2003, .

[99] B. Reid *et al*, "On the formation of string cavitation inside fuel injectors," *Exp. Fluids*, vol. 55, (1), pp. 1-8, 2014.

[100] N. Mitroglou *et al*, "Cavitation inside enlarged and real-size fully transparent injector nozzles and its effect on near nozzle spray formation," in *Proceedings of the DIPSI Workshop 2011. Droplet Impact Phenomena & Spray Investigations*, 2011, .

[101] C. Arcoumanis *et al*, "Cavitation in real-size multi-hole diesel injector nozzles," *SAE Technical Paper*

2000-01-1249, 2000.

[102] K. Nishida *et al*, "Characterization of cavitation flow in a simple hole nozzle," *International Journal of Fluid Mechanics Research*, vol. 24, (1-3), 1997.

[103] C. Soteriou, M. Smith and R. Andrews, "Diesel injection: Laser light sheet illumination of the development of cavitation in orifices," in *IMECHE Conference Transactions*, 1998, .

[104] (28th July 2016). *BETA CAE Systems*, Retrieved from website available at the following link: <http://www.beta-cae.com/epilysis.htm>.

[105] R. Lockett *et al*, "An Optical Characterization of the Effect of High-Pressure Hydrodynamic Cavitation on Diesel," *SAE Technical Paper 2016-01-0841*, (-), pp. -, 2016. . DOI: 10.4271/2016-01-0841.

[106] T. Sun, H. Ganesh and S. Ceccio, "X-ray densitometry based void fraction flow field measurements of cavitating flow in the wake of a circular cylinder," in *APS Meeting Abstracts*, 2015, .

[107] I. Lee *et al*, "Scaling of Gas Diffusion Into Limited Partial Cavities," *Journal of Fluids Engineering*, vol. 138, (5), pp. 051301, 2016.

[108] O. Coutier-Delgosha *et al*, "Internal structure and dynamics of sheet cavitation," *Phys. Fluids*, vol. 18, (1), pp. 017103, 2006.

